# Predictability of heavy precipitation events in the Mediterranean : Propagation of uncertainties related to the parameterisation of cloud micro-physics and atmospheric turbulence

Alan Hally


# THÈSE

**En vue de l'obtention du**

## DOCTORAT DE L'UNIVERSITÉ DE TOULOUSE

**Délivré par :** *l'Université Toulouse 3 Paul Sabatier (UT3 Paul Sabatier)*

---

**Présentée et soutenue le** *13/11/2013* **par :**

**Alan HALLY**

---

**Prévisibilité des épisodes méditerranéens de précipitations intenses: Propagation des incertitudes liées aux paramétrisations de la microphysique des nuages et de la turbulence**

---

**JURY**

| | |
|---|---|
| Sylvain Coquillat | Président du Jury |
| Silvio Davolio | Rapporteur |
| Christian Barthlott | Rapporteur |
| Victor Homar | Examinateur |
| Véronique Ducrocq | Directrice de thèse |
| Evelyne Richard | Directrice de thèse |

---

**École doctorale et spécialité :**
*SDU2E : Océan, Atmosphère et Surfaces Continentales*
**Unité de Recherche :**
*Laboratoire d'Aérologie (UMR 5560)*
**Directeur(s) de Thèse :**
*Evelyne Richard* et *Véronique Ducrocq*
**Rapporteurs :**
*Silvio Davolio* et *Christian Barthlott*

# Remerciements

Tout d'abord je tiens à remercier mes deux directrices de thèse, Evelyne Richard et Véronique Ducrocq. Je vous remercie beaucoup de m'avoir soutenu et guidé pendant mon travail de recherche, et d'avoir été patientes avec mes fautes de français !

J'aimerais aussi remercier Juan Escobar et Didier Gazen, les guerrièrs de Méso-NH. Vous étiez toujours disponible pour répondre à mes nombreuses questions avec patience et gentillesse.

Un grand merci à Soline Bielli de m'avoir aidé avec les complexités de NCL et aussi de m'avoir supporté dans son bureau. Merci également a Michael Faivre et Philipp Scheffknecht qui ont pris la suite de Soline.

Je remercie Frank Roux et tous les gens du Laboratoire d'Aérologie qui m'ont accueilli si chaleureusement.

Merci beaucoup aux membres du jury d'avoir accepté de se plonger dans mon manuscrit.

Pour dire un dernier mot, mais surtout pas le moindre, je tiens à remercier les doctorants de l'Observatoire Midi-Pyrénées et surtout ceux du LA. Ce n'est jamais facile de quitter chez soi pour un autre pays, mais vous l'avez rendu beaucoup plus facile avec vos propositions de sortie, votre aide pour trouver du logement et votre humour. Vous êtes tous les bienvenu(e)s en Irlande quand vous le voulez !

# Acknowledgements

The first and most important thank you goes to my family and especially to my parents. The possibility to come to Toulouse and undertake this work wouldn't have been possible without your continuous support and encouragement. A special thank you also to my Nana and grand-uncle, two people who gave me a love of learning that has gotten me to where I am today.

A huge thank you to all my friends in Toulouse, Ireland, Australia or wherever you may be!

Finally, I would like to thank Peter Lynch, Ray Bates, Rodrigo Caballero and all the other great lecturers at University College Dublin who instilled in me a passion for the world of meteorology.

# Contents

# Introduction en français

Les événements fortement précipitants sont des phénomènes naturels extrêmes qui se retrouvent dans toutes les régions du Monde. Leurs effets peuvent être dévastateurs : des crues soudaines et des glissements de terrain provoquent la perte de vies humaines et animales ainsi que l'interruption de l'activité économique. En se focalisant par exemple sur la seule année 2013, on compte déjà de nombreux événements catastrophiques. Suite à une activité cyclonique persistante en janvier 2013, l'est de l'Australie a souffert de crues étendues qui ont conduit à des dégâts d'une valeur de presque 2 milliards d'euros. Une dépression stationnaire, flanquée de deux centres anti-cycloniques, a provoqué de fortes précipitations sur les pays d'Europe centrale entre mai et juin 2013. Les crues qui en ont résulté ont été la source de dommages significatifs dans plusieurs pays tels que l'Autriche, l'Allemagne et la République tchèque. Le coût total de cet événement a été de l'ordre de 12 milliards d'euros.

Pendant les mois de septembre à novembre, la région de la Méditerranée nord-occidentale est exposée à un type d'événement fortement précipitant qui, en raison des reliefs avoisinants, est très spécifique à la région. En automne, la mer Méditerranée reste assez chaude par rapport aux terres qui l'entourent. Quand les vents de sud passent au-dessus de cette mer chaude, de l'humidité est collectée et transportée par l'écoulement de basses couches qui, contraint par le relief, va converger en direction du littoral. Ce flux chargé d'humidité est ensuite forcé à s'élever dans l'atmosphère, soit par la convergence dans les bases couches, soit par la présence d'une plage d'air froid ou soit encore par l'orographie, déclenchant ainsi de la convection susceptible de mener à des événements très violents et dont les conséquences sont largement amplifiées par la rapidité de la réponse hydrologique. Ces événements peuvent avoir des effets catastrophiques pour les populations locales. En automne 1987, dans le sud-est de l'Espagne, 800 mm de pluie sont tombés en moins de 24 h près de la ville de Gandia et y ont provoqué d'énormes dégâts (Fernandez *et al.* (1995)). La région du Piedmont en Italie a connu un événement particulièrement sévère en novembre 1994 quand 300 mm de pluie tombés en moins de 36 h ont conduit à une soixantaine de victimes et des dégâts d'une valeur de 12 milliards d'euros (Buzzi *et al.* (1998)). En 1999, une crue éclair faisant suite à de fortes précipitations dans le département de l'Aude dans le sud-est de la France a entraîné la mort d'au moins 23 personnes (Ducrocq *et al.* (2002)). En 2002, 700 mm de pluie sont tombés en 24 h sur le département du Gard dans le sud de la France. Cet épisode a causé 20 victimes et des dommages d'un milliard d'euros (Nuissier *et al.* (2008)).

La fiabilité et la précision des prévisions météorologiques de ces événements sont

d'un intérêt majeur pour l'anticipation des mesures de protection civile. Ceci a conduit la communauté scientifique à mettre en place divers projets de recherche ayant pour but d'améliorer notre compréhension du développement et de l'évolution de ces événements et d'en améliorer la prévision. MEDEX (MEDiterranean EXperiment), DRIHM (Distributed Research Infrastructure for Hydro-Meteorology) et HyMeX (HYdrological cycle in Mediterranean EXperiment) sont trois exemples de tels projets. MEDEX avait pour objectif d'examiner plus en détail la prévision des dépressions méditerranéennes et des événements extrêmes qui leur sont associés, ainsi que d'en étudier les impacts sociétaux. DRIHM, un projet lancé récemment et bénéficiant d'un financement de l'Union européenne, vise à améliorer la collaboration entre météorologues, hydrologues et experts en technologies de l'information et de la communication afin de conduire à de meilleures prévisions hydro-météorologiques pendant les épisodes de fortes pluies. HyMeX est un projet international de recherche qui vise à une meilleure compréhension du cycle de l'eau en Méditerranée. HyMeX a réalisé sa première campagne d'obervations intensives (*Special Observing Period*, SOP1) de septembre à novembre 2012. L'amélioration de la prévision des événements fortement précipitants en Méditerranée nord-occidentale était au coeur des objectifs la SOP1 d'HyMeX.

Un point important pour l'amélioration de la prévision d'événements fortement précipitants réside dans l'amélioration de la prévision de la convection profonde. Dans les modèles globaux, les processus convectifs sont paramétrés. La résolution horizontale de ces modèles ne permet pas de résoudre explicitement les interactions complexes et multi-échelles prenant place au sein des systèmes nuageux à fort développement vertical. Ces dernières années, avec l'augmentation de la puissance de calcul, les modèles régionaux sont devenus capables de fonctionner à l'échelle kilométrique, ce qui leur permet de résoudre explicitement les processus de la convection. Selon leur résolution spatiale, ces modèles sont désignés par *Convection-Permitting Models* ou *Convection-Resolving Models.* Cependant, malgré ces progrès, la précision de la prévision numérique de ces événements reste limitée. Cela est dû en grande partie à la nature de l'atmosphère qui est fondamentalement chaotique. Cette caractéristique limite la précision des prévisions numériques déterministes. En particulier, dans la prévision de la convection profonde, les erreurs et les incertitudes liées aux processus de petite échelle peuvent s'accroître rapidement, ce qui diminue la capacité du modèle à prévoir correctement l'évolution d'un événement météorologique. Ceci a conduit au développement de stratégies de prévision probabiliste dont le but est de prendre en compte les erreurs et les incertitudes inhérentes à l'état initial de l'atmosphère et aux paramétrisations du modèle. Plutôt que de produire une seule prévision déterministe, les systèmes de prévision d'ensemble produisent un éventail de prévisions, ou membres, qui ont des représentations des conditions initiales, conditions aux limites et processus physiques légèrement différentes entre elles. Ceci permet le développement d'une vision probabiliste de l'évolution de l'atmosphère et la description des erreurs liées aux incertitudes dans la formulation du modèle.

Deux sources d'incertitudes sont devenues de plus en plus importantes avec l'accroissement de la résolution des modèles, la représentation des processus de la physique des nuages (ou microphysique) et de la turbulence de la couche limite. Aux échelles où les

nuages sont explicitement résolus, les processus de la microphysique contrôlent le développement des nuages et des précipitations dans le modèle, ce qui les lie directement aux processus de la convection et à l'évolution des systèmes convectifs. Les processus de turbulence de la couche limite sont également d'une grande importance pour une meilleure représentation de la convection humide. Une augmentation de la résolution permet une description explicite partielle de la turbulence, mais les tourbillons de petite échelle restent non-résolus et donc paramétrés. Comme ces paramétrisations utilisent nécessairement des hypothèses et simplifications, elles introduisent des erreurs dans le système de prévision. Pour décrire ces incertitudes, des perturbations des paramétrisations de chaque processus peuvent être introduites. L'utilisation d'un grand nombre de perturbations permet ainsi de construire un système de prévision d'ensemble et donc de prendre en compte l'erreur des paramétrisations.

L'objectif de ce travail est d'évaluer l'importance de ces incertitudes et leur impact sur la distribution des précipitations simulées par un modèle de prévision à l'échelle kilométrique et pour des échelles de temps d'une courte durée. Le Chapitre 1 introduit les différentes méthodes par lesquelles les processus de la microphysique et la turbulence sont paramétrés en soulignant les zones d'incertitudes potentielles. Une introduction au domaine de la prévision d'ensemble est également fournie avec des exemples de plusieurs études ayant mis en oeuvre des systèmes de prévision probabiliste. Le Chapitre 2 décrit le modèle utilisé dans ce travail ainsi que la méthodologie adoptée pour construire une prévision d'ensemble fondée sur la perturbation des paramétrisations de la microphysique et de la turbulence. Cette méthodologie est utilisée pour étudier une super-cellule et une ligne de grain idéalisées. Inspirées par les résultats du chapitre 2, des simulations d'ensemble avec physique perturbée, effectuées pour une série de cas réels récents, sont décrites au chapitre 3. Le chapitre 4 est consacré à deux situations de lignes convectives observées pendant la SOP1 de HyMeX. La sensibilité des précipitations aux incertitudes de la physiques y est évaluée et comparée à celle induite par les incertitudes des conditions initiales et aux limites du modèle. Le manuscrit se termine avec les conclusions et perspectives du travail réalisé pendant cette thèse.

# Introduction

Heavy precipitation events (HPEs) are an extreme weather phenomenon frequently occurring in many parts of the world. The effects of such phenomena can be devastating: flash-flooding, landslides, loss of human and animal life, disruption of economic activity. Using solely the year 2013 as an example, numerous catastrophic events have occurred. In the aftermath of persistent cyclonic activity in January 2013, Eastern Australia suffered extensive flooding which led to almost €2 billion worth of damage. A stationary low-pressure system, flanked to the west and the east by blocking highs, brought persistent and heavy rainfall to Central Europe in May and June 2013. The resulting floods caused significant damage in many countries, including Austria, Germany and the Czech Republic. Total costs of this heavy rain event were reported to have been close to €16 billion.

Between the months of September and November, the Mediterranean region is affected by a type of HPE which, due to the complex geography of the surrounding area, is unique to this region. In the autumn months, the Mediterranean sea remains quite warm compared to the land basins which surround it. As southerly winds pass over this warmer sea, moisture is picked up and advected along with the flow, which is forced to converge on the south-eastern coastlines by the surrounding orography. This moisture laden-flow is then forced to rise into the atmosphere (either by low-level convergence, a low-level cold pool or by local orography) triggering convection which can lead to some very active and dangerous precipitation events. These Mediterranean HPEs can have devastating effects on the local economy. In autumn 1987, in south-eastern Spain, 800mm of rain fell in less than 24 h near the city of Gandia which led to enormous damage in the local community (Fernandez *et al.* (1995)). The Piedmont region of Italy also suffered a catastrophic heavy rain event in November 1994, when 300mm of rain in less than 36 h resulted in the deaths of 60 people and €12 billion worth of damage (Buzzi *et al.* (1998)). In 1999, flash-flooding after a HPE in the Aude department in southern France caused the death of at least 23 people (Ducrocq *et al.* (2002)). In 2002, 700mm of rain fell in 24 h over the Gard department in southern France resulting in the deaths of at least 20 people and €1 billion in damages (Nuissier *et al.* (2008)).

Accurate forecasts of these events are thus of the utmost importance, which has led to the establishment of numerous international research projects aiming to improve the understanding of their development and evolution. MEDEX (MEDiterranean EXperiment), DRIHM (Distributed Research Infrastructure for Hydro-Meteorology) and HyMeX (HYdrological cycle in Mediterranean EXperiment) are three examples of such projects. MEDEX concentrated on the forecasting of Mediterranean cyclones and on

the extreme weather events associated to them while also investigating the societal impacts of such phenomena. DRIHM is a recently launched EU funded project which aims to improve the collaboration between meteorologists, hydrologists and information and communication technology experts and thus lead to better hydrological forecasts for HPEs. HyMeX is an international research project which seeks to better understand and forecast the water cycle in the Mediterranean. It undertook its first Special Observing Period (SOP1) in September 2012. At the core of SOP1 is a desire to improve the forecasting of HPEs which, especially between the months of September to November, can greatly affect the water cycle in the Mediterranean region.

A key issue in the improvement of the forecasting of HPEs is an improvement in the forecasting of moist convection. In climate and global models, the convective processes are parameterised by different schemes as these models run at a horizontal resolution which is not capable of explicitly resolving the complex interactions which take place during convection initiation. In recent years, with the advance of computing power, regional models have been capable of performing simulations at kilometric scale resolutions, thus leading to nearly explicit resolution of the convective processes. Depending on the resolution, these models are referred to as Convection-Permitting Models or Convection-Resolving Models. However, despite these research efforts and advances in numerical weather prediction, the skill with which HPEs can be forecast remains limited. This is due in large part to the fundamental chaotic nature of the atmosphere which places a limit on the accuracy of deterministic numerical forecasts. In particular, when forecasting deep convection, errors and uncertainties related to small-scale processes can grow quickly, disrupting the ability of a model to accurately forecast the development of a future weather event. This has led to the development of a probabilistic forecasting strategy, which aims to represent the errors and uncertainties which are inherent in the initial atmospheric state and in the formulation of the numerical model. Instead of producing a single deterministic forecast for an event, ensemble prediction systems (EPSs) produce a number of forecasts, or members, which have slightly different representations of the initial conditions, boundary conditions and physical processes. This allows a probabilistic picture of the evolution of the atmosphere to be developed and the errors related to model formulation uncertainties to be represented.

Two sources of uncertainty, which have become increasingly important with increased model resolution, are the representation of the microphysical cloud processes and the processes of boundary layer turbulence. At cloud-resolving scales, microphysical processes control the development of cloud and rainfall within the model, linking them directly to the processes of convection, the evolution of a convective system and the localisation of the rainfall pattern. The boundary layer turbulence processes are also of great importance to the improved representation of moist convection. Increasing the resolution leads to the explicit representation of some of the turbulent properties but, the small-scale turbulent eddies remain unresolved, and thus remain parameterised. As these parameterisations use assumptions and simplifications when describing these processes, errors in their representation are introduced into the forecasting system. In order to represent these uncertainties, perturbations can be per-

formed upon the process parameterisations. Using numerous perturbations allows an EPS to be constructed and thus permits the parameterisation error to be represented.

The importance of these uncertainties and their impact upon the rainfall field simulated by a forecasting model at the kilometric scale and at short-range time-scales are the focus of this study. Chapter 1 introduces the different methods by which the microphysical and turbulence processes are parameterised, highlighting areas of potential uncertainty. An introduction to the domain of ensemble forecasting is given with examples of previous studies which successfully implemented probabilistic forecasting systems. Chapter 2 describes the research model used throughout this study, the ensemble forecasting methodology applied to an idealised supercell and idealised squall line set-up and the method employed to perturb the uncertainties associated to the microphysical and turbulence processes. Inspired by the results of the idealised simulations in Chapter 2, ensemble simulations with perturbed physical parameterisations are performed for real world cases in Chapter 3. The sensitivity of the rainfall field of two convective systems observed during the HyMeX SOP1 to physical parameterisation uncertainties is presented in Chapter 4. A comparison between the level of sensitivity to physical parameterisation uncertainties and that of initial and boundary condition uncertainties is also described in Chapter 4. The manuscript ends with conclusions and perspectives of the work undertaken during this thesis.

# Chapter 1

# Physical parameterisations and ensemble forecasting

## 1.1 Microphysical parameterisations

Clouds play a vital role in the drama that unfolds in our skies on a daily basis. They exert a strong influence on the short-wave and long-wave radiative transfer, they act as a stage upon which water vapour converts itself to precipitation and they are a very important part of heat transfer within the atmosphere, due to their release of latent heat. Because of this importance, it is of the utmost interest to represent accurately the various processes operating within clouds in order to properly forecast the state of the atmosphere. It is not yet possible however, due to the extreme complexity of the mechanisms involved, to model them explicitly, thus assumptions and simplifications in the form of parameterisations have to be made. These parameterisations come in two forms; bin models and bulk models. Bin models look to explicitly calculate the evolution of the particle size distribution by segregating the particles into different bins. These bins are defined according to different particles sizes and thus many bins are needed to describe cloud condensation nuclei, cloud droplets and raindrops, not to mention the large number of bins needed to explicitly define the different ice hydrometeors. There are many examples of such models including Feingold and Grund (1994), Harrington *et al.* (1999) and Jiang *et al.* (2000). Despite being more physically accurate in their description of the different particle distributions, bin models are rarely implemented in numerical weather prediction models due to the enormous computational cost that would be involved in doing so. To find a balance between cost and an accurate physical description of the atmosphere, one resorts to bulk models, which represent the hydrometeor sizes according to a distribution function, allowing for computationally less expensive simulations. For this reason, this state of the art will focus solely on bulk model representations.

### 1.1.1 Particle distributions and one and two-moment schemes

Bulk models usually describe a number of different classes of hydrometeor, and assume a distribution function for each class of particle, with raindrops, cloud droplets, graupel, ice, snow and sometimes hail being described. This idea of a distribution function began with the pioneering work of Marshall and Palmer (1948) (MP). They assumed that the raindrop particles were distributed according to the generalised form,

$$n(D) = N\ g(D) \tag{1.1}$$

with $n(D)$ being the number of drops as a function of the drop diameter $D$, $N$ being the total drop number concentration and $g(D)$ being a normalised distribution law. Observations led them to propose the following form for $g(D)$,

$$g(D) = \lambda\ \exp(-\lambda D) \tag{1.2}$$

with $\lambda$ being the slope parameter.

Passarelli (1978) later applied the MP distribution to snow flakes within an analytical model leading to “fair agreement“ between theoretical and observed values of snowfall rate. Ziegler (1985) later extended the use of the inverse exponential function to represent his hail/graupel category following the work of Houze *et al.* (1979). This same author also showed however that the MP distribution can be unrealistic at small diameters below which the observed distribution deviates from the MP distribution. This led several authors to choose a generalised gamma function when defining the raindrop distribution law (Williams and Wojtowicz (1982), Willis (1984) and Ziegler (1985)),

$$g(D) = \frac{\alpha}{\Gamma(\nu)}\ \lambda^{\alpha\nu}\ D^{\alpha\nu-1}\ \exp(-(\lambda\ D)^{\alpha}) \tag{1.3}$$

This distribution has two additional parameters and offers more flexibility than the MP distribution. Fig. 1.1 shows the different distributions possible with different values of the shape parameter $\nu$. This parameter controls the relative amount of smaller vs. larger hydrometeors in the distribution. $\alpha$, the scale parameter, controls the spread in the distribution, the larger its value, the more the distribution would spread to the right in Fig. 1.1. It can be noted that when $\alpha$ and $\nu$ both equal 1, the gamma distribution degenerates into the MP distribution. In principle, the gamma distribution allows a better match to observed distributions. However, suitable observations are not always available and often $\alpha$ and $\nu$ are arbitrarily prescribed. Meyers *et al.* (1997) and Milbrandt and Yau (2005) demonstrated that the value of $\alpha$ can affect the peak in accumulated surface precipitation as well as impacting upon the sedimentation and microphysical source/sink terms.

Bulk models are usually cast into two categories. If only the time evolution of the mixing ratio (or water content) of each particle type is predicted, the scheme is referred to as a one-moment scheme. These schemes differ from two-moment schemes, which additionally predict the time evolution of the number concentration of the particle type. In the absence of a prognosed concentration (one-moment scheme), further assumptions have to be made in order to define the distributions. The total number

concentration, $N$, is in this case either kept constant, or more commonly, related to the slope parameter ($\lambda$) through a power relationship,

$$N = N_0 \, \lambda^x \tag{1.4}$$

ls where $x$ and $N_0$ are constants which depend upon the particle class. For raindrops, classically $x$=-1, and in the case of the MP distribution, $N_0$ represents the intercept parameter of the distribution. Both $N_0$ and $x$ have to be prescribed for each particle type. Large discrepancies can exist in the values of these constants depending on the author and/or data-sets used. For instance, Waldvogel (1974) proposed a range for $N_{0r}$, or the raindrop intercept parameter, of between $0.4 \; 10^7 m^{-4}$ and $3.5 \; 10^7 m^{-4}$. Knight *et al.* (1982) proposed a range for $N_{0g}$, the graupel intercept parameter, of between $10^4 m^{-4}$ and $10^8 m^{-4}$. More recently, Gilmore *et al.* (2004) showed the impact of changing the value of $N_{0g}$ upon supercell characteristics by using a range of values stretching between $4 \; 10^2 m^{-4}$ and $4 \; 10^8 m^{-4}$. He showed that values of $N_{0g}$ from the upper end of this spectrum gave less accumulated precipitation at the ground. Solomon *et al.* (2009) reported values for $N_{0s}$, the snow intercept parameter, of between $2 \; 10^5 m^{-4}$ and $6 \; 10^5 m^{-4}$ which contrasts with the value of $2 \; 10^7 m^{-4}$ used in Dudhia (1989).

To summarise, in single-moment schemes, up to four parameters must be prescribed to fully describe the size distribution of each particle type. Given the wide range of their observed values (especially for the ice category), they present obvious sources of uncertainty.

Prognosing the time evolution of the number concentration of each particle type decreases the level of uncertainty but adds to the computational cost. Reisner *et al.* (1998) carried out simulations to underline the differences in using a one-moment and a two-moment scheme. Their one-moment scheme prescribed the mixing ratios for the water and ice species, while the two-moment scheme included prescribed relationships for the number concentrations of ice, snow and graupel. The results show a significant increase in agreement with observations when the two-moment scheme is implemented for a study of the supercooled liquid water for two winter storms which occurred over the Rocky Mountains in 1990. Thompson *et al.* (2004) also rigorously tested this scheme, examining the flow over an idealised two-dimensional mountain. They suggested several improvements to the scheme including introducing a snow intercept parameter which depended on temperature and a rain intercept parameter which was related to the rain mixing ratio. Seifert and Beheng (2006) described a slightly different two-moment scheme. Mass density and number concentration of five hydrometeor classes were prescribed including a full treatment of cloud droplet number concentration. This parameterisation was designed especially for use in high-resolution mesoscale models and, unlike the schemes of Reisner *et al.* (1998) and Thompson *et al.* (2004), allowed the effects of cloud condensation nuclei upon cloud formation to be evaluated. Morrison *et al.* (2005) presented a further double-moment parameterisation which differed slightly from the schemes previously introduced. The number concentration and mixing ratio of the specified hydrometeor species again serve as prognosis variables with new physically based parameterisations for simulat-

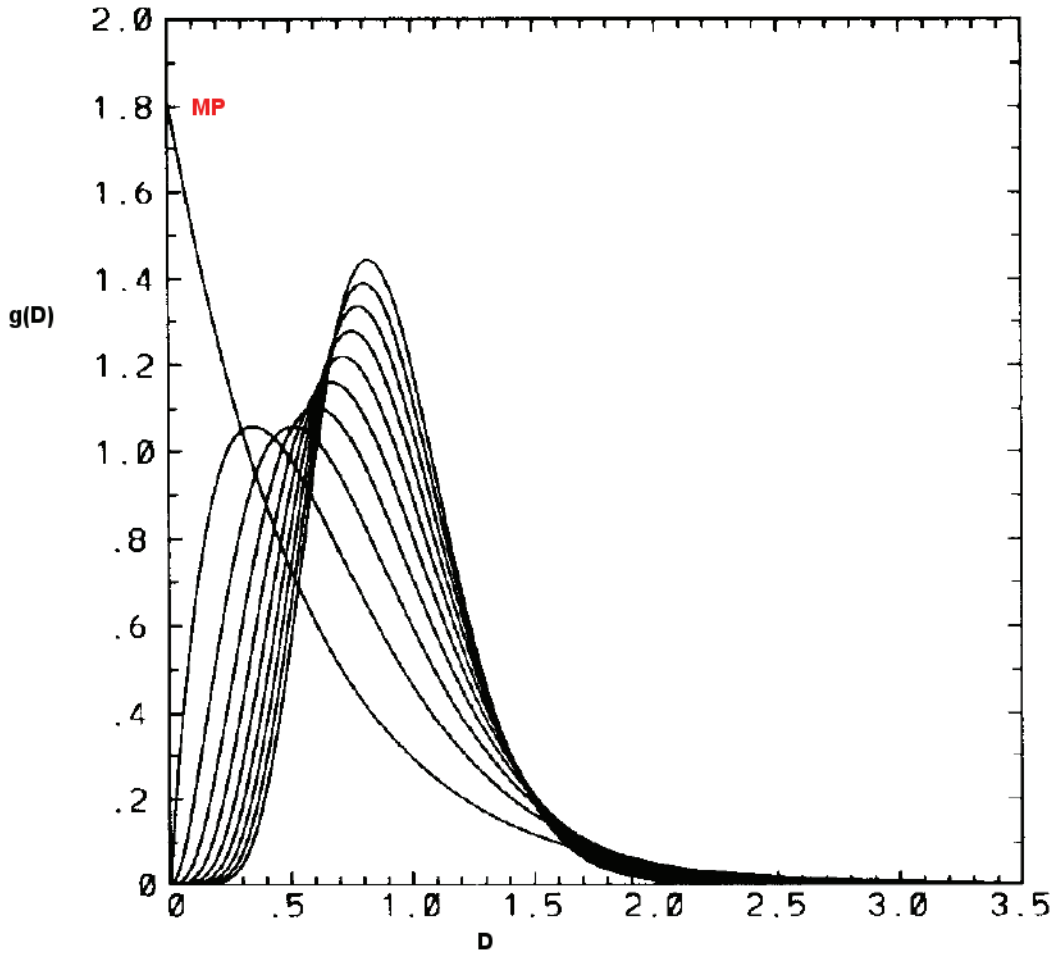


**Figure 1.1:** *Taken from Walko* et al. *(1995), this figure illustrates a set of gamma distribution curves for integer values of $\nu$ from 1 to 10, with $\alpha$ held fixed at 1. The values of $g(D)$ are given in function of the hydrometeor diameter. The curve labelled MP in red represents the Marshall-Palmer distribution with $\nu$ and $\alpha$ equal to one. The peaks of the curves shift progressively to the right as $\nu$ increases.*

ing homogeneous and heterogeneous ice nucleation outlined. Morrison *et al.* (2005) described two versions of the scheme, one to be implemented at high-resolutions and a second more suitable to coarser resolution models where supersaturation cannot be resolved.

Overall, two-moment schemes tend to give more accurate representations of the time evolution of the different drop species. However, the higher computational cost of these schemes means that their implementation in an operational forecasting system is rare and they are more often reserved for research activities.

### 1.1.2 Hydrometeor characteristics

The mass and fall speeds of each particle type are also user-defined within most bulk models. The most common method for defining these parameters is to follow the observational work of Locatelli and Hobbs (1974), who measured the fall speeds and masses of a large number of different precipitating particles. Fig. 1.2 illustrates the variety of solid particles which were noted during this observational work. Two key relationships were used to classify the hydrometeors; one related the mass of the particle to its diameter,

$$M = a\ D^b \tag{1.5}$$

and the other related the fall speed of the particle to its diameter,

$$V = c\ D^d \tag{1.6}$$

where the constants a,b,c and d describe the different characteristics of the precipitating particles, of which Locatelli and Hobbs (1974) measured 6 graupel and 8 snow categories. Foote and Toit (1969) and Liu and Orville (1969) described terminal velocities and mass-diameter distributions for raindrops, while Heymsfield and Musil (1982) and later Starr and Cox (1985) offered representations of the ice particle velocities and mass-diameter distributions. Sensitivity to the ice particle representation is shown by the work of Ferrier (1994). Two different sets of fall speed coefficients are used to perform simulations of an intense squall line over southeastern Virginia. Their results show that the precipitation distribution and fallout were affected by modifying the ice particle characteristics. Gilmore *et al.* (2004) reported on the sensitivity of ground precipitation to modifications in the graupel/hail density properties, thus in turn manipulating the mass and fall speeds. He demonstrated that the heavier (lighter) particles had the tendency to remain at higher altitudes (to fall faster) thus decreasing (increasing) the precipitation volume which reached the ground.

### 1.1.3 Warm process parameterisations

Parameterisation of the microphysical processes dates back to the late 60's and the famous work of Kessler (1969). In this monograph, where only warm-rain clouds were investigated, he observed that the liquid water species can be broken into cloud droplets and raindrops. The cloud water within his formulations comes from condensation, and consists of small droplets with negligible velocity. Cloud water can be converted into rain when the cloud water content (given as $q_{crit}$ in equation 1.7) reaches a value of between $0.5$ to $1gm^{-3}$. The raindrops can simultaneously grow by the accretion of cloud water droplets, or can evaporate below the cloud level. Kessler proposed formulae to describe these processes. His autoconversion process, or the conversion of cloud water (represented by mixing ratio $r_c$) into rain water, was parameterised by the following relationship,

$$CAUTR = k\ (r_c - \frac{q_{crit}}{\rho_{dref}}) \tag{1.7}$$

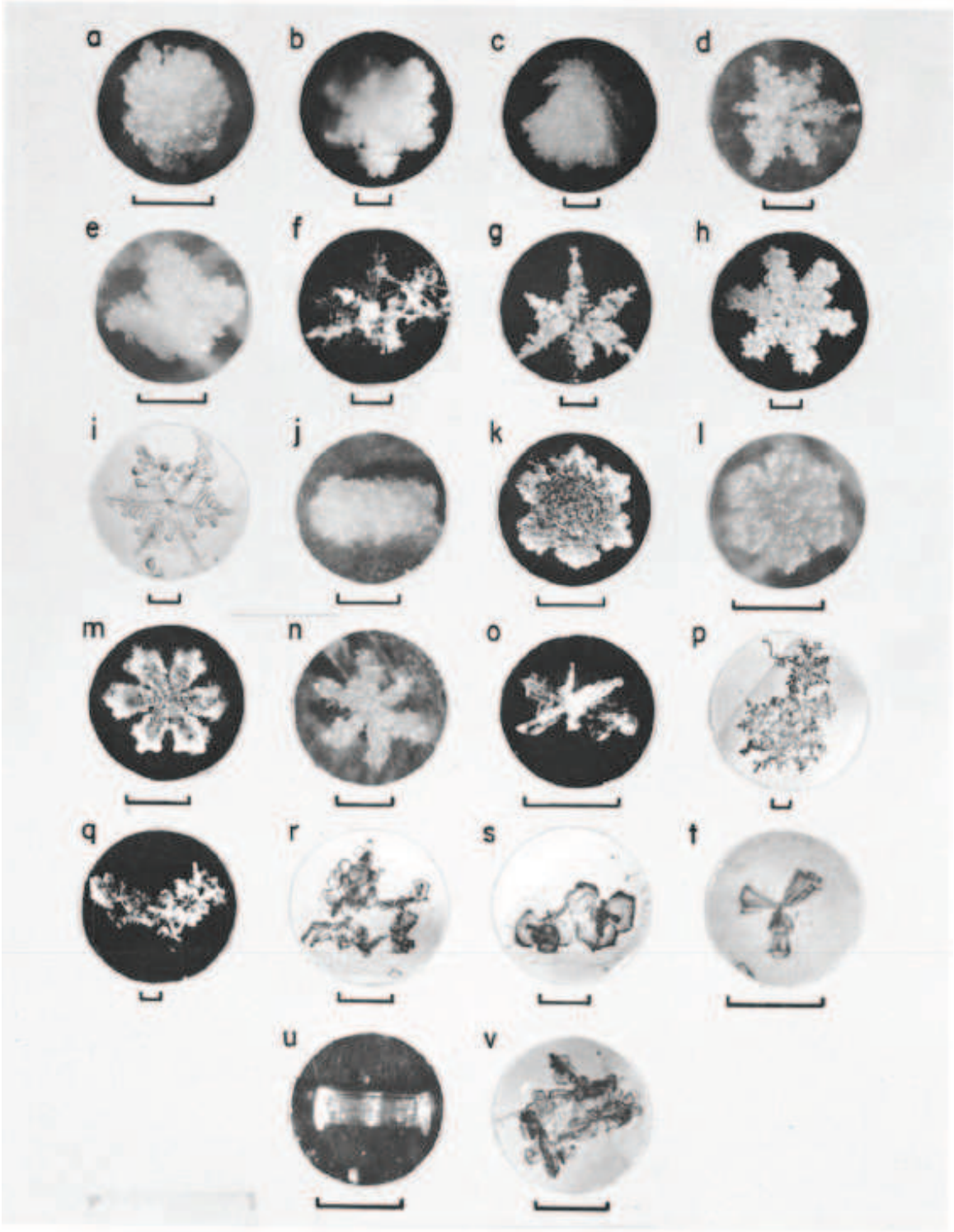


**Figure 1.2:** *From Locatelli and Hobbs (1974). This image displays the different types of solid precipitation particles on which measurements were made. The scaled line below each photograph represents 1mm.*

where $k$ is a time constant and $\rho_{dref}$ the air density. By this formulation, the autoconversion rate increases linearly with the cloud water mixing ratio. He also described suitably appropriate formulae for the accretion of raindrops and the evaporation of rainfall in terms of $N_0$ of the MP distribution, a capture efficiency E, the cloud content and the precipitation content. Klemp and Wilhelmson (1978), amongst others, used Kessler's formulations to simulate a three-dimensional convective storm. His formulations proved very effective in representing the warm microphysical processes, and are currently an option in many numerical forecasting models.

Despite the success of his parameterisations, due in large part to their simplicity and thus low computational cost, other warm-rain parameterisations have also been successful.

Berry and Reinhardt (1974a) and Berry and Reinhardt (1974b) proposed a slightly different approach to that of Kessler with their autoconversion parameterisations based upon results of the stochastic coalescence equations. The accretion and rain evaporation processes were also formulated in a slightly modified manner, with the accretion process being parameterised as a function of the collection kernal, while an extra term was added to the rain evaporation parameterisation in order to take into account the number of drops which disappear completely by evaporation per time step. A more complete comparison of the differences between the two parameterisations can be found in Richard and Chaumerliac (1989).

Pruppacher and Klett (1978) also reported upon warm cloud microphysical processes. They proposed a formula for calculating the evaporation of a raindrop of diameter D,

$$[\frac{dD}{dt}]_{evap} = \frac{4\ S\ \bar{f}}{\rho_{l\omega}\ A} \tag{1.8}$$

where $S$ and $A$ are defined as the following,

$$S = \frac{r_{vs} - r_v}{r_{vs}}, \tag{1.9}$$

$$A = \frac{R_v T}{e_s(T) D_v} + \frac{L_v(T)}{k_a T}(\frac{L_v(T)}{R_v T} - 1) \tag{1.10}$$

$$\simeq \frac{R_v T}{e_s(T) D_v} + \frac{L_v(T)^2}{k_a R_v T^2}. \tag{1.11}$$

and where $r_{vs}$ is the saturated vapor mixing ratio, $D_v$ is the diffusivity of water vapor in air and $k_a$ is the heat conductivity of air. All other terms are defined in Appendix A. This formulation involves a ventilation coefficient, $\bar{f}$, which in turn depends on the Reynolds number of the flow around the water drop. Comparisons of experimentally determined ventilation coefficients for water drops and a parameterisation of the coefficient is discussed within Pruppacher and Klett (1978). It is shown that at certain equivalent drop radii, the observed coefficient can differ from the theoretically derived version. A comparison of the observed and derived coefficient is shown in Fig. 1.3. This gives a degree of uncertainty to the definition of the process, and shows that no matter how mathematically correct a formulation, simplifications and assumptions must be made compared to the complex reality of the process.

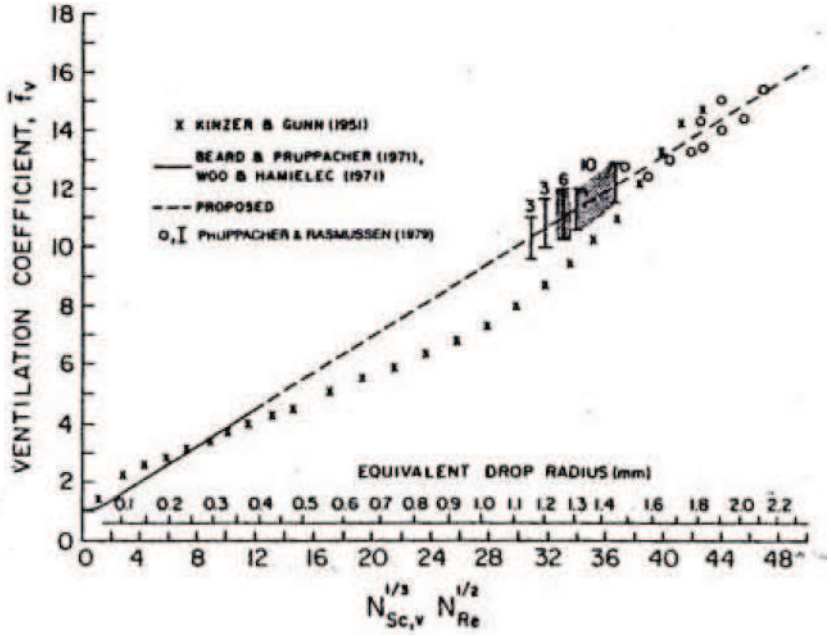


**Figure 1.3:** *From Pruppacher and Klett (1978). Displayed is a comparison of experimentally determined ventilation coefficients for water drops of large Reynolds numbers with an extrapolation of the theoretically computed ventilation coefficient for water drops at moderate Reynolds numbers.*

The evolution of the representation of the warm microphysical processes shows a tendency towards increasingly complex and realistic parameterisations. However, due in large part to the sparse collection of observational data, these parameterisations remain somewhat deficient in describing the exact nature of the warm microphysical processes.

### 1.1.4 Cold process parameterisations

The cold cloud microphysical processes also play a very important part in the interactions between the different water species. Thus representing them accurately is important for our understanding of atmospheric convection. One of the earliest bulk parameterisation schemes for the cold processes was proposed by Lin *et al.* (1983). They defined six different water species (water vapour, cloud water, cloud ice, rain, snow and graupel) and five classes of hydrometeor (cloud water, cloud ice, rain, snow and hail) in order to simulate a moderate intensity thunderstorm for the High Plains region. They used a single-moment scheme, as only the mixing ratio of the different particles was used as a prognosis variable. The graupel and snow particles were distributed according to an inverse exponential distribution following MP. With this parameterisation they succeeded in realistically simulating the transformation of cloud ice to snow and onto hail. They also showed that the presence of the snow variable within their parameterisation reduced the amount of rainfall forming early in the life history of the cloud. Finally, they illustrated that, at least for their case study, the hail/graupel

melting was the main source of rainwater, even when the process of autoconversion of cloud drops into raindrops was active.

More recently, Straka and Mansell (2005) formulated a single-moment microphysical scheme with 10 ice categories characterised by their habit, size and density (two ice crystal habits, rimed cloud ice, snow, three categories of graupel, frozen drops, small hail and large hail). They claimed that this large number of hydrometeor classes allowed a variety of convective storms to be simulated with minimal parameter tuning. All of the precipitating particles were distributed following the MP inverse exponential law. One of the advantages of this scheme is that it uses what they call a riming history to calculate the transitions between the graupel and frozen drop categories, which provides smoother transitions in particle density and fall speed. Having multiple categories of ice defined adds realism to their simulations, and it is shown to be especially useful for the simulation of electrification and lightning.

The two schemes of Lin *et al.* (1983) and Straka and Mansell (2005) clearly show differences in their representation of the cold process parameterisations. Making comparisons between these two schemes, it is evident that there exists uncertainty as to the most appropriate approach for formulating the parameterisations. The definition of the different water species, the number of water species to employ and the method used to describe their distributions being just a few important differences. This incertitude demonstrates that, as for the warm processes, no one scheme can claim superiority over another when it comes to the representation of the processes.

### 1.1.5 Key processes in rainfall production

While all the cold and warm microphysical processes have some impact upon rainfall production, there are certain processes which will have a greater degree of importance. For warm clouds, the autoconversion process is the sole rainwater initiation mechanism, thus it plays an important role, especially in determining the first occurrence of rain within the model. Secondly, the evaporation of raindrops will also be quite important. Bresson *et al.* (2009) and Nuissier *et al.* (2008) amongst others have shown that the convective cold pool which develops below certain HPEs plays a role in sustaining convection while it can also lead to the formation of new convective cells. These convective pools are mainly alimented by the evaporation of raindrops below the cloud base. As the raindrops pass through the non-saturated layers below the cloud, evaporation takes place due to a release of latent heat. This leads to an area of cooler air forming beneath the cloud which constitutes the convective cold pool (Miglietta and Rotunno (2009), Miglietta and Rotunno (2010)). Thirdly, the melting of graupel or snow particles while falling through the atmosphere will also significantly impact upon the rainfall output (Ducrocq *et al.* (2008)).

The study of Lascaux *et al.* (2006), in which numerical simulations were carried out upon 3 cases of heavy precipitation in the Alps, illustrated the relative contribution of certain processes to the rainfall output. The three episodes which were investigated represented an intense and moderately convective system, as well as a case of stratiform precipitation. As demonstrated in Fig. 1.4, the main normalised sources for the

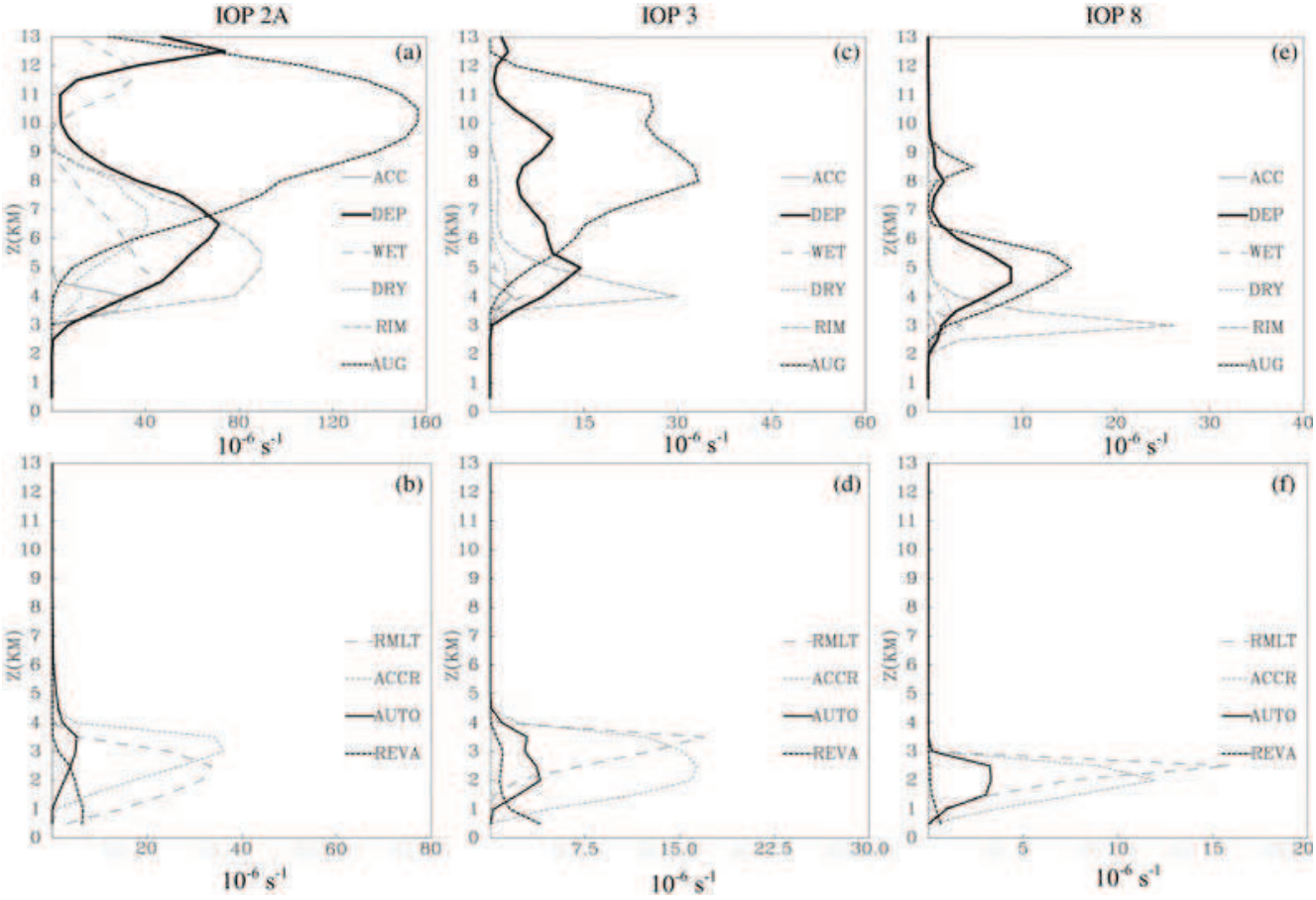


**Figure 1.4:** *Mean vertical structure of the main microphysical processes involved in IOP 2A of the Mesoscale Alpine Programme (MAP) (from Lascaux* et al. *(2006)); normalized sources acting on (a) the solid precipitation (snow, graupel. hail) and on (b) the liquid precipitation (rain). (c, d) and (e, f) are as (a, b), but for IOPs 3 and 8, respectively. The short-hand names for each process are taken from Fig. 1.6.*

liquid precipitation for each of the three cases were the melting of graupels, the accretion of cloud droplets by raindrops and the evaporation of raindrops. The autoconversion process was shown to be the trigger in the production of raindrops, but it was quickly outpaced by the melting and accretion sources at a height of 2 to 4km and by the evaporation of raindrops at heights of 1km or less. Further examination of Fig. 1.4 demonstrates that the relative importance of each process varied depending upon the nature of the situation.

### 1.1.6 Formulations used in convection-permitting NWP

Numerical models normally dispose of a range of microphysical parameterisations as, depending on the meteorological situation being studied, the suitability of a certain microphysical scheme will change. The WRF (Weather Research Forecasting) model offers a wide array of schemes, including the basic Kessler scheme (Kessler (1969)) and the breakthrough scheme of Lin *et al.* (1983). More recent schemes are also available for implementation. Hong *et al.* (2004) described a 5 class scheme with ice which

offered a number of modifications over earlier schemes such as Lin *et al.* (1983). They proposed a temperature dependent intercept parameter for snow, a new formula for diagnosing the cloud ice number concentration from cloud ice mass, a modified scheme for the autoconversion of cloud water to rain water and the inclusion of the sedimentation of falling ice crystals.

WRF, along with the NCAR/Penn State Mesoscale Model Version 5 (MM5), offers the use of the schemes described in Reisner *et al.* (1998) and Thompson *et al.* (2004), which were introduced in section 1.1.1. Thompson *et al.* (2008), also available as an option in WRF and MM5, is an improved bulk microphysical scheme compared to the latter two. This 6 class scheme has many observational based features including a rain intercept parameter that depends on the rain mixing ratio, a graupel intercept parameter that depends on the graupel mixing ratio and a variable gamma distribution shape parameter for cloud water droplets. Thompson also outlined other new features, notably an improved representation of vapour deposition, sublimation and evaporation along with improved rain-collection of snow and graupel.

The COSMO (Consortium for Small-scale Modelling) model offers a microphysical scheme based on the work of Seifert and Beheng (2001). This is a double-moment parameterisation of the microphysical processes in warm clouds and is directly derived from the stochastic collection equation. The authors described explicit rate equations for autoconversion, accretion and self-collection. An improved version of this scheme, described in Seifert and Beheng (2006) and also introduced in section 1.1.1, presents a revised scheme for the snow intercept parameter which becomes a function of temperature and the snow mixing ratio.

The non-hydrostatic model MOLOCH uses a scheme based on the methodology proposed by Drofa (1997), which was inspired in part by the work of Marecal *et al.* (1993) and Rutledge and Hobbs (1983). The one-moment scheme predicts the time evolution of the specific concentration of four microphysical species: cloud water, cloud ice, precipitating water (rain) and precipitating ice. Recently, upgrades have been performed and the scheme is now capable of being implemented as a double-moment parameterisation by integrating in time the spatial distribution of the number density of cloud water and ice which describe the cloud spectra evolution.

### 1.1.7 ICE3 formulation

This study will concentrate on the mixed-phase microphysical formulation ICE3 which is presented in Pinty and Jabouille (1998) and is used in the operational French model AROME (Seity *et al.* (2011)). The approach of Pinty and Jabouille (1998) follows that of Lin *et al.* (1983) closely, in that six water species (vapour, cloud droplets, raindrops, pristine ice, snow and graupel) are defined. The concentrations of the precipitating water drops and ice crystals are parameterised according to the work of Caniaux *et al.* (1994). The hydrometeor size-distributions are assumed to follow a generalised gamma-law of the form seen in equation (1.3). The mass-size and velocity-size relationships are defined according to Locatelli and Hobbs (1974).

The warm processes are parameterised using a Kessler type formulation, with the

autoconversion of cloud droplets to raindrops, the accretion of cloud water by raindrops and the raindrop evaporation being described. The autoconversion process equation is equivalent to that which was detailed in equation (1.7). The accretion of cloud water by raindrops ($CACCR$) takes the following form,

$$CACCR = \frac{\pi}{4} a N_0 (\frac{\rho_{00}}{\rho_{dref}})^{\alpha} r_c \Gamma(b+3) (\frac{\rho_{dref} r_r}{\pi \rho_{lw} N_0})^{\frac{b+3}{4}} \tag{1.12}$$

where $a$ and $b$ are numerical constants, $\rho_{dref}$ is the density at a reference level, $\rho_{lw}$ is the liquid water density. The meaning of all other symbols is given in Appendix A. The raindrop evaporation process is derived from the evaporation rate of a raindrop of diameter D given in equation (1.8). After replacing the factors $\bar{f}$, $S$ and $A$ by their full expressions and integrating over the raindrop spectrum, one obtains the following equation for the raindrop evaporation source ($REVAV$),

$$REVAV = \frac{2\pi S N_o}{A} \frac{1}{\rho_{dref}} \big[ (\frac{\rho_{dref} r_r}{\pi \rho_{lw} N_o})^{\frac{1}{2}} + F (\frac{\rho_{00}}{\rho_{dref}})^{\alpha/2} (\frac{a}{\nu})^{1/2} \Gamma(\frac{b+5}{2}) (\frac{\rho_{dref} r_r}{\pi \rho_{lw} N_o})^{\frac{b+5}{8}} \big] \tag{1.13}$$

where $S$ and $A$ retain their definitions given in equations (1.8)-(1.10). All other symbols have been previously defined or are given in Appendix A.

The cold process scheme involves the interaction of many processes (see Fig. 1.5 for process interactions and Fig. 1.6 for explanation of the sources and sinks of the different processes and the nomenclature used to describe each process). The pristine ice category is triggered within the scheme by homogeneous or heterogeneous nucleation. These ice crystals grow by the deposition of water vapour, and by the Bergeron-Findeisen effect. Autoconversion of the primary ice crystals initiates the snow phase and growth of these aggregates happens through the deposition of water vapour, the aggregation of small crystals and riming caused by impacting cloud and rain droplets. Graupel is formed by the continuous heavy riming of snow. As these graupel fall, they melt, becoming raindrops. The equations for all cold process equations can be found in the scientific documentation of the Méso-NH model, available here: http://mesonh.aero.obs-mip.fr/mesonh410/BooksAndGuides.

This scheme was tested on the tropical squall line described in Caniaux *et al.* (1994). The results show that the overall structure of the squall line was well reproduced by the model. Some limitations of the scheme were noted however as the vertical extent of the system compared to the observed radar reflectivity remained insufficient. It was reported that the evaporation of rainfall below the stratiform region helped to maintain the system, underlining the importance of correctly parameterising this process. As a second test, an area of orographic precipitation between the 12th and 13th of February 1985 over the Sierra Nevada in California was successfully modelled. Comparisons with observations showed that there was good ”quantitative agreement“ between observed and simulated values. The model also succeeded in maintaining a supercooled cloud droplet tongue within an area of glaciated cloud. This feature was observed by a field experiment conducted during this particular case and the schemes ability to correctly represent it illustrates that in particular the cold process parameterisations seem to be well formulated.

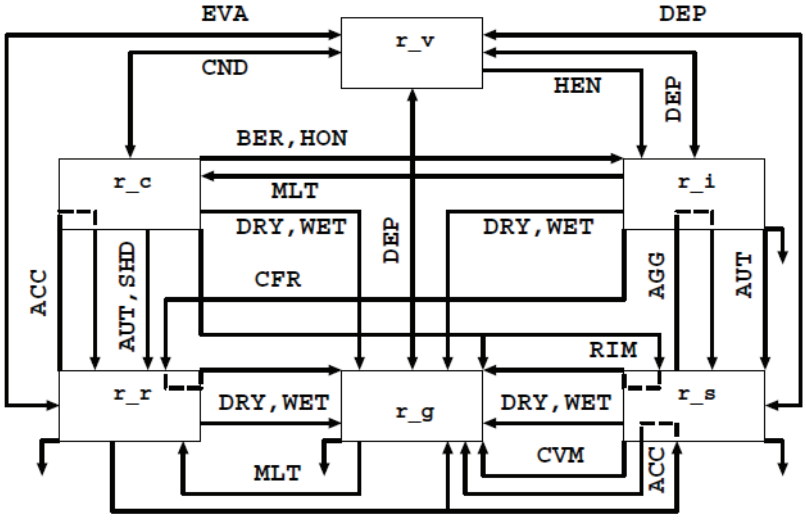


**Figure 1.5:** *The different interactions of the microphysical processes of ICE3. The short-hand explanation of each process is given in Pinty and Jabouille (1998). The $r_x$ represent the mixing ratios of the different water species.*

### 1.1.8 Summary of microphysical parameterisations

It has been seen that a large number of microphysical parameterisation schemes exist, whether it be for warm (Berry and Reinhardt (1974a)) or cold (Caniaux *et al.* (1994)) processes. Schemes can be of one (Lin *et al.* (1983)) or two-moments (Morrison *et al.* (2005)), have very few (Kessler (1969)) or very many (Straka and Mansell (2005)) defined water species. The schemes can differ by the way in which they define the processes that they parameterise (Kessler (1969), Berry and Reinhardt (1974b)) and in the choice of using MP (Lin *et al.* (1983)), generalised gamma (Pinty and Jabouille (1998)) or log-normal distributions (Berry and Reinhardt (1974a) and Berry and Reinhardt (1974b)).

All of these differences demonstrate that the best and most realistic way of reproducing the warm and cold cloud microphysical processes is unclear, with certain schemes being preferable according to the computational resources available and the situation being scrutinised. It also shows the large uncertainty there still exists in the world of parameterisation, whether it be a question of particle distribution choice, how best to describe the formation of ice and its progression into snow and eventually graupel, or how best to initiate the production of rainfall within a forecasting model. It is clear from this bibliographic synthesis that there is a large degree of sensitivity to these choices, and that depending on the choice made, the evolution and intensity of rainfall episodes forecast by the parent model will be impacted.

## 1.2 Turbulence parameterisations

Convection, and thus the rainfall of HPEs, are also quite sensitive to the simulation of the turbulent processes. One of the main factors to consider when simulating the turbulent processes is the horizontal resolution at which the simulation is performed.

| Symbol | Mechanism | Sink | Source | Process |
|---|---|---|---|---|
| V-HEN-I | $Rv \Rightarrow Ri$ | $Rv$ | $Ri$ | Heterogeneous nucleation |
| C-HON-I | $Rc \Rightarrow Ri$ | $Rc$ | $Ri$ | Homogeneous nucleation |
| R-HON-G | $Rr \Rightarrow Rg$ | $Rr$ | $Rg$ | Homogeneous nucleation |
| C-BER-I | $Rc \Rightarrow Ri$ | $Rc$ | $Ri$ | Bergeron-Findeisen effect |
| V-DEP-I | $Rv + Ri \Rightarrow Ri$ | $Rv$ | $Ri$ | Deposition (Sublimation) |
| V-DEP-S[d] | $Rv + Rs \Rightarrow Rs$ | $Rv$ | $Rs$ | Deposition (Sublimation) |
| V-DEP-G[d] | $Rv + Rg \Rightarrow Rg$ | $Rv$ | $Rg$ | Deposition (Sublimation) |
| V-CND-C | $Rv \Rightarrow Rc$ | $Rv$ | $Rc$ | Condensation (Evaporation) |
| C-AUT-R[g] | $Rc + Rc \Rightarrow Rr$ | $Rc$ | $Rr$ | Autoconversion of cloud droplets |
| I-AUT-S[c] | $Ri + Ri \Rightarrow Rs$ | $Ri$ | $Rs$ | Autoconversion of pristine ice |
| I-AGG-S[c] | $Ri + Rs \Rightarrow Rs$ | $Ri$ | $Rs$ | Aggregation of pristine ice |
| R-CFR-(I)G | $Ri + Rr \Rightarrow Rg$ | $Rr$ | $Rg$ | Raindrop contact freezing |
| I-CFR-(R)G | $Ri + Rr \Rightarrow Rg$ | $Ri$ | $Rg$ | Raindrop contact freezing |
| C-RIM-S[b] | $Rc + Rs \Rightarrow Rs$ | $Rc$ | $Rs$ | Light riming of aggregates |
| C-RIM-(S)G[b] | $Rc + Rs \Rightarrow Rg$ | $Rc$ | $Rg$ | Heavy riming of aggregates |
| S-RIM-(C)G | $Rc + Rs \Rightarrow Rg$ | $Rs$ | $Rg$ | Heavy riming of aggregates |
| C-ACC-R[f] | $Rc + Rr \Rightarrow Rr$ | $Rc$ | $Rr$ | Accretion of rain and cloud droplets |
| R-ACC-(S)G[e] | $Rr + Rs \Rightarrow Rg$ | $Rr$ | $Rg$ | Accretion of rain and aggregates |
| S-ACC-(R)G | $Rr + Rs \Rightarrow Rs$ | $Rs$ | $Rg$ | Accretion of rain and aggregates |
| C-DRY-G[a] | $Rc + Rg \Rightarrow Rg$ | $Rc$ | $Rg$ | Dry growth of graupel |
| R-DRY-G[a] | $Rr + Rg \Rightarrow Rg$ | $Rr$ | $Rg$ | Dry growth of graupel |
| I-DRY-G[a] | $Ri + Rg \Rightarrow Rg$ | $Ri$ | $Rg$ | Dry growth of graupel |
| S-DRY-G | $Rs + Rg \Rightarrow Rg$ | $Rs$ | $Rg$ | Dry growth of graupel |
| C-SHD-(G)R | $Rc + Rg \Rightarrow Rr$ | $Rc$ | $Rr$ | Water shedding |
| C-WET-G | $Rc + Rg \Rightarrow Rg$ | $Rc$ | $Rg$ | Wet growth of graupel |
| R-WET-G | $Rr + Rg \Rightarrow Rg$ | $Rr$ | $Rg$ | Wet growth of graupel |
| I-WET-G | $Ri + Rg \Rightarrow Rg$ | $Ri$ | $Rg$ | Wet growth of graupel |
| S-WET-G | $Rs + Rg \Rightarrow Rg$ | $Rs$ | $Rg$ | Wet growth of graupel |
| I-MLT-C | $Ri \Rightarrow Rc$ | $Ri$ | $Rc$ | Melting of pristine ice |
| G-MLT-R[i] | $Rg \Rightarrow Rr$ | $Rg$ | $Rr$ | Melting of graupel |
| S-CVM-G | $Rs \Rightarrow Rg$ | $Rs$ | $Rg$ | Conversion melting |
| R-EVA-V[h] | $Rr \Rightarrow Rv$ | $Rr$ | $Rv$ | Rain evaporation |

**Figure 1.6:** *Taken from Lascaux* et al. *(2006), this table lists the microphysical processes and corresponding sinks and sources of the ICE3 microphysical scheme and gives the nomenclature used to represent each process. In the symbol names, the first letter identifies the sink species (V, C, I, R, S, G, or H for vapour, cloud, pristine ice, rain, snow, graupel, or hail respectively), the next three letters give the short name of the microphysical process, and the last letter identifies the source species. An optional letter is added in parenthesis to recall the name of the reactant species in three-component processes. The superscripts ($^a$ ,$^b$, etc.) indicate which processes were grouped together for Fig. 1.4, which is also taken from Lascaux* et al. *(2006).*

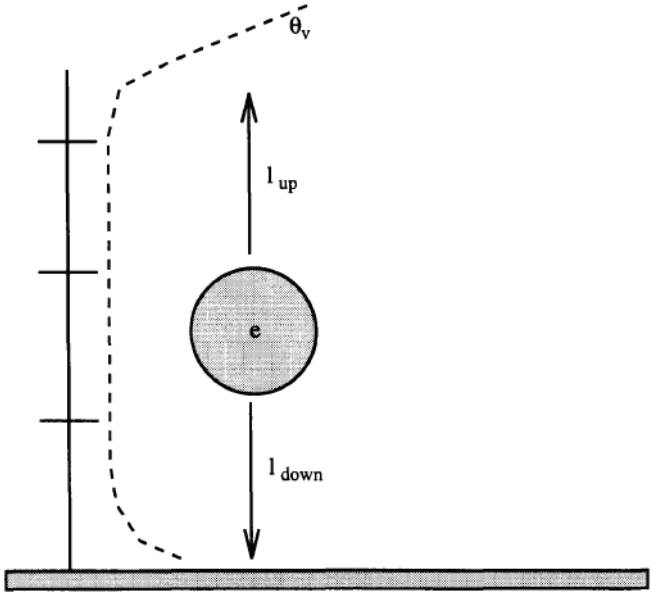


**Figure 1.7:** *A schematic explanation of BL89's mixing length formulation where the bubble, e, represents an air parcel, $l_{up}$ the maximum upward displacement of the parcel and $l_{down}$ the maximum downward displacement. The distances are calculated as functions of the virtual potential temperature $\theta_v$ at certain levels $z$. Appears as Fig.4 in Cuxart* et al. *(2000).*

The choice of horizontal resolution determines the representation of turbulent eddies. Bryan *et al.* (2003) showed that the details of a simulated squall line can change significantly as resolution is increased, with precipitation amounts, convective cell structure and mesoscale flow patterns all being modified. Weisman *et al.* (1997) studied squall-lines in mid-latitude type environments and suggested that a 4km horizontal resolution could reproduce the mesoscale structure and evolution of the squall-line with the same detail as 1km resolution simulations but that at 4km the system has a slower evolution due to the delayed strengthening of the convective cold pool. At 1km resolution, more turbulent eddies were explicitly resolved leading to a more correct representation of the mid-latitude squall line.

Unless simulations are performed at a horizontal resolution of a couple of ten's of metres, some form of turbulent parameterisation is needed. While there has been much progress in these parameterisations in recent years, problems remain. The Navier-Stokes equations present a closure problem when they are integrated in their Reynolds-averaged form due to the presence of non-linear terms. Many methods have been proposed in order to solve this closure issue. Smagorinsky (1963), Deardorff (1980) and Bougeault and Lacarrère (1989) use a method inspired by the mixing length approach of Prandtl (1925) developed in the early 20th century.

Smagorinsky (1963), along with the definition of the mixing length as in Prandtl (1925), proposes formulae for the eddy viscosity in numerical models, derived from the velocity field and the local grid size. The Deardorff (1980) scheme is a 1.5 order scheme which is typically employed at very fine horizontal resolutions where most turbulent eddies are explicitly resolved. He uses a sub-grid scale closure method where the mixing length is closely related to the grid spacing.

Within the French research community, and throughout this study, the scheme of Bougeault and Lacarrère (1989) (BL89) is used extensively. In Bougeault and Lacarrère (1989) (BL89), the mixing length ($L$) is defined as the distance a parcel of air can move vertically up ($l_{up}$) or down ($l_{down}$) before being stopped by buoyancy effects. Fig. 1.7 gives a schematic view of their mixing length definition which is governed by the following expressions,

$$\begin{aligned} \int_{z}^{z+l_{up}} \frac{g}{\theta_{v\,ref}}(\theta_v(z') - \theta_v(z))dz' &= e(z), \\ \int_{z-l_{down}}^{z} \frac{g}{\theta_{v\,ref}}(\theta_v(z) - \theta_v(z'))dz' &= e(z), \end{aligned} \tag{1.14}$$

$$L = (l_{up} l_{down})^{1/2} \tag{1.15}$$

where $e(z)$ is the value of the turbulent kinetic energy at a level $z$, $\theta_v(z)$ is the virtual potential temperature at the level $z$ and $\theta_{v\,ref}$ is the virtual potential temperature of the reference state. The definition of the mixing length will affect the coefficients of eddy momentum and heat transfer and thus impact upon the simulation of the turbulent flows, clearly suggesting that the choice of closure method and thus formulation of the mixing length has an impact upon the moist convective processes.

Inspired from the work of Redelsperger and Sommeria (1981)(RS81), the turbulence scheme proposed by Cuxart *et al.* (2000) (CU00) is an attempt to unify the 3D formulation used at large-eddy simulation (LES) resolutions and the standard 1D approach used at mesoscale resolutions. In CU00, the turbulent fluxes are expressed as,

$$\overline{u_i'\theta'} = -\frac{2}{3}\frac{L}{C_s}e^{\frac{1}{2}}\frac{\partial\overline{\theta}}{\partial x_i}\phi_i \tag{1.16}$$

$$\overline{u_i' r_v'} = -\frac{2}{3}\frac{L}{C_h}e^{\frac{1}{2}}\frac{\partial\overline{r_v}}{\partial x_i}\psi_i \tag{1.17}$$

$$\overline{u_i'\,u_j'} = \frac{2}{3}\delta_{ij}\,e - \frac{4}{15}\frac{L}{C_m}e^{\frac{1}{2}}\left(\overline{\frac{\partial u_i}{\partial x_j}} + \overline{\frac{\partial u_j}{\partial x_i}} - \frac{2}{3}\delta_{ij}\overline{\frac{\partial u_m}{\partial x_m}}\right) \tag{1.18}$$

$$\overline{\theta' r_v'} = C_2 L^2\left(\frac{\partial\overline{\theta}}{\partial x_m}\frac{\partial\overline{r_v}}{\partial x_m}\right)(\phi_m + \psi_m) \tag{1.19}$$

$$\overline{\theta'^2} = C_1 L^2\left(\frac{\partial\overline{\theta}}{\partial x_m}\frac{\partial\overline{\theta}}{\partial x_m}\right)\phi_m \tag{1.20}$$

$$\overline{r_v'^2} = C_1 L^2\left(\frac{\partial\overline{r_v}}{\partial x_m}\frac{\partial\overline{r_v}}{\partial x_m}\right)\psi_m \tag{1.21}$$

where $L$ is the eddy length scale, the $C$ variables are numerical constants, $\phi$ and $\psi$ are stability functions whose definitions are detailed in RS81, $e$ is the turbulent kinetic energy, $\theta$ is the potential temperature, $r_v$ is the water vapour mixing ratio and $\delta_{ij}$ is the Kronecker delta tensor. The subscript m denotes that the Einstein summation convention applies. These equations govern the heat, moisture, momentum and buoyancy flux production within the turbulence scheme. The time evolution of the turbulent kinetic

energy is governed by the following equation,

$$\begin{aligned}\frac{\partial e}{\partial t} &= -\frac{1}{\rho_{dref}}\frac{\partial}{\partial x_j}(\rho_{dref}e\overline{u_j}) - \overline{u_i'u_j'}\frac{\partial \overline{u_i}}{\partial x_j} + \frac{g}{\theta_{vref}}\overline{u_3'\theta_v'} \\ &\quad + \frac{1}{\rho_{dref}}\frac{\partial}{\partial x_j}(C_{2m}\rho_{dref}Le^{\frac{1}{2}}\frac{\partial e}{\partial x_j}) - C_\epsilon\frac{e^{\frac{3}{2}}}{L} \end{aligned} \tag{1.22}$$

where the terms on the right-hand side represent the turbulent advection, shear and buoyancy production, turbulent diffusion and turbulent dissipation respectively.

If an appropriate parameterisation of the eddy length-scale is used, the same scheme can be run in 3D or 1D by dropping all the horizontal terms. The mixing-length specification is then the only aspect of the scheme which differs from the LES to the mesoscale configuration, as the numerical constants used for the closure terms are the same in both configurations. However, the closure issue remains. At very fine horizontal resolutions, LES closure methods such as Smagorinsky (1963) and Deardorff (1980) are suitable, as a mixing length value equal to that of the horizontal grid spacing would be sufficiently accurate to resolve the energy and flux-containing turbulent eddies. At coarser resolutions, on the order of 10km, the energy-containing turbulent eddies are not explicitly resolved and are thus parameterised, with a closure scheme such as that of Bougeault and Lacarrère (1989) being appropriate. However, in the horizontal resolutions between mesoscale and LES, neither approach is appropriate. This led Wyngaard (2004) to call this horizontal resolution ”terra incognita”, due to the lack of realistic closure methods at this scale.

This phenomenon was investigated in three related papers (Fiori *et al.* (2009), Fiori *et al.* (2010) and Fiori *et al.* (2011)). They found that the initiation of convection was slower at coarser resolutions as a longer time was needed to obtain a complete cell splitting process. It was also illustrated that the choice of turbulence parameterisation scheme impacts remarkably upon the forecast, with an LES closed run giving a larger area of rainfall than a mesoscale run closed by a 1D scheme such as that of Bougeault and Lacarrère (1989). They showed that the LES closure made the turbulent diffusion at finer resolutions more efficient favouring the organisation of smaller intense precipitation structures. They concluded by saying that the choice of turbulence closure parameter is an important source of uncertainty when modelling deep moist convective processes.

The work of Honnert *et al.* (2011) also investigated turbulence closures at the kilometric scale. They proposed a new diagnostic capable of evaluating turbulence parameterisations at mesoscales which aims to comprehend which current or future schemes are suitable at these scales. They used this diagnostic to examine a number of schemes and concluded by saying that at horizontal resolutions of between 500m and 1km, none of the parameterisations were appropriate.

### 1.2.1 Summary of turbulence parameterisations

It has been demonstrated that finer resolutions are needed in order to simulate certain storm-scale dynamical features, such as the development of a cold pool, which are instrumental in the processes which lead to concentrated rainfall events. It is also clear

that the small-scale turbulent eddies are quite important in terms of the development of convection and that their representation within a forecasting model must be accurate in order to have quality forecasts of convection related weather events such as HPEs.

From the bibliographic synthesis given above there exists a clear degree of uncertainty as to which methods are most suitable to describe the turbulent flows and turbulent eddy characteristics within a model. Evidently, the rainfall pattern produced by a forecasting model will be impacted by this uncertainty and will exhibit a large degree of sensitivity to the choice of methodology.

## 1.3 Ensemble forecasting

As has been demonstrated, within a forecasting model, the processes leading to the development of cloud and precipitation often display a large degree of uncertainty in their representation, even at kilometric scales. This obviously has a significant impact upon the ability of these models to accurately forecast important weather phenomena such as HPEs. The skill of deterministically forecasting these events, despite much progress in recent years, still remains quite limited. Lorenz (1969)'s famous paper discusses the predictability limitations of large-scale flow forecasting, giving an accuracy limit of only two weeks, while at the same time suggesting that cumulus scale motions can only be efficiently predicted one hour in advance.

More recently, Walser *et al.* (2004) and Fritsch and Carbone (2004) suggested that especially for deep convective events, problems still existed in obtaining a skillful deterministic forecast. Fritsch and Carbone (2004) went as far as to say that the prediction of moist convection will likely be limited to less than 3 hours for the foreseeable future. They acknowledged that there is a shortage of microphysical information, which leaves model developers with a limited data-set from which to improve microphysical parameterisations.

Their suggestion for improvement was to use ensemble prediction systems (EPSs), where the goal is to generate a probabilistic representation of future states of the atmosphere by performing a number of forecasts starting from a set of perturbed scenarios. The main idea behind this strategy is to represent the inherent uncertainties present in the observed atmospheric state and in model parameterisations. Designing such systems can be challenging however, as appropriate perturbations which give satisfactory statistical scores can be difficult to develop.

### 1.3.1 Definition of terms and ensemble scores

Throughout this study, the words "model skill", "predicitability" and "dispersion" will be used extensively. In order to have better clarity as to their meaning, they are here defined explicitly. We use the phrase model skill to refer to a forecasting model's ability to predict the time and spatial distribution of observed rainfall. By predictability, we understand the degree to which an atmospheric state can be correctly forecast. Dispersion is defined as the distribution of rainfall values predicted by an ensemble which

is quantified by using a number of statistical measures such as standard deviation from the mean or the root-mean squared error (rmse).

The quality of ensembles will also be commented upon throughout this study. When an ensemble is labelled as ”good“, this ensemble is deemed to have a good degree of dispersion between its members and to have largely succeeded in capturing the error of the process that was perturbed within the ensemble members. The ability to capture the observed variability in the rainfall field is also desirable of a ”good“ ensemble.

These qualities are measured by a number of ensemble based statistics such as the Brier Skill Score (BSS), Relative Operating Characteristic curve (ROC, Mason and Graham (2002)) and the reliability diagram. The BSS serves as a measure of the skill of a probabilistic forecast over that of climatology in terms of predicting whether or not an event occurred. This allows the improvements of using a probabilistic approach to be easily identified. The ROC curve evaluates the ability of the ensemble to distinguish between an event and a non-event and is conditioned on the observations. The fact that the ROC curve measures the resolution of the ensemble means that it is a potential measure of the usefulness of a probabilistic forecast. Being conditioned on the forecast, the reliability diagram is a good accompanying method to the ROC curve. These diagrams serve principally to answer the question of how well predicted probabilities of an event correspond to their observed frequencies. A more complete description of the meaning of these statistical scores can be found in Wilks (1995).

### 1.3.2 Ensemble strategies

EPSs have been used in large-scale models for a number of years. NCAR, the ECMWF, the UK Met Office and Météo France all run daily ensembles. Their use at the mesoscale however is relatively new, and it is only in recent years that it has become feasible due to increased computational resources being more easily available.

The perturbations used in an EPS are usually introduced upon the initial conditions (IC), lateral boundary conditions (LBC) or the parameterisations of important physical processes. One of the earliest systems was that described in Molteni *et al.* (1996) and implemented in the ECMWF model. They outlined a system which contained 32 perturbed members in which dynamically defined perturbations were added to the operational analysis to give perturbed ICs. Ensemble tests were performed for a number of weather events from 1993. Ensemble skill-scores demonstrated that this method performed particularly well in summer and autumn but had a greater difficulty in forecasting winter events.

More recently, Houtekamer *et al.* (2009) presented the ensemble Kalman filter which is used to generate ICs for the medium-range EPS of the Meteorological Service of Canada. It was shown that for a perfect-model environment, the spread introduced by the Kalman filter perturbations remains representative of the ensemble mean error. This allowed the impact upon the quality of the ensemble mean of various other sources of error to be quantified.

At cloud-resolving scales, Vié *et al.* (2011) described an ensemble where perturbations were introduced upon the IC and LBCs of the operational French model, AROME.

The perturbed ICs were generated by using perturbed observations in the ensemble data assimilation process. For the LBCs, the ensembles used LBCs from members of a global short-range EPS. These ensembles were evaluated in the context of 2 Mediterranean HPEs. It was demonstrated that overall the ensembles are under-dispersive but that they provide useful probabilistic information for the HPEs investigated. As a generality, they concluded that IC uncertainties have an impact in the short-range (12h), while the LBC uncertainties are more pronounced at longer ranges.

Studies such as Schwartz *et al.* (2010), Gebhardt *et al.* (2011) and Bouttier *et al.* (2012) are examples of convection-permitting ensembles which examine uncertainties associated with physical parameterisations in order to better predict precipitation events. Schwartz *et al.* (2010) chose to introduce their perturbations by using a number of distinctive microphysical and planetary boundary layer schemes. A strong influence upon the rainfall fields was seen for these perturbations, and it was suggested that spread in precipitation can be achieved by varying the physical parameterisations within an ensemble system that uses one dynamic core.

Gebhardt *et al.* (2011) used different sets of physical and LBC perturbations in order to create his ensembles. Certain adjustable parameters, such as the number concentration of the raindrop size distribution, were perturbed by modifying their value within the parameterisation scheme. The perturbations were non-stochastic and uniform which meant that the perturbation was kept constant over the entire forecast range and for all the forecast days. He illustrated, using a number of statistical scores, that there seems to be a general switch between the impact of perturbing the physics and the LBC's, with physics perturbations dominating during the first few hours of a forecast while the LBC perturbations become more important with longer lead times. It is concluded that the effects of the perturbations are positive, and that the perturbation methods were useful within the development of a convection-permitting ensemble.

Bouttier *et al.* (2012) showcased another method for perturbing the microphysical processes, employing the stochastic perturbation of physics tendencies (SPPT) scheme. Within the parameterisation scheme, physical tendencies of wind, temperature and water vapour content were multiplied at each time step by a perturbing parameter, f. This factor was defined in terms of a set of random patterns r and a uniform standard deviation, $\alpha$. The same factor was used to multiply the tendencies of all the prognostic model variables at each grid point. Rain forecasts were shown to be significantly impacted by the SPPT scheme, with no-rain frequencies being increased at the expense of light rain prediction. This was explained by an enhancement of the rain evaporation at low levels caused by the SPPT scheme disturbing the local physical balance of certain convective cells.

One further method, from which the method of Bouttier *et al.* (2012) was inspired, is that proposed by Buizza *et al.* (1999). This scheme is also stochastically-driven, where each ensemble member, $e_j$, is described by the following relationship,

$$e_j(t) = \int_0^t A(e_j;t) + P`(e_j;t)dt \tag{1.23}$$

with $A(e_j;t)$ symbolising the non-parameterised processes, and $P`(e_j;t)$ representing

the perturbed parameterised tendency, defined as,

$$P^{'}(e_j;t) = r_j(\lambda,\phi,t)_{DT} \cdot P_j(e_j;t) \tag{1.24}$$

where $r_j(\lambda,\phi,t)_{DT}$ means that the same random number $r_j$ has been used for all grid points inside a specified area $(\lambda,\phi)$ and over t time steps, and $P_j(e_j;t)$ stands for the non-perturbed parameterised processes. The random numbers were sampled from three different intervals, high, medium and low amplitude, with high being a number between 0 and 2, medium between 0.5 and 1.5, and low between 0.75 and 1.25. Through a number of statistical tests and measures of ensemble skill, Buizza showed that the most useful ensemble was found when the random numbers were selected from the medium range, i.e. 0.5 and 1.5. It was noted in particular that the stochastic physics method increased the spread of the ensemble and improved its performance, especially with regard to the probabilistic prediction of precipitation.

### 1.3.3 Short-range ensembles and number of members

EPSs of large-scale models have advanced to have a period of forecast on the order of days and even weeks. In contrast, using ensembles in the very short term, for example over a 24 h period, is a relatively new venture. Squall lines and mesoscale convective systems (MCSs) tend to have very short lifetimes, but often have devastating social and economic impacts. Thus, being able to produce accurate and useful ensemble predictions of these events is clearly of great importance.

A number of related studies have looked at this issue; Stensrud *et al.* (1999), Stensrud *et al.* (2000) and Stensrud (2001). Stensrud *et al.* (1999) looked at using an ensemble of 15 members to forecast the position of a cyclone at 36 hours using perturbations introduced upon the initial conditions. They found that there was little correlation between the spread in the ensemble members and the accuracy of the ensemble mean in predicting the location of the cyclone. They argue that this lack of correlation between spread and forecast uncertainty would present a challenge to the production of short-range ensemble forecasts.

Stensrud *et al.* (2000) offered a more optimistic view by constructing two different ensembles. The first ensemble perturbed the physical processes by choosing different parameterisation schemes. The second ensemble consisted of using different initial conditions which were formulated using a Monte Carlo approach. It was demonstrated that the variance in the physics based ensemble was produced 2 to 6 times faster in the first 12h of simulation than the variance in the initial-condition ensemble, suggesting that varying the model physics is a potentially powerful method for creating ensembles, even at short ranges. Another interesting point evoked in this work was that when the large-scale forcing for upward motion was weak, the physics ensemble was more skillful than the initial condition one, while the opposite was true in a strong large-scale forcing scenario.

Stensrud (2001) showed the importance of ensemble systems in predicting strongly convective events using examples of events over France, Belgium and the Netherlands which had lifetimes of approximately 24 hours. It was argued that as convection is

perhaps the most difficult process to correctly model, a single model forecast cannot be trusted to provide accurate forecasts. He concluded that the sensitivities shown to perturbing certain physical processes highlights the value of an ensemble system at short-ranges.

The number of perturbed members used when constructing the ensemble is another important factor to consider when developing EPSs. Du *et al.* (1997) showed that, for ensembles of perturbed physics and initial conditions performed upon cases of wintertime cyclogenesis, an ensemble with 10 members gave a ranked probability score (RPS) roughly equal to that of a 25-member ensemble. They also illustrated that a 90% improvement in the rmse is obtained using a small ensemble size of between 8 and 10 members compared to an ensemble of 25 members.

This fact is further underlined by the two papers of Clark *et al.* (2009) and Clark *et al.* (2011). In Clark *et al.* (2009), a convection-permitting ensemble with less members performed better than a convection-parameterised ensemble with more members when studying precipitation over the central United States. In terms of the number of members, there was a larger increase in the Relative Operating Characteristic (ROC) score obtained from performing an ensemble with 10 instead of 5 members, than with 15 instead of 10.

Concurrently, Clark *et al.* (2011) demonstrated that a relatively small ensemble of between 3 and 9 members had a statistically indistinguishable average ROC area relative to a 17-member ensemble when examining probabilistic precipitation forecast skill. It was admitted however that more members would be needed in order to capture rarer events with greater accuracy, especially as lead time increases and spatial scale decreases due to the resulting error growth which would mean that individual members would be less likely to verify.

### 1.3.4 Summary of ensemble forecasting

Several conclusions can be drawn from the studies previously introduced. It seems that the most promising solution to the problem of representing uncertainties related to model parameterisations is the use of an EPS, as they allow a number of different possible atmospheric states to be simultaneously modelled. A number of methodologies can be chosen from; using different physical parameterisations (Stensrud *et al.* (1999), Schwartz *et al.* (2010)), employing different sets of parameters (Gebhardt *et al.* (2011)) or using stochastic physics approaches (Buizza *et al.* (1999), Bouttier *et al.* (2012)).

Using different physical parameterisations requires that a number of different parameterisation schemes be available within the model being used, which is not always the case. Using different sets of parameters and stochastic physics perturbations would seem to be the most convenient of the three options to implement as they can be introduced within a single physical parameterisation scheme. It has also been seen that physics perturbations introduced by these methods are quite quickly integrated into model interactions, making them suitable for short-range ensembles. As to the question of how many members makes up a statistically sound ensemble, the works of Du *et al.* (1997), Clark *et al.* (2009) and Clark *et al.* (2011) suggest that 10 perturbed

members are sufficient enough to successfully reproduce the uncertainties inherent in the model formulation for the majority of weather events.

## 1.4 Thesis objectives

Concluding from this bibliographic synthesis, it is clear that there exists a large uncertainty in the representation of processes which play important roles in the development of HPEs. These uncertainties can lead to incorrect descriptions of the microphysical and turbulence processes which can affect the ability of a model to skillfully forecast an event. To take this error into account, probabilistic forecasts, known as ensemble prediction systems (EPSs), present a suitable methodology. According to this method, a number of forecasts are produced which give slightly different representations of the physical processes and thus present a more probabilistic view of the future state of the atmosphere. This gives improved information on the atmospheric state compared to a single deterministic forecast.

The principle aim of this thesis is to construct an EPS where perturbations are introduced on the microphysical and turbulence time tendencies and to test its usefulness in the forecasting of HPEs. The relative importance of each individual microphysical process and of the turbulence processes to the development of deep convection will be examined, as will the sensitivity of the surface rainfall field to the perturbations introduced. This is done using three idealised convective events and seven real world HPEs which occurred in south-eastern France in the autumns of 2010, 2011 and 2012. These real world cases occurred under differing large-scale atmospheric conditions and thus the mechanisms by which the HPEs developed also differed. This permits an evaluation of the importance of the physical processes depending on the nature of the HPE. As a secondary aim, two of the real world HPEs from autumn 2012 are used to investigate whether the degree of sensitivity to physical perturbations is comparable to the sensitivity introduced by modifying the initial (IC) and boundary conditions (BC).

# Chapter 2

# Idealised simulations and testing of ensemble strategy

## 2.1 Methodology

In order to represent the uncertainties associated with the microphysical and turbulent processes, various methodologies have been explored and firstly assessed in the context of idealised simulations. Regarding the microphysical scheme, a first series of experiments addressed the sensitivity of the ICE3 scheme to a number of adjustable (or user specified) parameters, while a second series was constructed by introducing random perturbations upon the various microphysical sources and sinks.

Similarly for the turbulence scheme, various simulations were performed. They consisted in introducing random perturbations on either the turbulent time tendencies or on the difference sources of the turbulent energy equation.

The idealised simulations were performed at kilometric resolutions for two archetypes of deep convective systems, an idealised storm and a squall line. For the idealised storm, two domains were employed. A first, relatively small domain was used to perform a large number of sensitivity tests, with a confirmation of the most dispersive results on a second larger domain. The most sensitive parameters were then re-tested on the more convectively complex situation of a squall line. Table 2.1 gives the list and characteristics of each of the simulations. Further details of the adjustable parameter series of experiments are given in Tables 2.2, 2.3 and 2.4.

### 2.1.1 Méso-NH

The model used to undertake these simulations is the research model Méso-NH (Mesoscale Non-Hydrostatic model), which is described in detail in Lafore *et al.* (1998).

Méso-NH, jointly developed by the Laboratoire d'Aérologie (LA) and the Centre National de Recherches Météorologiques (CNRM), is an anelastic grid-point model where the governing equations follow a Eulerian system of partial differential equations. The following variables are prognosed: the three components of the velocity $u$,$v$ and $\omega$, the dry potential temperature $\Theta$, the various mixing ratios of the different water species

| Sim. name | Parameter/Process perturbed | No.pert.sims. | Domain(km) |
|---|---|---|---|
| 24-Dist | Particle Distributions | 4 | 24x24 |
| 24-N0r | Rain Intercept | 9 | 24x24 |
| 24-N0s | Snow Intercept | 9 | 24x24 |
| 24-N0g | Graupel Intercept | 9 | 24x24 |
| Snow | Mass-diameter relations | 7 | 24x24 |
| Graupel | Mass-diameter relations | 5 | 24x24 |
| 24-Auto-KK | Slope of Auto rate | 9 | 24x24 |
| 24-Auto-KQ | Auto threshold mixing length | 10 | 24x24 |
| 24-TKE | TKE | 10 | 24x24 |
| 24-TKE-S | TKE Sources | 10 | 24x24 |
| 24-C-Group1 | Vap dep. on snow and graupel, auto ice to snow | 10 | 24x24 |
| 24-C-Group2 | Riming | 10 | 24x24 |
| 24-C-Group3 | Acc of rain and aggs by snow and graupel | 10 | 24x24 |
| 24-C-Group4 | Wet and dry growth of graupel | 10 | 24x24 |
| 24-C-Group5 | Melting of snow and graupel | 10 | 24x24 |
| 24-C | Cold microphysical | 10 | 24x24 |
| 24-Auto | Autoconversion | 10 | 24x24 |
| 24-Acc | Accretion cloud droplets | 10 | 24x24 |
| 24-Evap | Evaporation raindrops | 10 | 24x24 |
| 24-WA | Warm microphysical | 10 | 24x24 |
| 24-WC | Warm and cold microphysical | 10 | 24x24 |
| 24-MT | Microphysical and turbulent | 10 | 24x24 |
| 96-N0r | Rain Intercept | 9 | 96x96 |
| 96-N0g | Graupel Intercept | 9 | 96x96 |
| 96-WA | Warm microphysical | 10 | 96x96 |
| 96-WA-30 | Warm microphysical | 30 | 96x96 |
| 96-WC | Warm and cold microphysical | 10 | 96x96 |
| 96-MT | Microphysical and turbulent | 10 | 96x96 |
| WK82-WA | Warm microphysical | 10 | 512x256 |
| WK82-WC | Warm and cold microphysical | 10 | 512x256 |
| WK82-MT | Microphysical and turbulent | 10 | 512x256 |

**Table 2.1:** *Characteristics of all of the idealised simulations presented within this chapter. The column labelled Domain refers to the $i$ x $j$ dimensions of the grid. The column labelled No.pert.sims. gives the number of perturbed members within a specified ensemble.*

$r_*$ and the turbulent kinetic energy (TKE) $e$.

The model makes use of a number of parameterisations in order to represent the processes which occur at sub-grid resolutions. A Rapid Radiative Transfer Model (Mlawer *et al.* (1997)) is used to calculate the radiation. Four possible surface types are allowed within the model (natural surfaces, urban areas, oceans and lakes) which determine the exchanges of energy between the surface and the lower atmospheric levels. These exchanges are parameterised according to the SURFEX scheme described in Masson *et al.* (2013). The natural land surfaces are represented by the ISBA (Interactions Soil-Biosphere-Atmosphere) scheme (Noilhan and Mafhouf (1996)) with the maritime surfaces described by the work of Fairall *et al.* (2003). Shallow convective processes are parameterised according to the formulation of Pergaud *et al.* (2009). The scope of this study is simulations at the kilometric scale thus deep convective processes are considered resolved and the parameterisation of deep convection is not activated. The microphysics, turbulence and turbulence closure schemes follow the works of Pinty and Jabouille (1998), Cuxart *et al.* (2000) and Bougeault and Lacarrère (1989) respectively. These schemes are detailed in sections 1.1.7 and 1.2.

Méso-NH has been extensively used as research tool for simulating extreme weather phenomena. Pantillon *et al.* (2012) utilised Méso-NH in order to investigate the role of a North-Atlantic Rossby wave train in the extra-tropical transition of Hurricane Helene. Bresson *et al.* (2012) performed idealised simulations of quasi-stationary convective systems over the complex terrain of the Northwestern Mediterranean using Méso-NH. Ducrocq *et al.* (2008) and Nuissier *et al.* (2008) employed Méso-NH to investigate the synoptic ingredients and stationarity factors which led to three devastating HPEs in south-eastern France. Argence *et al.* (2008) and Richard *et al.* (2003) both employed Méso-NH to run high-resolution numerical simulations of real world convective situations over the Mediterranean and Alpine regions respectively.

### 2.1.2 Adjustable microphysical parameters

Various adjustable parameters were perturbed by modifying their default value within an accepted range of values. These parameters include the shape ($\nu$) and scale parameter ($\alpha$) of the hydrometeor distribution, the intercept parameter of the hydrometeor distribution ($N_0$), the mass-diameter and fall speed-diameter coefficients ($a, b, c, d$), the autoconversion threshold cloud water content ($q_{crit}$) and the autoconversion time constant ($k$).

The distribution of each hydrometeor was manipulated by changing the $\nu$ and $\alpha$ values from their default setting. Particles which had a MP distribution by default, were given a gamma distribution, while those with gamma distributions were perturbed to follow a MP distribution. Precendent for this can be drawn from the work of Ziegler (1985) who used a gamma like distribution for the raindrops. Walko *et al.* (1995) represented all of the hydrometeor species with gamma distributions. These simulations formed an ensemble referred to as 24-Dist. Table 2.2 details the different values of $\nu$ and $\alpha$, the normalised distribution law to which they correspond and the hydrometeor distribution being perturbed.

| Hydrometeor | CTRL law | $\alpha$(CTRL) | $\nu$(CTRL) | Perturbed law | $\alpha$(Perturbed) | $\nu$(Perturbed) |
|---|---|---|---|---|---|---|
| Rain | MP | 1 | 1 | gamma | 3 | 3 |
| Ice | gamma | 3 | 3 | MP | 1 | 1 |
| Snow | MP | 1 | 1 | gamma | 1 | 1 |
| Graupel | MP | 1 | 1 | gamma | 1 | 1 |

**Table 2.2:** *The characteristics of the different members of the 24-Dist ensemble.*

| Intercept Parameter($m^{-4}$) | CTRL Value | 1 | 2 | 3 | 4 | 5 | 6 | 7 | 8 | 9 |
|---|---|---|---|---|---|---|---|---|---|---|
| $N_{0r}(10^7)$ | 0.8 | 0.4 | 1.0 | 1.2 | 1.6 | 2.0 | 2.4 | 2.8 | 3.2 | 3.6 |
| $N_{0s}$ | 5 | 1 | 2 | 4 | 8 | 10 | 15 | 18 | 22 | 25 |
| $N_{0g}(10^6)$ | 0.5 | 0.1 | 0.2 | 0.3 | 0.4 | 0.6 | 0.7 | 0.8 | 0.9 | 1.0 |

**Table 2.3:** *The value of the intercept parameter for each member of the 24-N0r, 24-N0s and 24-N0g ensemble.*

For the $N_{0r}$ parameter, values of between $0.4\ 10^7 m^{-4}$ and $3.5\ 10^7 m^{-4}$ were used, inspired by the work of Waldvogel (1974). The range $1m^{-4}$ to $25m^{-4}$ used to perturb the $N_{0s}$ parameter was taken from Caniaux (1993). while the value of the $N_{0g}$ parameter was modified between $0.1\ 10^6 m^{-4}$ and $1.0\ 10^6 m^{-4}$ in order to have an equal number of values above and below its default value of $0.5\ 10^6$. Although the range of values for $N_{0g}$ was not inspired by the studies introduced in section 1.1.1, the values remain within accepted bounds. Secondly, as the spacing used in the values of $N_{0r}$ and $N_{0s}$ was small, it was thought appropriate to employ the same approach for $N_{0g}$ and to avoid using large extended ranges such as those presented in Gilmore *et al.* (2004). For each intercept parameter, 9 perturbed values were chosen within the corresponding ranges. The values chosen for each member of each of these 3 ensembles, referred to as 24-N0r, 24-N0s and 24-N0g, are given in Table 2.3.

In order to represent the large variety of forms of snow and graupel presented in Locatelli and Hobbs (1974), EPSs were constructed by using the different mass-diameter and fall speed-diameter relationships. These two ensembles are referred to as Snow and Graupel. Details of the values of the coefficients $a, b, c$ and $d$ for each ensemble member are given in Table 2.4. The snow (1-8) categories represent particles which appear as aggregates of densely rimed radiating assemblages (Snow 1), graupel-like snow of lump type (Snow 2) and hexagonal type (Snow 3), densely rimed dendrites (Snow 4), densely rimed (Snow 5) and unrimed (Snow 6) radiating assemblages of dendrites, aggregates of unrimed radiating assemblages of plates, side planes, bullets and columns (Snow 7) and aggregates of unrimed side planes (Snow 8). The different categories of graupel that are parameterised are lump graupel 2 (Graupel 1), lump graupel 1 (Graupel 2), lump graupel 3 (Graupel 3), conical graupel (Graupel 4), hexagonal graupel (Graupel 5) and densely rimed columns (Graupel 6). The Snow ensemble contained 7 perturbed members while the Graupel ensemble was made up of 5 perturbed members.

The ICE3 microphysical scheme makes use of an autoconversion process parameterised by equation 1.7 given in section 1.1.3. This equation depends on the value

| Class | Type | a | b | c | d |
|---|---|---|---|---|---|
| Snow | MesoNH: Snow-1 (CTRL) | 0.02 | 1.9 | 5.1 | 0.27 |
| | Snow-2 | 0.12 | 2.1 | 7.6 | 0.28 |
| | Snow-3 | 0.33 | 2.4 | 4.8 | 0.25 |
| | Snow-4 | 0.12 | 2.3 | 6.1 | 0.33 |
| | Snow-5 | 0.078 | 2.1 | 2.5 | 0.12 |
| | Snow-6 | 0.0012 | 1.4 | 2.4 | 0.16 |
| | Snow-7 | 0.02 | 1.9 | 11.7 | 0.41 |
| | Snow-8 | 0.0006 | 1.4 | 1.9 | 0.12 |
| Graupel | MesoNH: Graupel-1 (CTRL) | 19.6 | 2.8 | 124.2 | 0.66 |
| | Graupel-2 | 42 | 3.0 | 27.8 | 0.46 |
| | Graupel-3 | 17.6 | 2.7 | 19.3 | 0.37 |
| | Graupel-4 | 4.6 | 2.6 | 106.9 | 0.65 |
| | Graupel-5 | 22.05 | 2.9 | 56.4 | 0.57 |
| | Graupel-6 | 0.26 | 2.3 | 52.6 | 0.56 |

**Table 2.4:** *The values of a, b, c and d for the mass-diameter and velocity-diameter relationships taken from Locatelli and Hobbs (1974). The values by default are marked "MesoNH" or "CTRL".*

of two constants, $k$ a time constant, and $q_{crit}$ a threshold cloud water content, below which no autoconversion takes place. $Q_{crit}$ was perturbed around its default value of $0.5gm^{-3}$ by using the range $0.1gm^{-3}$ to $1.0gm^{-3}$, with this ensemble being referred to as 24-Auto-KQ. The perturbation range for $k$, representing the slope of the curve of the autoconversion rate, was taken from Richard and Chaumerliac (1989). Fig. 2.1 shows the autoconversion rate as a function of the cloud water content for a Kessler and two formulations of the Berry and Reinhardt (Berry and Reinhardt (1974a)) autoconversion parameterisation. BR1(BR2) indicates the autoconversion rate of maritime(continental) clouds. The maritime clouds are characterised by less numerous but larger droplets than the continental clouds meaning that the maritime clouds are more efficient in converting cloud water to rain water. Taking the average of these two curves gives a range of values of between $0.3\ 10^{-3}$ and $1.1\ 10^{-3}$ for the members of the $k$ ensemble, which is labelled as 24-Auto-KK.

For each parameter, the new perturbed values were introduced at the beginning of the simulation and remained constant in time and space throughout the duration of the simulation.

### 2.1.3 Microphysical time tendencies

The time tendencies of the cold and warm cloud microphysical processes were perturbed following the work of Buizza *et al.* (1999). As detailed in section 1.3.2, he suggested perturbing the set of parameterised physical processes for each ensemble member by using a stochastically generated random number. His tests showed that a value for this random number, $r$, of between 0.5 and 1.5 gave the most improved probabilistic prediction of precipitation. For the ICE3 formulation, the perturbations were

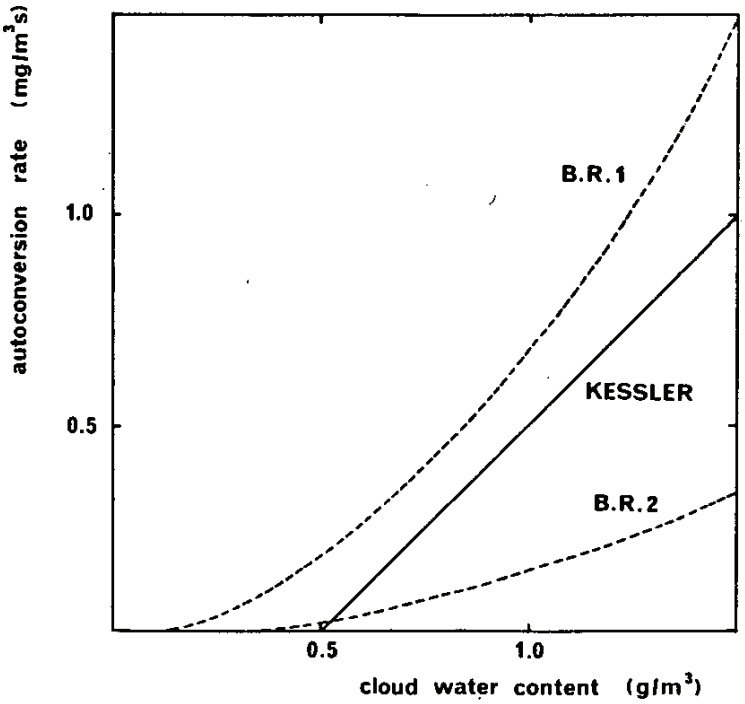


**Figure 2.1:** *Autconversion rates as a function of cloud water content for Kessler and for two formulations of the Berry and Reinhardt parameterisation. BR1(BR2) is representative of martime(continental) clouds.*

introduced upon the time tendencies using the following method,

$$(\frac{\partial(r*)}{\partial t})_{mic} = \sum_j r_j \, PROCj \tag{2.1}$$

where $(\frac{\partial(r*)}{\partial t})_{mic}$ represents the microphysical time tendency of any water specie $r*$ (i.e. water vapour, cloud water, pristine ice, etc.) and $r_j$ the random multiplication factor applied to the source or sink, $PROCj$, of the microphysical process being perturbed. As both the sources and sinks of a given process are simultaneously perturbed by the same $r_j$ value, mass conservation is respected. Each of the microphysical ensembles contained 10 perturbed members, each with a different set of values for $r_j$. The perturbations were introduced at the beginning of each simulation and remained constant in space and time throughout the duration of the simulation.

The time tendencies of the cold and warm microphysical processes were perturbed separately. The cold processes were perturbed by group, forming 4 different groups. The collective dispersion induced by perturbing the deposition of vapour on the snow and graupel along with the autoconversion of ice to snow formed group 1 (labelled 24-C-Group1); the light and heavy riming processes were group 2 (labelled 24-C-Group2); the accretion of the rain and aggregates by snow and graupel constituted group 3 (labelled 24-C-Group3); the dry and wet growth of the graupel species were group 4 (labelled 24-C-Group4); while the processes of melting made up group 5 (labelled 24-C-Group5). An ensemble where all the cold processes were simultaneously perturbed was also constructed (24-C).

The time tendencies of the warm rain microphysical processes of autoconversion (ensemble 24-Auto) , accretion of cloud droplets (ensemble 24-Acc) and rain evaporation (ensemble 24-Evap) were perturbed in the same manner. These three processes were simultaneously perturbed in the ensemble referred to as 24-WA, and also perturbed along with the cold processes in ensemble 24-WC.

### 2.1.4 TKE and turbulent time tendencies

The prognostic TKE equation ($e$) can be broken down into its different components,

$$\frac{De}{Dt} = -S(e) + B(e) + Dif(e) - Dis(e) \tag{2.2}$$

where $S(e)$ represents turbulent shear production, $B(e)$ represents buoyancy production, $Dif(e)$ represents turbulent diffusion and $Dis(e)$ turbulent dissipation. Sensitivities to uncertainties within this parameterisation were highlighted by perturbing the TKE in different ways. As a first test, the TKE (labelled ensemble 24-TKE) was perturbed, that is to say that $e$ was multiplied by ten randomly generated values of $r$, after values for each of the sources were compiled. Secondly, the main sources of the TKE equation (referred to as ensemble 24-TKE-S) were simultaneously perturbed according to,

$$\frac{De}{Dt} = -r_S\ S(e) + r_B\ B(e) + Dif(e) - r_D\ Dis(e) \tag{2.3}$$

with $r_S$, $r_B$ and $r_D$ representing the random factors used to perturb the shear, buoyancy and dissipation respectively. The motivation for this test was to create an ensemble based on the different values of the critical Richardson number.

Finally, perturbations to the turbulent scheme were introduced by multiplying the turbulent tendency of any state variable $X$ by the same random factor $r$ according to,

$$(\frac{\partial X}{\partial t})_{turb} = r\ \frac{\partial(u_i' X')}{\partial x_i} \tag{2.4}$$

This last set of perturbations (introduced in ensembles labelled *-MT, with * being either 24, 96 or WK82) was not employed in individual ensembles but was coupled with perturbations upon the warm and cold microphysical processes. The relative sensitivity to these perturbations was then determined from the increase (or decrease) in the dispersion of the surface rainfall.

## 2.2 Isolated storm description and Méso-NH set-up

The academic situation used to test the ensemble strategy was that outlined in Klemp and Wilhelmson (1978)(KW78). They aimed to develop a 3D cloud model which had the ability to simulate the significant features of convective storms. In order to test their cloud model, they described an idealised storm where convection was triggered by a perturbation of 1.5K on the potential temperature field at an altitude of approximately 1700m. The

idealised hodograph used had vertical wind shear, with the wind turning in lower levels but becoming constant in speed and direction at higher altitudes. They showed that their cloud model, which contained a Kessler parameterisation of the microphysical processes and a computation of the turbulent energy based upon buoyancy, shear and dissipation rates, was successful in reproducing the convective dynamics of the idealised situation. Precipitation was triggered after 30 minutes of simulation, corresponding to the maximum in condensation. Between 30 and 60 minutes of simulation the storm split into two cells, one larger than the other. The larger cell produced the strongest precipitation amounts but disappeared after 1 and a half hours of simulation, while the second smaller cell produced weaker rainfall amounts but remained until the end of the simulation at 2 h after initialisation.

The work of KW78 has been used in various studies. Dudhia (1993) used the KW78 test case to validate a new non-hydrostatic version of the NCAR model. Lafore *et al.* (1998) implemented the KW78 test case in order to evaluate the convective abilities of Méso-NH. KW78 is now available as a test case in the Méso-NH package.

The KW78 case was first simulated on a 24km x 24km x 20km domain with a horizontal resolution of 1km, a vertical resolution of 500m, a time step of 10s and a duration of 2h. The small domain and large time step allowed the many ensembles described in sections 2.1.1, 2.1.2 and 2.1.3 to be constructed at low computational cost. The results for these ensembles are presented in the section titled “Domain 1”.

Although KW78 conclude their simple theoretical considerations present a high degree of realism in representing flow at the boundary for this small domain, problems may arise if the cloud begins to grow too close to the boundary. In order to account for this eventuality, the most dispersive ensembles from the 24km x 24km x 20km domain were re-tested on a domain of 96km x 96km x 20km. Results for these ensembles are presented in the section titled “Domain 2“. The horizontal and vertical resolution, time step and duration were retained from the Domain 1 set-up.

A control (CTRL) simulation was constructed on each domain using Méso-NH. The different parameters had the following CTRL settings: MP distributions for the rain, graupel and snow particles and a generalised gamma law distribution for the ice particles; the snow and graupel mass-diameter relationships labelled Meso-NH in Table 2.4; the ICE3 microphysical formulations; the turbulent closure method proposed by BL89 and the 1D version of the CU00 turbulence scheme. For simulations with Méso-NH at this 1km horizontal resolution, this is the standard configuration.

## 2.3 Domain 1

The CTRL simulation depicting the rainfall evolution over the 2h of simulation is presented in Fig. 2.2. The production of the second cell can be seen as an extension of the first larger cell in Fig. 2.2 (b). Between Fig. 2.2 (c) and (d) this cell continues to grow while the first cell dissipates. The precipitation maximum, shown in the 2h accumulated rainfall in Fig. 2.3, is concentrated in the centre of the first cell with approximately 40mm.

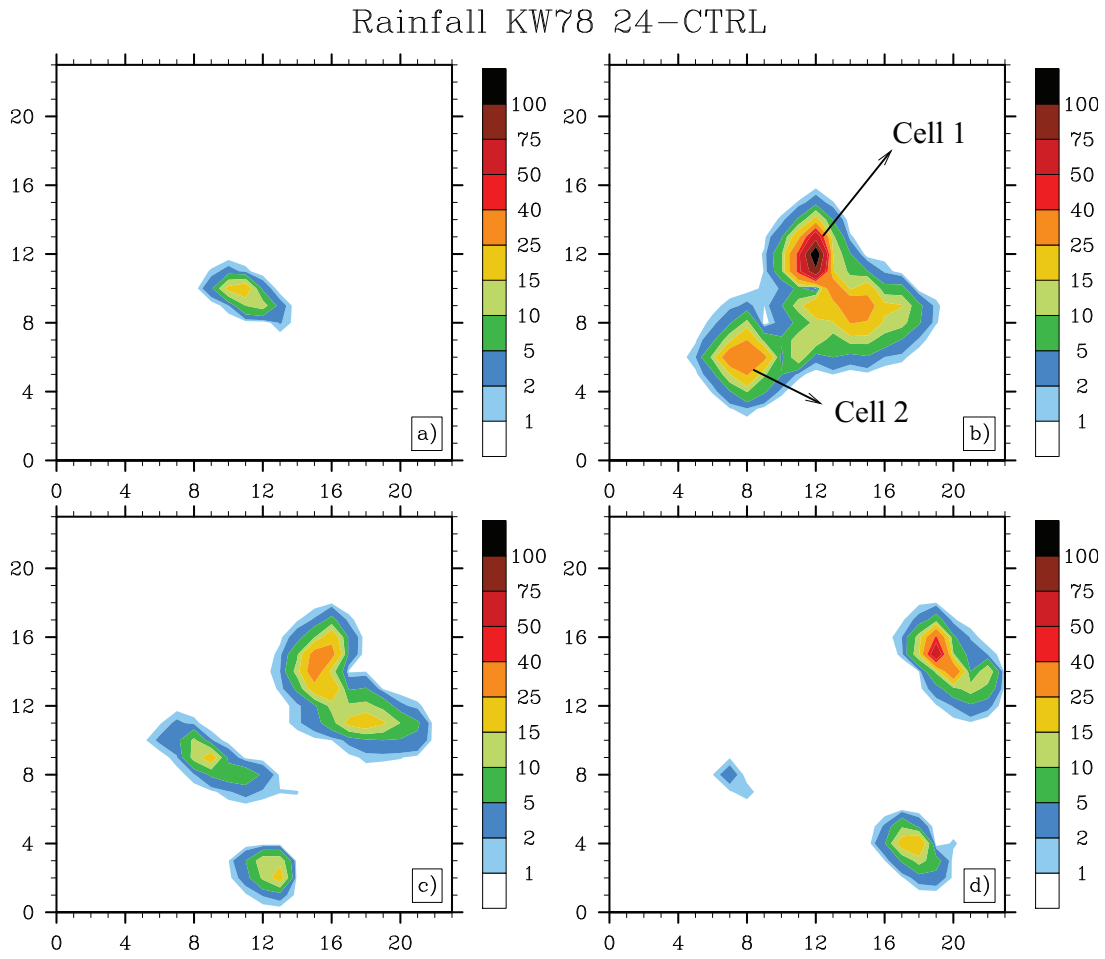


**Figure 2.2:** *CTRL simulation for KW78 showing the instantaneous rainfall (in mm/hr) at 30 minute intervals ((a)-(d)) throughout the 2h simulation.*

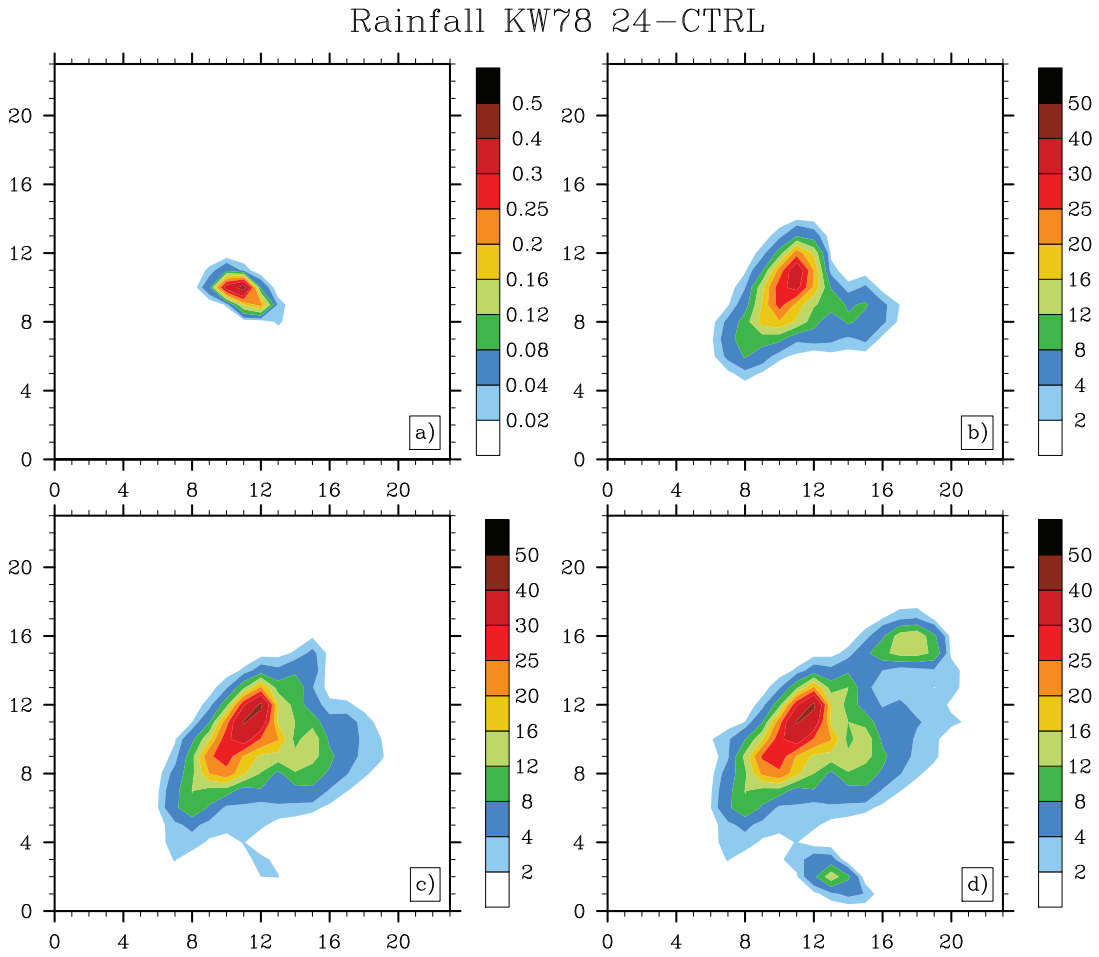


**Figure 2.3:** *CTRL simulation for KW78 showing the accumulated rainfall (in mm) at 30 minute intervals ((a)-(d)) throughout the 2h simulation.*

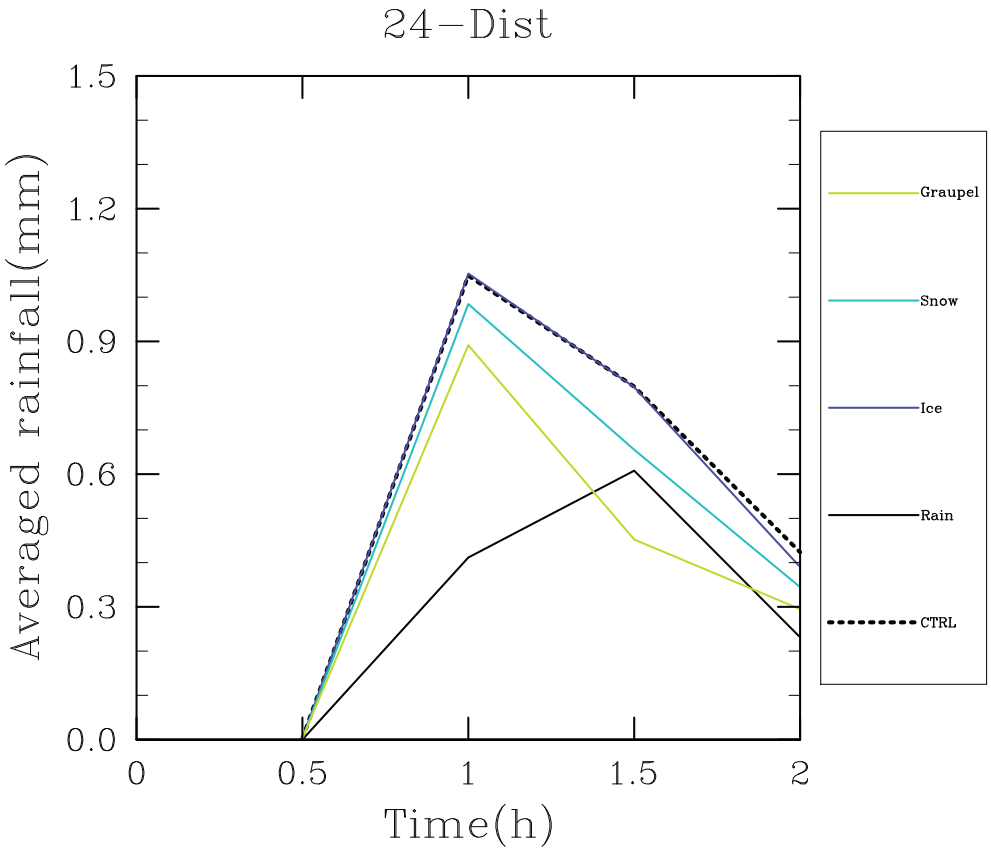


**Figure 2.4:** *Temporal evolution plot showing the rainfall evolution of the CTRL simulation and the members of the 24-Dist ensemble.*

### 2.3.1 Particle distribution

The 24-Dist ensemble perturbed the particle distribution of each hydrometeor class. This was done by modifying the $\alpha$ and $\nu$ values for each hydrometeor. Table 2.2 indicates the characteristics of each of the ensemble members of 24-Dist. The evolution of the instantaneous precipitation for each ensemble member compared to the CTRL member is shown in Fig. 2.4.

Modifying the rain particle distribution induces the greatest change in surface rainfall. The ice, snow and graupel distributions show much less sensitivity, with the ice particle evolution in particular deviating only slightly from that of the CTRL simulation. While physically more representative of the true distribution of ice particles the added complexity of a gamma-law distribution, at least for this limited test case, does not lead to a drastically different rainfall field. Modifying the snow and graupel distributions leads to changes in the rainfall maximum but does not change by a large extent the triggering of precipitation production within the model. The initial triggering and evolution of the rainfall field for the modified rainfall particle simulation differs noticeably from the others with the maximum being delayed by 30 minutes and its value being diminished by almost 50%.

The relative impact of changing a given particle distribution can be related to the processes which are modified by that distribution change. Examining the in-line bud-

gets of Méso-NH allows the relationships between the parameters of the particle distributions and other physical processes to be uncovered.

Using a generalised gamma law distribution for the raindrop spectra impacts upon the constants for the accretion of cloud droplets by raindrops and the evaporation of raindrops, two of the main warm microphysical processes which are strongly related to the production of surface rainfall. The accretion of raindrops onto aggregates as well as the rain contact freezing, raindrop collection by graupel and sedimentation are also affected by the modified particle distribution.

Using a generalised gamma law distribution for the graupel also has an impact upon several processes, modifying the vapour deposition on ice, cloud droplet collection by the graupel and the cloud ice, and the aggregate and raindrop collection by the graupel.

Replacing the MP law with a gamma law for the snow spectra has consequences for the vapour deposition on ice also, with the snow aggregation, riming of the aggregates and other cold processes also being modified.

The almost negligible impact upon the rainfall evolution of changing the ice particle spectra can be explained by the fact that the vapour deposition of ice process is the only cold microphysical process to be modified by such a change. This process while important for the production of graupel particles is not one of the more important processes in the production of rainfall.

### 2.3.2 Intercept parameter

Within Méso-NH, the intercept parameter of the particle distribution for each of the rain, snow and graupel classes is prescribed. Table 2.3 shows the different perturbation ranges used for the ensembles 24-N0r, 24-N0s and 24-N0g.

The time series plot for each ensemble is presented in Fig. 2.5. For the 24-N0r ensemble, increasing values lead to less intense rainfall and a flatter temporal evolution, with a decrease of almost 50% between the lowest and highest value of $N_{0r}$. From the MP distribution law, increasing the value of $N_{0r}$ produces a greater number of small water drops while decreasing the size of the biggest drops. This leads to a reduction in surface rainfall within the model. The snow and graupel particles also follow a MP distribution, thus the same conclusions can be drawn. With increasing values, greater numbers of small snow (graupel) particles are produced and the size of the biggest snow (graupel) particles decreases. The three ensembles present differing levels of dispersion. The 24-N0r ensemble members tend to differentiate from each other earlier than the members in the other two ensembles. The 24-N0s ensemble members begin to differ from each other only after 1 h of simulation, indicating that perturbations upon the value of $N_{0s}$ take longer to propagate within the model. For the 24-N0s ensemble, each member follows a distinct rainfall evolution compared to the members of the 24-N0r ensemble which tend to converge towards the end of the 2 h simulation.

The 24-N0g ensemble shows that with increasing $N_{0g}$, the intensity of the rain decreases. The rainfall maximum lasts 30 minutes longer in the member with the lowest $N_{0g}$ value compared to the member with the highest. The higher $N_{0g}$ values lead to less rainfall production through graupel melting due to an increased amount of smaller

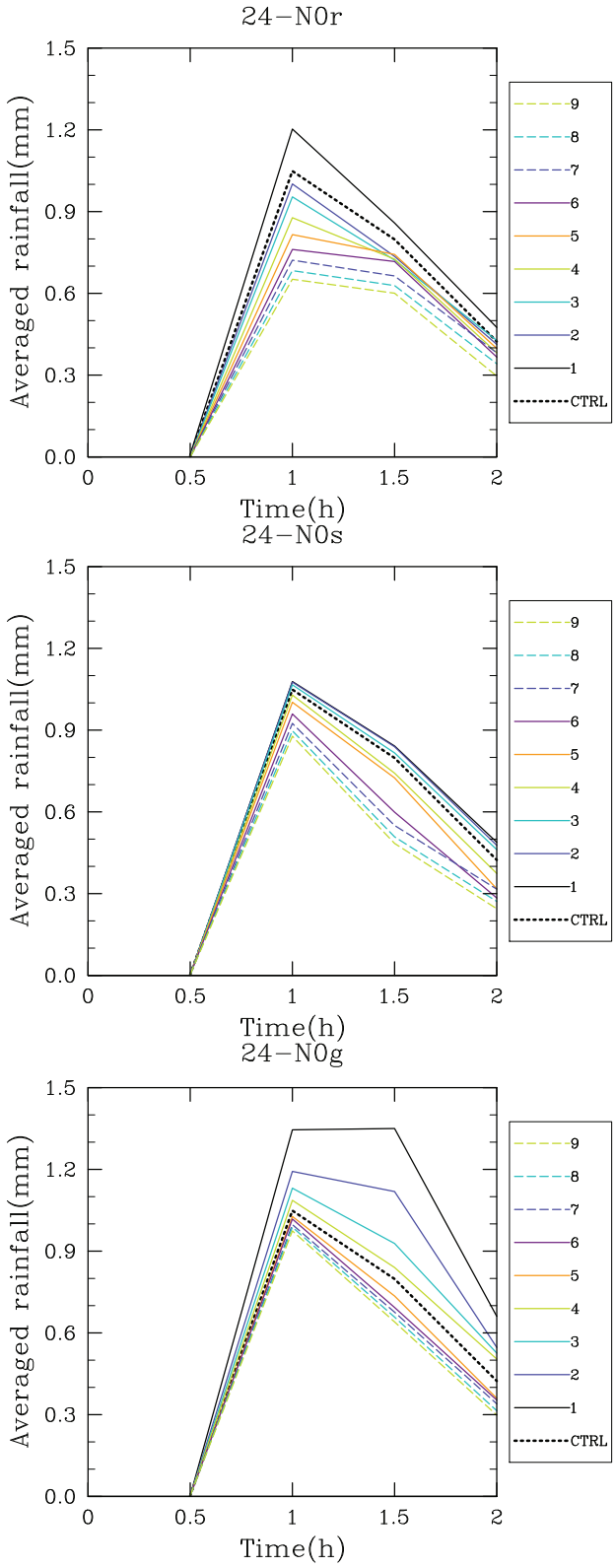


**Figure 2.5:** *Temporal evolution plots for 24-N0r (Row1), 24-N0s (Row2) and 24-N0g (Row3) ensembles.*

particles and a reduction in the size of the biggest particles. With a lower $N_{0g}$ value, the size of the biggest particles increases according to the particle distribution, which will increase their contribution to the graupel melting process as they descend below the melting level. The 24-N0s ensemble presents characteristics similar to those of the 24-N0r ensemble, albeit with less dispersion around the peak value. The differences between the three ensembles can be related to the microphysical processes impacted by modifying each intercept parameter. Coupled with the effects on drop size and number already detailed, changing the $N_{0g}$ value modifies the collection processes by the graupel of the cloud ice, aggregates and raindrops. Perturbing the $N_{0r}$ value impacts upon the accretion of cloud droplets by raindrops, evaporation of raindrops and accretion of raindrops onto aggregates while $N_{0s}$ perturbations lead to modifications in the snow aggregation, riming of aggregates, vapour deposition on ice and the accretion of raindrops by aggregates.

### 2.3.3 Autoconversion cloud content and time constants

Ensembles 24-Auto-KK and 24-Auto-KW showed limited sensitivity to the introduced perturbations and are thus not reported upon directly. The corresponding plots have been included in Appendix B.

### 2.3.4 Hydrometeor classes

The characteristics of each member of the Snow and Graupel ensembles are detailed in Table 2.4 along with the CTRL values for each hydrometeor class.

The results show a weak sensitivity to the numerous snow configurations (the related plots are added in Appendix B). The Snow-8 structure differs the most from the other members of the ensemble, giving the maximum in precipitation. The differences between the other members are minimalistic demonstrating a faint connection between the representation of the snow particles and the precipitation at the surface. The dispersion in the Graupel ensemble is greater than that of the Snow ensemble but remains of no big importance. The CTRL run, with the lump graupel 2 (Graupel 1) configuration, gave the maximum rainfall amount. The point of maximum intensity is modified for the Graupel ensemble but the triggering point of the precipitation remains common to all members. The dispersion in both ensembles is less remarkable than that seen for the 24-N0r, 24-N0s and 24-N0g ensembles, thus giving a sense of the level of importance of each factor for rainfall production. The snow and graupel mass-diameter and fall speed-diameter relationships are concluded to be less important for rainfall production than the value of the particle intercept parameters.

### 2.3.5 Microphysical processes

The mean and standard deviation plot along with the temporal evolution of the most dispersive cold process group ensemble (24-C-Group5) are given in Fig. 2.6. The plots for all of the other groups are given in Appendix B. In order of dispersive importance as

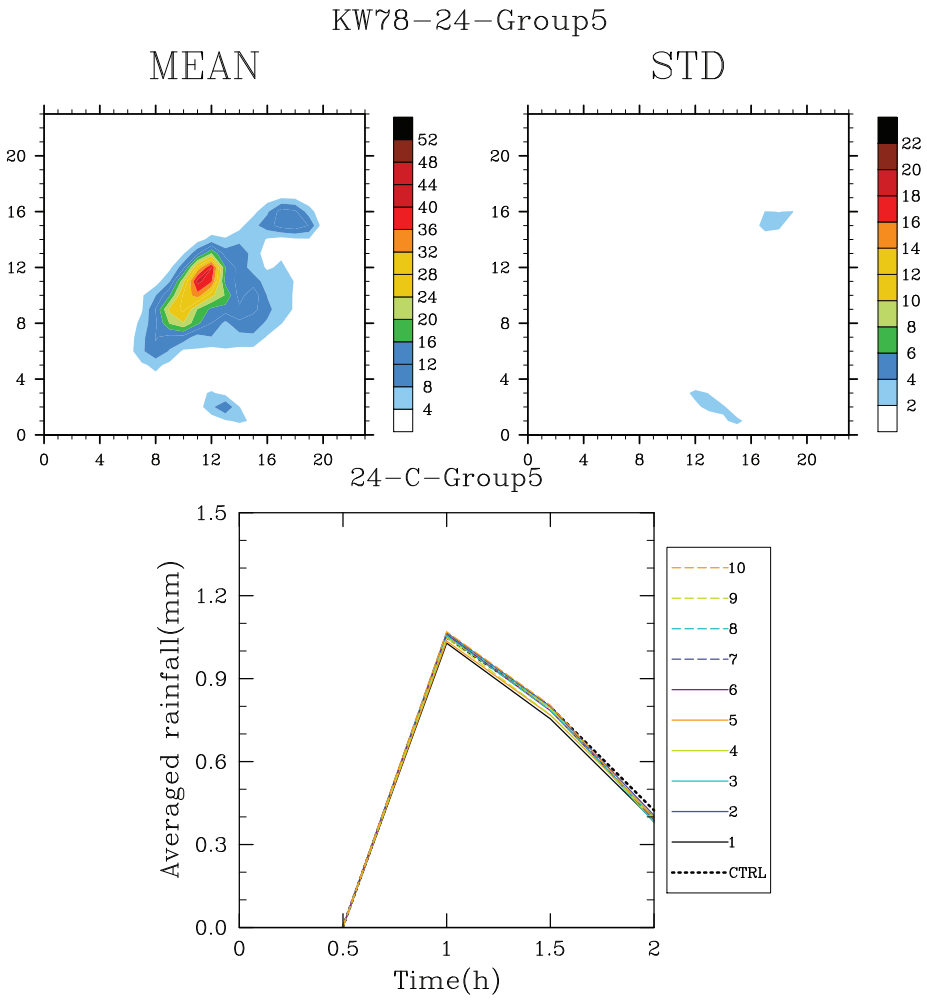


**Figure 2.6:** *The mean and standard deviation from the mean of the rainfall field along with the temporal evolution of the rainfall for the ensemble 24-C-Group5.*

demonstrated by the plots, ensembles 24-C-Group5, 24-C-Group4 and 24-C-Group2 induce the most dispersion in the surface rainfall. Ensembles 24-C-Group1 and 24-C-Group3 give negligible dispersion. The ensemble 24-C shows an increase in dispersion compared to any one of the 24-C-Group(1-5) ensembles.

A larger degree of dispersion was expected for the 24-C ensemble. The sensitivity to the melting processes in particular was expected to be greater, seen as increased graupel melting can lead to an increase in the supply of rainwater. This underimportance of the cold processes demonstrates one weakness in using the KW78 as a test case. An examintation of the maximum cloud height (not shown), shows that the convective clouds produced do not reach heights (maximum height of 4km) sufficient enough for the cold processes to strongly impact the rainfall production. The small horizontal expanse and short life-time of the convective cells would also have impacted upon the contribution of the cold processes to the development of the surface rainfall.

The mean and standard deviation plots for the 24-Auto, 24-Acc and 24-Evap ensembles are presented in Fig. 2.8. Very little sensitivity is shown for the 24-Auto ensemble. As the autoconversion process is the sole rainwater initiation mechanism within

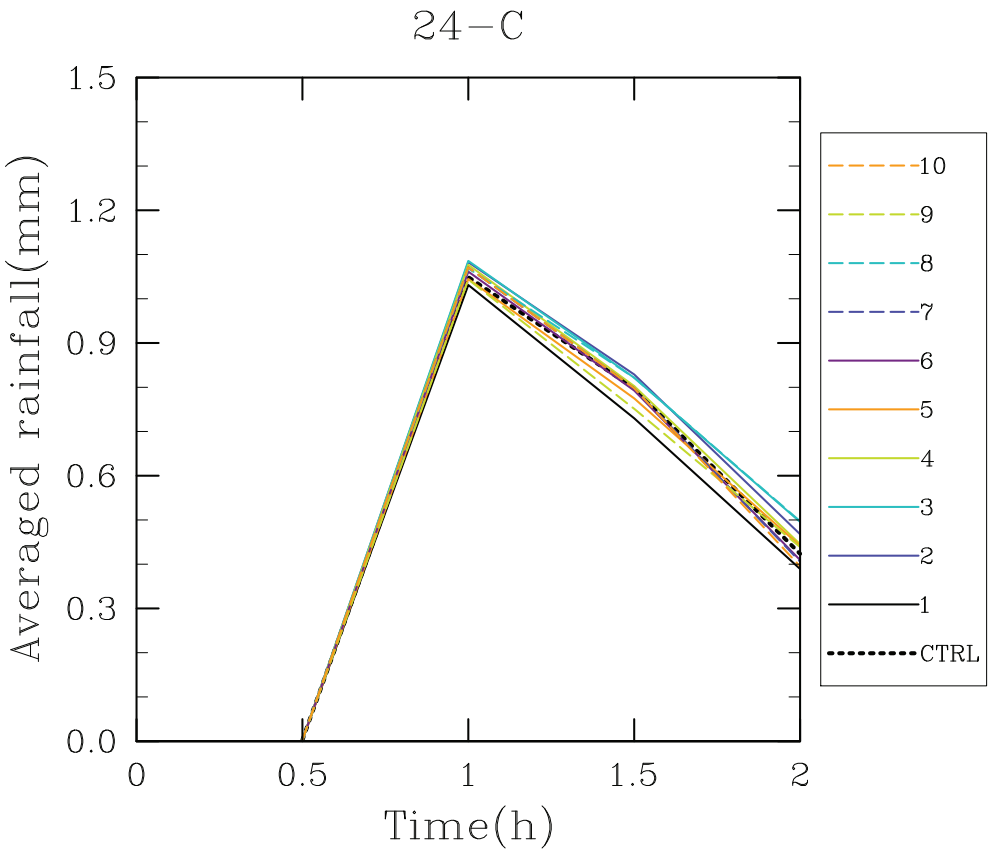


**Figure 2.7:** *Temporal evolution of the rainfall for the 24-C ensemble.*

the ICE3 microphysical parameterisation scheme, a greater degree of dispersion was expected. Manipulating the accretion and evaporation processes has a greater impact upon the surface rainfall than manipulating the autoconversion process as shown by the increased dispersion in the 24-Acc and 24-Evap ensembles compared to the 24-Auto ensemble. The time series plots given in Fig. 2.9 underline the different levels of sensitivity. At the peak in precipitation the members of the 24-Evap ensemble differ more distinctly than the members of the 24-Acc ensemble. The almost negligible impact of the perturbations upon the autoconversion is distinctly seen.

Perturbing the three processes simultaneously in one ensemble (24-WA) increases the ensemble dispersion. The mean, standard deviation and temporal evolution plots for the 24-WA ensemble are presented in Fig. 2.10. Comparing the standard deviation plot for the 24-WA ensemble to that of the 24-Auto, 24-Acc or 24-Evap ensembles, the increase in dispersion is clearly seen. The temporal evolution plot shows an increase in dispersion around the peak in precipitation compared to the 24-Auto, 24-Acc or 24-Evap ensembles. Comparisons of these plots also demonstrate that for the 24-WA ensemble, the evolution of the different members does not converge toward the end of the simulation. This indicates that the perturbations were sustained for the duration of the simulation. The 24-WA ensemble also shows a more even distribution of members around the CTRL simulation making it more statistically sound than the 24-Auto, 24-Acc or 24-Evap ensembles as the probability distribution would appear more Gaussian.

An ensemble combining perturbations upon the cold and warm microphysical processes (24-WC) was also constructed. A slight increase in the standard deviation signal, shown in Fig. 2.11, compared to that of the 24-WA ensemble, confirms the low level of sensitivity to cold process perturbations demonstrated by Fig. 2.7. The temporal evolution plot for the 24-WC ensemble in Fig. 2.11 is indistinguishable in comparison to that of the 24-WA ensemble, again underlining the almost negligible effect of including cold process perturbations for this case.

### 2.3.6 Turbulent tendencies

Perturbations were introduced upon the turbulent time tendencies in the manner presented in section 2.1.4. An ensemble was constructed combining perturbations upon the cold and warm microphysical and turbulent time tendencies (24-MT). This allowed the change in the rainfall evolution, compared to the 24-WA and 24-WC ensembles, brought about by these perturbations, to be highlighted. The plots presented in Fig. 2.12 show that the 24-MT ensemble has a reduced precipitation peak compared to the 24-WA and 24-WC ensembles. The temporal evolution plot illustrates that the dispersion in instantaneous rainfall evolution for the members is increased for the 24-MT ensemble and that the members begin to deviate from each other earlier in the 24-MT ensemble in comparison to 24-WA and 24-WC. This indicates that the perturbations introduced into the 24-MT ensemble began to grow more quickly within the model. Comparing the mean and standard deviation plots of the three ensembles shows that the 24-MT ensemble gives a slightly increased mean while also demonstrating an increased standard deviation from the mean.

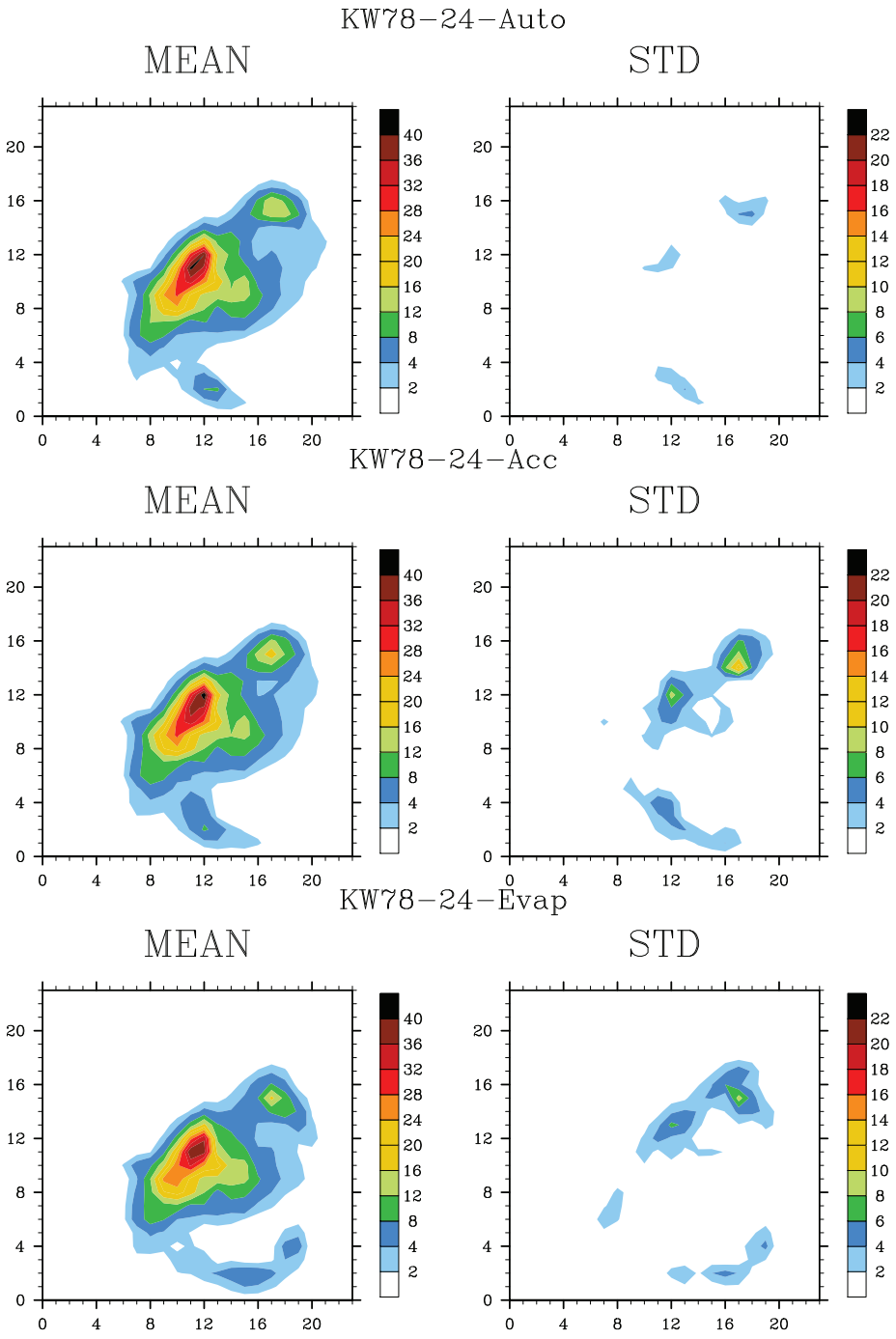


**Figure 2.8:** *The mean and standard deviation from the mean of the rainfall field for the 24-Auto (Row1), 24-Acc (Row2) and 24-Evap (Row3) ensembles.*

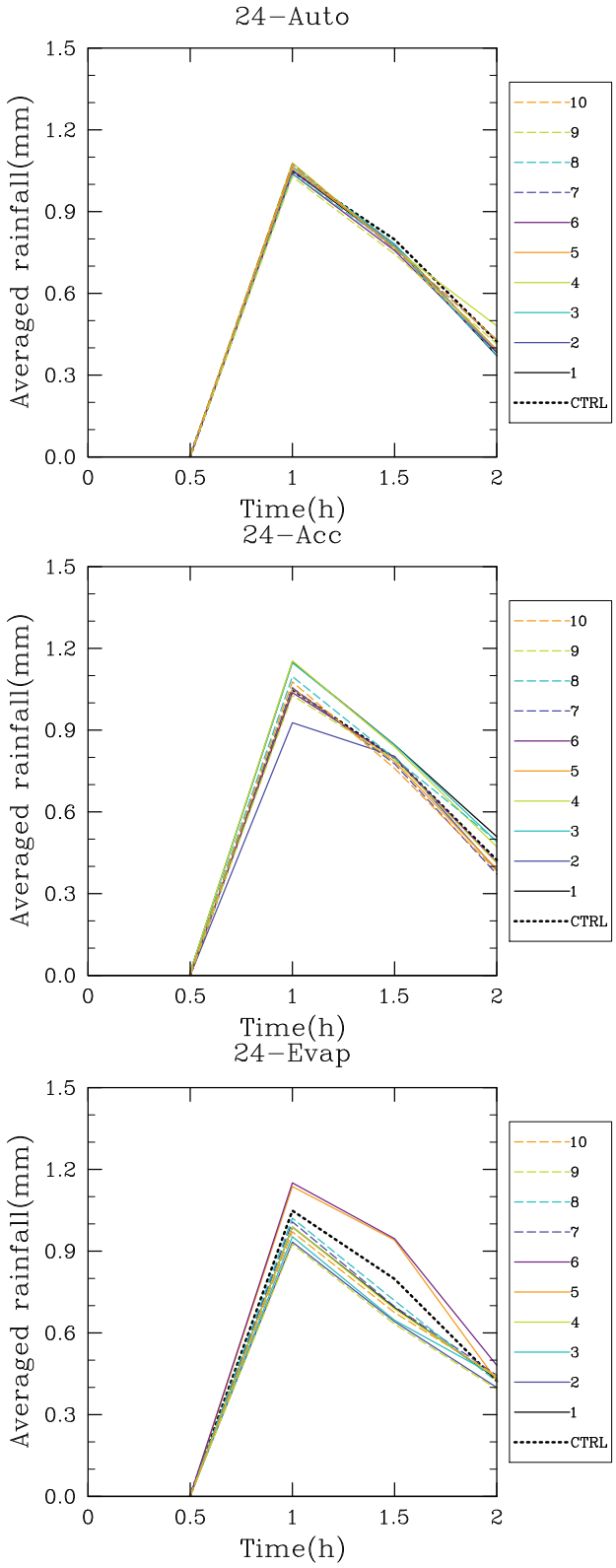


**Figure 2.9:** *The temporal evolution plots of the rainfall for the 24-Auto (Row1), 24-Acc (Row2) and 24-Evap (Row3) ensembles.*

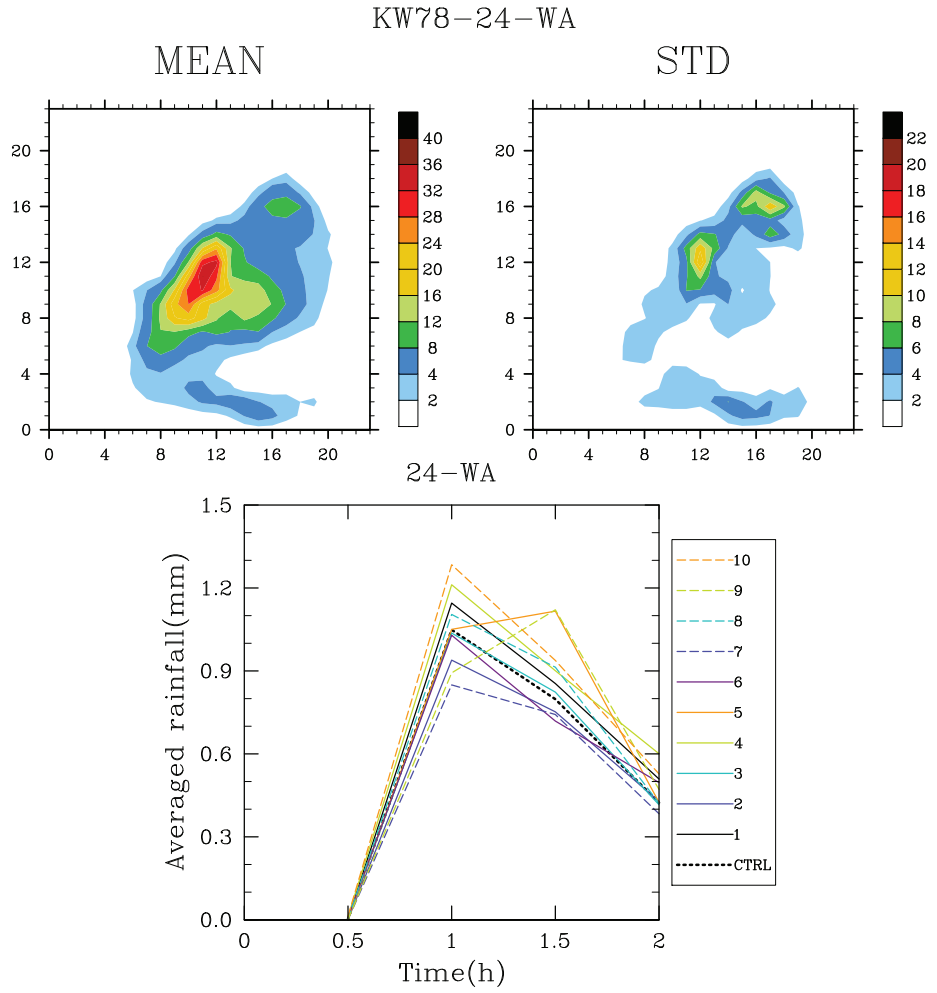


**Figure 2.10:** *The mean and standard deviation from the mean of the rainfall field along with the temporal evolution of the rainfall for the 24-WA ensemble.*

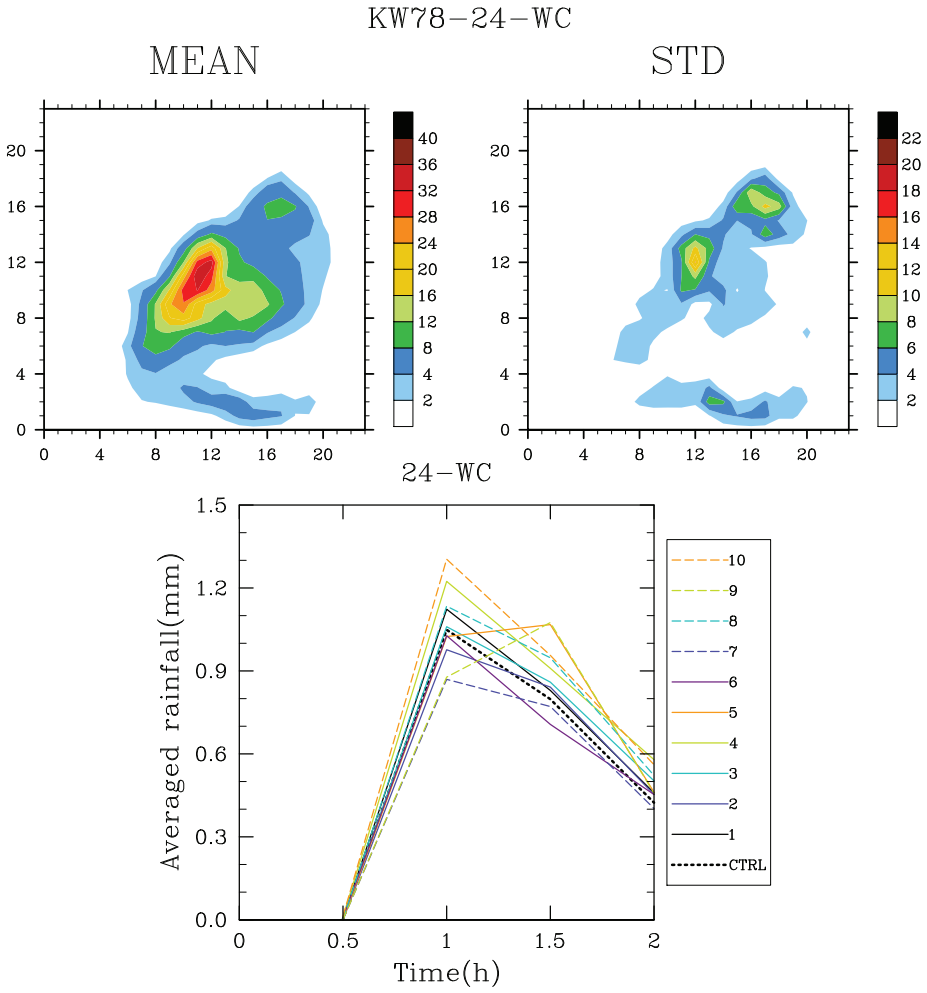


**Figure 2.11:** *The mean and standard deviation from the mean of the rainfall field along with the temporal evolution of the rainfall for the 24-WC ensemble.*

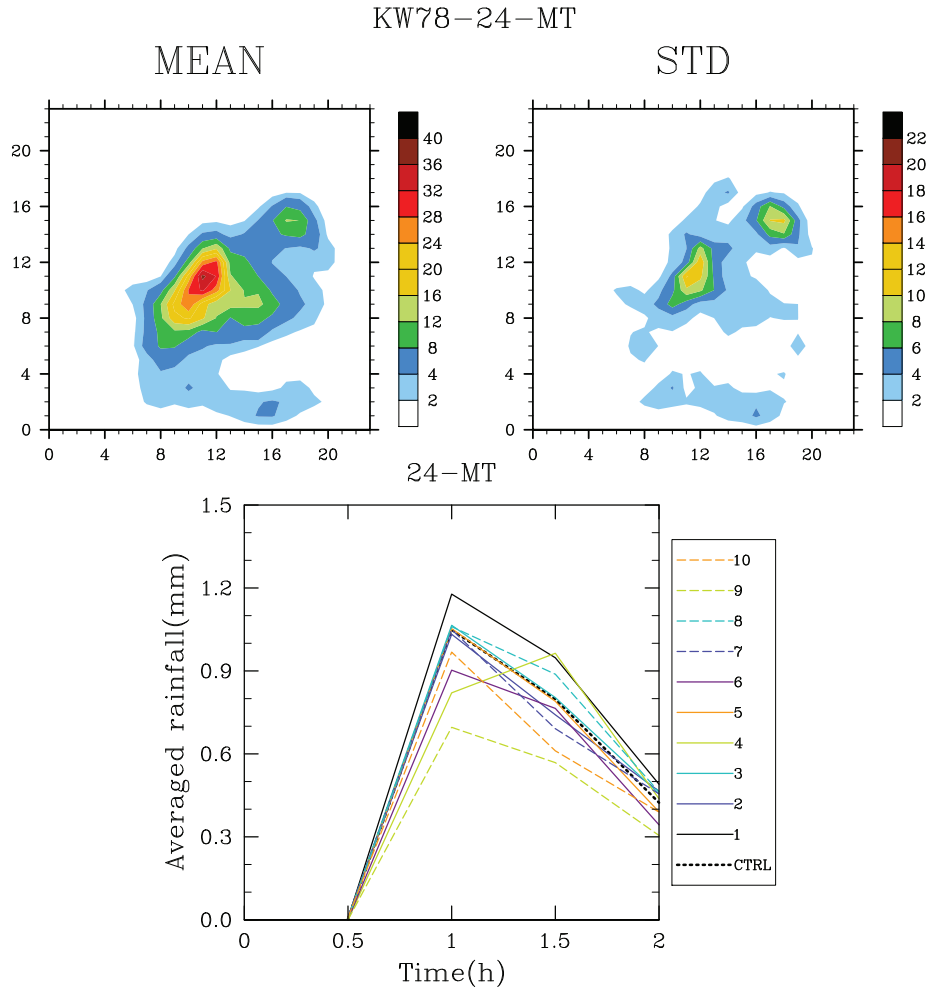


**Figure 2.12:** *The mean and standard deviation from the mean of the rainfall field along with the temporal evolution of the rainfall for the 24-MT ensemble.*

### 2.3.7 TKE and TKE sources

Ensembles 24-TKE and 24-TKE-S showed limited sensitivity to perturbations and are thus not reported upon directly. The corresponding plots have been included in Appendix B.

### 2.3.8 Conclusions - Domain 1

The convective situation described in Klemp and Wilhelmson (1978) was used to test the sensitivity of the surface rainfall to perturbations introduced upon microphysical and turbulent parameterisations. These perturbations were introduced by adjusting constants within ranges of admitted possibility or by modifying the time tendencies of the microphysical and turbulent processes. Ensembles were then constructed from the perturbed simulations. Depending on the dispersion induced in the ensemble, the level of sensitivity of the surface rainfall to the perturbed process was deduced.

The results show that a sensitivity hierarchy exists. For the time tendency ensembles, the 24-MT ensemble gave the greatest degree of dispersion. The evolution of the surface rainfall was shown to be very sensitive to perturbations introduced upon a combination of the cold and warm microphysical and turbulent processes. In terms of individual processes, the dispersion induced in the 24-Acc and 24-Evap ensembles demonstrated that these are pertinent factors in the evolution of the rainfall. The 24-Auto ensemble showed that the rainfall has a weak sensitivity to modifications in the autoconversion process. In general, the surface rainfall was weakly sensitive to perturbations introduced upon the cold microphysical processes with very little dispersion found for the 24-C ensemble. Investigations into perturbing adjustable microphysical parameters showed that the evolution of the rainfall was quite sensitive to the value of $N_{0r}$ and $N_{0g}$, as shown by the dispersion in ensembles 24-N0r and 24-N0g.

To further investigate the sensitivity of the surface rainfall to certain parameters, the most dispersive ensembles, notably 24-N0r, 24-N0g, 24-WA, 24-WC and 24-MT, were re-constructed for the same convective situation, but on a larger domain of 96km x 96km x 20km. This increase in domain size decreases the likelihood of boundary errors affecting the rainfall pattern and thus underlines more realistically the change in rainfall evolution brought about by the microphysical and turbulent perturbations. These new ensembles are presented in section “Domain 2”.

## 2.4 Domain 2

The instantaneous rainfall pattern produced at 30 minute intervals over the 2 h simulation is presented in Fig. 2.13 while the accumulated rainfall is given in Fig. 2.14. A zoom has been performed over the area of Domain 1 in order to compare the rainfall evolution within both domains (Domain 1 CTRL presented in Fig. 2.2). Overall, the shape of the convective cells is more defined than in Domain 1. The storm still splits into two cells but in contrast with Domain 1, the first convective cell remains more active

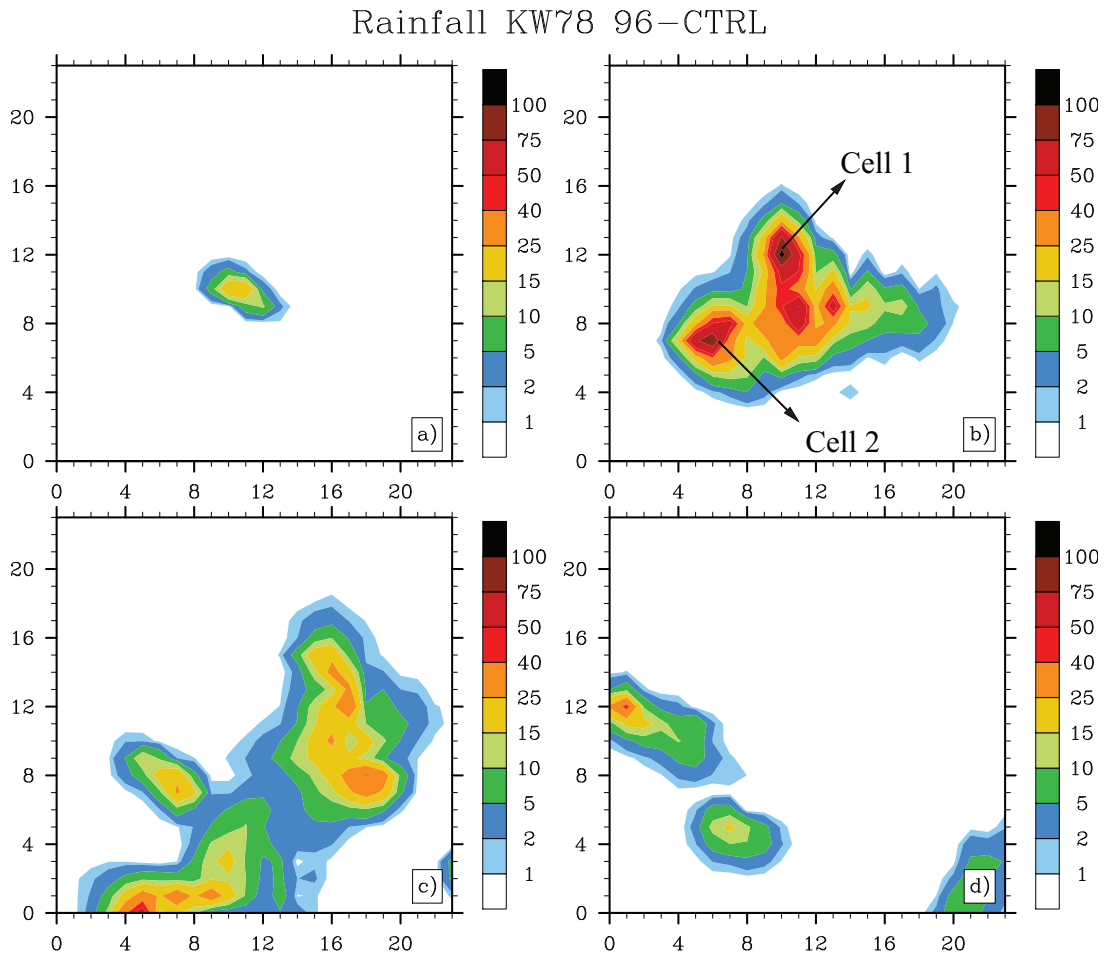


**Figure 2.13:** *The CTRL simulation showing the instantaneous rainfall (in mm/hr) at 30 minute intervals ((a)-(d)) for Domain 2 zoomed in over Domain 1 and comparable with Fig. 2.2.*

for longer (plots (c) in Fig. 2.13 and Fig. 2.2. The second cell occupies a larger area than in Domain 1 suggesting that the proximity of the domain boundaries restricted its development.

### 2.4.1 Intercept parameter

The temporal evolution, mean and standard deviation plots of the surface rainfall for the 96-N0r and 96-N0g ensembles are given in Fig. 2.15 and Fig. 2.16. As was done for the CTRL simulation, a zoom was performed over the area of Domain 1 in order to have comparable statistics. Comparing the temporal evolution plot in Fig. 2.15 and Fig. 2.16 to those in Fig. 2.5, the level of dispersion remains largely unchanged. The maximum averaged rainfall value has increased for Domain 2 while its peak value now appears approximately 30 minutes later than for Domain 1. As seen in Domain 1, the dispersion in the rainfall evolution for the 96-N0r ensemble is greater and appears more quickly between the members than for the 96-N0g ensemble. The 96-N0g ensemble clearly gives a stronger mean precipitation value than the 96-N0r ensemble, while also presenting heavier precipitation over a more widespread area (see mean and standard

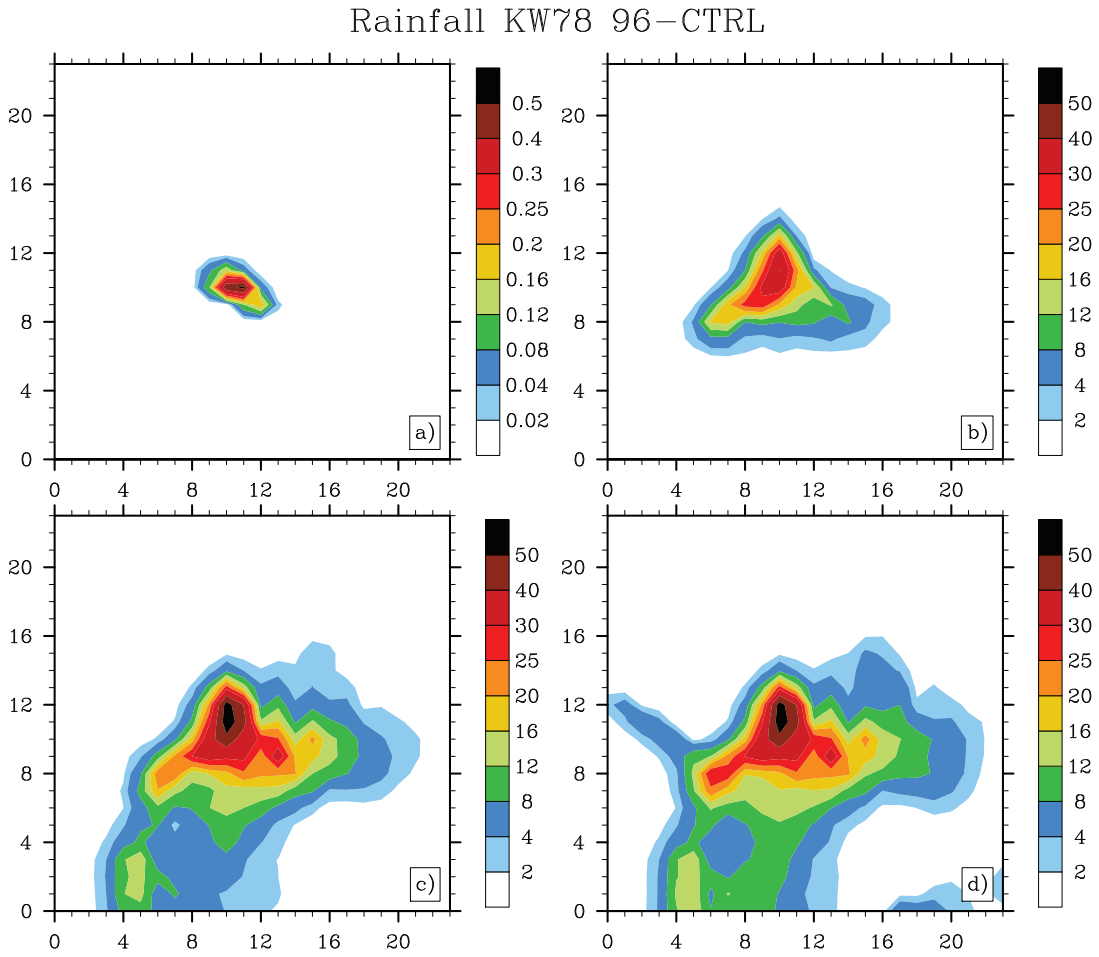


**Figure 2.14:** *The CTRL simulation showing the accumulated rainfall (in mm) at 30 minute intervals ((a)-(d)) for Domain 2 zoomed in over Domain 1 and comparable with Fig. 2.3.*

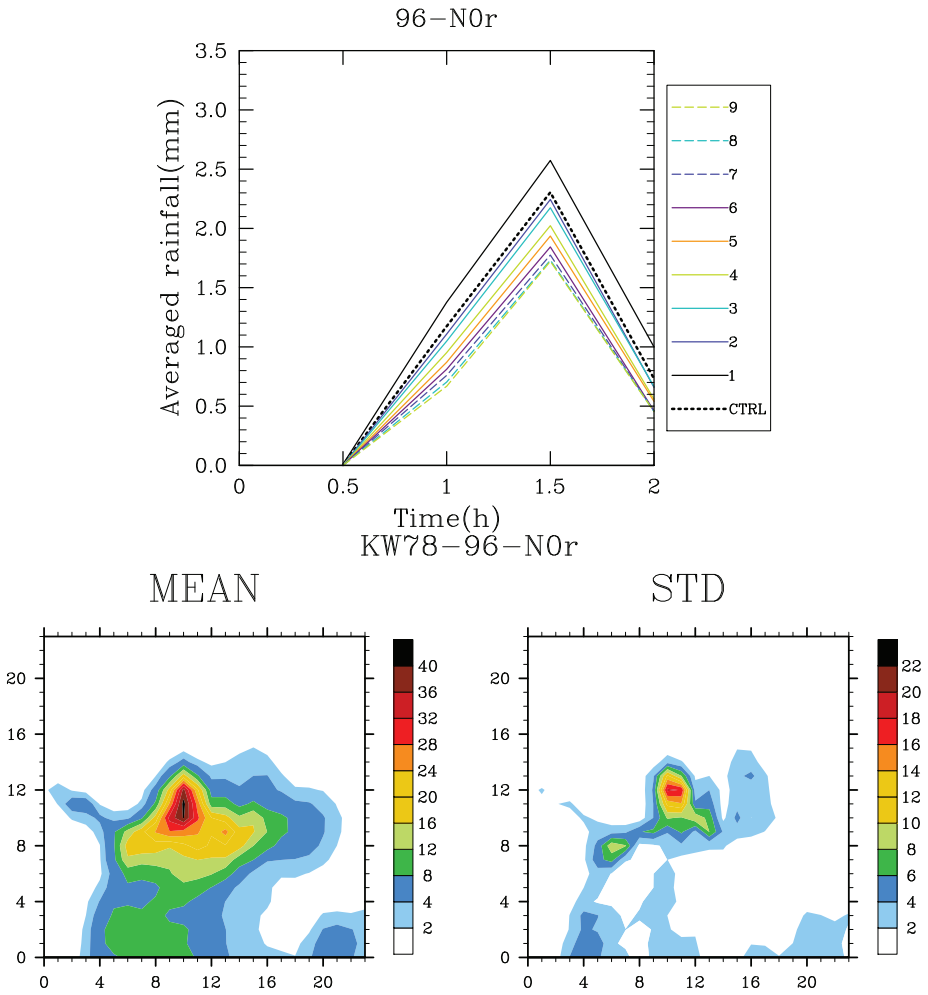


**Figure 2.15:** *The temporal evolution and mean and standard deviation plots for the 96-N0r ensemble zoomed over Domain 1.*

deviation plots in Fig. 2.15 and Fig. 2.16). Evidently the value of $N_{0g}$ is strongly linked to the intensity of the surface rainfall.

### 2.4.2 Microphysical processes

The temporal evolution, mean and standard deviation plots for the 96-WA and 96-WC ensembles are presented in Fig. 2.17 and Fig. 2.18. The level of dispersion induced by these perturbations is, as was the case for the 96-N0r and 96-N0g ensembles, comparable to the dispersion seen in the 24-WA and 24-WC ensembles. There is an increase in the mean rainfall and a shift in the timing of the precipitation peak, but these factors are attributed to the increased domain size as they were seen in both the 96-N0r and 96-N0g ensemble. Comparing the dispersion in the 96-N0r and 96-N0g ensembles to that in the 96-WA and 96-WC ensembles, there is a clear increase in dispersion when the warm and cold microphysical tendencies are perturbed, especially when comparing the standard deviation signals of each of the ensembles (96-N0r in Fig. 2.15, 96-N0g in Fig. 2.16). Between the 96-WA and 96-WC ensemble, the change

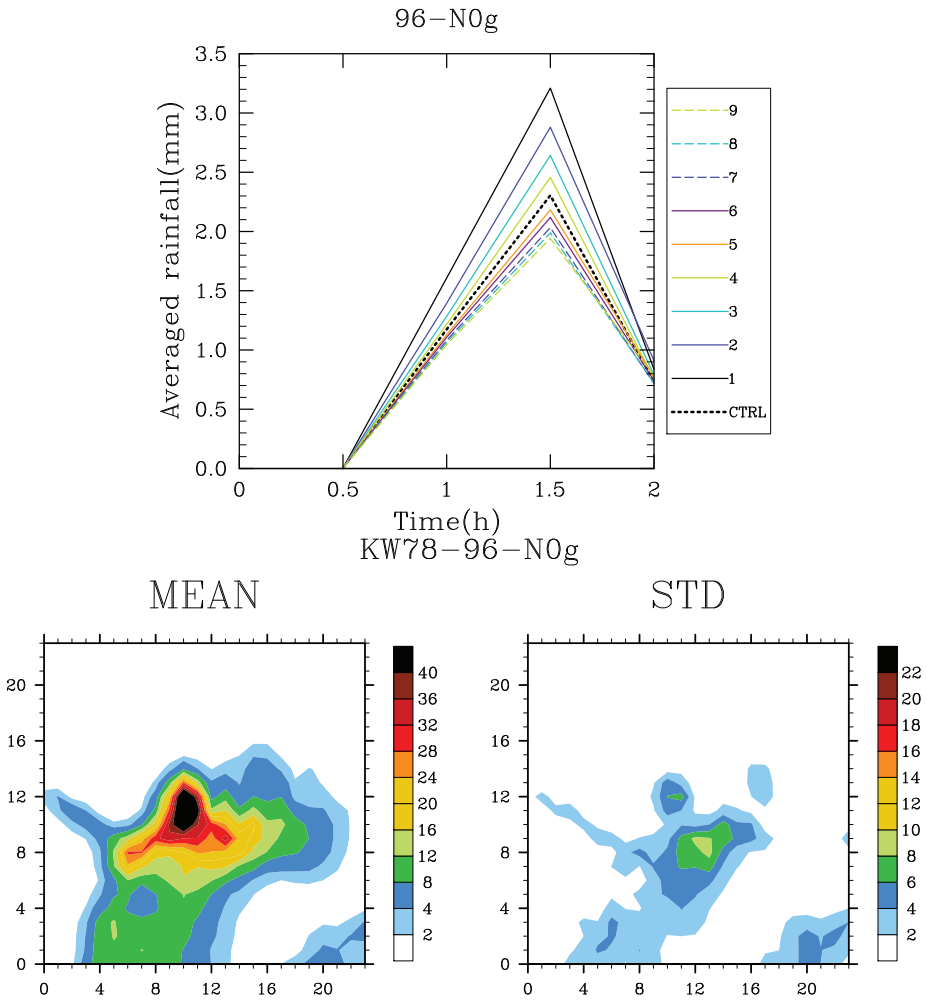


**Figure 2.16:** *The temporal evolution and mean and standard deviation plots for the 96-N0g ensemble zoomed over Domain 1.*

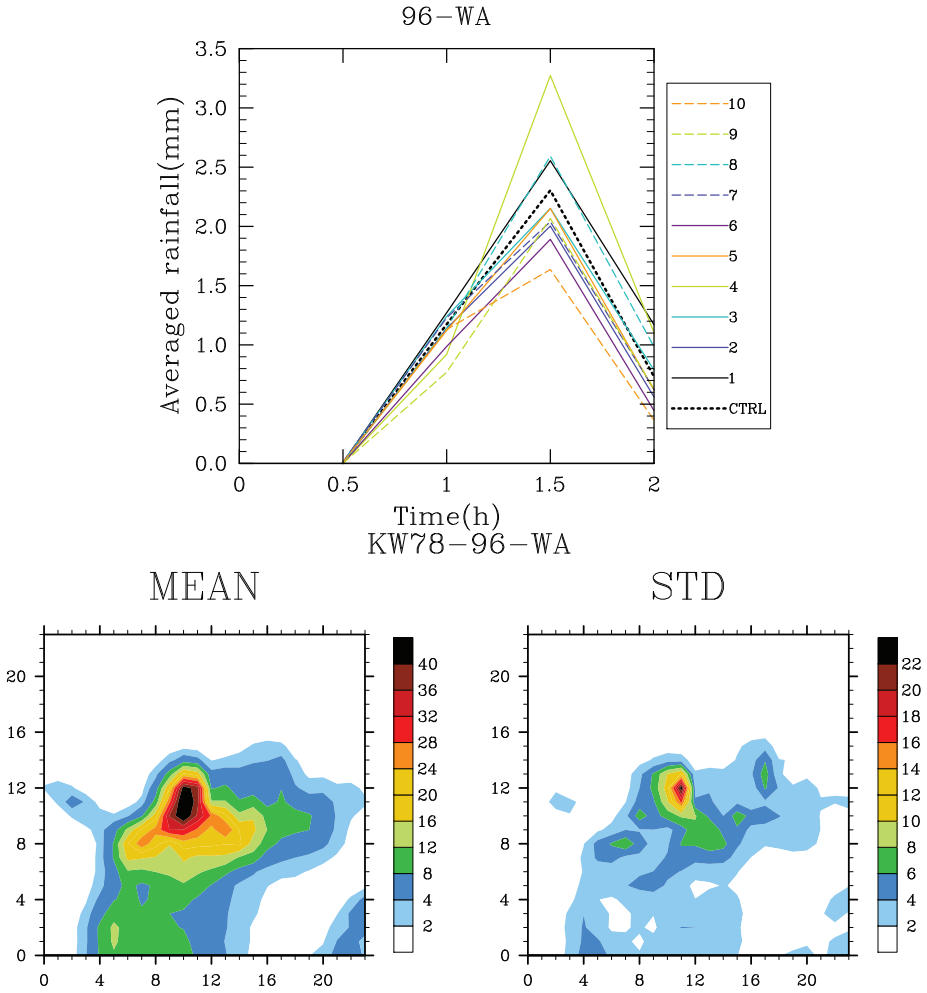


**Figure 2.17:** *The temporal evolution and mean and standard deviation plots for the 96-WA ensemble zoomed over Domain 1.*

in dispersion in the ensemble is even less remarkable than that seen between 24-WA and 24-WC. The temporal evolution plots are almost identical, again underlining the weak sensitivity of the surface rainfall to cold process perturbations.

### 2.4.3 Turbulent tendencies

The mean and standard deviation plot for the 96-MT ensemble presented in Fig. 2.19 shows a decrease in the mean rainfall value compared to the 96-WA and 96-WC ensembles. As in the 24-MT ensemble, an increase in the standard deviation signal is seen. For the 96-MT ensemble the increase is seen around the fringes of the main convective cell in the centre of the domain. The decrease in the rainfall mean is confirmed by the temporal evolution plot given in the manuscript Appendix B as Fig. B.11.

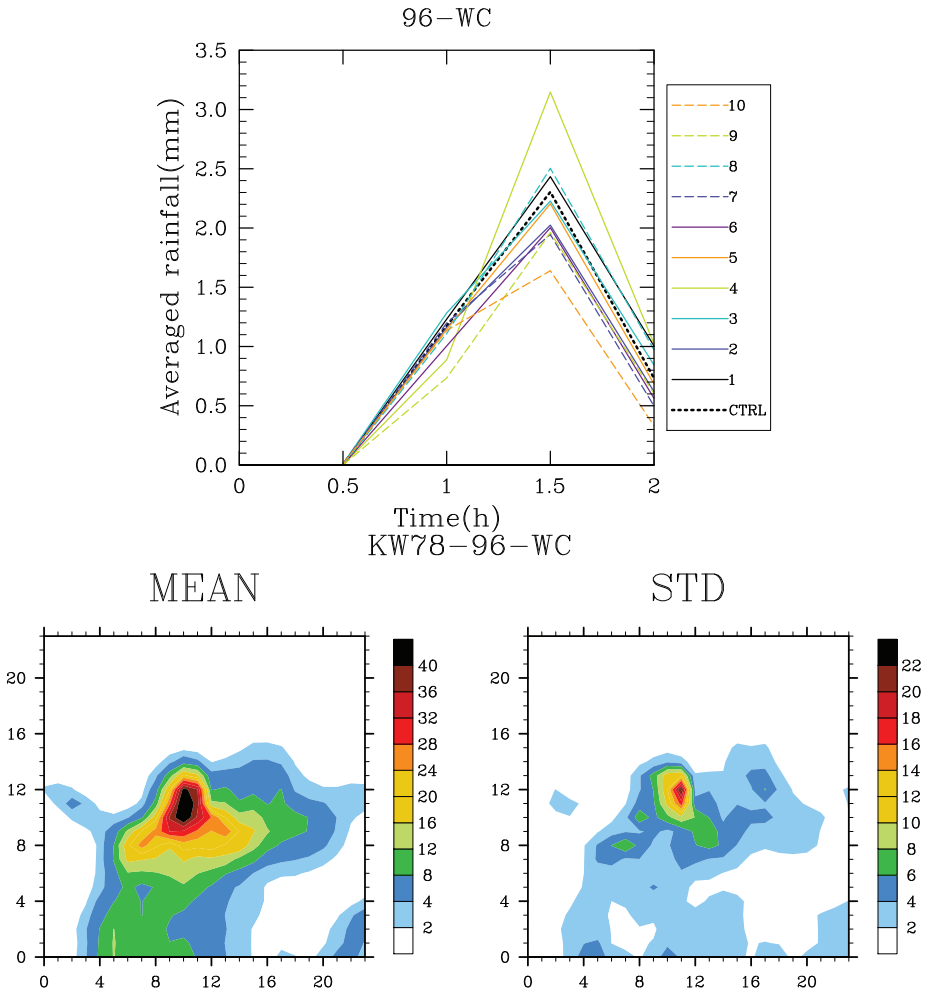


**Figure 2.18:** *The temporal evolution and mean and standard deviation plots for the 96-WC ensemble zoomed over Domain 1.*

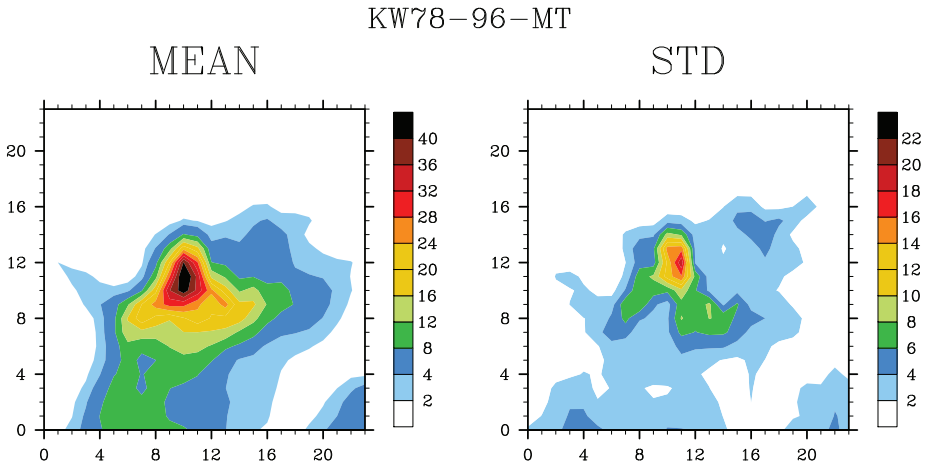


**Figure 2.19:** *The mean and standard deviation plots for the 96-MT ensemble zoomed over Domain 1.*

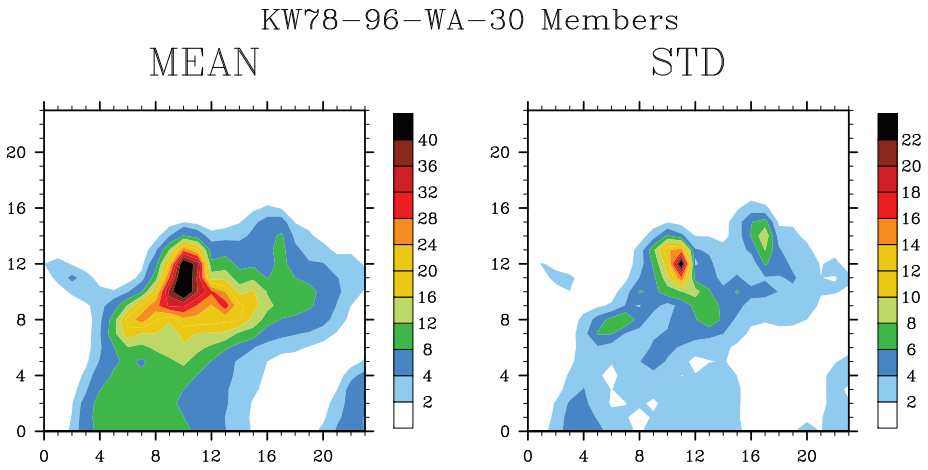


**Figure 2.20:** *The mean and standard deviation plots for the warm process ensemble performed with 30 members as opposed to 10.*

### 2.4.4 Testing ensemble size

All of the ensembles have thus far been performed with 10 perturbed members. In order to test the effect of adding more perturbed members to an ensemble, the 96-WA ensemble was re-constructed with 30 perturbed members. As expected, comparisons between the mean and standard deviation plots in Fig. 2.20 and Fig. 2.17 show that having increased ensemble size does little to change the level of ensemble dispersion.

### 2.4.5 Conclusions - Domain 2

The most dispersive ensembles (24-N0r, 24-N0g, 24-WA, 24-WC and 24-MT) from the tests performed on Domain 1 were re-constructed on a 96km x 96km x 20km domain (Domain 2). Results showed that the ensembles where the microphysical and turbulent time tendencies were perturbed (96-WA, 96-WC, 96-MT) gave the greatest degree of dispersion. For the adjustable parameter ensembles, 96-N0r and 96-N0g, the dispersion was less. The 96-N0r ensemble gave more dispersion than the 96-N0g ensemble, while the 96-N0g ensemble had a very strong ensemble mean rainfall. Comparing the ensembles of Domain 2 (96-N0r, 96-N0g, 96-WA, 96-WC, 96-MT) to their respective ensembles on Domain 1 (24-N0r, 24-N0g, 24-WA, 24-WC, 24-MT) the relative level of dispersion is maintained. Differences are remarked in the mean value of the ensemble rainfall, which is stronger for all ensembles on Domain 2, and in the timing of the precipitation peak, which occurs 30 minutes later on Domain 2 than on Domain 1. Thus, the hierarchy of sensitivity that was established by the Domain 1 ensembles remains, with 96-WA, 96-WC and 96-MT confirmed as the most dispersive.

The KW78 case study describes the evolution of a convective supercell system in a particular environment over a limited domain and over a short time period. For other forms of deep convective events, the sensitivity to perturbations upon the microphysical and turbulent parameters may differ. In order to investigate the possibility of these differences, the 96-WA, 96-WC and 96-MT ensembles were constructed for another

deep convective organisation, i.e. a squall line.

## 2.5 Idealised squall line description and simulation set-up

Weisman and Klemp (1982)(WK82) described an idealised structure constructed in a horizontally homogeneous atmosphere which contained an axially symmetrical thermal perturbation with a horizontal radius of 10km and a vertical radius of 1400m. A temperature excess of 2°C was defined at the thermal centre, gradually decreasing to 0°C at the thermal's edge. The vertical profiles of the temperature, moisture and wind speed were defined by analytic expressions designed to provide smooth data profiles. The environmental potential temperature $\overline{\Theta}$ was defined by,

$$\overline{\Theta(z)} = \Theta_0 + (\Theta_{tr} - \Theta_0)\,(\frac{z}{z_{tr}})^{\frac{5}{4}} \tag{2.5}$$

for $z \leq z_{tr}$, and as

$$\overline{\Theta(z)} = \Theta_{tr}\ \exp\ [\frac{g}{c_p\,T_{tr}}\,(z - z_{tr})] \tag{2.6}$$

for $z > z_{tr}$.

The humidity profile was defined as a function of height, $H$, as,

$$H(z) = 1 - \frac{3}{4}\,(\frac{z}{z_{tr}})^{\frac{5}{4}} \tag{2.7}$$

for $z \leq z_{tr}$, and as 0.25 for heights greater than the tropopause height, which is defined to be at 12km, with its potential temperature ($\Theta_{tr}$) to be 343K and its temperature ($T_{tr}$) to be 213K. The surface potential temperature ($\Theta_0$) was given as 300K with a fixed value for the mixing ratio near the surface in order to approximate a well-mixed boundary layer. $Q_{v0}$ was given a value of $11gkg^{-1}$. The wind shear magnitude was varied proportional to the parameter $U_s$, which was given an initial value of $15ms^{-1}$. The wind profile was defined as,

$$U = U_s \cdot tanh(\frac{z}{z_s}) \tag{2.8}$$

where $z_s$ was kept constant at 3km throughout the simulations. This set-up was chosen due to the ease in modifying the idealised framework, which could be adjusted by changing a few appropriate coefficients. WK82 used this framework to successfully demonstrate the dependence of convective storm structure on environmental wind shear and buoyancy.

In contrast to WK82, the domain size was increased to 256km x 512km and the horizontal resolution was decreased to 1km with a simulation time of 6 h. The CTRL simulation showing the rainfall evolution at each hour of simulation is shown in Fig. 2.21. In plot (a), the idealised squall line perturbation signal is clearly visible. The rainfall produced by this perturbation propagates eastwards in the domain throughout the simulation.

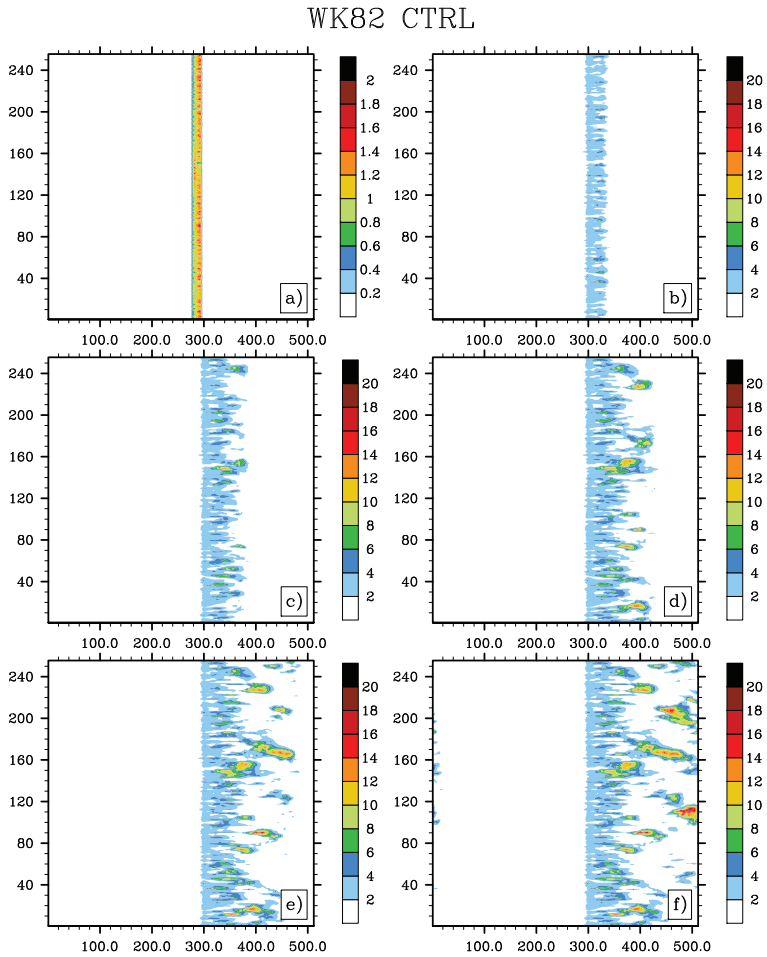


**Figure 2.21:** *The CTRL simulation for the idealised WK82 simulation showing the precipitation pattern every hour ((a)-(f)) over the 6h simulation.*

### 2.5.1 Microphysical and turbulent processes

The temporal evolution plots for the WK82-WA, WK82-WC and WK82-MT (see Table 2.1 for explanation of ensemble characteristics) ensembles are given in Fig. 2.23. Owing to the large domain size, the mean and standard deviation plots do not give a comprehensible picture of the ensemble dispersion or the rainfall field and are thus not plotted for these ensembles. Examining the WK82-WA ensemble, perturbing the warm processes induces considerable dispersion starting from before the third hour of simulation. The perturbations tend to produce heavier rainfall with many ensemble members giving a stronger average than the CTRL simulation. Members 1 and 3 give a lower average than the CTRL simulation and the other ensemble members. This is explained by examining the value of $r$, the perturbation factor, which was used for these members. In both cases, the rain evaporation processes were diminished by 50%. As shown by the 24-Evap ensemble, the surface rainfall is quite sensitive to this process. Reducing its value would lead to less evaporation of raindrops and less evaporative cooling. A reduction in evaporative cooling would impact upon the size of the evaporative cold pool which has been known to aid in self-maintaining convection. A comparison of the cold pool size (displayed using the value of the virtual potential temperature, $\theta_v$, in K at the surface) between the CTRL simulation and member 1 of the WK82-WA shown in Fig. 2.22 supports this argument.

Contrary to what was seen for the 24-WC and 96-WC ensembles, the WK82-WC ensemble shows increased dispersion compared to the WK82-WA ensemble. The introduction of perturbations upon the cold processes also leads to increased dispersion between ensemble members earlier in the simulation at around 2 h after initialisation. Members 1 and 3 of the WK82-WC ensemble continue to produce less rainfall than the other ensemble members. Combined with the 50% reduction in the rain evaporation process, the melting of graupels has been reduced by 20% due to the value of the perturbation factor. The 24-C-Group5 ensemble demonstrated that the surface rainfall was more sensitive to the value of this cold microphysical process than any of the others. A reduction in this process impacts upon the amount of rainfall water formed from graupel sources and may lead to a reduction in surface rainfall. Secondly, cooling due to the melting processes also contributes to the cold pool, thus a reduction in melting would also impact the cold pools intensity and lessen the self-sustaining properties of the convective line.

As was seen for the 24-MT and 96-MT ensembles, the WK82-MT ensemble gives a reduction in the rainfall maximum compared to the WK82-WA and WK82-WC ensembles. As in the WK82-WC ensemble, the rainfall evolutions begin to deviate 2 h after initialisation. Compared to the WK82-WA and WK82-WC ensembles, several members experience a reduction in maximum surface rainfall. Ensemble members 1 and 3 again separate from the other members. These ensemble members were perturbed by a value of $r$ less than 1 thus leading to a reduction in the value of the turbulent flux sources. Coupled with the previous reductions in the rain evaporation and the graupel melting sources, this led to a rapid dissipation of the convective system for these two members. The time series plot for the WK82-MT demonstrates that a combination of

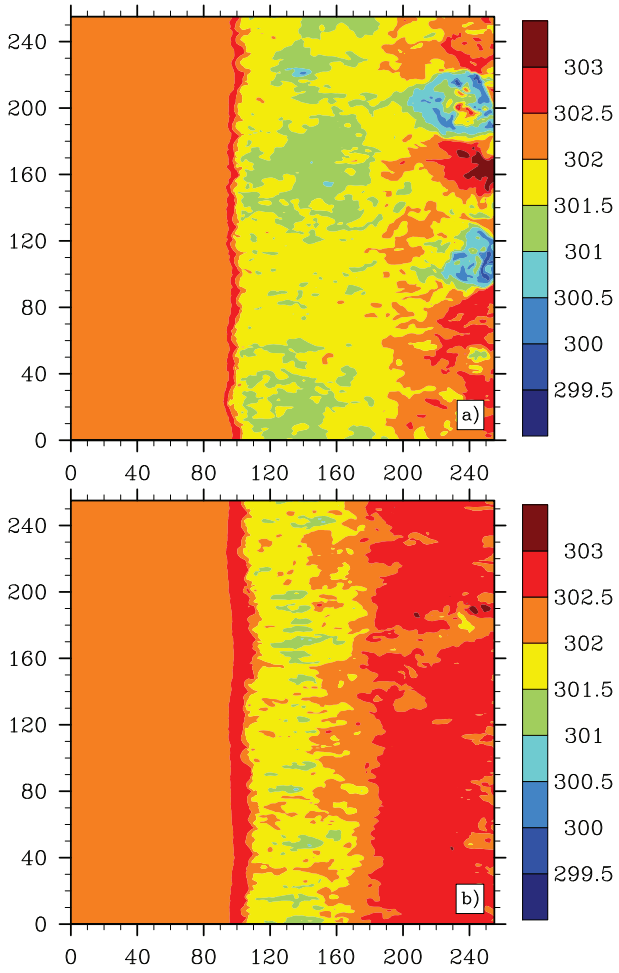


**Figure 2.22:** *A comparison between the evaporative cold pool of the CTRL simulation (a) and member 1 of the WK82-WA ensemble (b) shown in terms of virtual potential temperature ($\theta_v$) in $K$ at the surface. A zoom has been performed over the eastern half of the domain shown in Fig. 2.21 in order to improve the visualisation of the cold pool characteristics.*

cold, warm and turbulent perturbations produced a more even distribution for the rainfall evolution. The 10 perturbed members of the ensemble are distributed between 5 which gave a stronger rainfall evolution and 5 which gave a weaker rainfall evolution, than the CTRL simulation.

### 2.5.2 Conclusions - idealised squall line simulations

An idealised squall line framework, described in Weisman and Klemp (1982), was used to investigate the sensitivity of the evolution of the surface rainfall to perturbations upon the cold and warm microphysical and turbulent time tendencies. The results confirm the sensitivities that were uncovered by the 24-WA, 24-WC, 24-MT, 96-WA, 96-WC and 96-MT ensembles. Contrary to these ensembles, the WK82-WC ensemble gave the greatest degree of dispersion. The WK82-MT ensemble, where perturbations upon the turbulent time tendencies were introduced, slightly reduced the ensemble dispersion. The temporal evolution plot for this ensemble shows that perturbing the turbulent processes acts to modify the rainfall intensity, with a greater change in the rainfall evolution here shown compared to the WK82-WA and WK82-WC ensembles.

In contrast with the 24-WA, 24-WC, 96-WA and 96-WC ensembles, the sensitivity of the surface rainfall to the introduction of cold process perturbations is greater. Dispersion between the ensemble members begins earlier in the WK82-WC ensemble than in the WK82-WA ensemble. Also, the overall dispersion between the ensemble members is larger for the WK82-WC ensemble than for the WK82-WA ensemble. Overall, all ensembles show a large degree of dispersion, indicating that, at least in this idealised framework, microphysical and turbulent processes play an important role in the development of a squall line. In real world situations, boundary and initial conditions would be expected to play a greater role than in this idealised set-up. Based on these tests however, it is concluded that the microphysical and turbulent processes would also play a significant part in the evolution of a real world squall line.

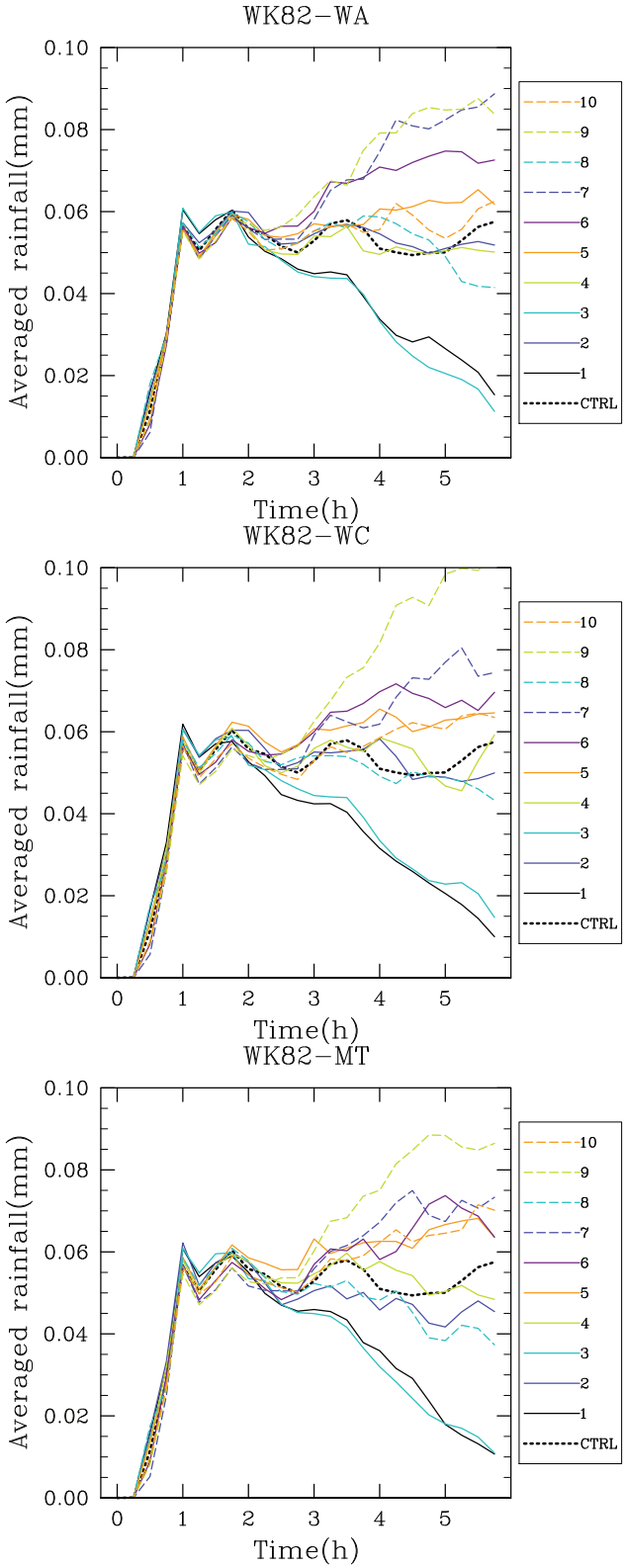


**Figure 2.23:** *The temporal evolution plots for the WK82-WA, WK82-WC and WK82-MT ensembles.*

# Chapter 3

# Real case studies

## 3.1 Presentation of article

The results presented in sections 2.3 and 2.4 demonstrated that the surface rainfall was most sensitive to perturbations upon the warm microphysical and turbulent processes. Ensembles 24-Acc and 24-Evap showed that the rain evaporation and accretion of cloud droplets by raindrops were the most important warm microphysical factors for the development of the rainfall field in the KW78 idealised supercell. For a real world HPE, other factors come into play. The rainfall evolution will also be influenced by the initial and boundary conditions used by the forecasting model (Vié *et al.* (2011)). Mountainous regions can act as triggers for convective events by forcing warm moist air to rise quickly into the atmosphere. The direction and strength of the impeding flow can also be a factor which influences the triggering point of convection (Bresson *et al.* (2012)). While the importance of these factors has been somewhat established, the role of the microphysical and turbulent processes in the evolution of an HPE remains open to debate.

Fresnay *et al.* (2012) studied two HPEs which occurred over south-eastern France in the months of October and November 2008 in the context of warm microphysical perturbations. They constructed EPSs using the methodology presented in sections 2.1.2 and 2.1.3. They found that depending on the predictability of the event, the sensitivity to microphysical perturbations was moderate (October case) or negligible (November case). They also postulated that according to the large-scale conditions of the atmosphere the episode would be more (less) sensitive to the perturbations. The October case had weak large-scale conditions and showed moderate ensemble dispersion while the November case had strong large-scale conditions and showed little if any sensitivity to microphysical perturbations.

The research article which here follows is a continuation of this preliminary work and had the aim of expanding the methodology and hypothesis to a number of new events. Five HPEs which took place over south-eastern France from September 2010 and November 2011 were chosen. CTRL simulations were performed at a horizontal resolution of 2.5km using the French research model Méso-NH. Using the HPE from September 2010 as a test case, 2 other slightly different methodologies for perturbing

the time tendencies were tested and the results compared to that of the methodology presented in section 2.1.3 of this manuscript, with the aim of uncovering the most dispersive method. Using the most suitable methodology, ensembles were then constructed for the 4 HPEs from November 2011 where perturbations were introduced upon the time tendencies of the rain evaporation, rain accretion and turbulent processes. The microphysical and turbulence processes were perturbed individually and also in a combined ensemble.

The results showed that for situations with low model skill, the surface rainfall is quite sensitive to microphysical and turbulent perturbations, while for situations with high model skill, the rainfall field showed little sensitivity. The link between weak (strong) large-scale conditions and reasonable (negligible) sensitivity that was introduced by Fresnay *et al.* (2012) is confirmed. The spatial correlation of the simulated rainfall to observed rainfall and the ratio of simulated to observed standard deviation was shown to be more sensitive to perturbations introduced upon the turbulence time tendencies than for perturbations upon the warm microphysical tendencies. When both sets of tendencies were simultaneously perturbed, the level of ensemble spread increased. This confirmed what was seen in the idealised ensembles 24-MT and 96-MT. It was concluded that EPSs where the warm microphysical and turbulent processes were perturbed would be useful in the forecasting of HPEs but that the uncertainty related to the parameterisation of these processes is perhaps less important than uncertainties related to other factors such as the initial and boundary conditions.

## 3.2 Ensemble simulations with perturbed physical parameterisations: Pre-HyMeX case studies

Article accepted for publication in the Quaterly Journal of the Royal Meteorological Society on the 16th of September 2013.

Quarterly Journal of the Royal Meteorological Society *Q. J. R. Meteorol. Soc.* (2013) DOI:10.1002/qj.2257

RMetS
Royal Meteorological Society

# Ensemble simulations with perturbed physical parametrizations: Pre-HyMeX case studies

A. Hally,* E. Richard, S. Fresnay and D. Lambert
*Laboratoire d'Aérologie, Université de Toulouse, France*

*Correspondence to: A. Hally, Laboratoire d'Aérologie, Observatoire Midi-Pyrénées, 14 avenue Edouard Belin, 31400 Toulouse, France. E-mail: alan.hally@aero.obs-mip.fr

**Heavy precipitation events (HPEs) affect the southeastern area of France frequently during the months of September–November. Very high amounts of rain can fall during these events, with the ensuing flash floods causing widespread damage. The cases of 6 September 2010 and 1–4 November 2011 represent the different large-scale conditions under which these episodes can occur. These HPEs are forecast with differing levels of skill by the Méso-NH model at 2.5 km resolution. The case of 6 September 2010 is used to test different methods of addressing cloud physics parametrization uncertainties. Three ensembles are constructed, where the warm-process microphysical time tendencies are perturbed by different methods. Results are compared by examining the spatio-temporal distribution of the precipitation field as well as looking at ensemble statistics. The ensemble methodology that induces the most dispersion in the rainfall field is deemed the most suitable. This method is then used to examine the sensitivity of four cases from November 2011 to errors in the microphysical and turbulent parametrizations. It appears that the sensitivity to microphysical perturbations varies according to the model skill for the HPE. Events where the model skill is high (low) show low (moderate) sensitivity. These cases show a stronger sensitivity to perturbations performed upon the turbulent tendencies, while perturbing the microphysical and turbulent tendencies together produces even greater dispersion. The results show the importance and usefulness of ensembles with perturbed physical parametrizations in the forecasting of HPEs.**

*Key Words:* precipitation; microphysics; parametrization; convection; ensembles

*Received 10 January 2013; Revised 19 July 2013; Accepted 16 September 2013*

## 1. Introduction

The Mediterranean region is susceptible to heavy precipitation and severe flooding on an almost yearly basis. These events can be very devastating in densely populated coastal regions. They cause major economic damage and too often loss of human life. The Algiers flood of November 2001, with nearly 900 fatalities, was particularly tragic. Clearly it is essential that these events are well forecast, justifying the important international research efforts deployed to improve their observation and understanding (e.g. the MEDiterranean EXperiment (MEDEX[†]), the Distributed Research Infrastructure for Hydro-Meteorology (DRIHM[‡]) and the Hydrological cycle in the Mediterranean EXperiment (HyMeX[§]).

In particular, the HyMeX project, initiated in 2010, undertook its first Special Observing Period, or SOP1, in autumn 2012. This observing period focused especially on heavy precipitation events (HPEs) in the northwestern Mediterranean and provided a unique opportunity to implement and test new methodologies that aim to improve the forecasting of such episodes. For clarity purposes, two important terms are defined explicitly. The expression 'model skill' as used herein refers to the model's ability to predict the time and spatial distribution of the observed rainfall. The word 'predictability' refers to the degree to which an atmospheric state can be forecast correctly.

In southeastern France, HPEs occur most frequently between the months of September and November, as the sea-surface temperature of the Mediterranean remains warmer for longer in comparison with the rapidly cooling land basins that surround it. Moisture-laden flows from the south and southeast interact with the local orography, creating convective lifting and thus leading to some intense local downpours. The location and intensity of the episode are related to the strength of the flow, its interaction with the mountainous regions and whether or not a cold pool induced by rain evaporation develops (Bresson *et al.*, 2009). The orography in the south of France is quite complex, with the Alps, the Pyrenees, the Massif Central and locally the Cévennes mountains all affecting flows within the region. However, it is not always certain which factors control these situations and some

[†]http://medex.aemet.uib.es
[‡]http://www.drihm.eu
[§]http://www.hymex.org

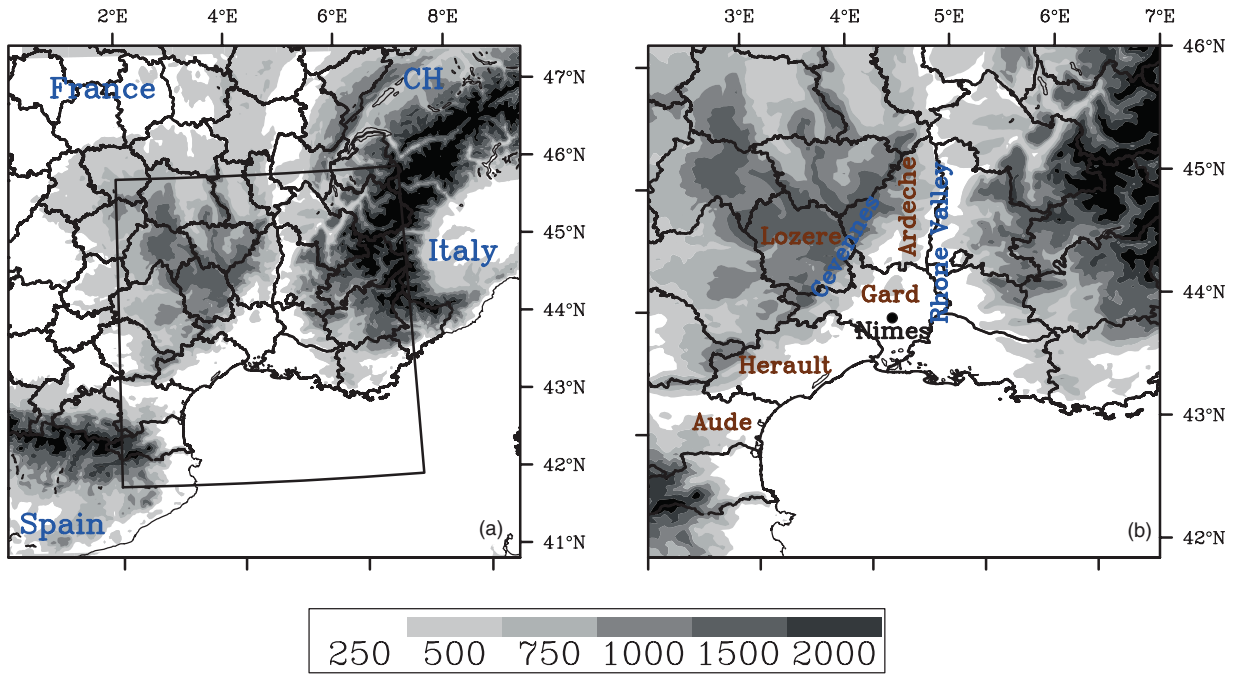


**Figure 1.** (a) Map of the domain of southern France used for the simulations. The area under the solid line, referred to as the target area in the text, is presented in (b). All simulation statistics are performed over the domain in (b). Shading represents altitudes (in metres) over 250 m. Geographical names and French administrative regions are recalled, in particular five *départements* of the southern France region, which are given in (b) (in brown in the online article). Two important geographical features, the Cévennes mountain ranges and the Rhône Valley, are also given in (b) (in blue in the online article). The location of the Nîmes sounding is also given for reference.

particularly severe episodes (e.g. the 1999 Aude case or 2002 Gard case: see Figure 1 for geographical location) have required several studies in order to understand how the different factors interplay (Bechtold and Bazile, 2001; Ducrocq *et al.*, 2008; Nuissier *et al.*, 2008). The microphysical processes involved in the formation of a cold pool were shown to be especially important factors, as they controlled the stationarity of the mesoscale convective system (MCS) for the 2002 Gard case (Ducrocq *et al.*, 2008).

The forecast accuracy for these types of events is still fairly limited, despite recent progress in numerical weather prediction. This is due in part to the involvement of many multiscale processes. Lorenz (1969), with his famous article, laid the foundations of predictability limitations by suggesting that the prediction of large-scale flow was limited to a few weeks in advance, while the limit for cumulus-scale motions was only 1 h in advance. More recent articles have investigated the predictability issues associated with deep convection. Walser *et al.* (2004) conclude that predictability limitations increase rapidly with decreasing scale, with individual convective cells being rendered practically unpredictable by chaotic aspects of the moist dynamics. They also underline that growing small-scale uncertainties and nonlinear atmospheric interactions can disrupt predictability quickly. Further studies have investigated error growth at the convective scale in more detail. Hohenegger and Schär (2007) found that initial perturbations can propagate throughout the entire domain within a few hours and can amplify at far remote locations. The rapid propagation of sound and gravity waves is shown to communicate these initial uncertainties quickly throughout the domain. Furthermore, Hohenegger and Schär (2007) and Leoncini *et al.* (2010) suggested that the perturbation growth is only weakly sensitive to the initial perturbation characteristics and reaches a similar value at saturation regardless of the perturbation methodology and/or amplitude.

Fritsch and Carbone (2004) suggested that ensemble prediction systems (EPSs) present the most promising strategy for overcoming predictability limitations. Starting from a set of perturbed scenarios, which represent inherent uncertainties in the initial atmospheric state and in the model formulation, EPSs give the probability of an event occurring. However, designing such systems can be complex, as realistic and appropriate perturbations that give satisfactory dispersion and statistical scores can be difficult to formulate. In particular, knowing which uncertainties to include in the ensemble design in order best to describe the model error is a challenge, with the decision most often depending upon the situation being studied and the relative biases of the computational model being employed.

One source of error that, as reported in Fritsch and Carbone (2004), is of special concern, is the representation of microphysical processes. These processes, like turbulence processes, are represented within models by different parametrizations. These are representations of processes that occur at subgrid resolutions and thus are not explicitly resolved by the model. As such, the processes cannot always be represented in their true form, thus creating some uncertainty surrounding their parametrization. Various studies have investigated the issues associated with physical parametrization uncertainties. Some of them made use of different physical parametrization schemes or different sets of parameters (e.g. Houtekamer *et al.*, 1996; Stensrud *et al.*, 1999; Clark *et al.*, 2008) whereas others relied upon stochastic perturbations applied either to the physical tendencies (Buizza *et al.*, 1999) or directly to the dynamical and/or thermodynamical variables of the model (e.g. Shutts, 2005; Plant and Craig, 2008). However, it is only recently that these methods have started to be used in the design of convection-permitting ensembles (Clark *et al.*, 2010; Schwartz *et al.*, 2010; Gebhardt *et al.*, 2011; Bouttier *et al.*, 2012; Fresnay *et al.*, 2012; Leoncini *et al.*, 2013). A number of conclusions can be drawn from these works:

(1) spread in precipitation can be achieved by varying the physical parametrizations and enlarged when these perturbations are combined with initial state and/or boundary-condition pertubations;
(2) in the first hours of the simulation, physical perturbations have a larger impact than boundary-condition pertubations;
(3) the impact of physical perturbations (in strength and duration) appears to be case-dependent, with events controlled by strong upper-level forcing being less sensitive than those with weak forcing; and

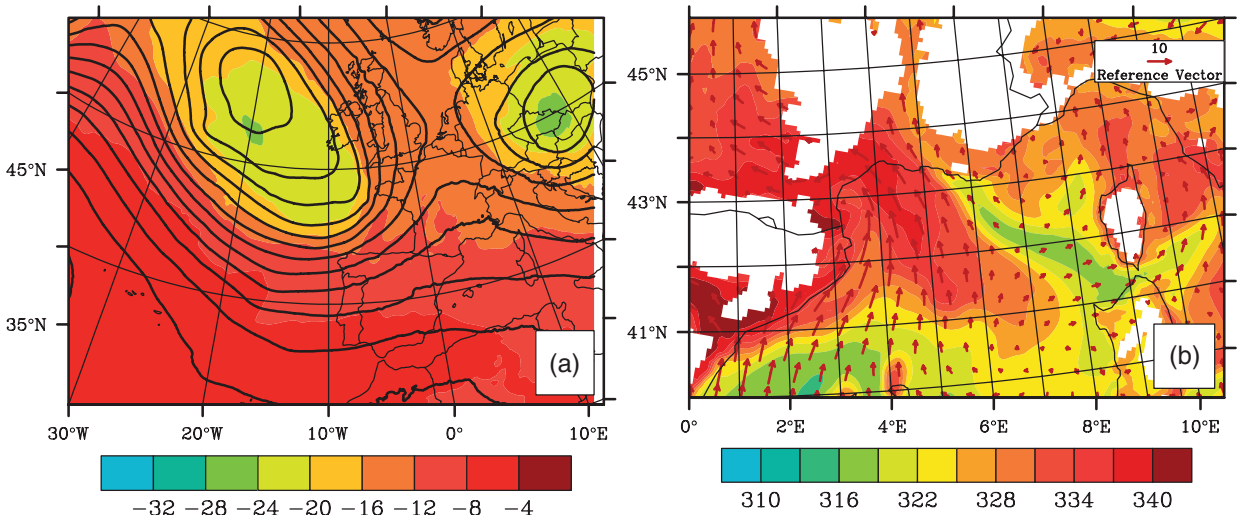


**Figure 2.** ECMWF large-scale analysis at 1200 UTC on 6 September 2010, showing (a) temperature (°C) and geopotential height at 500 hPa and (b) potential temperature (K) and wind speed at 950 hPa.

(4) an ensemble of ten members seems to be sufficient enough to capture the variability of the model.

One further point that can be gleamed from the different approaches employed in the previous works is that the most effective way of perturbing the physical parametrizations at the convective scale is still debated, with no one methodology being clearly superior to any of the others.

The present study is a continuation of the work of Fresnay *et al.* (2012), who investigated the role of microphysical scheme uncertainties for the case of two HPEs in the Mediterranean region. The methodology was based upon random perturbations applied to the time tendencies of some key microphysical processes. It was concluded that, as was suggested by Vié *et al.* (2012), while microphysical uncertainties seem to have less impact than initial and lateral boundary condition errors, they do contribute to the improvement of the probabilistic forecast of an HPE. The aim of the present work is first to extend the study to a larger sample of events while also seeking to clarify the usefulness of the tendency perturbation methodology. In a second step, the sensitivity to turbulent process perturbations will also be investigated. As shown by Zampieri *et al.* (2005), Fiori *et al.* (2009) and Fiori *et al.* (2011), the parametrization of the boundary-layer turbulence has a significant impact upon the resulting precipitation field. Furthermore, the issue of turbulence parametrization uncertainty is becoming crucial with the current increase in model resolution. At the kilometric scale, 1D closure methods are questionable and the formulation used in large-eddy simulations is not appropriate (Wyngaard, 2004; Honnert *et al.*, 2011). In order to investigate these uncertainties, the turbulence time tendencies will be perturbed.

The layout of the article is as follows. An introduction of the chosen case studies, the reasons for which they were chosen, the atmospheric model settings and the perturbations applied are given in section 2. Section 3 details the outcome of perturbing the microphysical processes for each of the case studies presented, while section 4 contains the results of ensembles where the turbulent tendencies are modified. Summaries and conclusions of our findings can be found in section 5.

## 2. Case studies, model settings and perturbation design

### 2.1. Case studies

The events studied occurred in September 2010 and November 2011, mainly over the plains of the Gard and Hérault departments and the Cévennes mountain range, which are located in the southern Massif Central region (see Figure 1). As has been stated in past works (e.g. Ducrocq *et al.*, 2008) this area experiences these types of devastating events on an almost yearly basis and was selected as one of the main observational sites for the HyMeX SOP1. The September 2010 case was chosen due to its similarity to the Gard case described in Fresnay *et al.* (2012), for which the rainfall field was found to be sensitive to perturbations in the microphysical time tendencies. Because of these findings, it was believed that the impact of the different perturbation methods could be more easily distinguished by using this type of case as a test. The four cases from November 2011 were chosen as they represented the most exceptional cases of heavy rainfall to occur in the southeast of France during this pre-HyMeX SOP1 period. Due to the devastating flash floods that developed as a result of the heavy rainfall, these episodes were chosen as test cases for the DRIHM project, which aims at developing a distributed research infrastructure for hydrometeorological forecasting (see http://www.drihm.eu/ for a description of the project objectives). Also, the five cases are good examples of the two main ways by which HPEs develop in the region: (i) when an upper-level trough is located west of the target area, vertical motion is amplified due to the conjunction of orographic forcing and upper-level divergence (3 and 4 November) or (ii) a quasi-stationary convective system forms over the Rhône Valley in the absence of significant upper-level forcing (6 September and 1 November).

The September 2010 case study, which will be used here as a test case, took place between 1200 UTC on 6 September and 1200 UTC on 7 September and resulted in a 336 mm maximum rainfall accumulation in the 24 h period. Plots of the temperature and geopotential height at 500 mb (Figure 2(a)) give an indication of the large-scale conditions that led to this situation. A low-pressure system off the coast of Ireland was blocked by a high-pressure system over Scandinavia, which forced the low to remain in place for several days. An upper-level trough associated with this low was located to the northwest of the target area, which brought about a moderate westerly flow in the mid-troposphere and led to a low-level southerly flow (Figure 2(b)) over the Gulf of Lion towards the southern French coast. This southerly flow brought warm and humid air (see Figure 2(b) for equivalent potential temperature values) from the Mediterranean, which caused the formation of a stationary convective system upstream of the Cévennes mountains and in turn led to the severe rainfall. The most severe rainfall (over 300 mm) was observed over the plains of the western and eastern Gard, while the accumulations over the Cévennes mountain ranges remained comparatively weak (isolated maxima of 100 mm).

The remaining four case studies took place between 0000 UTC on 1 November and 0000 UTC on 5 November 2011. 1 and

 

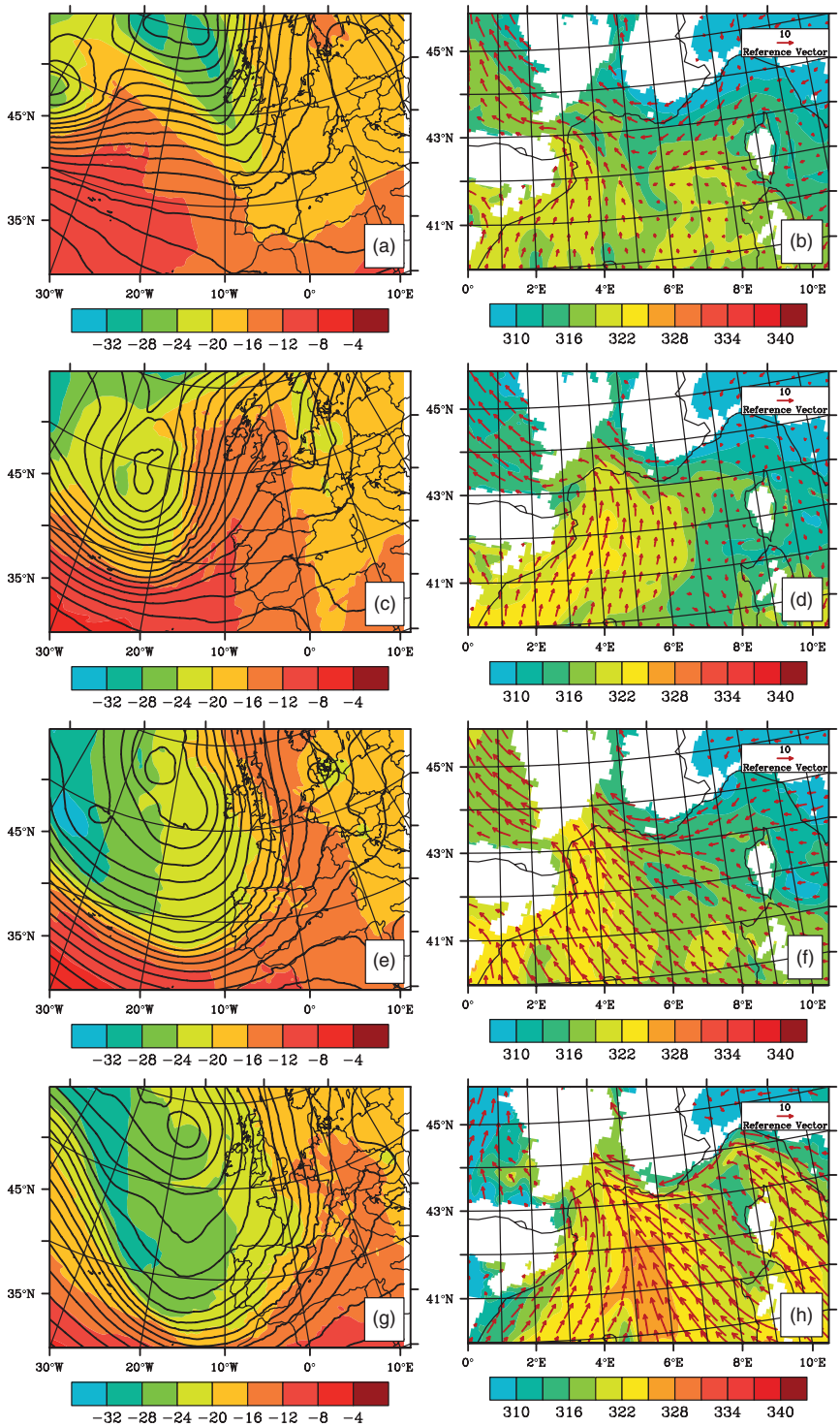


**Figure 3.** ECMWF large-scale analysis at 0000 UTC for 1, 2, 3 and 4 November respectively. The left column (panels (a), (c), (e) and (g)) shows temperature (°C) and geopotential height at 500 hPa and the right column (panels (b), (d), (f) and (h)) potential temperature (K) and wind speed at 950 hPa.

2 November were associated with a weakening upper-level trough just to the west of France, which brought about west-to-southwesterly flow in the mid-troposphere for 1 November and westerly flow for 2 November (see Figure 3(a) and (c)). Both days were similar in their weak south-to-southeasterly low-level flow, with 1 November in particular having very moderate inflow towards the target area (Figure 3(b) and (d)). An examination of the equivalent potential temperature at 950 hPa indicates that humid air over the Mediterranean was brought in over the cooler land masses in a similar fashion to that of 6 September 2010 (Figure 3(b) and (d)). 1 and 2 November presented rainfall maxima of 108 and 138 mm respectively. The majority of the rain that occurred on 1 November was observed on the plains of the Hérault department and the southern regions of the Gard. For 2 November, the rain was concentrated on the foothills of the Cévennes. Convective available potential energy (CAPE) values taken from the Nîmes sounding at 0000 UTC on both days were low, at 67 and 31 J kg$^{-1}$ respectively. The skew-$T$ diagram (not shown) for 1 November indicates the presence of convective instability, while the diagram for 2 November (not shown) displays a thick layer of mid-atmospheric cloud but little evidence of convective instability.

3 and 4 November present slightly different meteorological conditions, with a deeper and colder upper-level trough now approaching from the North Atlantic (Figure 3(e) and (g)). This led to a period of diffluence (not explicitly shown) over the

Table 1. Characteristics of the different ensembles.

| Ensemble name | Time initialized | No. of perturbed members | MIC | TURB | Range of $r$ | Random | Specified |
|---|---|---|---|---|---|---|---|
| E6a | 6-9-10-1200 UTC | 10 | ✓ | | (0.5, 1.5) | ✓ | |
| E6b | 6-9-10-1200 UTC | 10 | ✓ | | (0.1,10) | ✓ | |
| E6c | 6-9-10-1200 UTC | 8 | ✓ | | (0.5, 1, 1.5) | | ✓ |
| E1-(MIC) | 1-11-11-0000 UTC | 10 | ✓ | | (0.5, 1.5) | ✓ | |
| E2-(MIC) | 2-11-11-0000 UTC | 10 | ✓ | | (0.5, 1.5) | ✓ | |
| E3-(MIC) | 3-11-11-0000 UTC | 10 | ✓ | | (0.5, 1.5) | ✓ | |
| E4-(MIC) | 4-11-11-0000 UTC | 10 | ✓ | | (0.5, 1.5) | ✓ | |
| E1-(TURB) | 1-11-11-0000 UTC | 10 | | ✓ | (0.5, 1.5) | ✓ | |
| E2-(TURB) | 2-11-11-0000 UTC | 10 | | ✓ | (0.5, 1.5) | ✓ | |
| E3-(TURB) | 3-11-11-0000 UTC | 10 | | ✓ | (0.5, 1.5) | ✓ | |
| E4-(TURB) | 4-11-11-0000 UTC | 10 | | ✓ | (0.5, 1.5) | ✓ | |
| E1-(MIC)-(TURB) | 1-11-11-0000 UTC | 10 | ✓ | ✓ | (0.5, 1.5) | ✓ | |
| E2-(MIC)-(TURB) | 2-11-11-0000 UTC | 10 | ✓ | ✓ | (0.5, 1.5) | ✓ | |
| E3-(MIC)-(TURB) | 3-11-11-0000 UTC | 10 | ✓ | ✓ | (0.5, 1.5) | ✓ | |
| E4-(MIC)-(TURB) | 4-11-11-0000 UTC | 10 | ✓ | ✓ | (0.5, 1.5) | ✓ | |

A tick in the MIC column signifies that the microphysical processes were perturbed, a tick in the TURB column that the turbulent tendencies were perturbed and ticks in both columns that both were simultaneously perturbed. The date appears in the dd-mm-yy format. The values of $r$ for the E6c ensemble are detailed in Table 2.

Table 2. Characteristics of the E6c ensemble, showing the value of $r$ subjectively chosen and applied to each process for each member.

| Ensemble member | Value of $r$ for evaporation perturbation | Value of $r$ for accretion perturbation |
|---|---|---|
| 1 | 0.5 | 0.5 |
| 2 | 1.0 | 0.5 |
| 3 | 1.5 | 0.5 |
| 4 | 0.5 | 1.0 |
| 5 | 1.5 | 1.0 |
| 6 | 0.5 | 1.5 |
| 7 | 1.0 | 1.5 |
| 8 | 1.5 | 1.5 |

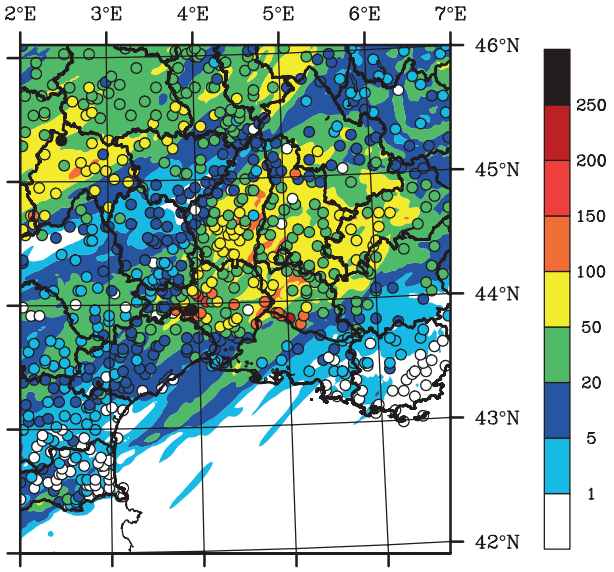


**Figure 4.** CTRL simulation for the event of 6 September 2010. The coloured circles represent the observed rainfall amounts (in mm) collected from the Météo France network of surface stations. The rainfall amounts (in mm) predicted by the Méso-NH model are superimposed. The area shown represents the target area plotted in Figure 1.

target area for 3 November, which may explain why this day experienced the heaviest precipitation of the four days, with a maximum of 536 mm being recorded. The mid-tropospheric flow became stronger and definitively southwesterly in direction, with the low-level flow remaining southeasterly but becoming more intense compared with the flow for the previous two days (Figure 3(f)). For 4 November, the upper-level trough deepened further with the surface flow increasing in strength, albeit from a slightly more southerly direction than the previous three days (Figure 3(h)). All of these conditions contributed to produce 193 mm of rainfall for the 24 h period between 0000 UTC on 4 November and 0000 UTC on 5 November. CAPE values as taken from the Nîmes radiosound at 0000 UTC on both days show that there was a slight increase compared with 1 and 2 November, with values of 110 and 126 J kg$^{-1}$ being recorded respectively. The modest increase in CAPE for 3 and 4 November over the previous two days suggests atmospheric conditions more favourable for convection. This is confirmed by the skew-$T$ diagrams (not shown), which exhibit convective instability for both days.

### 2.2. *Model set-up*

The numerical experiments outlined in this article were performed with the French mesoscale non-hydrostatic research model Méso-NH (Lafore *et al.*, 1998).[¶] Méso-NH has been widely used in the French research community and the previous works of Richard *et al.* (2003), Argence *et al.* (2008), Bresson *et al.* (2012) and Chaboureau *et al.* (2012), among others, have shown the suitability of this model for simulating severe weather phenomena. Designed as a research tool, Méso-NH is more flexible than the operational model AROME and was therefore chosen for this study. As the two models share the same physical parametrizations, the implementation of the perturbation method in the operational model would be straightforward.

The turbulence scheme used within the model follows Cuxart *et al.* (2000), while the radiation is calculated using the Rapid Radiative Transfer Model (Mlawer *et al.*, 1997). Exchanges of surface energy are represented by four possible surface-type patches (natural surfaces, urban areas, oceans and lakes) included within a grid mesh. The Interactions Soil–Bioshpere–Atmosphere scheme (ISBA: Noilhan and Mafhouf, 1996) is the scheme used for natural land surfaces. Shallow and deep convection are parametrized according to Pergaud *et al.* (2009) and Bechtold *et al.* (2001) respectively. The prognostic equations of six water species (vapour, cloud water, rainwater, primary ice, snow aggregates and graupel) are governed by the ICE3 bulk microphysical scheme (Pinty and Jabouille, 1998). See also Lascaux *et al.* (2006) for a detailed description of the different microphysical processes of the scheme.

The grid used for the numerical simulations has a 2.5 km spacing and covers a 288 × 288 point horizontal domain located

[¶]http://mesonh.aero.obs-mip.fr/mesonh

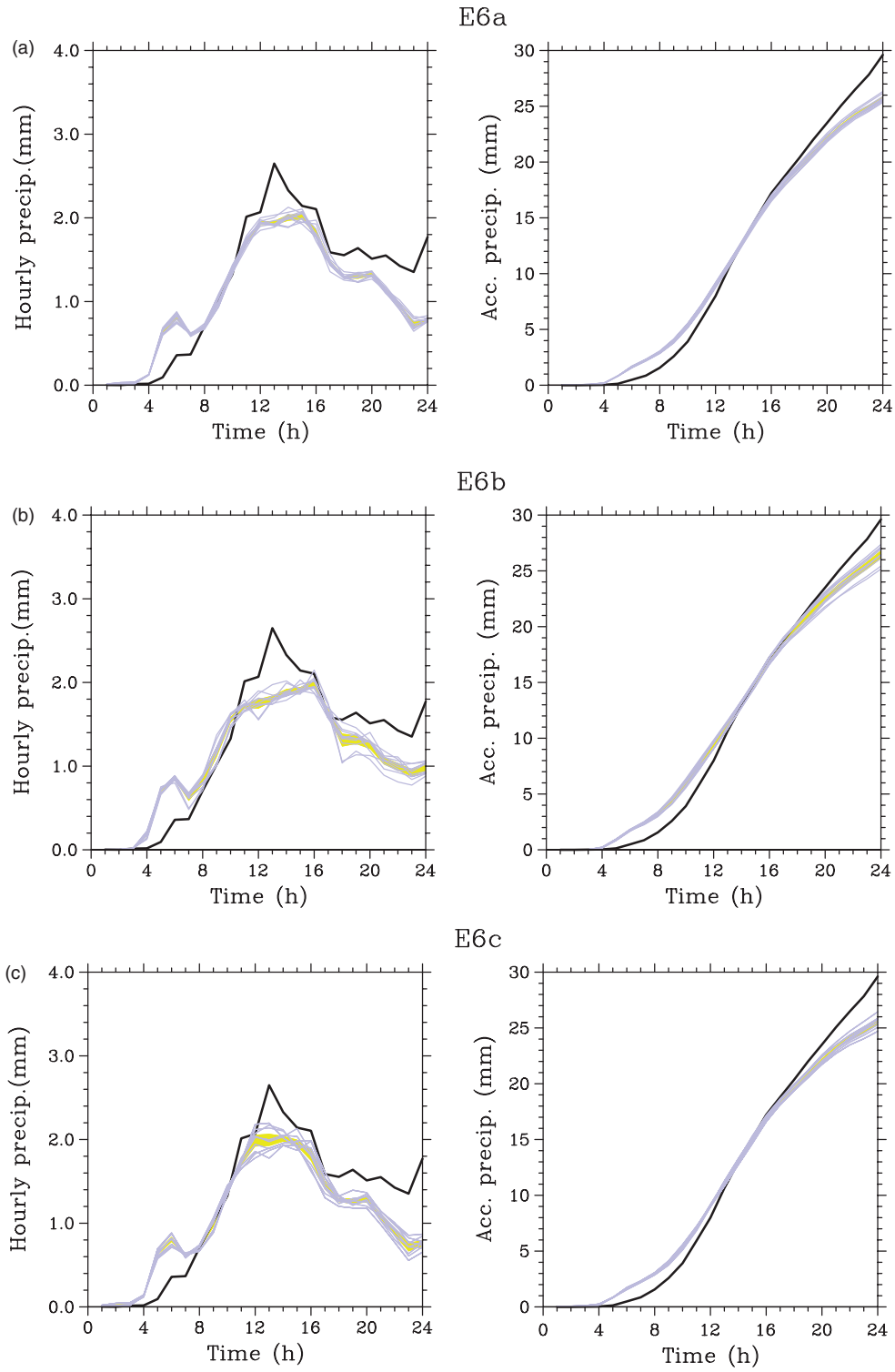


**Figure 5.** Time evolution of the spatially averaged hourly accumulation of precipitation (left) and accumulated precipitation (right) for the 24 h period between 1200 UTC on 6 September and 1200 UTC on 7 September for the ensembles E6a, E6b and E6c. The ensemble members are shown in grey and the observations in black. The light shading (yellow in the online article) corresponds to the standard deviation from the ensemble mean.

over southern France and the northwestern Mediterranean (Figure 1). The deep convection scheme was disabled, while shallow convection parametrization was maintained. As the focus of this study was to investigate domain-internal errors, initial (IC) and lateral boundary conditions (LBC) were taken from the French operational AROME analyses. All ensemble members had identical IC and LBC conditions, meaning that differences between ensembles could be attributed to the tendency perturbations introduced. These analyses are available every 3 h and on the same 2.5 km resolution grid. For the case of 6 September 2010, the simulations were started at 1200 UTC and lasted 24 h. For the four cases from November 2011, all simulations began at 0000 UTC on the day in question and were also performed over 24 h.

### 2.3. *Configuration of perturbations*

In the context of idealized situations (isolated storm, squall line), preliminary tests (not shown) suggested that perturbing the microphysical tendencies led to greater dispersion in the rainfall field than varying the parameters of the microphysical scheme within their plausible ranges. These results motivated the choice of

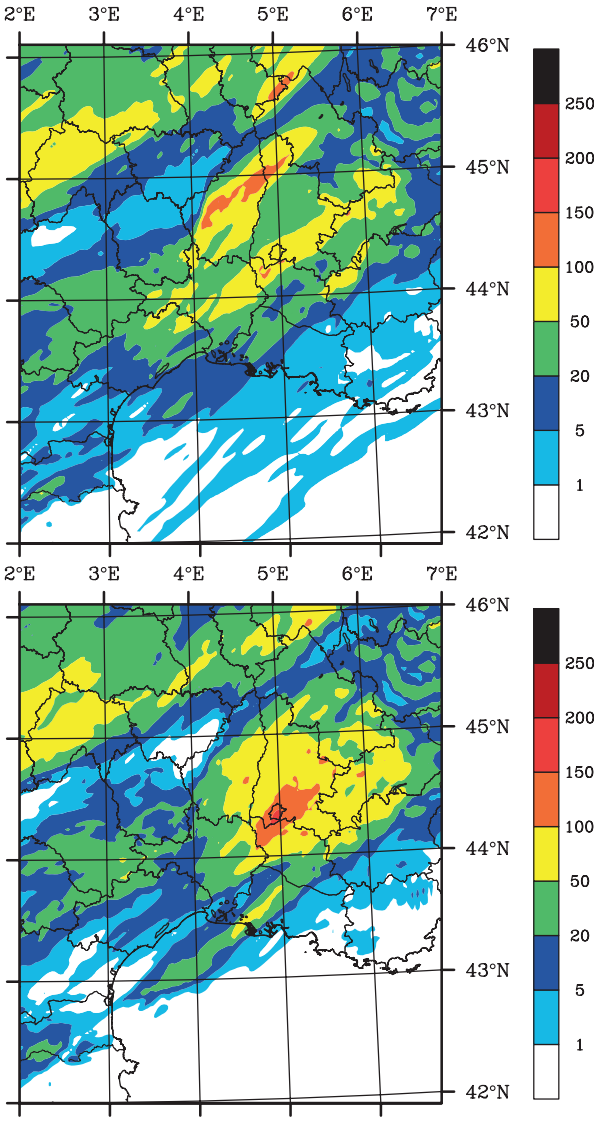


**Figure 6.** Comparison of the simulated rainfall field for two members of the E6c ensemble. The time tendency of the rain evaporation process is given perturbations of (top plot) 0.5 and (bottom plot) 1.5, while the perturbation upon the accretion process remains constant.

the process-pertubation approach made by Fresnay *et al.* (2012). In this exploratory study, carried out for only two HPEs, the surface rainfall was shown to be sensitive to microphysical time tendency perturbations for one case, while for the second case little sensitivity was demonstrated.

The present study is based upon the same approach, which was inspired by Buizza *et al.* (1999) and aims at representing the random errors that can exist within parametrized microphysical processes. This is done by introducing random perturbations upon the time tendencies of the microphysical processes. Specifically, the value of the sources and sinks of each process are multiplied by a random factor ($r$) homogeneously in time and space, which leads to an artificial increase or decrease in the process being considered. The factor by which these processes are perturbed will be tested using two specific ranges: one range taken from the work of Buizza *et al.* (1999), where the value of $r$ is randomly selected between 0.5 and 1.5, and a second larger range where $r$ has a random value between 0.1 and 10. Admittedly this second range will lead to unrealistic values of the physical processes but in the scope of a sensitivity test it was thought useful to verify whether stronger perturbations would lead to wider, more intense changes in the surface rainfall. This process-perturbation scheme has been chosen due to its successful implementation in the EPS at the European Centre for Medium-Range Weather Forecasts (ECMWF), although in this case it is implemented at a much finer resolution. The ease with which the scheme can be implemented into the model was also a determining factor. The perturbations are only applied to the warm microphysical processes of rain evaporation and accretion of cloud droplets by raindrops. The results of idealized tests (not shown) indicate that the rainfall field is most sensitive to perturbations to the time tendencies of these two processes, while perturbing the autoconversion process led to negligible sensitivity. The methodology could be easily extended to the cold processes. However, additional tests (not shown) suggest that the surface rainfall is more sensitive to perturbations upon the warm microphysical processes. It is acknowledged, however, that the ice processes can have an impact on the precipitation pattern during certain types of convective events (Richard *et al.*, 2003; Gilmore *et al.*, 2004; Lascaux *et al.*, 2006).

Table 1 details the characteristics of each of the ensembles performed during this study. The ensemble where the value of $r$ is generated from the 0.5–1.5 range will be referred to as E6a. In ensemble E6b, the value of $r$ is randomly selected from the range 0.1–10. The number 6 in the ensemble name refers to 6 September. Both of these ensembles have ten perturbed members. When applying the random perturbations, a new value of $r$ in the 0.5–1.5 or 0.1–10 range is generated at the beginning of each simulation, ensuring that each ensemble member is unique. Inspired by the work of Vié *et al.* (2012), an additional ensemble (referred to as E6c) was included, where the value of $r$ was not randomly generated but chosen directly by the user. In other words, the rain evaporation and accretion processes were perturbed individually by a value of $r$ of 0.5, 1 or 1.5. The value of $r$ for each member of the E6c ensemble is detailed in Table 2. This ensemble consisted of eight perturbed members, as there were eight possible combinations of 0.5, 1 and 1.5 that ensured a unique perturbation for both processes. This methodology was chosen in order to visualize the impact and contribution of each process to the overall rainfall pattern more clearly. It must be underlined that, regardless of the methodology used, mass conservation is still respected, as the source and sink of each process are enhanced and decreased by the same factor.

A control simulation (CTRL) without any perturbed physical parametrizations was performed for each case study. Experimental set-ups E6a, E6b and E6c have been used for the case study of 6 September, with the aim of uncovering which of the three methods introduced most sensitivity in the surface rainfall. Following these results, the most suitable ensemble was then used to run ensemble simulations on the four days from November 2011.

## 3. Microphysical perturbations

### 3.1. *Test ensembles performed for the case of 6 September 2010*

The 24 h simulated rainfall of the control member (CTRL) compared with the observations for the Gard case of 6 September 2010 is presented in Figure 4. Overall, it can be said that the model captures the structure of the system. However, there are some discrepancies in terms of rainfall amount and localization. The heaviest rain in the model is shifted to the north and east of where it is observed. This means that the rain in the western part of the Gard is missed by the model. Accumulations of only 20 mm in 24 h are forecast by the model, when upwards of 300 mm is recorded at some stations. The rainfall over the eastern Gard region is captured somewhat better, although some localized maxima of up to 150 mm are still missed. This is quite a significant difference and would have large consequences for hydrological prediction. An analysis of the time evolution of the spatially averaged hourly rainfall (not shown) indicates that the model begins to produce rainfall earlier than occurred in reality, while also showing that it underestimates the precipitation peak. The surface rainfall of this HPE could

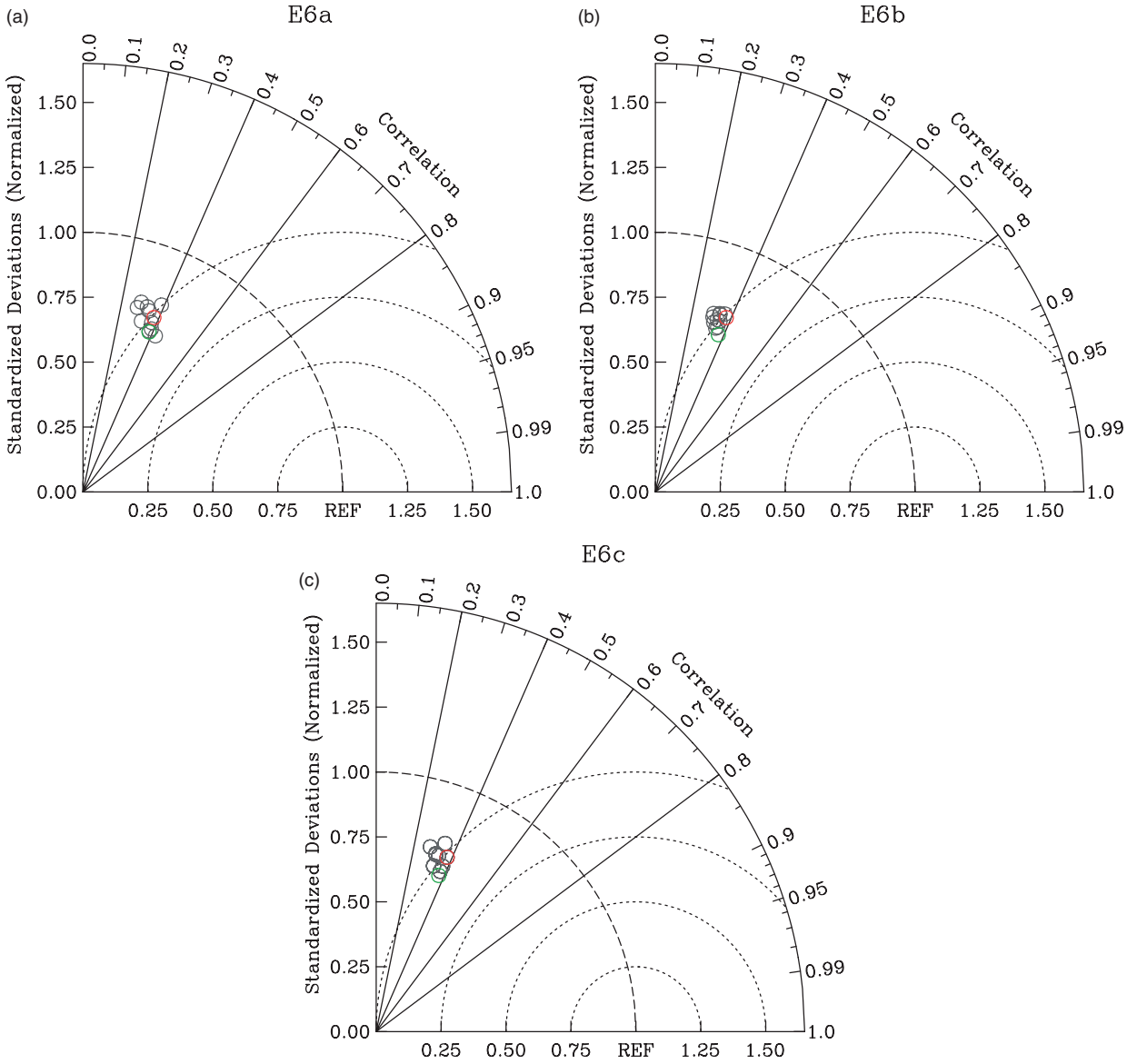


**Figure 7.** Taylor diagram for each of the ensembles E6a, E6b and E6c for 6 September 2010. The ensemble members are represented by the grey circles, the CTRL simulation by the red circle in the online article and the ensemble mean by the green circle in the online article.

be expected to be sensitive to microphysical perturbations due to its similarities to the case of 20 October 2008 studied in Fresnay *et al.* (2012).

Starting from this CTRL simulation, the ensembles E6a, E6b and E6c were then tested. The behaviour of the different ensembles was examined through various diagnostics: the time evolution of the domain-averaged simulated precipitation compared with the observed one, along with standard statistics applied to the 24 h accumulated rainfall, including the root-mean-square error (RMSE), the spatial correlation with observations and a normalized standard deviation. Although these domain-wide statistics may be insensitive to the displacement of rain features when there is little or no spatial overlap between observation and model output, they do highlight missed or misplaced rainfall maxima and allow potentially unrealistic configurations to be detected. Figure 5 shows the hourly evolution and accumulation of rainfall for the E6a, E6b and E6c ensembles. It is seen that none of the simulations succeeds in reaching the highest accumulations seen in the observations over the 24 h period investigated. It is also shown that none of the ensembles manages to forecast the peak in precipitation (which can be seen after 12 h), with ensemble E6c possibly coming closest. There is a strong bias in all of the ensembles towards overestimating the rainfall at the beginning of the simulation, which is most likely due to model spin-up within the first hours of simulation. These diagrams also demonstrate that ensemble E6b has the greatest standard deviation for rainfall accumulations over the 24 h period, as illustrated by the area of light shading (yellow in the online article). For the hourly rainfall evolution, ensemble E6c produces the most significant standard deviation value between its members. However, ensemble E6c is constructed of just nine members and thus a direct comparison of standard deviation between it and the other two ensembles is perhaps unjust.

The E6c ensemble perturbs the rain evaporation and accretion processes individually, according to the combination of perturbation factors presented in Table 2. This allows the contribution from each microphysical process to the development of the rainfall to be seen. The accretion process affects the development of the precipitation bands, with increased accretion causing the rain to fall further southwards (not shown). The effect of perturbing the rain evaporation rate is more pronounced, however, as illustrated by a comparison of the two rainfall plots in Figure 6, with one having its rain evaporation rate diminished by 50% (top panel) and the other having it increased by 50% (bottom panel). Cutting the rain evaporation rate in half displaces the rainfall to the north, causing the heaviest precipitation to fall over the Ardèche department. The rain bands in the eastern Gard also appear less intense. This could be explained by the

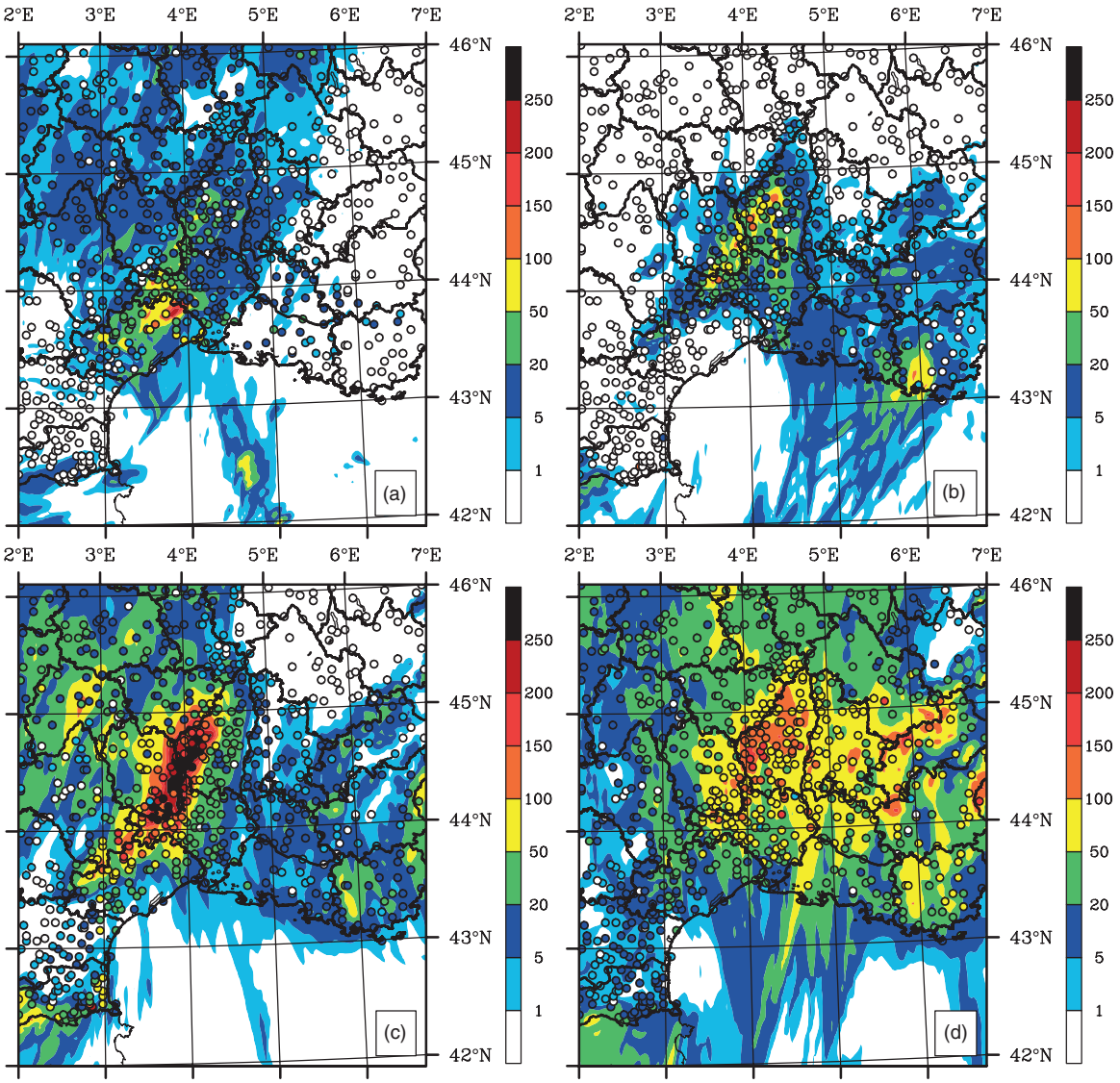


**Figure 8.** CTRL simulation for (a) 1, (b) 2, (c) 3 and (d) 4 November 2011. The coloured circles represent the observed rainfall amounts (in mm) collected from the Météo France network of surface stations. The rainfall amounts (in mm) predicted by the Méso-NH model are superimposed. The area shown represents the box referred to as the target area in Figure 1.

fact that the decreased rainfall evaporation rate would lead to a smaller cold pool and suggests that cold pools helped intensify the convective cells responsible for these rain bands. Cold pool development is important in triggering rainfall over the plains rather than the mountain ridges, as was seen in Bresson *et al.* (2012). In comparison with the CTRL simulation in Figure 4, the rainfall intensity is also affected, with smaller accumulations found in the regions of the observed maxima. Increasing the evaporation process by 50% has the effect of concentrating the heaviest rainfall further south. The maximum in the eastern Gard is now forecast more accurately by the model than in the CTRL run. Contrastingly, the maximum in the western Gard is found less accurately with an enhanced evaporation process. These differences in system evolution underline the role of microphysical processes in modifying the characteristics of convective episodes, but also serve to indicate their limitations. As in the CTRL run, the triggering point of the convective system is incorrectly located.

In order to have more information regarding the dispersiveness of each ensemble, the results are also examined in the form of Taylor diagrams, which communicate three statistics on one plot: spatial correlation with observations, normalized standard deviation and a centred (i.e. unbiased) RMSE. A complete description of the formulation of the diagram can be found in Taylor (2001). A Taylor diagram for each of E6a, E6b and E6c for 24 h accumulated precipitation is presented in Figure 7. Ensemble method E6a induces the greatest dispersion in terms of correlation with observations. The normalized standard deviation improves compared with ensembles E6b and E6c. A further point to note is that, apart from two members of the E6a ensemble, none of the ensembles succeed in increasing the correlation above that of the CTRL run, which was 0.4.

Following the different statistics presented here, it is concluded that the methodology used in ensemble E6a gives the most dispersion. The differences in correlation, along with the dispersion seen in RMSE and normalized standard deviation values on the Taylor diagrams, are deemed more important indicators of dispersion than the plots of rainfall temporal evolution. The averaging performed for the temporal evolution plots can mask differences in the precipitation structures. The point-by-point verification methods, such as spatial correlation, RMSE and standard deviation, allow these differences to be more easily recognized. The methodology of ensemble E6a is thus deemed the most suitable. It will be this perturbation method that will be used to investigate the sensitivity of the rainfall to the microphysical processes for the four episodes from November 2011. This microphysical ensemble for the four days in November will be referred to as E(1-4)-MIC.

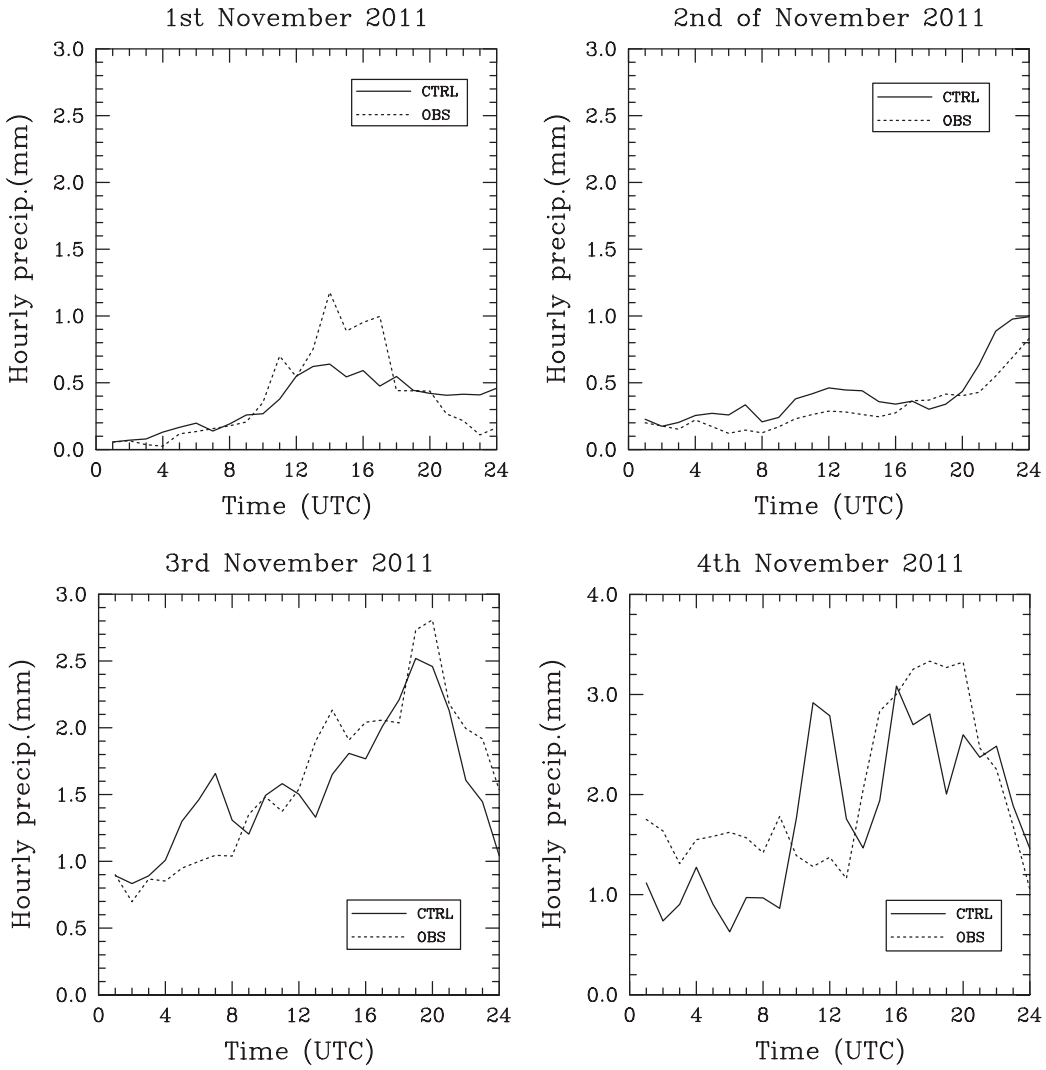


**Figure 9.** Time evolution of the spatially averaged hourly accumulated precipitation rate for each of the four days from November 2011, showing the observations collected from the Météo France network and predicted by the model Méso-NH. Model results were interpolated at rain-gauge locations and the average was performed over the target area shown in Figure 1.

### *3.2. Test of most suitable ensemble methodology on 1–4 November 2011 case studies*

Figure 8 shows the 24 h simulated rainfall for the CTRL simulation of each November case plotted against the 24 h observed rainfall. For 1 November (Figure 8(a)), the heaviest of the rain falls on the plains of the Hérault department and further south towards the coast. Méso-NH does succeed in finding some of the rain that falls on the plains, but the rain further south is missed by the model. Méso-NH also overestimates the total amount that falls, with accumulations of up to 200 mm, whereas the observational maximum is closer to 100 mm. This case, like that of 6 September 2010 and the case of 20 October 2008, which was studied by Fresnay *et al.* (2012), would be expected to show some sensitivity to microphysical processes as, like the other two days, this case had weak low-level inflow accompanied by weak synoptic forcing. The cases of 2, 3 and 4 November (Figure 8(b), (c) and (d), respectively) give rainfall patterns that can be compared with the situation of 1 November 2008, which was also studied by Fresnay *et al.* (2012). They showed that this type of precipitation episode, where the rain falls mainly on the foothills of the Cévennes, shows very little, if any, sensitivity to microphysical perturbations. The patterns of rainfall seen on 2 and 4 November do show that areas outside the Cévennes are affected, but that the heaviest and most concentrated rain falls in mountainous areas. The suspected key role of the orography in these situations would limit the sensitivity to microphysical processes. It is also likely, as suggested by Leoncini *et al.* (2013), that having high amounts of precipitable water can make the storm less sensitive to changes in the microphysics because a large degree of water will condensate away, regardless of the details of the scheme. Also, for the days of 3 and 4 November, the presence of a strong low-level southerly jet towards the affected area has been shown to make these types of situation quite predictable (Hohenegger *et al.*, 2006; Bresson *et al.*, 2012).

An analysis of the time evolution of the spatially averaged hourly rainfall for these four days (Figure 9) shows that for 1 November the model fails to properly capture the peak in precipitation, which occurred around 1400 UTC. It is also noticed that, as the intensity in rainfall begins to weaken towards the end of the day, the model continues to produce precipitation. For 2 November, the model almost always overestimates the amount of rainfall when compared with observations. The pattern of rainfall, however, is well captured by the model, with the increase in precipitation towards the end of the day quite accurately predicted by the model. When looking at the time evolution for 3 and 4 November, it can be seen that in general the CTRL simulation tends to follow the pattern found in the observations but that the two differ as to when the peaks in intensity occur. The time evolution for 4 November shows this most strikingly. The model produces a large peak around 1100 UTC that does not correspond to an observed peak in intensity, while the observed peak that occurs between 1600 and 1900 UTC is underestimated by the model. These discrepancies

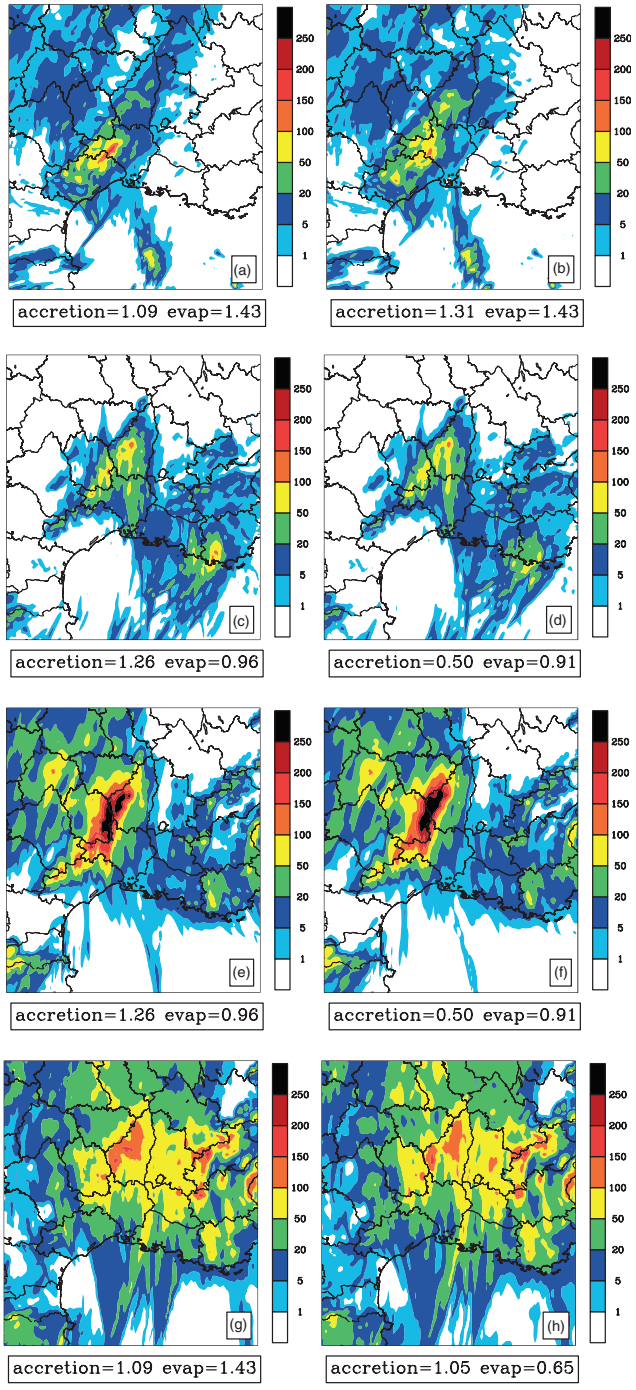


**Figure 10.** 24 h model rainfall for two members of ((a) and (b)) E1-MIC, ((c) and (d)) E2-MIC, ((e) and (f)) E3-MIC and ((g) and (h)) E4-MIC ensembles. The two members of each ensemble that contrasted with each other the most were chosen, in order to underline the relative level of dispersion. The random perturbation factor applied to the accretion and evaporation process for each member is given below the corresponding image.

have little impact on the spatial correlation between the observed and the simulated 24 h accumulated rainfall, with a value of 0.8 obtained for 4 November. The time evolution for 1 November, where the differences between the simulated and observed peaks could be said to be less severe, produces a lower correlation of 0.6. This is most likely due to the fact that after 1200 UTC on 1 November the simulated and observed rainfall evolution are poorly correlated. This is masked somewhat by the weak rainfall signal. For 4 November, the simulated and observed evolution are generally correlated, with the exception of the peak at 1100 UTC. This discrepancy would not impact on the spatial correlation, as differences in rainfall amounts do not impact on its calculation.

As was done for the test case of 6 September, ensembles were then produced starting from these four reference simulations. The rainfall produced by two contrasting ensemble members for each day for the ensemble E(1-4)-MIC is shown in Figure 10. The two contrasting members were selected by visualizing the rainfall pattern of each ensemble member and subjectively selecting the two members that seemed to contrast each other the most in terms of system structure and rainfall amount. The perturbation factor applied to each process for each member is specified below the plots in Figure 10. For the case of the E1-MIC ensemble, the dispersion between the two members is deemed greater than the difference between the members of the E2-MIC, E3-MIC and E4-MIC ensembles. These results are not surprising. As shown in Bresson *et al.* (2012), in the case of strong inflow (such as for the cases of 3 and 4 November), the main trigger for heavy precipitation tends to be the local orography, thus limiting the role of microphysical processes in storm development. The dispersion between the members for the case of 1 November is not spectacular, but it does suggest that microphysical processes play a role in controlling the lifetime of the convective cells. It is also clear from Figure 10 that perturbing the rain accretion and rain evaporation processes has an impact upon the rainfall intensity, but plays little role in determining the rainfall localization. Perturbing other factors, such as the turbulent tendencies, may affect the rainfall localization more strongly. This notion is examined in greater detail in section 4.

When looking at the situation from a statistical point of view, the relative dispersiveness of each of the cases is clearer. The Taylor diagram for each episode is shown in Figure 11. The dispersion between the members for 1 November is clearly stronger than for the other cases. Most of the members have a standard deviation around 1, which shows that overall the model does a decent job in predicting the observed variability, with errors being mostly due to the rain falling in an incorrect location. When looking at the days of 3 and 4 November, the results are contrasting. The correlation of the observations with the simulated model rainfall is approximately 0.8 for both days, which is an increase over the two other days (1 November gave 0.6, with 0.7 seen for 2 November). Overall, and for this limited sample at least, the microphysical perturbations lead to moderate dispersion in the surface rainfall for cases where the model skill is low, while little dispersion is seen for cases where the model skill is high.

## 4. Turbulence perturbations

It has been seen that the four days have distinct levels of model skill. It would also appear that the dispersion introduced in the surface rainfall by microphysical tendency perturbations depends on whether or not the model skill is high for the episode in question. As shown by Zampieri *et al.* (2005) and Fiori *et al.* (2011), boundary-layer parametrization is another source of large uncertainty. On the one hand, none of the standard turbulence parametrizations is really suited to kilometre-order resolution and, on the other hand, turbulent mixing may strongly impact the location and timing of convecting triggering and thus the precipitation pattern. In order to represent this uncertainty, perturbations were performed upon the turbulent tendencies. These tendencies were perturbed in the same manner as the microphysical processes, i.e. using a random factor ($r$) generated between 0.5 and 1.5. These ensembles will be labelled E(1-4)-TURB. Furthermore, an ensemble where the microphysical and turbulent tendencies were simultaneously perturbed was also performed, with these ensembles carrying the tags E(1-4)-MIC-TURB.

### 4.1. *Perturbations upon turbulent tendency terms*

Simulations of all events are more sensitive to turbulence tendency perturbations. This is verified by looking at the Taylor diagrams for the E(1-4)-TURB ensembles, which are shown in Figure 12.

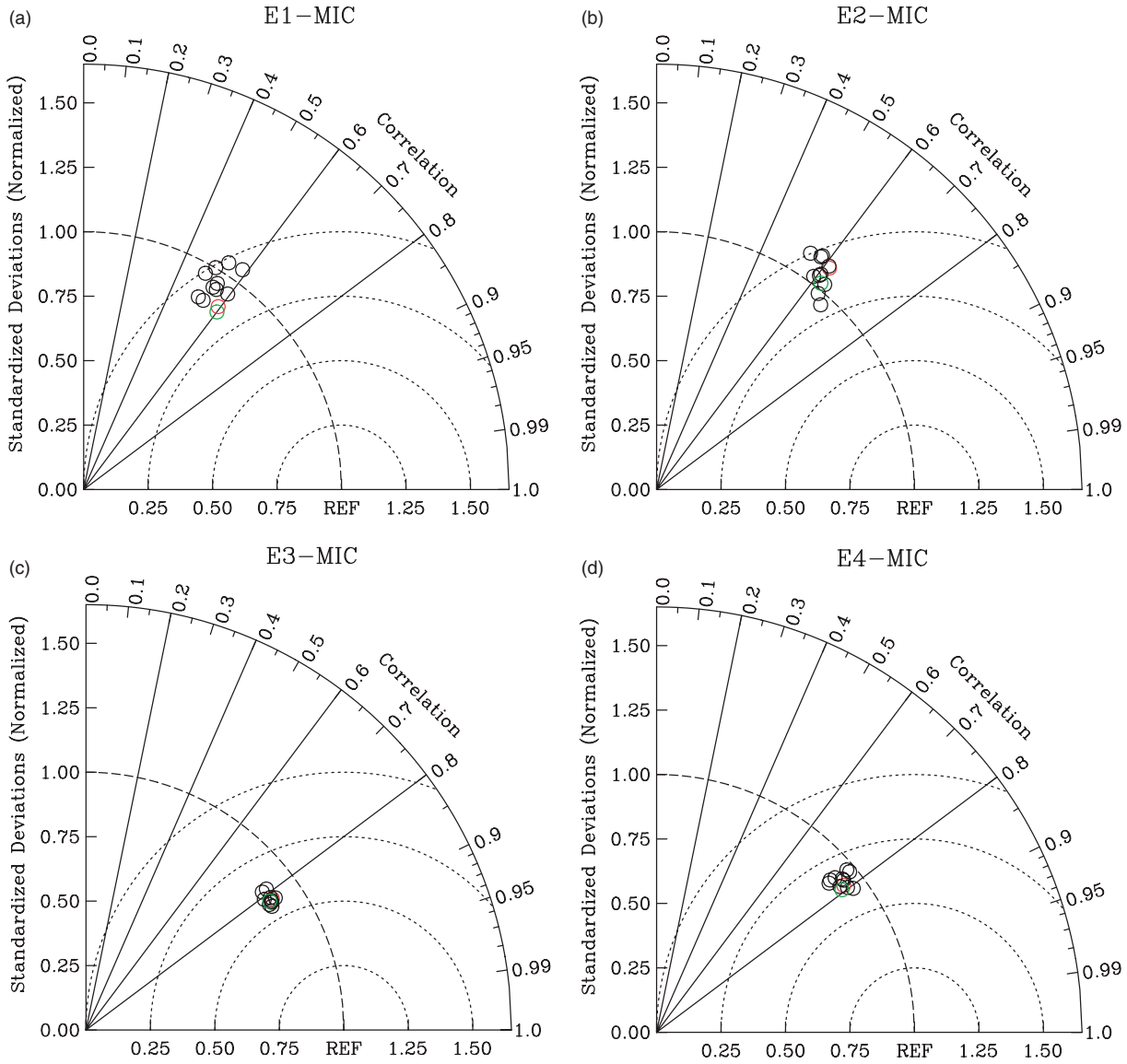


**Figure 11.** Taylor diagram for E1-MIC, E2-MIC, E3-MIC and E4-MIC ensembles. The ensemble members are represented by the black circles, the CTRL simulation by the red circle in the online article and the ensemble mean by the green circle in the online article.

Comparing the dispersion seen in these diagrams with that shown in the Taylor diagrams of E(1-4)-MIC (Figure 11) leads one to conclude that the resulting precipitation field is more sensitive to the turbulent tendency parametrization than to that of the microphysical processes. The increased dispersion is most prevalent for 1 November. Perturbing the turbulent tendencies for 2 November improves the standard deviation of the model output compared with the observations, with most members having a value of 1.0. 3 and 4 November, which showed the least sensitivity to the microphysical perturbations, show a growth in dispersion in terms of the standard deviation. Apart from a few members of ensemble E2-TURB, perturbing the turbulent tendencies does not succeed in increasing the correlation with the observations for any of the cases with respect to the correlation seen for the microphysical ensembles.

The increased sensitivity brought about by perturbing the turbulent tendencies can be most easily seen by looking at the ensemble rainfall average and the ensemble standard deviation plots, which are shown in Figure 13. These figures represent a comparison between the MIC ensembles and the TURB ensembles. Compared with the MIC ensembles, the standard deviation signal for the TURB ensembles for all four days is more dispersive, indicating the importance of the turbulence parametrization in determining the intensity of these rainfall cases. Another point worth noting is that, in the MIC ensembles, the standard deviation and ensemble mean exhibit similar patterns with colocalized maxima. This effect is not as strong for the TURB ensemble. In particular, for 3 and 4 November, the maximum spread was found shifted towards the eastern edge of the precipitation core. For these two cases, the perturbations have much less impact in mountainous areas (where the orographic forcing is strong enough to trigger and sustain deep convection regardless of the perturbation applied) than over the plains and the foothills (where a subtle modification of the turbulent mixing and therefore stability can alter the precipitation pattern more easily).

### 4.2. *Microphysical and turbulence perturbations*

If the turbulent tendencies and microphysical processes are perturbed in the same ensemble, even further dispersion is seen in the ensemble statistics (Figure 14). The effect of these perturbations is different for each of the four days. For 1 November, there is a greater degree of dispersion in the values of the correlation with the observations. The spatial correlation value now ranges from 0.3–0.7, instead of being concentrated around 0.5 and 0.6 as was seen for the E1-MIC ensemble (see Figure 11 for Taylor diagrams of E(1-4)-MIC ensembles, Figure 12 for E(1-4)-TURB ensembles and Figure 14 for E(1-4)-MIC-TURB ensembles). While the increase in dispersion shows that the

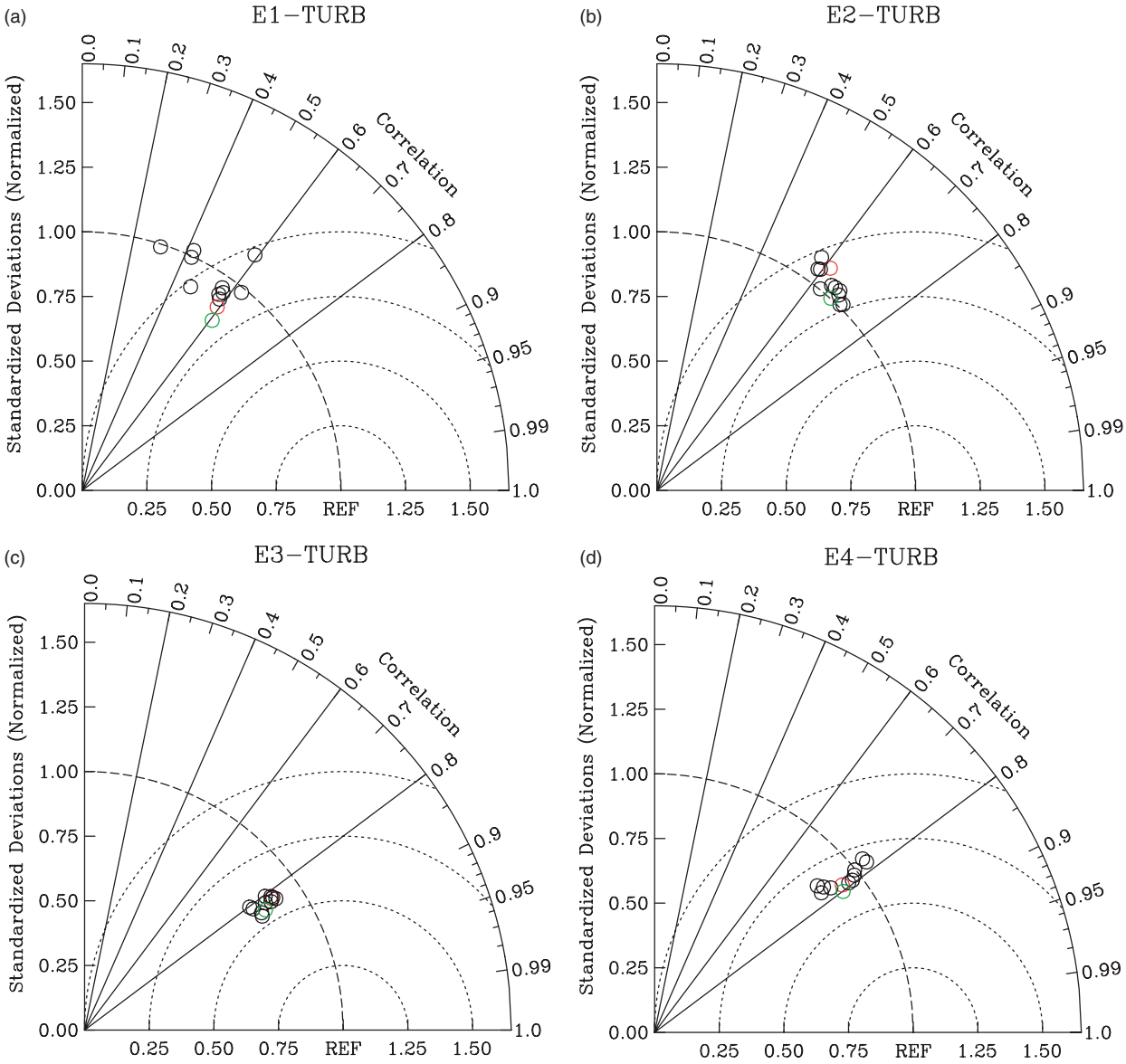


**Figure 12.** Taylor diagram for E1-TURB, E2-TURB, E3-TURB and E4-TURB ensembles. The ensemble members are represented by the black circles, the CTRL simulation by the red circle in the online article and the ensemble mean by the green circle in the online article.

rainfall is sensitive to errors in microphysical and turbulence parametrizations, the fact that some members give a spatial correlation of 0.3 also shows that, if used in an operational sense, limits should be placed on the value of the perturbation so as to avoid worsening the quality of the forecast. 2 November presents an increase in correlation, with the most skilful member of the ensemble now giving a correlation of almost 0.8. Almost all of the ensemble members for this case are now more skilful than the control simulation. For this case at least, this underlines the usefulness of an EPS and its advantages compared with a single deterministic forecast. For 3 November, there is no large improvement in the correlation value with the observations, but there is an increase in dispersion in terms of standard deviation, as was seen for the ensemble where solely the turbulent processes were perturbed. A similar pattern is seen for 4 November.

A better assessment of the value of each of the ensembles performed can be discerned from Figure 15(a) which compares the area under the Relative Operating Characteristic (ROC) curve and Brier Skill Score (BSS) for the microphysical, turbulent tendency and combined ensembles. The ROC shows the ratio of hit rates to the number of false alarm rates for prescribed rainfall thresholds, with the objective of having an area under the ROC of greater than 0.7 for the studied ensemble in order for it to be considered useful. More detailed information on the formulation and statistical significance of a ROC and the area beneath it can be found in Mason and Graham (2002). The BSS is computed using the CTRL simulation of each day as the reference forecast. A reliability diagram for each ensemble is also performed and is shown in Figure 15(b). The improvement in ROC area between the microphysical ensemble and the combined ensemble is small (an increase of 0.8–0.82), although the differences at higher precipitation thresholds are an important factor to notice. The BSS shows greater differences between the ensembles at smaller thresholds and it is again the combined ensemble that gives the greatest score, with a value of just under 0.22. The reliability diagram displays further information. All of the ensembles overforecast probabilities above 0.4 and underforecast those below it. The ensembles have difficulties forecasting very low probabilities, as for an event with an observed frequency of 0.05 the forecast probability was 0. Concurrently, for an observed frequency of between 0.85 and 0.9 the forecast probability was 1.0, indicating that the ensembles have a tendency to overforecast high probabilities. Based upon these statistics, it is concluded that the TURB ensemble performs better than the MIC ensemble and that in turn the MIC-TURB ensemble performs better than the TURB ensemble. The improvement in BSS values shows this most clearly. As has been demonstrated, there is no significant increase

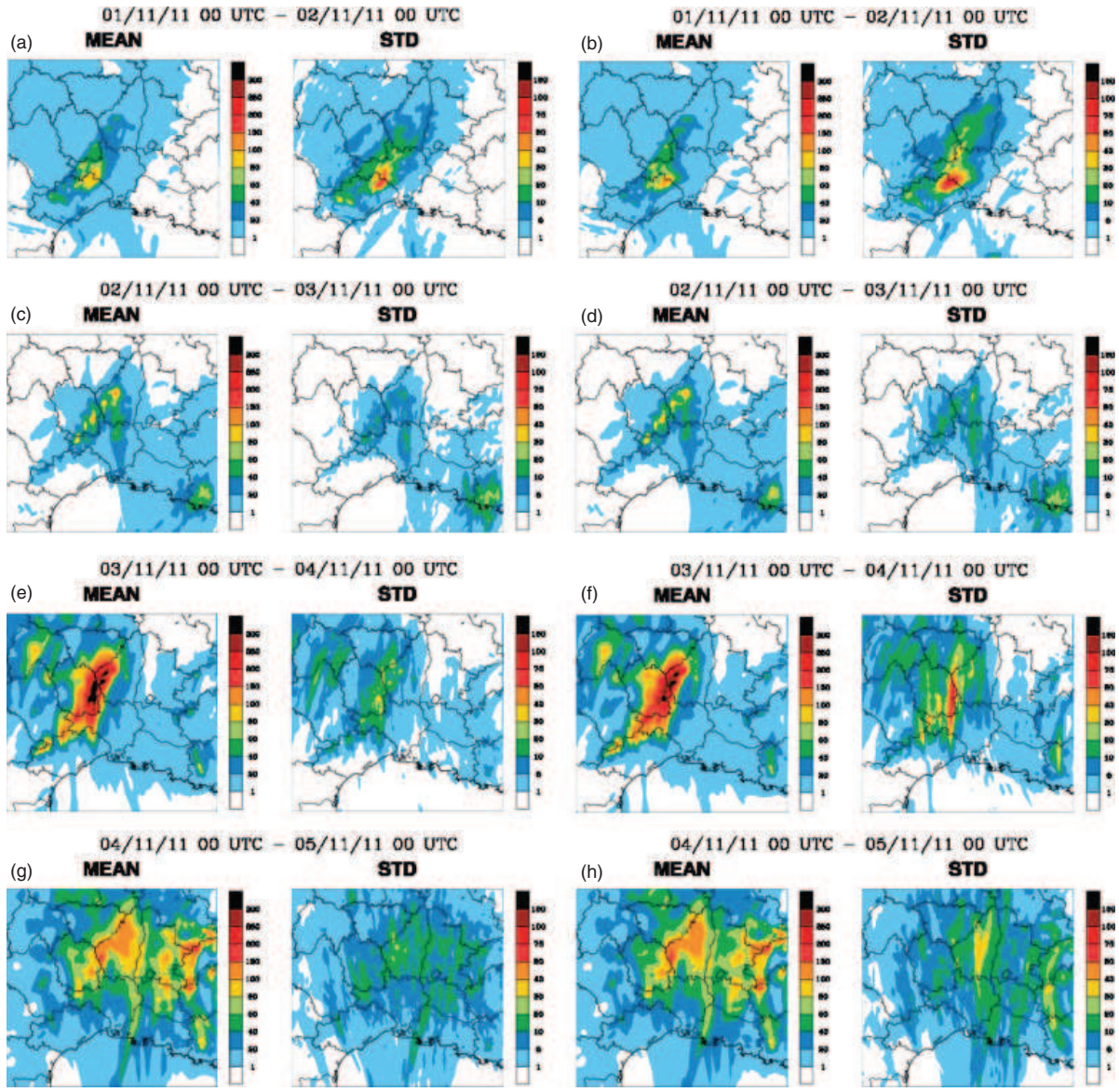


**Figure 13.** Mean and standard deviation of the model precipitation for (left) E(1-4)-MIC ensembles and (right) E(1-4)-TURB ensembles.

in correlation with observations from one ensemble to the next, but more so in the dispersion induced in the standard deviation values of the ensemble members.

## 5. Conclusion and discussion

Southeastern France is often affected by heavy rainfall episodes during the autumn months, which can lead to very devastating flash flood events. This rain occurs most frequently when an upper-level trough to the west of the target area directs warm moist air from the Mediterranean towards the region's topography. However, these events may also occur through the formation of a quasi-stationary convective system, which can form over the Rhône valley. These two types of events have differing large-scale conditions and contrasting levels of model skill, with the former showing strong southeasterly flows, rain, more so on the Cévennes mountain range, and a high level of model skill and the latter having weaker southerly flows, lower model skill and rain that is for the most part found in the plains of the Hérault and Gard departments. 6 September 2010 and 1–4 November 2011 can be taken as good examples of these two types of heavy precipitation events.

Control (CTRL) experiments for the five days mentioned illustrate the different levels of model skill that these rain episodes can present. The test case of 6 September 2010 had the least skilful deterministic forecast. The deterministic forecasts for 1 and 2 November were also only moderately skilful. The CTRL simulations for 3 and 4 November were much more skilful. An analysis of the large-scale meteorological situation showed that these two days had stronger flows towards the target area than the other three case studies, which is known to increase the model forecasting accuracy (Bresson *et al.*, 2012).

Ensemble forecasting was put forward as a suitable option in order to address the forecasting issues encountered for these cases, with particular focus being put on the uncertainties related to the physical parametrizations of the model. The test case was used to investigate the most pertinent configuration for performing simultaneous perturbations on the rain evaporation rate and the rain accretion rate. These ensembles had different perturbing factors and methods: ensemble E6a used a range between 0.5 and 1.5 and the factor was randomly chosen; ensemble E6b used a range between 0.1 and 10 and the factor was randomly chosen; and ensemble E6c used specific user-defined factors to perturb the different microphysical parameters. The most pertinent and useful ensembles were defined to be those that gave the most dispersion between the different members, with different methods used for observing this including assessing the time and spatial distribution of the observed and forecast rainfall and performing a number of statistical tests.

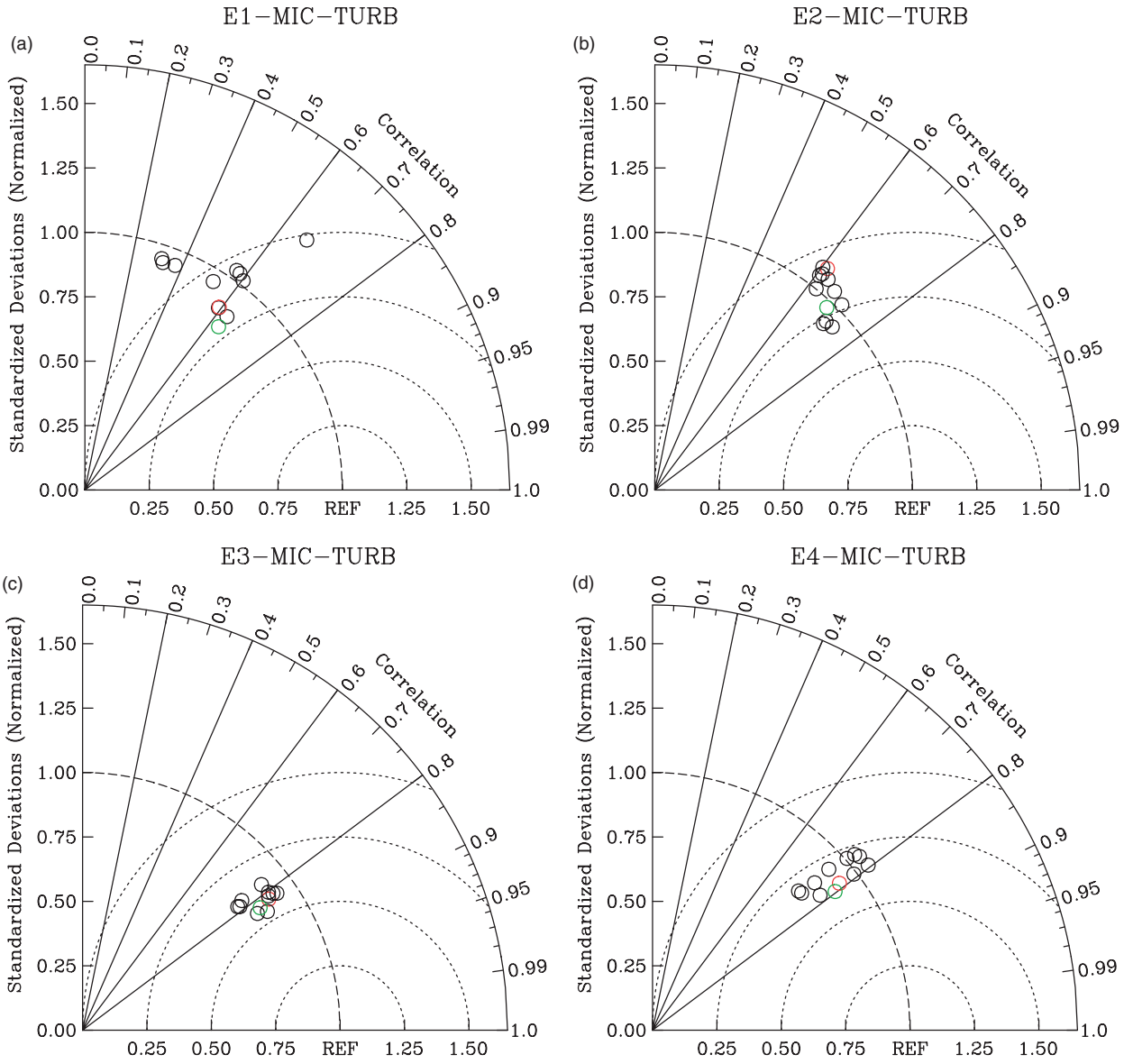


**Figure 14.** Taylor diagram for E(1-4)-MIC-TURB ensembles. The ensemble members are represented by the black circles, the CTRL simulation by the red circle in the online article and the ensemble mean by the green circle in the online article.

For the test case, the CTRL simulation missed the heaviest rainfall, which fell in the western Gard, instead placing it to the north over the Ardèche department. None of the three ensemble methodologies tested succeeded in correcting this localization error. A comparison of the three ensembles led to the conclusion that ensemble methodology E6a gave the greatest degree of dispersion amongst its members and was thus deemed the most suitable way in which to perturb the microphysical parametrizations. Dispersion was most easily seen in the standard deviation values of the ensemble members, while the dispersion in correlation with the observations was less remarkable.

This same perturbation method was then used to perform ensemble forecasts on four days of heavy rainfall in the southeast of France from November 2011. These ensembles (E(1-4)-MIC) gave differing results for the four days. 1 November showed a good deal of dispersion between its members, again mostly in terms of RMSE and standard deviation. 2, 3 and 4 November exhibited less dispersion, with 3 and 4 November displaying little if any. This seems to illustrate, as has been indicated by Fresnay *et al.* (2012) and was suggested by Stensrud *et al.* (1999), that sensitivity to the microphysical processes and thus the usefulness of an ensemble prediction system based upon such perturbations is case-dependent. Cases where the model skill was high showed little sensitivity to the tendency perturbations, while cases with low model skill gave greater sensitivity.

The E(1-4)-MIC perturbations of the microphysical processes were compared with an E(1-4)-TURB ensemble, where perturbations were carried out on the turbulent time tendencies. It was seen that, for each of the four days in November, this brought about more dispersion within the model. The increase in sensitivity was seen in increased dispersiveness of the values of the correlation coefficient for 1 and 2 November, while it was the value of the standard deviation and RMSE that changed for 3 and 4 November. This ensemble was seen to be more useful than an ensemble where solely the microphysical processes were perturbed, although it was in the E(1-4)-MIC-TURB ensemble, where both were manipulated, that the greatest dispersion was induced. Combining both ensembles led to an increase in correlation for 1 and 2 November, with 2 November in particular gaining skill, as almost all ensemble members gave higher correlations with the observations than the CTRL. 3 and 4 November benefited once again in terms of increased dispersion within the RMSE and standard deviation values. In particular, the weakly predictable situations associated with deep convection triggered upstream of the topography were found to be much more sensitive to the physical perturbations than the more predictable situations strongly controlled by the

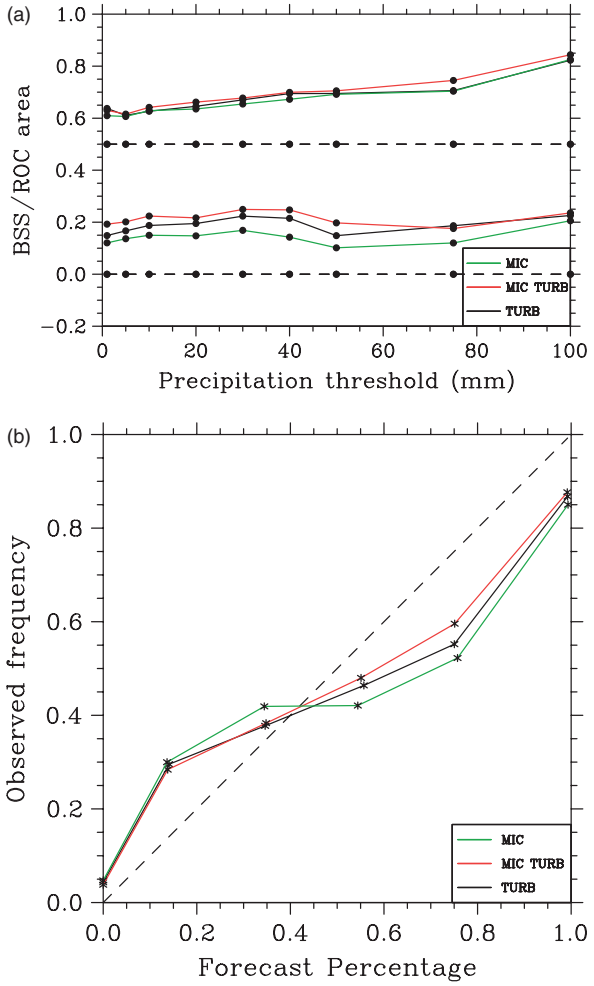


**Figure 15.** Brier Skill Score (BSS) (bottom curves of top plot), area under the ROC curve (top curves of top plot) and reliability diagram (bottom plot) for the E(1-4)-MIC, E(1-4)-TURB and E(1-4)-MIC-TURB ensembles.

orographic forcing. This study demonstrates that, while there is some sensitivity to cloud physics parametrization errors and an even greater one related to errors in the parametrization of the turbulent processes, the significance of that sensitivity is case-dependent.

As was suggested in Vié *et al.* (2012), errors related to domain internal parametrizations are probably less important than errors coming from initial and boundary conditions. Despite a certain level of dispersion being demonstrated, ensembles where microphysical and turbulence processes are perturbed remain somewhat underdispersive and do not give a full representation of the forecast uncertainty. However, it is considered that the sensitivity shown here to errors within these physical parametrizations demonstrates that ensembles in which they are perturbed could bring extra information that would be of use in helping to better forecast these types of HPEs. Future work will include the extension of the methodology to cold microphysical processes, the test of non-uniform perturbations and the use of this ensemble strategy at finer resolutions for which turbulence parametrizations no longer fall within the range known as 'terra incognita' (Wyngaard, 2004).

## Acknowledgements

The authors thank Dr Giovanni Leoncini and another, anonymous, reviewer, whose comments and suggestions helped to improve this article substantially. This work was carried out in the framework of the DRIHM EU project. Computing resources were allocated by Grand Equipement National de Calcul Intensif (GENCI project 2013010569) and calcul en Midi Pyrenees (CALMIP, project P1247).

## References

Argence S, Lambert D, Richard E, Chaboureau JP, Soehne N. 2008. Impact of initial condition uncertainties on the predictability of heavy rainfall in the Mediterranean: A case study. *Q. J. R. Meteorol. Soc.* **134**: 1775–1788.

Bechtold P, Bazile E. 2001. The 12–13 November 1999 flash flood in southern France. *Atmos. Res.* **56**: 171–189.

Bechtold P, Bazile E, Guichard F, Mascart P, Richard E. 2001. A mass flux convection scheme for regional and global models. *Q. J. R. Meteorol. Soc.* **127**: 869–886.

Bouttier F, Vie B, Nuissier O, Raynaud L. 2012. Impact of stochastic physics in a convection-permitting ensemble. *Mon. Weather Rev.* **140**: 3706–3721.

Bresson R, Ricard D, Ducrocq V. 2009. Idealized mesoscale numerical study of Mediterranean heavy precipitating convective systems. *Meteorol. Atmos. Phys.* **103**: 45–55.

Bresson E, Ducrocq V, Nuissier O, Ricard D, de Saint-Aubin C. 2012. Idealized numerical simulations of quasi-stationary convective systems over the Northwestern Mediterranean complex terrain. *Q. J. R. Meteorol. Soc.* **138**: 1751–1763.

Buizza R, Miller M, Palmer TN. 1999. Stochastic representation of model uncertainties in the ECMWF ensemble prediction system. *Q. J. R. Meteorol. Soc.* **125**: 2887–2908.

Chaboureau JP, Pantillon F, Lambert D, Richard E, Claud C. 2012. Tropical transition of a Mediterranean storm by jet crossing. *Q. J. R. Meteorol. Soc.* **138**: 596–611.

Clark AJ, Gallus WA, Chen TC. 2008. Contributions of mixed physics versus perturbed initial/lateral boundary conditions to ensemble-based precipitation forecast skill. *Mon. Weather Rev.* **136**: 2157–2185.

Clark AJ, Gallus WA, Xue M, Kong F. 2010. Convection-allowing and convection-parameterizing ensemble forecasts of a mesoscale convective vortex and associated severe weather environment. *Weather and Forecasting* **25**: 1052–1081.

Cuxart J, Bougeault P, Redelsperger JL. 2000. A turbulence scheme allowing for mesoscale and large-eddy simulations. *Q. J. R. Meteorol. Soc.* **126**: 1–30.

Ducrocq V, Nuissier O, Ricard D, Lebeaupin C, Thouvenin T. 2008. A numerical study of three catastrophic precipitating events over southern France. II: Mesoscale triggering and stationarity factors. *Q. J. R. Meteorol. Soc.* **134**: 131–145.

Fiori E, Parodi A, Siccardi F. 2009. Dealing with uncertainty: Turbulent parameterizations and grid-spacing effects in numerical modelling of deep moist convective processes. *Nat. Hazards Earth Syst. Sci.* **9**: 1871–1880.

Fiori E, Parodi A, Siccardi F. 2011. Uncertainty in prediction of deep moist convective processes: Turbulence parameterizations, microphysics and grid-scale effects. *Atmos. Res.* **100**: 447–456.

Fresnay S, Hally A, Garnaud C, Richard E, Lambert D. 2012. Heavy precipitation events in the Mediterranean: Sensitivity to cloud physics parameterisation uncertainties. *Nat. Hazards Earth Syst. Sci.* **12**: 2671–2688.

Fritsch JM, Carbone RE. 2004. Improving quantitative precipitation forecasts in the warm season: A USWRP research and development strategy. *Bull. Am. Meteorol. Soc.* **85**: 955–965.

Gebhardt C, Theis SE, Paulat M, Ben Bouallegue Z. 2011. Uncertainties in COSMO-DE precipitation forecasts introduced by model perturbations and variation of lateral boundaries. *Atmos. Res.* **100**: 168–177.

Gilmore MS, Straka JM, Rasmussen EN. 2004. Precipitation uncertainty due to variations in precipitation particle parameters within a simple microphysics scheme. *Mon. Weather Rev.* **132**: 2610–2627.

Hohenegger C, Schär C. 2007. Predictability and error growth dynamics in cloud-resolving models. *J. Atmos. Sci.* **64**: 4467–4478.

Hohenegger C, Luethi D, Schär C. 2006. Predictability mysteries in cloud-resolving models. *Mon. Weather Rev.* **134**: 2095–2107.

Honnert R, Masson V, Couvreux F. 2011. A diagnostic for evaluating the representation of turbulence in atmospheric models at the kilometric scale. *J. Atmos. Sci.* **68**: 3112–3131.

Houtekamer P, Lefaivre L, Derome J, Ritchie H, Mitchell H. 1996. A system simulation approach to ensemble prediction. *Mon. Weather Rev.* **124**: 1225–1242.

Lafore JP, Stein J, Asencio N, Bougeault P, Ducrocq V, Duron J, Fischer C, Héreil P, Mascart P, Masson V, Pinty JP, Redelsperger JL, Richard E, Vilà-Guerau de Arellano J. 1998. The Meso-NH atmospheric simulation system. Part I: Adiabatic formulation and control simulations. *Ann. Geophys.* **16**: 90–109.

Lascaux F, Richard E, Pinty JP. 2006. Numerical simulations of three different MAP IOPs and the associated microphysical processes. *Q. J. R. Meteorol. Soc.* **132**: 1907–1926.

Leoncini G, Plant RS, Gray SL, Clark PA. 2010. Perturbation growth at the convective scale for CSIP IOP18. *Q. J. R. Meteorol. Soc.* **136**: 653–670.

Leoncini G, Plant RS, Gray SL, Clark PA. 2013. Ensemble forecasts of a flood-producing storm: Comparison of the influence of model-state perturbations and parameter modifications. *Q. J. R. Meteorol. Soc.* **139**: 198–211.

Lorenz EN. 1969. The predictability of a flow which possesses many scales of motion. *Tellus* **21**: 289–307.

Mason S, Graham N. 2002. Areas beneath the relative operating characteristics (ROC) and relative operating levels (ROL) curves: Statistical significance and interpretation. *Q. J. R. Meteorol. Soc.* **128**: 2145–2166.

Mlawer EJ, Taubman SJ, Brown PD, Iacono MJ, Clough SA. 1997. Radiative transfer for inhomogeneous atmospheres: RRTM, a validated corrolated-*k* model for the longwave. *J. Geophys. Res.* **102D**: 16663–16682, doi: 10.1029/97JD00237.

Noilhan J, Mafhouf J. 1996. The ISBA land surface parameterisation. *Global Planet. Change* **13**: 145–159.

Nuissier O, Ducrocq V, Ricard D, Lebeaupin C, Anquetin S. 2008. A numerical study of three catastrophic precipitating events over southern France. I: Numerical framework and synoptic ingredients. *Q. J. R. Meteorol. Soc.* **134**: 111–130.

Pergaud J, Masson V, Malardel S, Couvreux F. 2009. A parameterization of dry thermals and shallow cumuli for mesoscale numerical weather prediction. *Boundary-Layer Meteorol.* **132**: 83–106.

Pinty JP, Jabouille P. 1998. 'A mixed-phase cloud parameterization for use in a mesoscale non-hydrostatic model: Simulations of a squall line and of orographic precipitations'. *Tenth AMS Cloud Physics Conference* 217220. American Meteorological Society: Everett, WA.

Plant RS, Craig GC. 2008. A stochastic parameterization for deep convection based on equilibrium statistics. *J. Atmos. Sci.* **65**: 87–105.

Richard E, Cosma S, Tabary P, Pinty JP, Hagen M. 2003. High-resolution numerical simulations of the convective system observed in the Lago Maggiore area on 17 September 1999 (MAP IOP 2a). *Q. J. R. Meteorol. Soc.* **129**: 543–563.

Schwartz CS, Kain JS, Weiss SJ, Xue M, Bright DR, Kong F, Thomas KW, Levit JJ, Coniglio MC, Wandishin MS. 2010. Toward improved convection-allowing ensembles: Model physics sensitivities and optimizing probabilistic guidance with small ensemble membership. *Weather and Forecasting* **25**: 263–280.

Shutts G. 2005. A kinetic energy backscatter algorithm for use in ensemble prediction systems. *Q. J. R. Meteorol. Soc.* **131**: 3079–3102.

Stensrud DJ, Brooks HE, Du J, Tracton MS, Rogers E. 1999. Using ensembles for short-range forecasting. *Mon. Weather Rev.* **127**: 433–446.

Taylor KE. 2001. Summarizing multiple aspects of model performance in a single diagram. *J. Geophys. Res* **106**: 7183–7192, doi: 10.1029/2000JD900719.

Vié B, Molinié G, Nuissier O, Vincendon B, Ducrocq V, Bouttier F, Richard E. 2012. Hydro-meteorological evaluation of a convection-permitting ensemble prediction system for Mediterranean heavy precipitating events. *Nat. Hazards Earth Syst. Sci.* **12**: 2631–2645.

Walser A, Luthi D, Schar C. 2004. Predictability of precipitation in a cloud-resolving model. *Mon. Weather Rev.* **132**: 560–577.

Wyngaard JC. 2004. Toward numerical modeling in the 'terra incognita'. *J. Atmos. Sci.* **61**: 1816–1826.

Zampieri M, Malguzzi P, Buzzi A. 2005. Sensitivity of quantitative precipitation forecasts to boundary layer parameterization: A flash flood case study in the western Mediterranean. *Nat. Hazards Earth Syst. Sci.* **5**: 603–612.

 

## 3.3 Cold process perturbations for a real world situation

The 24-C, 24-WC and 96-WC ensembles illustrated that the evolution of the rainfall field of the KW78 supercell case study had little sensitivity to the microphysical cold processes. Gilmore *et al.* (2004), Richard *et al.* (2003) and Lascaux *et al.* (2006) demonstrated that for real world situations, cold processes can have an impact on the surface precipitation pattern for certain types of convective events.

The methodology presented in section 2.1.3 was tested upon a real world convective HPE from September 2010. The meteorological conditions of this situation are presented in section 2.1 of the research article which forms section 3.2 of this manuscript. The model set-up is given in section 2.2 of the research article while a comparison of the simulated and observed rainfall patterns is plotted in Fig.4 of the article. An ensemble simulation, labelled E6CO with the 6 referring to the 6th of September, was constructed consisting of 10 perturbed members. As for the idealised cases, temporal evolution and mean and standard deviation plots of the accumulated rainfall were used to visualise the dispersion between the ensemble members. Ensemble statistics are also presented in the form of Taylor diagrams (Taylor (2001)). A description of the different statistics displayed by this diagram are given in section 3.1 of the research article.

The time series and Taylor diagrams presented in Fig. 3.1 are plotted over the target area shown in Fig.1 of the article. Compared to the Taylor diagram for a warm process (E6a) ensemble (Fig.7 in article), the dispersion between the ensemble members is reduced. None of the members of the E6CO ensemble succeed in increasing the spatial correlation with the observations, whereas for the E6a ensemble, at least two members lead to more accurate spatial representations of the observed rainfall field. The temporal evolution plot shows dispersion between the ensemble members around the observed rainfall peak but demonstrates limited spread for other periods of the rainfall evolution.

The mean and standard deviation plots of the rainfall field for the E6CO and E6a ensembles presented in Fig. 3.2 are performed over the target area shown in Fig.1 of the research article. The E6a ensemble gives a stronger standard deviation signal than the E6CO ensemble over the area of heaviest observed rainfall in the eastern Gard region (see Fig.1 and Fig.4 of research article for location of French departments and localisation of observed rainfall patterns). The E6a ensemble also shows greater spread over areas of substantial rainfall in the western Gard.

The hierarchy of sensitivity seen for the idealised cases is here respected. The ensemble 24-C demonstrated that the surface rainfall field for an idealised supercell storm had little sensitivity to the microphysical cold processes and certainly less sensitivity than was shown to the microphysical warm processes in the 24-WA ensemble. The level of dispersion seen in the E6CO ensemble is more significant than that which was seen in the idealised tests ensembles where the cold processes where perturbed. The case of the 6th of September 2010 is clearly much more meteorologically com-

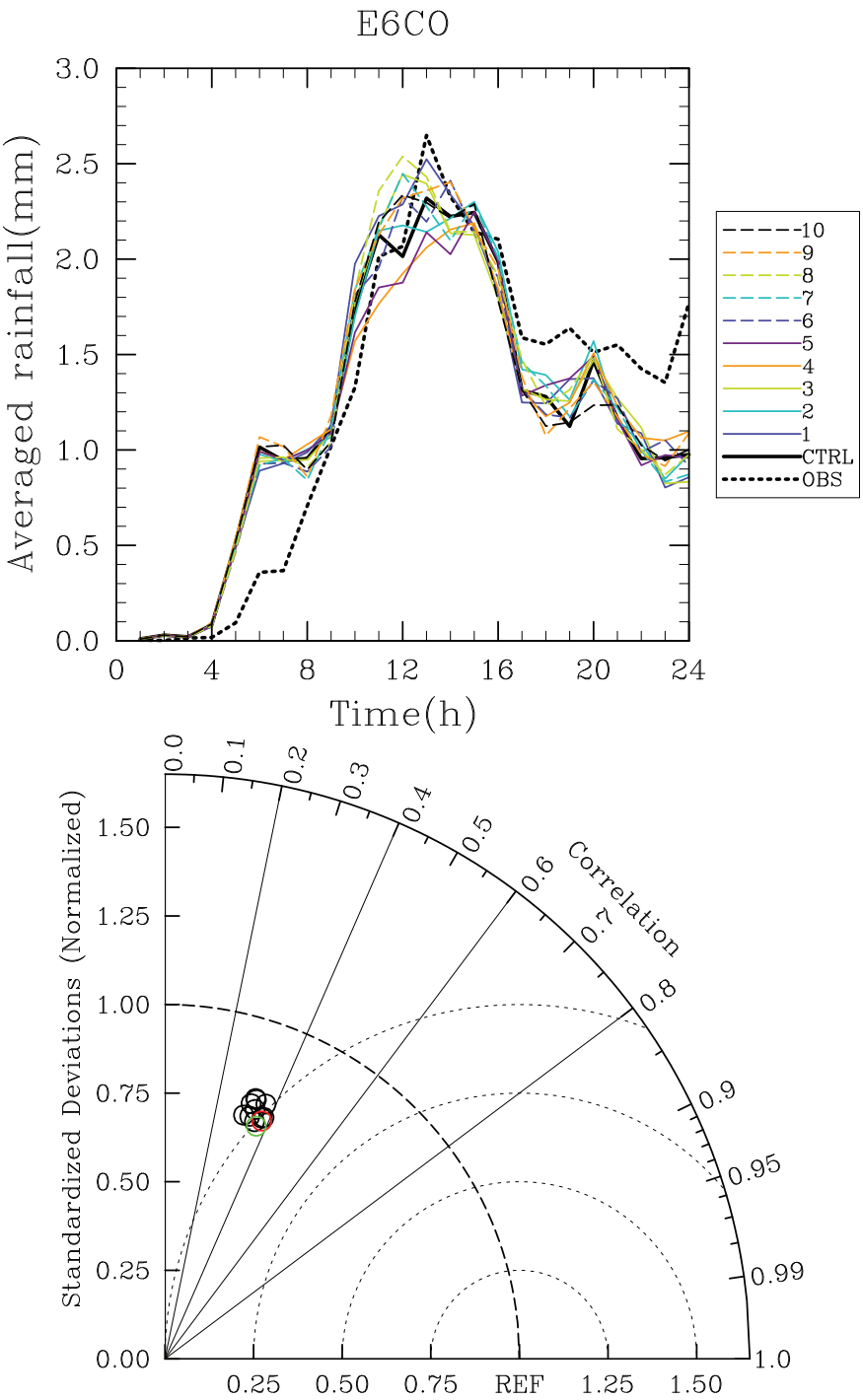


**Figure 3.1:** *The temporal evolution of the rainfall and Taylor diagram for the E6CO ensemble.*

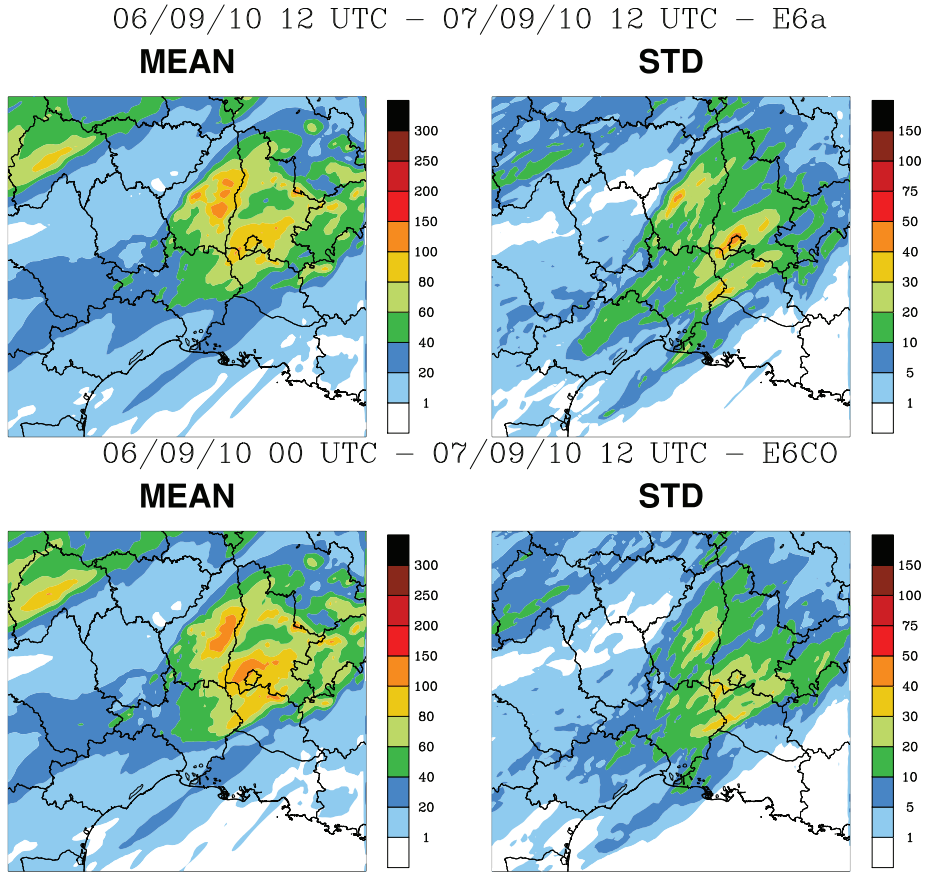


**Figure 3.2:** *The mean and standard deviation plots for the E6a ensemble and E6CO ensemble.*

plex than the idealised supercell storm described in KW78. The convective activity of the real world case allowed deeper convective clouds to develop which led to an increased contribution to the rainfall water budget from the cold processes, augmenting the importance of the ice processes in the evolution of the surface rainfall.

# Chapter 4

# HyMeX convective lines

## 4.1 Presentation of article

In section 2.5, idealised simulations demonstrated the sensitivity of a squall line to perturbations upon the warm and cold microphysical and turbulence time tendencies. Contrastingly to the supercell ensembles described in sections 2.3 and 2.4, adding perturbations to the microphysical cold processes led to an increase in dispersion in the surface rainfall. In agreement with the supercell results, an ensemble where the warm and cold microphysical and turbulence time tendencies were perturbed led to the most dispersive ensemble. The level of dispersion displayed by this ensemble was large. In the examination of a real world case, the same degree of dispersion would not be expected due to the impact of other important factors. Vié *et al.* (2012) and Vié *et al.* (2011) demonstrated that initial (IC) condition and boundary (BC) condition errors tend to produce a larger level of sensitivity in the rainfall field than microphysical perturbations. However, the sensitivity of the rainfall field of a real world convective line to perturbations upon the turbulence processes and a combination of perturbations upon the microphysical and turbulence processes remains largely unknown.

The research article which follows in section 4.2 presents an investigation into two convective lines which were observed during the Special Observing Period (SOP1) of the HyMeX campaign, which began in September 2012. These two events, known as Intensive Observing Period 6 (IOP6) and Intensive Observing Period 7a (IOP7a), were chosen as they represented two of the most significant rainfall episodes to have taken place during the SOP1 over south-eastern France. The aim of the study was to implement, for a real world convective line, the perturbation methodology used to construct an EPS for the idealised squall line in section 2.5. As a secondary aim, a comparison between the sensitivity to physical parameterisation and IC and BC perturbations is presented.

To begin with, for each IOP, an ensemble of 4 members using different IC and BC from the AROME, AROME-WMED, ECMWF and ARPEGE analysis was designed (labelled ICBC6 or ICBC7a, depending on the IOP). This permitted a basic evaluation of the level of dispersion which could be attributed to changing the IC and BC. Using comparative statistics and plots of the temporal evolution of the rainfall, the member

of the ICBC ensemble which gave the most accurate representation of the observed rainfall field was chosen as a control (CTRL) simulation. Starting from this CTRL, ensembles were then produced where the warm and cold microphysical and turbulence processes were perturbed in the same manner as is described in section 2.5.

The results confirm the hierarchy of perturbation sensitivity illustrated for the idealised ensembles. An ensemble where the microphysical and turbulence processes were simultaneously perturbed (labelled MT6 or MT7a, depending on the IOP) gave the greatest level of dispersion. It was also shown that, as was demonstrated in Hally *et al.* (2013) and Fresnay *et al.* (2012), the sensitivity of the rainfall field to perturbations upon the physical parameterisations depends on the nature of the convective system. An episode which took place in the presence of moderate to weak low-level flow (IOP6) displayed a greater degree of sensitivity to physical perturbations than an episode which developed under strong low-level flow (IOP7a). This feature is not seen for the ICBC ensembles as for both IOP6 and IOP7a the level of dispersion is similar. Comparisons between the level of dispersion introduced in the physical perturbation ensembles and ICBC ensembles shows that when the low-level flow is moderate to weak (IOP6), the degree of dispersion is comparable, whereas for cases with stronger low-level flow (IOP7a), the ICBC ensemble presents a greater degree of dispersion. It is concluded that an ensemble where the physical processes are perturbed may be useful, depending on the nature of the rainfall episode.

## 4.2 An ensemble study of HyMeX IOP6 and IOP7a: Sensitivity to physical and initial and boundary condition uncertainties

Article prepared for publication in the journal of Natural Hazards and Earth System Sciences.

Manuscript prepared for Nat. Hazards Earth Syst. Sci.
with version 3.2 of the LaTeX class copernicus.cls.
Date: 10 December 2013

# An ensemble study of HyMeX IOP6 and IOP7a: Sensitivity to physical and initial and boundary condition uncertainties

**A. Hally**[1], **E. Richard**[1], **and V. Ducrocq**[2]

[1]Laboratoire d'Aérologie, Université de Toulouse and CNRS, Toulouse, France
[2]CNRM, Météo-France, Toulouse, France

**Abstract.**

The first Special Observation Period of the HyMeX campaign took place in the Mediterranean between September and November 2012 with the aim of better understanding the mechanisms which lead to heavy precipitation events (HPEs) in the region during the autumn months. Two such events, referred to as Intensive Obseration Period 6 (IOP6) and Intensive Observation Period 7a (IOP7a), occurred respectively on the 24th and 26th of September over south-eastern France. IOP6 was characterised by moderate to weak low-level flow which led to heavy and concentrated convective rainfall over the plains near the coast, while IOP7a had strong low-level flow and consisted of a convective line over the mountainous regions further north and a band of stratiform rainfall further east. Firstly, an ensemble was constructed for each IOP using analyses from the AROME, AROME-WMED, ARPEGE and ECMWF operational models as initial (IC) and boundary (BC) conditions for the research model Meso-NH at a resolution of 2.5km. A high level of model skill was seen for IOP7a, with a lower level of agreement with the observations for IOP6. Using the most accurate member of this ensemble as a CTRL simulation, three further ensembles were constructed in order to study uncertainties related to cloud physic and surface turbulence parameterisations. Perturbations were introduced by perturbing the time tendencies of the warm and cold microphysical and turbulence processes. An ensemble where all three sources of uncertainty were perturbed gave the greatest degree of dispersion in the surface rainfall for both IOPs. Comparing the level of dispersion to that of the ICBC ensemble demonstrated that when model skill is low (high) and low-level flow is weak to moderate (strong), the level of dispersion of the ICBC and physical perturbation ensembles is (is not) comparable. The level of sensitivity to these perturbations is thus concluded to be case dependent.

*Correspondence to:* A. Hally
(alan.hally@aero.obs-mip.fr)

## 1 Introduction

The Mediterranean basin is a complex geographic region prone to extreme rainfall events during the autumn months. The resulting flash-floods can lead to economic damage and even fatalities (see Llasat et al. (2013) for a list of such events over the north-western Mediterranean). Clearly these high-impact weather events need to be accurately forecast, leading to the development of dedicated international research projects. MEDEX (MEDiterranean EXperiment, http://medex.aemet.uib.es/), DRIHM (Distributed Research Infrastructure for Hydro-Meteorology, http://www.drihm.eu/) and HyMeX (HYdrological cycle in Mediterranean EXperiment, http://www.hymex.org/) are three such projects. MEDEX aimed to forecast more accurately the important weather events associated to Mediterranean cyclones while simultaneously investigated the societal impacts of these events. DRIHM seeks to provide easier access to hydrometeorological data while also facilitating the collaboration between meteorologists and hydrologists with the aim of accelerating scientific advances in hydrometeorological research. Such advances will include enhanced modelling and data processing capabilities through the integration of dedicated hydrometeorological services throughout the European e-Infrastructure network. The overall aim of the HyMeX project (Drobinski et al. (2013)) is to better understand and forecast the water cycle in the Mediterranean with an emphasis on intense hydrometeorological events. The first Special Observation Period (SOP1), which took place between September and November 2012, focused on HPEs in the north-western Mediterranean. Twenty Intense Observation Periods (IOPs) were undertaken during the SOP1, with a survey of HPEs in Spain, France and Italy (Ducrocq et al., 2013).

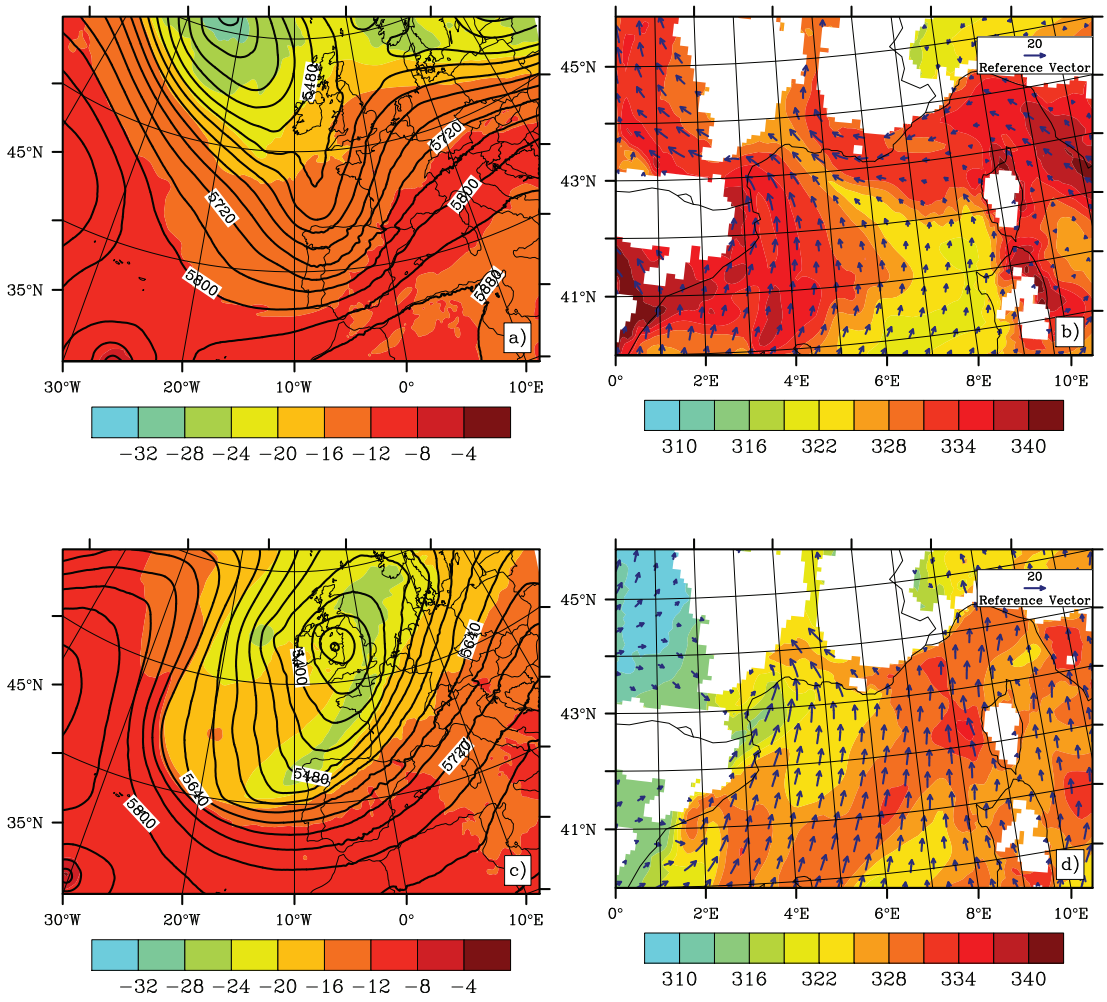


**Fig. 1.** ECMWF large-scale analysis at 18UTC on the 23rd of September 2012 showing (a) Temperature ($^{\circ}C$) and geopotential height ($m$) at 500hPa and (b) potential temperature ($K$) and winds ($m/s$) at 950hPa. Identical plots for the 26th of September 2012 at 00UTC are given as (c) and (d).

In south-eastern France, these HPEs develop principally associated with a large upper-level trough over the North Atlantic which brings southerly low-level marine flows towards Mediterranean coastlines. These flows are laden with moisture as the sea surface temperature during the autumn months remains greater than the temperature of the surrounding land basins. When heavy rainfall accumulations are observed on the foothills of the Cévennes, deep convection is more likely to be triggered by the orography. When heavy rainfall accumulations are observed on the plains or the sea, other mechanisms of convection triggering and sustainment are suggested, such as low-level convergence or an evaporative cold pool (Bresson et al.,2012, Ducrocq et al.,2008).

Numerical weather prediction (NWP) of convective rainfall events has improved in recent years due to advances in computing power. NWP models can now run at mesoscale resolutions and thus explicitly resolve the dynamics of mesoscale convective systems. However, despite this progress, limitations still apply due to the involvement of many multi-scale processes, the quick propagation of initial errors throughout the forecasting domain and the complexity in correctly simulating deep convective processes. Walser et al. (2004) and Hohenegger and Schär (2007) have investigated these issues. Walser et al. (2004) argued that the development of convective cells become increasingly difficult to predict at decreasing scales due to chaotic aspects of certain convective processes. They also show that the growth of small-scale uncertainties and nonlinear interactions between atmospheric processes can quickly disrupt predictability. Hohenegger and Schär (2007) demonstrated that initial

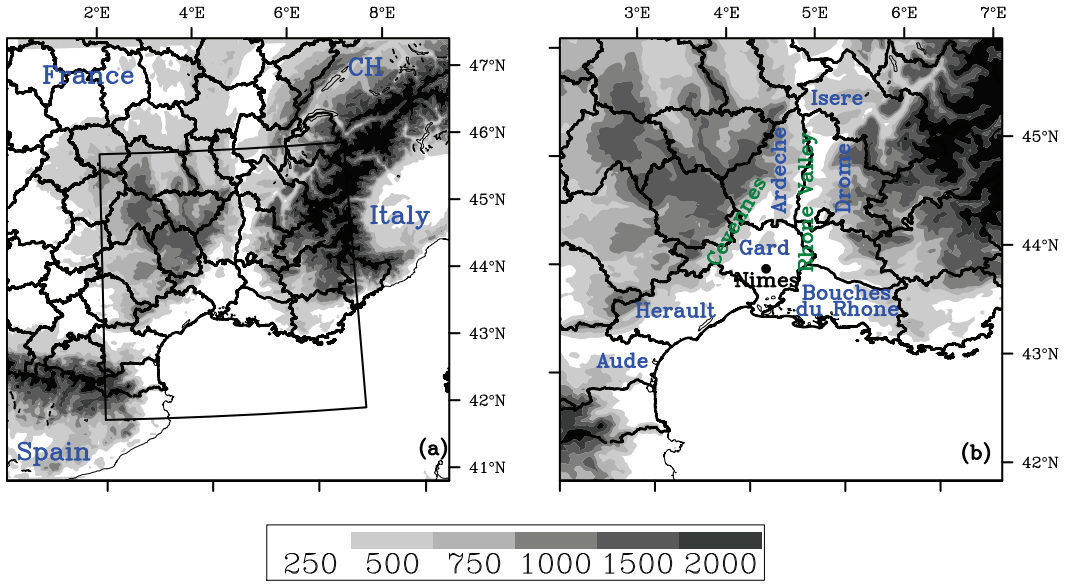


**Fig. 2.** (a) Map of the domain of southern France used for the simulations. The area under the solid line, referred to as the target area in the text, is enlarged in (b). All simulation statistics are performed over the domain in (b). Shading represents altitudes over 250 m. Geographical names and French administrative regions are recalled, in particular 7 *départements* of the southern France region which are given in blue. Two important geographical features, the Cévennes mountain ranges and the Rhône Valley, are indicated in green. The location of the Nîmes sounding is also given for reference.

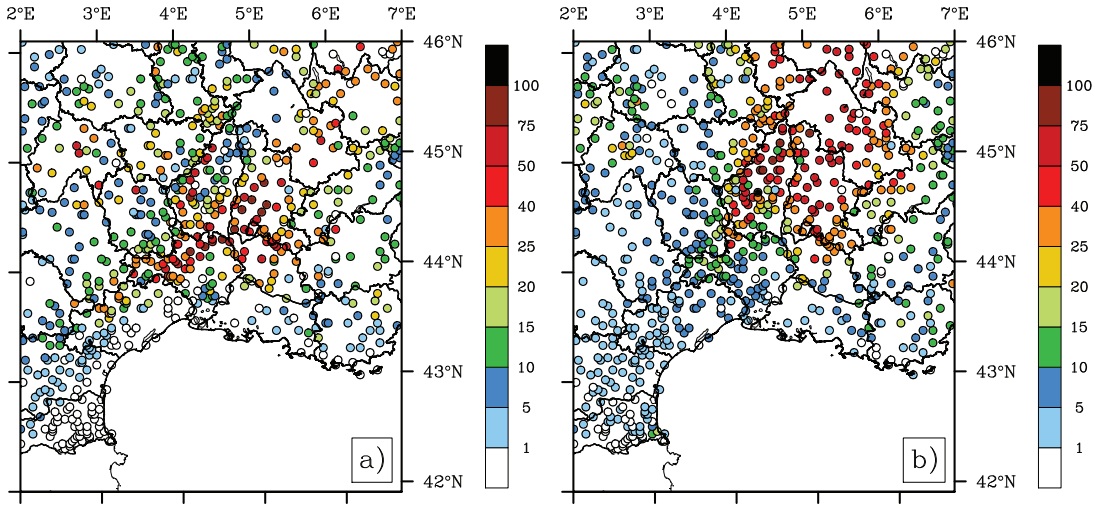


**Fig. 3.** The rainfall amounts (in mm) observed at Météo France stations between 18UTC on the 23rd of September and 18UTC on the 24th of September (a) and between 00UTC on the 26th of September and 00UTC on the 27th of September (b).

perturbations can disperse throughout the entire forecasting domain within a couple of hours, becoming amplified at far remote locations. Leoncini et al. (2010) suggested that the growth of the perturbation is weakly sensitive to the characteristics of the initial perturbation and that a similar value is reached at saturation independent of the amplitude of the perturbation.

Ensemble prediction systems (EPSs) have been put forward as a suitable strategy for overcoming predictability limitations (Houtekamer et al. (1996), Fritsch and Carbone (2004)). They give the probability of an event occurring by starting from a set of perturbed scenarios which represent the inherent uncertainties in the initial atmospheric state and in model parameterisations. Knowing which uncertainties should be accounted for in the ensemble design is a challenge and depends on the biases of the computational model and on the situation under examination. Ducrocq et al. (2008) showed that for HPEs in the south of France the microphysical processes were important factors which can control the stationarity of a mesoscale convective system (MCS). An accurate description of these processes is thus imperative. As they occur at sub-grid resolutions, they must be parameterised, which introduces a level of uncertainty in their representation. Many studies have attempted to examine the issues related to physical parameterisation uncertainties. Houtekamer et al. (1996), Buizza et al. (1999) and Stensrud et al. (2000) were some of the first to construct ensemble simulations using perturbed physical processes. Different methodologies have been employed, ranging from the use of different physical parameterisation schemes to stochastic perturbations applied upon the time tendencies of physical processes. More recently, Clark et al. (2011), Bouttier et al. (2012), Fresnay et al. (2012), Leoncini et al. (2013) and Hally et al. (2013) constructed convection-permitting short-range ensembles. The existence of such a breath of ensemble methodologies demonstrates that the most suitable approach remains open to debate, as no one methodology is found to be superior to the others.

Increases in model resolution have also brought to light the uncertainties associated with the parameterisation of boundary layer turbulence (Bryan et al. (2003), Fiori et al. (2011)). The rainfall field and the evolution of convective systems have been shown to be sensitive to its representation (Fiori et al. (2009), Wisse and de Arellano (2004)). Wyngaard (2004) and Honnert et al. (2011) also demonstrated that at a kilometric resolution, the use of 1D turbulence closure methods is questionable, while the formulation used in Large Eddy Simulations (LES) is not appropriate.

The present work uses the methodology described in Hally et al. (2013) and inspired by the previous works of Buizza et al. (1999) and Fresnay et al. (2012). These studies described ensemble simulations using stochastic perturbations upon the physical processes. Hally et al. (2013) and Fresnay et al. (2012) concentrated on errors associated to the boundary layer turbulence and warm microphysical processes. They investigated the possible use of ensembles containing perturbations upon these processes in the forecasting of HPEs in the Mediterranean region. The aim of the present study is to extend this methodology to include perturbations upon the cold microphysical processes, which can also have an impact upon convective storm development (Gilmore et al. (2004), Richard et al. (2003), Lascaux et al. (2006)). Secondly, the sensitivity of the simulated rainfall field to perturbations upon the physical processes is compared to the sensitivity introduced by modifying the initial (IC) and boundary (BC) conditions. Vié et al. (2011) and citetVie2012 demonstrated that Mediterranean HPEs are quite sensitive to the IC and BC employed and also suggested that the rainfall development displays a more important level of sensitivity to errors in the IC and BC than to errors in the physical parameterisations. This hypothesis will also be scrutinised within the scope of this study.

The layout of the paper is as follows: an introduction of the chosen case studies, the reasons for their selection and the large-scale atmospheric conditions under which they developed are described in Sect. 2, along with a description of the model set-up and an explanation of the configuration of the different ensembles. Sect. 3 presents the results of the physical perturbation and IC and BC perturbation ensembles for each case study. A comparison and discussion of the level of dispersion and the sensitivity of the rainfall field to the different perturbations is given in Sect. 4. Summaries and conclusions of the paper's main results are outlined in Sect. 5.

## 2 Description of cases, model set-up and configuration of ensembles

### 2.1 Description of cases

The two heavy rainfall episodes that were chosen for this study are HyMeX IOP6 and IOP7a which occurred on the 24th and 26th of September 2012 respectively. Both were extensively measured and observed at the time and represent two of the most significant rainfall episodes to have taken place within France during the HyMeX SOP1 campaign.

#### 2.1.1 IOP6

On the evening of the 23rd of September 2012, an upper-level trough extended in over western Europe (see Fig. 1(a)). This was associated to a low pressure system which was situated to the north-west of Ireland and led to convectively inducive low-level conditions. Surface winds from the south-west brought moist air sweeping in from the Mediterranean as shown by the plots of 10m wind and potential temperature at 950hPa in Fig. 1(b). These conditions instigated the development of an intense and fast moving convective line which caused approximately 100mm rainfall in the 24 h period between 00UTC on the 24th and 00UTC on the 25th. Most of

the precipitation fell during the 6 h window between 00UTC and 06UTC on the 24th with intensities of up to 50 or 60mm per hour been observed. The heaviest rainfall was organised in a south-west to north-easterly line extending from the northern Gard department into the Drôme department (see Fig. 2 for location of important geographical features and French departments). Soundings taken at the Nîmes station gave a CAPE value of $57 Jkg^{-1}$ at 00UTC on the 24th.

#### 2.1.2 IOP7a

In the early hours of the 26th of September, the low pressure system had propagated eastwards and was now centred over the British Isles (see Fig. 1(c)). The upper-level trough deepened and began to edge its way in over France as the day progressed. This brought moderate to strong south to south-easterly flow in over the southern regions of France. These winds were laden with warm moist air, picked up as they passed over the relatively warm Mediterranean Sea (Fig. 1(d)). This led to the development of a mesoscale convective system in the early morning over the Ardèche and Gard regions as the warm unstable air converged. A cold front associated to the low pressure system further to the north approached the area during the afternoon, merged with the convective system and moved eastwards as evening arrived. Upwards of 100mm of rain was observed during the 24 h period between 00UTC on the 26th and 00UTC on the 27th. The majority of the rain fell over the Ardèche department but the Drôme also experienced accumulations of up to 75mm in 24 h. The Nîmes sounding taken at 12UTC on the 26th gave a CAPE value of $109 Jkg^{-1}$.

### 2.2 Model set-up

The French research model Meso-NH (Mesoscale Non-Hydrostatic model, Lafore et al. (1998), http://mesonh.aero.obs-mip.fr/mesonh) was used to conduct the simulations presented in this study. Meso-NH was developed jointly by the Laboratoire d'Aérologie (LA) and the Centre National de Recherches Météorologiques (CNRM) and it shares the same set of physical parameterisations as the operational model of Météo-France, AROME. The turbulence scheme follows the work of Cuxart et al. (2000) while the radiation fluxes are calculated using the Rapid Radiative Transfer Model (Mlawer et al. (1997)). Shallow convection is parameterised according to Pergaud et al. (2009) while for the purposes of this study the deep convection scheme was deactivated as the simulations are performed at a convection-resolving resolution. Six water species (vapour, cloud water, rainwater, primary ice, snow aggregates and graupel) are prognosis variables whose equations are managed by the ICE3 bulk microphysical scheme of Pinty and Jabouille (17-21 August 1998). The exchanges of energy at the surface are represented according to four possible surface types (natural surfaces, urban areas, oceans and lakes). The ISBA (Interactions Soil-Biosphere-Atmosphere scheme Noilhan and Mafhouf (1996)) is used for natural land surfaces.

The grid spacing used for the simulations here presented is that of the Météo-France operational forecasting model AROME, or 2.5km. The simulated area covers a 288x288 point domain located over southern France and the north-western Mediterranean (see Fig. 2 for description of domain). All of the simulations described were performed over 24 h periods. For IOP6, the maximum observed rainfall occurred at 02UTC on the 24th. In order to avoid the influence of spin-up errors, simulations for this case were initialised at 18UTC on the 23rd of September. For IOP7a, the maximum observed rainfall occurred at 08UTC on the 26th of September. The simulations were initialised at 00UTC on the 26th allowing sufficient time before the onset of convection and for the dissipation of model spin-up errors.

### 2.3 Configuration of ensembles

Four ensembles were constructed for each convective episode, the characteristics and details of which are given in Tables 1 and 2. The first ensemble (which will be labelled ICBC(6)(7a), with the 6 and 7a representing either IOP6 or IOP7a) contained 4 members. Each of the members was given a different set of initial (IC) and boundary conditions (BC) derived from the ECMWF/IFS and Météo France/ARPEGE, AROME and AROME-WMED analysis. The AROME and AROME-WMED analysis files are available every 3 h compared to every 6 h for the ARPEGE and ECMWF outputs. The AROME and AROME-WMED files are available at the same 2.5km resolution that was used within this study. AROME covers the region of Metropolitan France with further details of the model available in Seity et al. (2011). AROME-WMED, designed especially for HyMeX, is similar to AROME but takes in a larger geographical region including the western half of the Mediterranean Sea. ARPEGE runs at a 10.5km resolution over France while the horizontal resolution of the ECMWF mesh size is approximately 16km. No intermediary downscaling step was performed between these resolutions and that of the 2.5km resolution employed by the Meso-NH model. Each member was run over the periods described in section 2.2.

The second ensemble WA(6)(7a), the 6 and 7a again representing either IOP6 or IOP7a, was constructed of 11 members, 10 perturbed members and one control (CTRL) member. The most skillful member of the ICBC(6)(7a) ensemble was used as the CTRL member. Here the definition of skillful is the ensemble member which modelled the observed rainfall in the most realistic and statistically satisfying manner. Simple statistical tests such as correlation with observed values, standard deviation and root-mean squared error were used to determine this statistical skill. For the other 10 members, the time tendencies of the warm rain processes of the ICE3 microphysical scheme were perturbed by a random fac-

| Ensemble name | Case study | ICBC perturbations | Warm perts. | Warm and Cold perts. | Warm, Cold and turbulent perts. |
|---|---|---|---|---|---|
| ICBC6 | IOP6 | ✓ | | | |
| ICBC7a | IOP7a | ✓ | | | |
| WA6 | IOP6 | | ✓ | | |
| WC6 | IOP6 | | ✓ | ✓ | |
| MT6 | IOP6 | | ✓ | ✓ | ✓ |
| WA7a | IOP7a | | ✓ | | |
| WC7a | IOP7a | | ✓ | ✓ | |
| MT7a | IOP7a | | ✓ | ✓ | ✓ |

**Table 1.** Characteristics of the different ensembles.

| Processes perturbed | WA ensemble | WC ensemble |
|---|---|---|
| Autoconversion of cloud drops to raindrops | ✓ | ✓ |
| Accretion of cloud droplets by raindrops | ✓ | ✓ |
| Evaporation of raindrops | ✓ | ✓ |
| Autoconversion of ice particles to snow particles | | ✓ |
| Vapour deposition on snow and graupel | | ✓ |
| Light and heavy riming of snow aggregates and graupel | | ✓ |
| Accretion of rain and aggregates | | ✓ |
| Dry and wet growth of graupel | | ✓ |
| Melting of snow aggregates and graupel | | ✓ |

**Table 2.** Processes perturbed in the 6(7a)WA and 6(7a)WC ensembles.

tor ranging between 0.5 and 1.5. This random factor was generated in the same manner as in Hally et al. (2013) and Fresnay et al. (2012). Each random factor multiplied simultaneously the sources and sinks of a given microphysical process to ensure mass conversation was met. For the third ensemble (WC(6)(7a)), perturbations were performed upon the cold microphysical processes as well as the warm processes. The ensemble had the same CTRL simulation as the WA ensemble and also contained 10 perturbed members. A unique random factor was generated for each cold process. The fourth and final ensemble (MT(6)(7a)) consisted in adding perturbations to the turbulent time tendencies, while simultaneously maintaining the perturbations upon the warm and cold microphysical processes. Perturbations were introduced upon the turbulent tendencies in the same manner as was done for the warm and cold processes and as is also described in Hally et al. (2013). As for the WA(6)(7a) and WC(6)(7a) ensembles, the ensemble consisted of a CTRL member and 10 perturbed members.

## 3 Ensemble simulations

### 3.1 IOP6

#### 3.1.1 ICBC ensemble

The simulated rainfall for each member of the ICBC6 ensemble is shown in Fig. 4 with the corresponding observed rainfall amounts displayed in Fig. 3 (a). The signal of the convective system can be seen forming a south-west to north-easterly line from the Gard department into the Ardèche department. The AROME forced simulation (Fig. 4 (a)) simulates the heaviest rainfall to the north of the convective line over the ridges of the Cévennes mountain ranges. Over the areas of the observed maximums (upwards of 75mm) simulated accumulations only reached values of between 20 and 40mm. This is however the most accurate representation of the convective system of all the four members. The AROME-WMED member simulates the precipitation maxima over the Cévennes ridges, as in the AROME member, but also produces rainfall to the north-east of the convective line over the central Ardèche. The localisation of the convective line is almost completely missed by the ECMWF simulation as it places a large rainfall maximum to the north-east of the Cévennes mountains. The ARPEGE member produces no discernible maximum but does succeed in finding the north-eastern tail of the convective line over the Ardèche albeit with

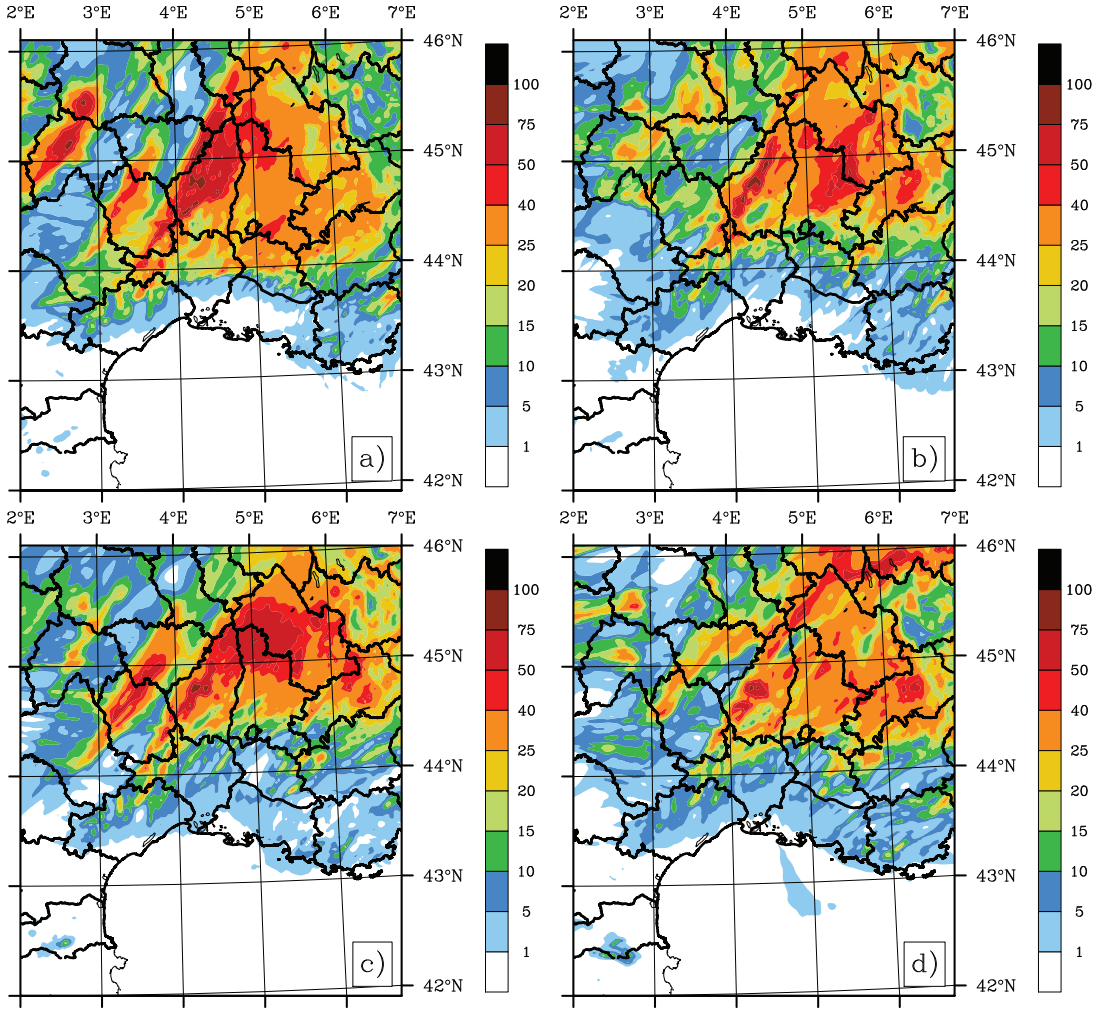


**Fig. 4.** The rainfall amounts (in mm) of the AROME (a), AROME-WMED (b), ECMWF (c) and ARPEGE (d) members of the ICBC6 ensemble.

less accumulated rainfall than was observed. Overall, 3 out of the 4 sets of initial and boundary conditions (AROME, AROME-WMED, ARPEGE) succeed in localising the rainfall over the south-western Ardèche but fail to simulate the correct intensities. The AROME member most accurately captured the convective line over the western and northern Gard, while all other members failed to simulate it correctly.

Fig. 5 shows a time series of the hourly accumulated rainfall averaged over the model domain. The peak in observed precipitation occurred at 02UTC. This peak is missed by all simulations, regardless of their initial and boundary conditions The AROME simulation is closest in terms of timing and averaged rainfall amounts with a difference of 3 h between the simulated and observed maxima. The AROME-WMED, ECMWF and ARPEGE members of the ensemble present less accurate representations of the observed maximum but simulate more accurately the second peak at 07UTC.

The Taylor diagram for the ICBC ensemble is presented in Fig. 6. The AROME member presents a spatial correlation of 0.45 with the observations, as do the AROME-WMED and ARPEGE simulations. The AROME member gives a normalised standard deviation of almost 1. Given that the normalised standard deviation is a ratio of observed versus simulated variability, one could say that the AROME simulation describes most accurately the level of observed dispersion. The AROME-WMED and ARPEGE members give lower standard deviations illustrating their weaker degree of dispersion. The root-mean-squared-error (RMSE), shown on the Taylor diagram as the distance between the model point and the REF point, illustrates that the AROME-WMED and ARPEGE members are slightly more accurate than the AROME member. However, the improved spatial correlation, normalised standard deviation and the fact that

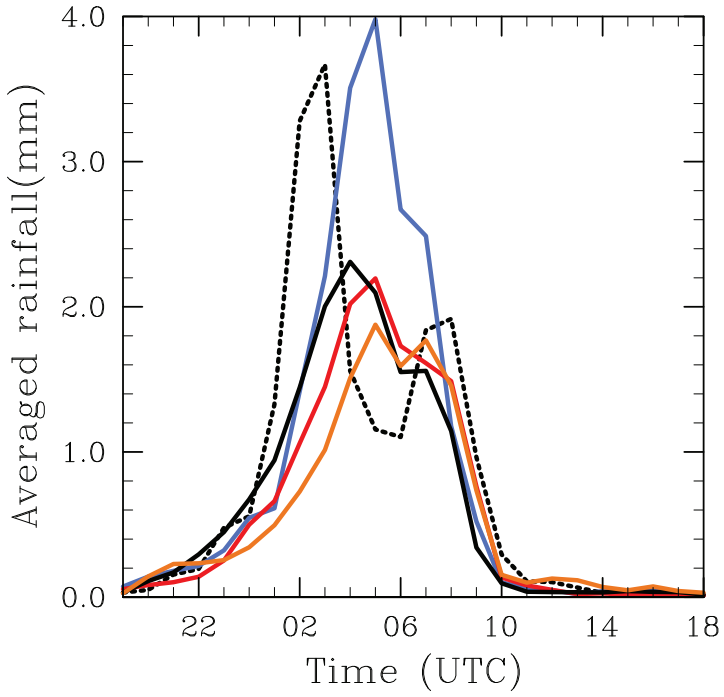


**Fig. 5.** Temporal evolution of the spatially-averaged hourly accumulation for each member of the ICBC6 ensemble. The AROME member appears in blue, the AROME-WMED member in red, the ECMWF member in black and the ARPEGE member in orange. The black dotted line represents the evolution of the observed rainfall.

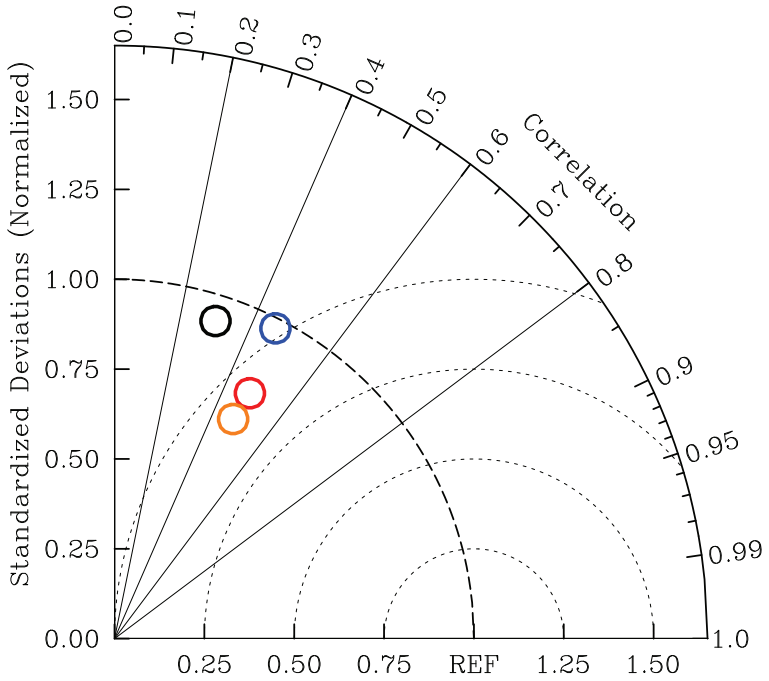


**Fig. 6.** Taylor diagram for the ICBC6 ensemble showing the spatial correlation, standard deviation and RMSE of the simulated accumulated rainfall with the observed rainfall for the AROME (blue circle), AROME-WMED (red circle), ECMWF (black circle) and ARPEGE (orange circle) members of the ICBC6 ensemble.

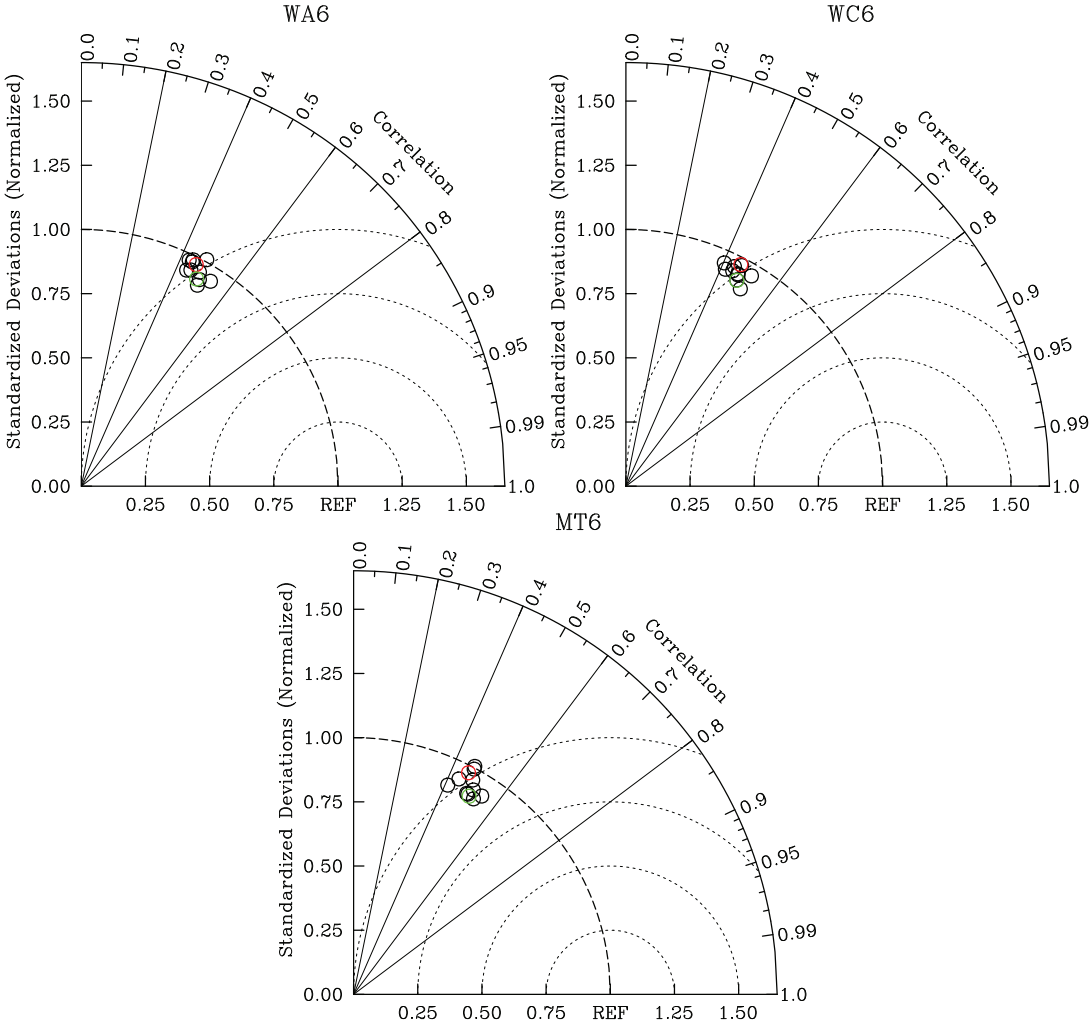


**Fig. 7.** Same as Fig. 6 except for the WA6, WC6 and MT6 ensembles. The CTRL simulation is given in red, the ensemble members in black and the ensemble mean in green.

the AROME member captures most accurately the observed peak were judged to be more important measures of statistical skill.

Concluding from Fig. 4, Fig. 5 and Fig. 6, a hierarchy of forecasting accuracy is deduced for this case. The AROME simulation is deemed the most accurate at representing the observed rainfall pattern as it was the only member of the ensemble to simulate the amplitude of the observed peak. The AROME member also gave the highest spatial correlation and was quite accurate in forecasting the observed rainfall variability. The AROME-WMED and ARPEGE rainfall representations were similar but the AROME-WMED member simulated more accurately the rainfall intensities. The ECMWF member gave the least realistic rainfall localisation and evolution, as it completely missed the convective activity in the northern Gard.

### 3.1.2 Physical process ensembles

The AROME simulation from the ICBC6 was thus chosen as the CTRL simulation to which the members of the WA6, WC6 and MT6 ensembles were compared. The Taylor diagram for each of these ensembles is presented in Fig. 7. Examining the diagram for the WA6 ensemble, some members show increased spatial correlation with the observations compared to the CTRL simulation. The most correlated member now has a correlation of 0.55 compared to 0.45 for the CTRL. Spread between the ensemble members is more remarkable in the differing spatial correlation values than in the normalised standard deviation values as most members retain a value of 1.0. This would suggest that the perturbations impact more strongly upon the localisation of the simulated rainfall rather than upon the intensity. In comparison with WA6, WC6 has more members with lower spatial cor-

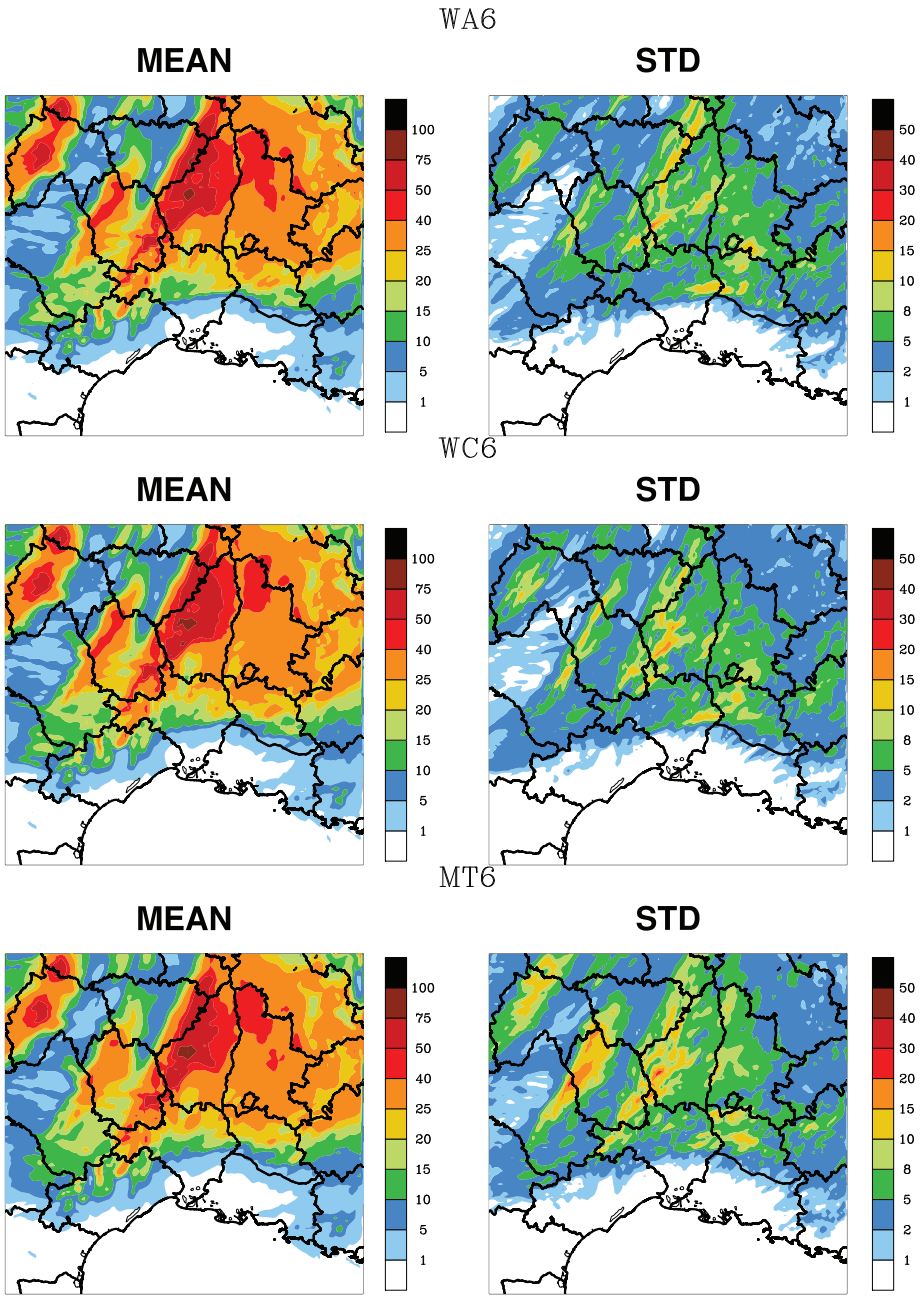


**Fig. 8.** Mean and standard deviation of the 24 h accumulated rainfall for the WA6 (top), WC6 (middle) and MT6 (bottom) ensembles.

relation. There is little increase in spread between the members of the WC6 ensemble suggesting that the sensitivity of the surface rainfall field to these processes is small. A comparison of the WA6 and MT6 ensembles shows that adding in perturbations to the turbulent time tendencies does increase dispersion. The range of spatial correlation values for the members of the MT6 ensemble extends from 0.4 to 0.6 with the normalised standard deviations varying between 0.75 and 1.0. Thus simultaneously perturbing the cold and warm microphysical and turbulent processes impacts upon the spatial localisation and intensity of the surface rainfall field.

Fig. 8 shows the mean and standard deviation from the 24 h accumulated surface rainfall for each of the WA6, WC6 and MT6 ensembles. The standard deviation signal for the WA6 and WC6 ensembles are similarly weak. Some spread is seen in the eastern Gard and to the east of the Cévennes mountain ridges where the heaviest rain was simulated. Little dispersion is seen over the mountain ridges which indicates that in these areas, the rainfall field is very weakly controlled by the microphysical processes. The standard deviation signal for the MT6 ensemble shows a larger degree of dispersion, especially in the south-western Ardèche where strong convective activity was observed. This increase in dispersion for the MT6 ensemble compared to the WA6 and WC6 ensembles would indicate that the rainfall field is more sensitive to boundary layer turbulence perturbations than to perturbations upon the microphysical processes. Compared to the WA6 and WC6 ensembles, MT6 shows increased dispersion over the mountainous ridges. However, like WA6 and WC6, the strongest standard deviation values are located east of the Cévennes.

### 3.2 IOP7a

#### 3.2.1 ICBC ensemble

The simulated rainfall for each member of the ICBC7a ensemble is illustrated in Fig. 9 with the corresponding observations being displayed in Fig. 3 (b). In contrast with the convective line seen in IOP6, the precipitation of IOP7a fell mainly over the mountainous regions in the Cévennes area, increasing the role of the orography in the evolution and development of the convective system. As mentioned in the case description, this convective line merged with a cold front which arrived from the west during the afternoon of the 26th and then propagated eastwards, which led to a second rainfall maximum concentrated mainly over the Ardèche and Isère departments. The model performs much more accurately for this case than for the IOP6 with all sets of initial and boundary conditions capturing the convective line. The AROME member (Fig. 9 (a)) simulates quite well the rainfall over the mountainous areas with accumulations of between 75 and 100mm corresponding well with the observed values. The AROME-WMED member (Fig. 9 (b)) gives the least accurate representation as it shifts the convective line eastwards away from the mountainous regions. The simulated rainfall values do not compare as well as the AROME member with the observed values as maxima remained between 50 and 75mm. An investigation of the state of the large-scale dynamics present in the initial conditions for this case (not shown) indicate that the aforementioned cold front arrived in over the target area too early in the AROME-WMED conditions, thus preventing the convective system from fully developing and pushing the heaviest of the rainfall eastwards. The ECMWF member also performs well in localising the rainfall pattern but tends to over-forecast the rainfall amounts, with a simulated maximum of 194mm versus an observed maximum of 100mm. The ARPEGE member succeeds in simulating the rainfall pattern over the mountain ranges but in contrast with the ECMWF member the simulated values were less than what was observed.

The temporal evolution of the instantaneous rainfall for the ICBC7a ensemble is presented in Fig. 10. In general, all of the ensemble members succeed in reproducing the observed rainfall evolution. As for the ICBC6 ensemble, the AROME member gives the most accurate description of the evolution, successfully capturing both the precipitation peak at 8 h after initialisation time or 08UTC and the peak at 17 h after initialisation time or 17UTC. The over-forecasting in the ECMWF simulation is not as clear on this plot but the simulated rainfall does exceed the observed one between 10 and 13UTC. The AROME-WMED member produces a very weak signal for the first observed peak at 08UTC which corresponds with its inaccuracy in forecasting the most convectively active period of the system. The weak ARPEGE accumulations are also easily visible on this plot.

The Taylor diagram in Fig. 11 confirms the increase in forecasting skill of the different sets of conditions for this case compared to IOP6. Both the AROME and ECMWF members present a spatial correlation of 0.8. The ECMWF member gives a normalised standard deviation value of almost 1.25 indicating the over-forecasting of the rainfall compared to the observed values. Like the IOP6 case, the AROME member gives a normalised standard deviation value close to 1.0 demonstrating that of the four sets of conditions, it gave the most realistic description of the observed variability. The AROME-WMED member shows the lowest spatial correlation owing largely to its misplacement of the convective system. The ARPEGE member's normalised standard deviation was close to 0.5 indicating this simulation's inability to model the observed variability.

These plots show that as for the previous case of the IOP6, a hierarchy of forecasting accuracy is present. The AROME forced member of the ensemble gave the most accurate representation of the rainfall field, resulting in a high spatial correlation and a favourable normalised standard deviation value. Also, its temporal evolution followed the observed evolution quite adeptly. The ECMWF simulation gave a good spatial localisation of the convective system but gives a slight overforecast of the rainfall intensity. The AROME-WMED and

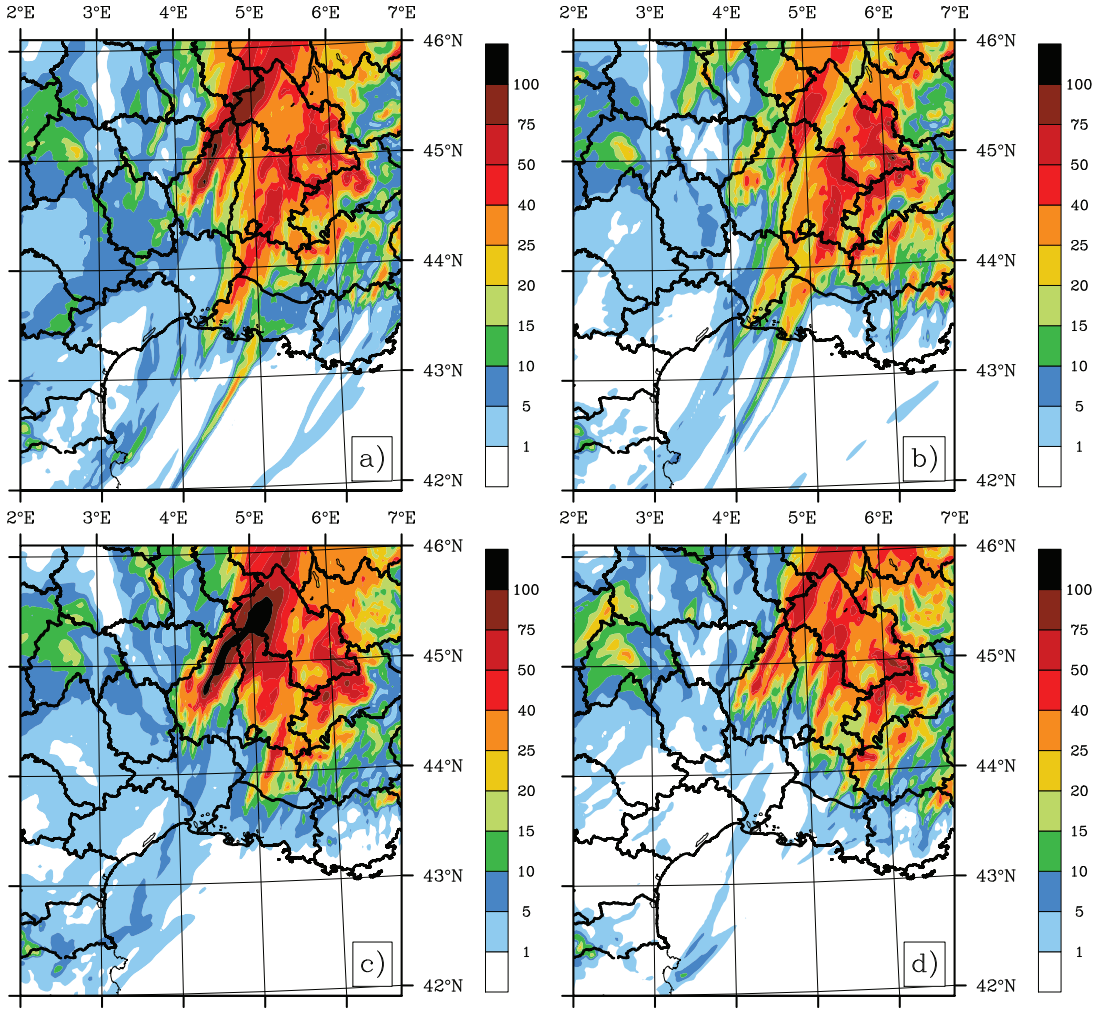


**Fig. 9.** The rainfall amounts (in mm) of the AROME (a), AROME-WMED (b), ECMWF (c) and ARPEGE (d) members of the ICBC7a ensemble.

ARPEGE members gave weaker rainfall accumulations with the ARPEGE member slightly out-performing the AROME-WMED member in terms of spatial localisation.

### 3.2.2 Physical process ensembles

The ensembles WA7a, WC7a and MT7a were constructed using the AROME member of the ICBC7 ensemble as a CTRL. The Taylor diagram for each ensemble is shown in Fig. 12. Very little dispersion is produced between the members of the WA7a ensemble. All members maintain the spatial correlation of 0.8 that the CTRL simulation presented with slight differences appearing in the standard deviation values. This lack of spread in the members' representation of the rainfall underlines the small role played by the microphysical processes for cases where the precipitation falls mainly in mountainous areas. Adding cold process perturbations to those of the warm processes does little to change the ensemble spread as the Taylor diagram for WC7a illustrates. Examining the Taylor diagram for MT7a, there is a significant increase in dispersion between the members compared to the WA7a and WC7a ensembles. The correlation now ranges from 0.7 to approximately 0.85. The normalised standard deviation values are also much more dispersed than for the WA7a and WC7a ensembles.

The mean and standard deviation plots for the rainfall field are given in Fig. 13. These plots reinforce the results gleamed from the Taylor diagrams. Little if any deviation from the mean is produced by the WA7a and WC7a ensembles. Comparatively the MT7a ensemble displays a much stronger standard deviation signal. This is most clearly in evidence in the northern Ardèche region where some of the heaviest rain fell. Deviation from the mean can also be seen to the south and further eastwards where the less convectively intense rainfall occurred. This ensemble even presents some dispersion

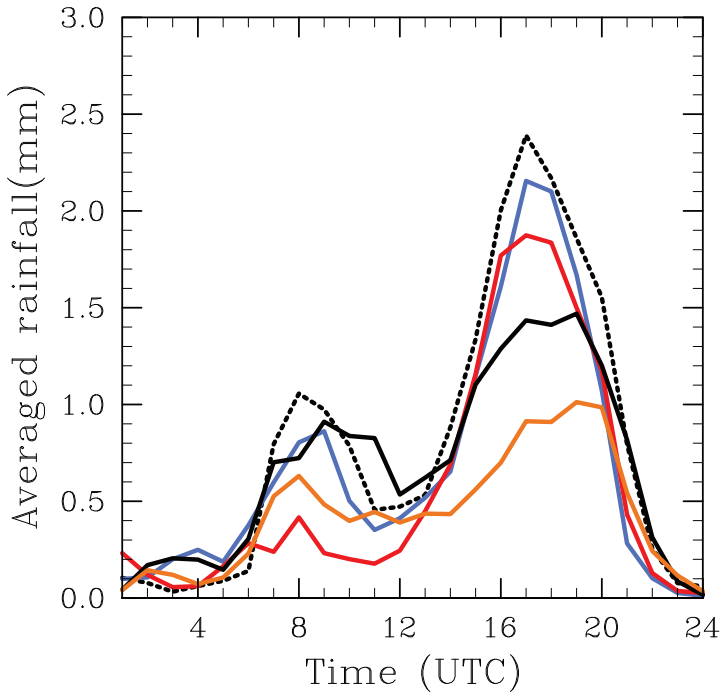


**Fig. 10.** Temporal evolution of the spatially-averaged hourly accumulation of the rainfall field for each member of the ICBC7a ensemble. The AROME member appears in blue, the AROME-WMED member in red, the ECMWF member in black and the ARPEGE member in orange. The black dotted line represents the evolution of the observed rainfall field.

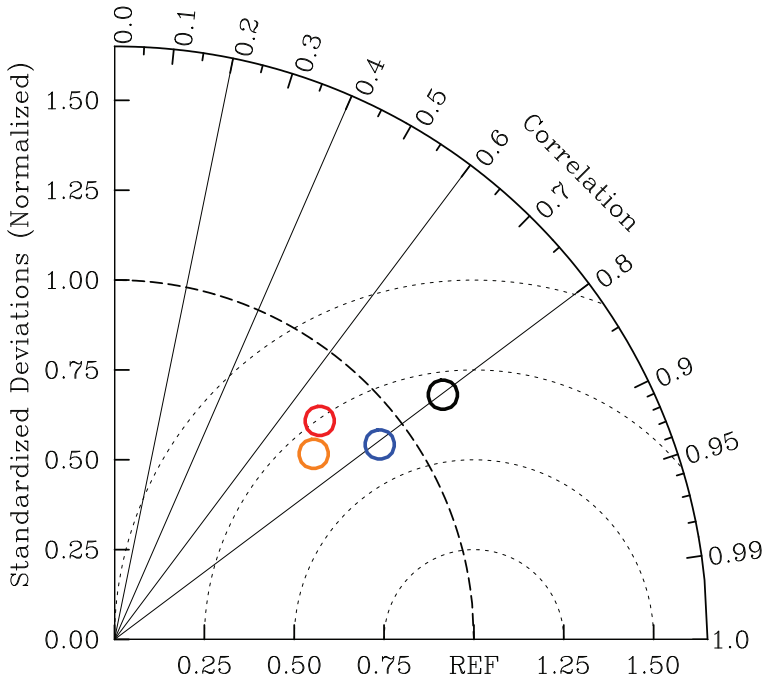


**Fig. 11.** 24 h Taylor diagram for the ICBC6 ensemble showing the spatial correlation, standard deviation and RMSE of the simulated rainfall with the observed rainfall for the AROME (blue circle), AROME-WMED (red circle), ECMWF (black circle) and ARPEGE (orange circle) members of the ICBC7a ensemble.

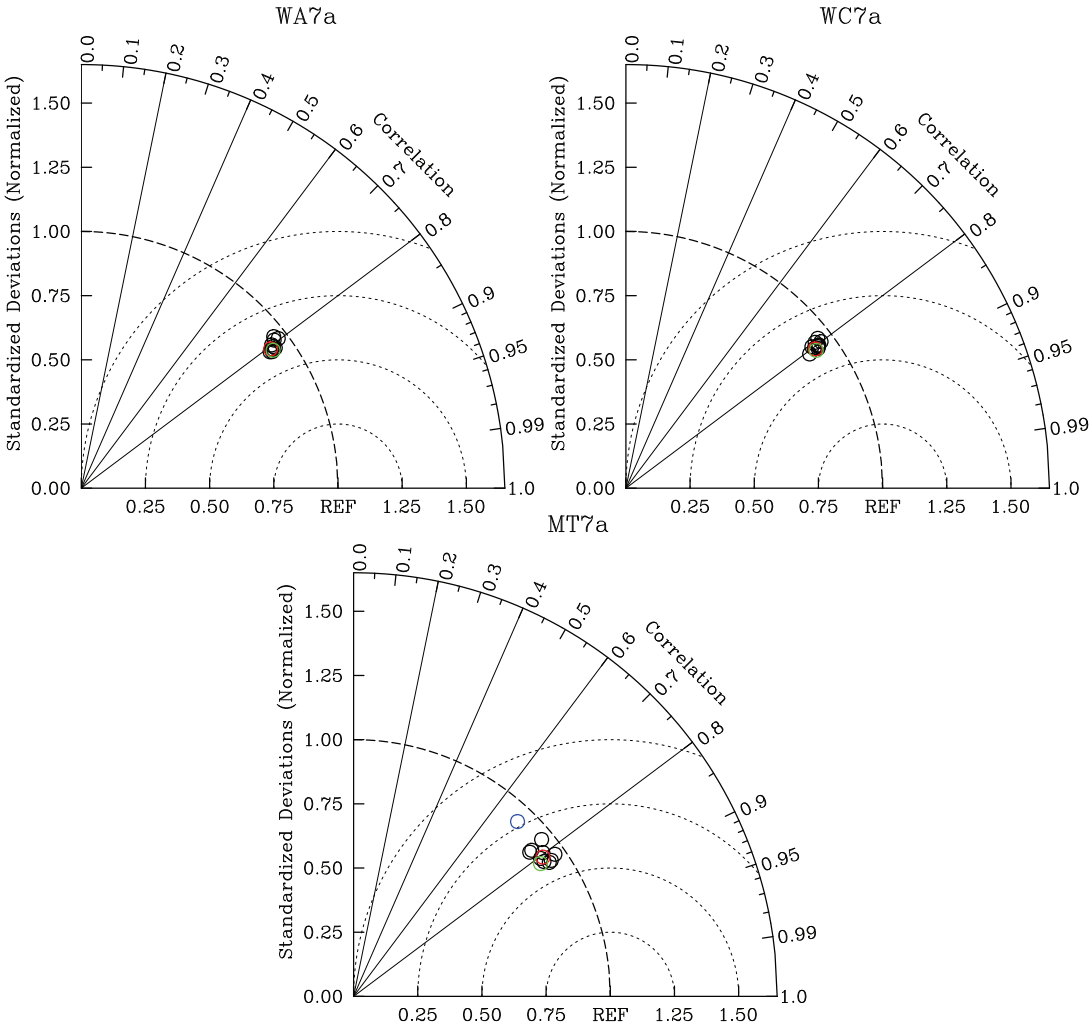


**Fig. 12.** 24 h Taylor diagram for the WA7a, WC7a and MT7a ensembles. The CTRL simulation is given in red, the ensemble members in black and the ensemble mean in green.

over the mountainous regions, although the most significant spread occurs just to the east of the Cévennes.

One member in particular (displayed in blue on the MT7a ensemble) separates itself quite distinctly from the other members. Investigating the perturbations introduced for this member shows that the value of the turbulent time tendencies was cut by 50%, the graupel melting process was at 80% of its original value while the evaporation process was decreased by 40%. The members' spatial correlation decreased from 0.8 to less than 0.7 between the WA7a and MT7a ensembles due to the effect of these perturbations. However, this change in spatial correlation was not observed between the WA7a and WC7a ensembles indicating that the turbulence perturbations were responsible for the modification in the simulated rainfall. Plots (not shown) illustrate that the turbulence perturbations change the interaction of the flow with the local orography, and thus displace the point of convective initiation. Vertical velocity plots (also not shown) indicate that the turbulence perturbations also led to weaker convective updrafts and thus weaker accumulated rainfall amounts. This may lead to the conclusion that such perturbation configurations should be avoided as they lead to a decrease in model skill. However, the set of perturbation coefficients employed for MT6 were identical. The member of MT6 which experienced blue member perturbations gives an increase in spatial correlation (not shown) between WC6 and MT6. This underlines the case dependency of these types of perturbation.

## 4 Sensitivity in the different ensembles

Comparisons between the dispersion induced by changing IC and BC and modifying the physical parameterisations are

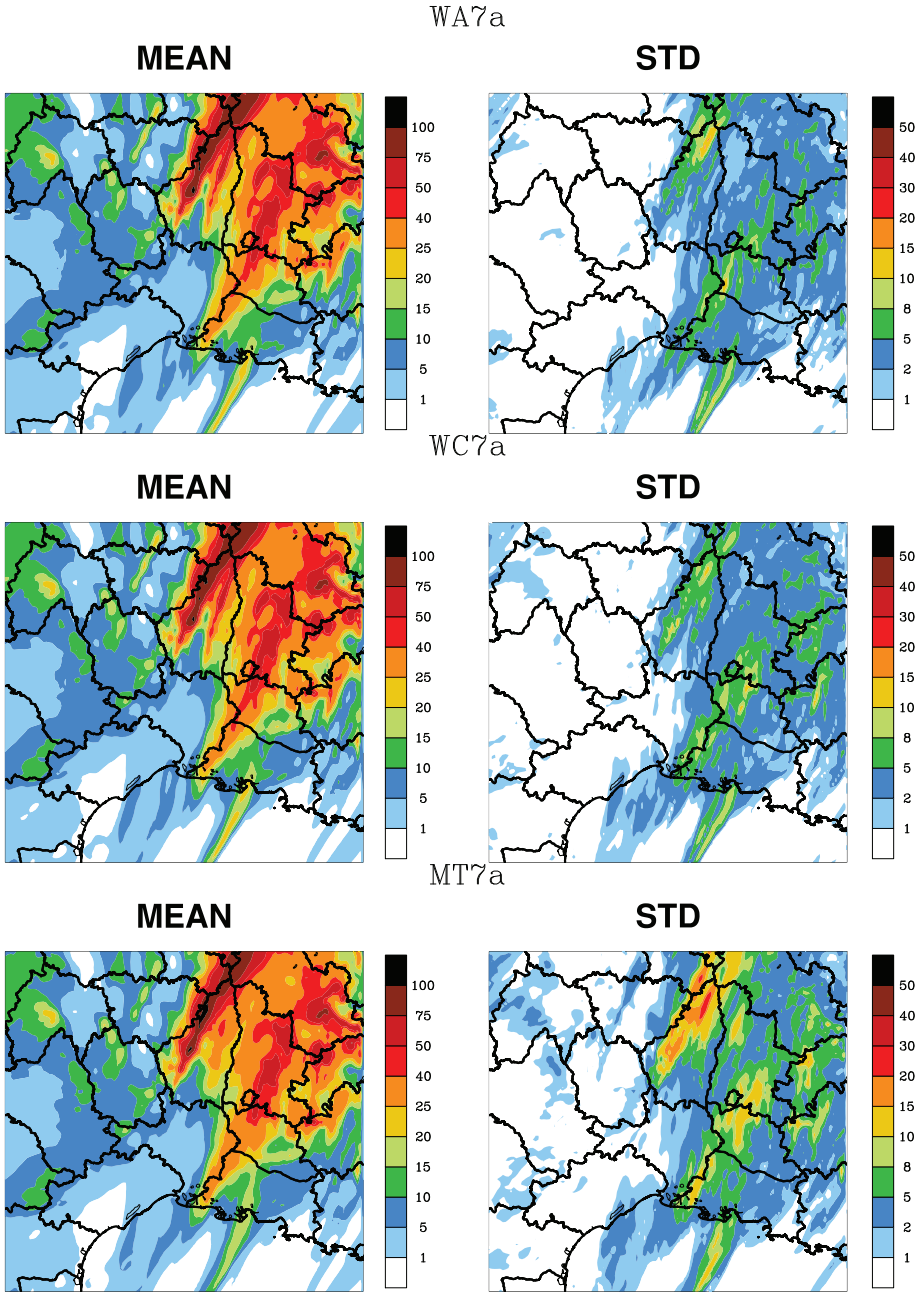


**Fig. 13.** The 24 h mean and standard deviation of the rainfall field for the WA7a (top), WC7a (middle) and MT7a (bottom) ensembles.

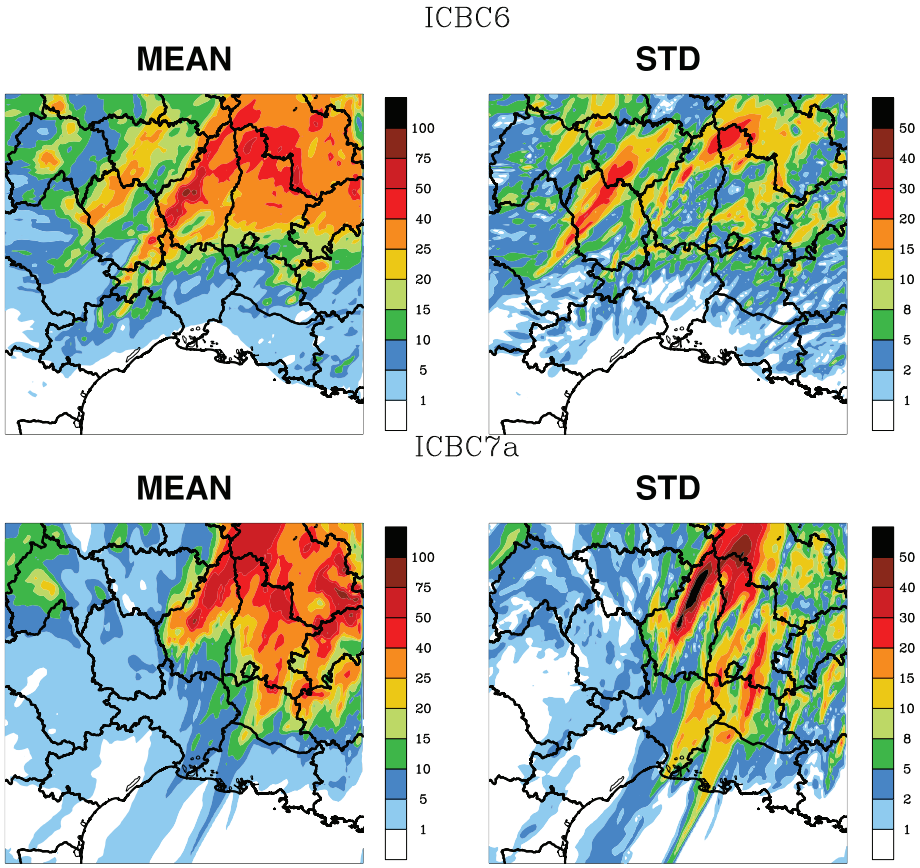


**Fig. 14.** The 24 h mean and standard deviation of the rainfall field for the ICBC6 (top) and ICBC7a (bottom) ensemble.

drawn from the Taylor diagrams in Fig. 6, Fig. 7, Fig. 11 and Fig. 12 and the mean and standard deviation of rainfall plots in Fig. 14, Fig. 8 and Fig. 13. Clearly there is a greater degree of dispersion for the WA6, WC6 and MT6 ensembles compared to the WA7a, WC7a and MT7a ensembles. This agrees with the results reported in Hally et al. (2013), Fresnay et al. (2012) and Stensrud et al. (2000) where the authors illustrate that sensitivity to perturbations upon physical processes is case dependent. Hally et al. (2013) demonstrated that the sensitivity of Mediterranean HPEs to physical perturbations is dependent upon the model skill and the strength of the low-level flow. IOP6 and IOP7a confirm this tendency.

Ensembles with changing IC and BC do not show this tendency. Examining the Taylor diagrams in Fig. 6 and Fig. 11 shows that both ensembles display similar levels of dispersion. The ICBC7a ensemble gives a larger range of standard deviation values, which is confirmed by the plots in Fig. 14, with the ICBC7a demonstrating a large deviation from the mean for the convective rainfall pattern. This contrasts to the weaker deviation exhibited by the ICBC6 ensemble over the convective rainfall region. This seems to suggest that the IC and BC were more important to the development of the convective rainfall in IOP7a than in IOP6.

For IOP6, the most dispersive physical ensemble, MT6, displays a degree of dispersion comparable to that of ICBC6. The mean and standard deviation plots in Fig. 14 and Fig. 8 underline this most evidently. However, the ICBC and physical process ensembles differ as to where the deviation from the mean is located. The MT6 ensemble shows a greater level of dispersion over the regions of convective rainfall compared to the ICBC6 ensemble, suggesting an enhanced role in the development of this rainfall pattern for the physical processes over the IC and BC. For IOP7a, the physical process ensembles display a lesser degree of dispersion compared to the ICBC ensemble. A comparison of the plots in Fig. 14 and Fig. 13 illustrates this quite clearly. Apart from the MT7a ensemble, the physical process ensembles do not demonstrate any significant deviation from the mean rainfall pattern. Contrastingly, the ICBC7a ensemble gives a large area of dispersion over the Ardèche, where the convective rainfall was observed, and also further to the east, where the stratiform peak occurred. This again underlines the more important role of the IC and BC conditions in the development of IOP7a compared to the physical processes. The patterns exhibited in these ensembles seem to suggest that when the model skill is low (low-level flow is moderate - IOP6), the

sensitivity of the rainfall pattern to physical and ICBC perturbations is comparable, but that when the model skill is high (low-level flow is strong - IOP7a), the rainfall pattern is more sensitive to ICBC perturbations.

## 5 Conclusion and perspectives

South-eastern France experiences heavy precipitation events (HPEs) during the months of September to November each year. These HPEs can lead to devastating flash-flood events causing economic damage and even loss of human life. IOP6 and IOP7a of the HyMeX SOP1 are two good examples of the meteorological conditions in which these events occur. IOP6 occurred in the presence of moderate to weak low-level flow from the south-east bringing moist air in over the cooler land basins. This led to the development of a convective rainfall event on the coastal plains which peaked at 02UTC. IOP7a occurred under the influence of a large upper-level trough to the west of the target area, which led to strong low-level flow from the south-east over the Mediterranean Sea. This moist flow was lifted into the atmosphere by local orography, triggering convective precipitation. A peak in convective precipitation was seen at 08UTC for this case. A second peak was observed at 17UTC, associated to a cold front which moved in over the target area during the afternoon of IOP7a.

An ensemble of simulations using different initial (IC) and boundary (BC) conditions was constructed for each of these cases with analysis files from the AROME, AROME-WMED, ECMWF and ARPEGE models. This ensemble aimed to uncover the most accurate control (CTRL) simulation for each of the cases and to measure the sensitivity to IC and BC modifications. Temporal evolution plots and simple statistical comparisons demonstrated that the level of dispersion induced in the surface rainfall by simultaneously changing the IC and BC was similar for both cases. A CTRL simulation with IC and BC from the analysis of the AROME forecasting model displayed the most realistic representation of the observed rainfall field for both cases.

Starting from this CTRL simulation, ensembles were constructed in order to represent sources of error inherent in the model parameterisations. Particular attention was paid to the microphysical and boundary layer turbulence processes with random perturbations introduced upon the parameterised time tendencies of these processes. For IOP6, an ensemble where solely the warm microphysical processes were perturbed led to moderate dispersion in the rainfall field. Little sensitivity was demonstrated when perturbations were added to the microphysical cold processes, however, introducing perturbations upon the turbulence time tendencies led to a more significant increase in dispersion, especially over regions where the most convective rainfall occurred. For IOP7a, the level of sensitivity to physical perturbations was less than that of IOP6. As for IOP6, the rainfall pattern displayed an increased sensitivity to perturbations upon the turbulent time tendencies than upon the microphysical tendencies.

Comparisons between the ICBC and physical process ensembles showed that for IOP6, the area of convective rainfall was less sensitive to modifications in the IC and BC than to perturbations upon the physical processes. This was not the case for IOP7a, where the rainfall pattern, convective and stratiform, demonstrated a much larger degree of sensitivity to changing IC and BC. These comparisons illustrate that for HPEs which have weak to moderate low-level flow and low model skill (IOP6), the level of dispersion introduced in the rainfall pattern by ICBC or physical process perturbations is comparable. Concurrently, when the HPE develops in the presence of strong low-level flow and high model skill (IOP7a), the level of dispersion related to ICBC modifications is greater.

The ensembles presented in this study indicate that the sensitivity to perturbations upon the physical processes and IC and BC is case dependent. The relative importance of each source of error depends on the nature of the rainfall pattern and on the atmospheric conditions in which the precipitation event develops. This confirms the results reported in the previous studies of Hally et al. (2013) and Fresnay et al. (2012). However, further work is needed to investigate the relative contribution of the IC and BC to the rainfall pattern for these types of HPEs.

Both cases presented within this study developed under strong synoptic-forcing, thus indicating a larger contribution from the atmospheric rather than the surface conditions. For weakly forced Mediterranean HPEs, the specific influence of surface conditions deserves further examination. This would highlight the importance of the surface processes to the development of the rainfall pattern and would thus permit the construction of ensemble simulations which directly target the error related to the representation of such processes (Lebeaupin et al. (2006), Barthlott and Kalthoff (2011)).

*Acknowledgements.* This study was carried out in the framework of the HyMeX and DRIHM projects. The authors acknowledge Météo France and the HyMeX database for supplying the observational data used within the study. Computational resources were allocated by Grand Equipement National de Calcul Intensif (GENCI project 2013010569) and calcul en Midi Pyrenees (CALMIP, project P1247).

## References

Barthlott, C. and Kalthoff, N.: A Numerical Sensitivity Study on the Impact of Soil Moisture on Convection-Related Parameters and Convective Precipitation over Complex Terrain, J. Atmos. Sci., 68, 2971–2987, 2011.

Bouttier, F., Vie, B., Nuissier, O., and Raynaud, L.: Impact of stochastic physics in a convection-permitting ensemble, Mon. Wea. Rev., 140, 3706–3721, 2012.

Bresson, E., Ducrocq, V., Nuissier, O., Ricard, D., and de Saint-Aubin, C.: Idealized numerical simulations of quasi-stationary convective systems over the Northwestern Mediterranean complex terrain, Quart. J. Roy. Meteor. Soc., 138, 1751–1763, 2012.

Bryan, G. H., Wyngaard, J. C., and Fritsch, J. M.: Resolution requirements for the simulation of deep moist convection, Mon. Wea. Rev., 131, 2394–2416, 2003.

Buizza, R., Miller, M., and Palmer, T. N.: Stochastic representation of model uncertainties in the ECMWF Ensemble Prediction System, Quart. J. Roy. Meteor. Soc., 125, 2887–2908, 1999.

Clark, A. J., Kain, J. S., Stensrud, D. J., Xue, M., Kong, F., Coniglio, M. C., Thomas, K. W., Wang, Y., Brewster, K., Gao, J., Wang, X., Weiss, S. J., and Du, J.: Probabilistic Precipitation Forecast Skill as a Function of Ensemble Size and Spatial Scale in a Convection-Allowing Ensemble, Mon. Wea. Rev., 139, 1410–1418, 2011.

Cuxart, J., Bougeault, P., and Redelsperger, J.-L.: A turbulence scheme allowing for mesoscale and large-eddy simulations, Quart. J. Roy. Meteor. Soc., 126, 1–30, 2000.

Drobinski, P., Ducrocq, V., Alpert, P., Anagnostou, E., Béranger, K., Borga, M., Braud, I., Chanzy, A., Davolio, S., Delrieu, G., Estournel, C., Filali Boubrahmi, N., Font, J., Grubisic, V., Gualdi, S., Homar, V., Ivancan-Picek, B., Kottmeier, C., Kotroni, V., Lagouvardos, K., Lionello, P., Llasat, M., Ludwig, W., Lutoff, C., Mariotti, A., Richard, E., Romero, R., Rotunno, R., Roussot, O., Ruin, I., Somot, S., Taupier-Letage, I., Tintore, J., Uijlenhoet, R., and Wernli, H.: HyMeX, a 10-year multidisciplinary program on the Mediterranean water cycle, Bull. Amer. Meteor. Soc., submitted, 2013.

Ducrocq, V., Nuissier, O., Ricard, D., Lebeaupin, C., and Thouvenin, T.: A numerical study of three catastrophic precipitating events over southern France. II: Mesoscale triggering and stationarity factors, Quart. J. Roy. Meteor. Soc., 134, 131–145, 2008.

Ducrocq, V., Braud, I., Davolio, S., Ferretti, R., Flamant, C., Jansa, A., Kalthoff, N., Richard, E., Taupier-Letage, I., Ayral, P., Belamari, S., Berne, A., Borga, M., Boudevillain, B., Bock, O., Boichard, J., Bouin, M., Bousquet, O., Bouvier, C., Chiggiato, J., Cimini, D., Corsmeier, U., Coppola, L., Cocquerez, P., Defer, E., Delanoë, J., Di Girolamo, P., Doerenbecher, A., Drobinski, P., Dufournet, Y., Fourrié, N., Gourley, J., Labatut, L., Lambert, D., Le Coz, J., Marzano, F., Molinié, G., Montani, A., Nord, G., Nuret, M., Ramage, K., Rison, B., Roussot, O., Said, F., Schwarzenboeck, A., Testor, P., Van, J., Vincendon, B., Aran, M., and Tamayo, J.: HyMeX-SOP1, the field campaign 1 dedicated to heavy precipitation and flash flooding in the northwestern Mediterranean, Bull. Amer. Meteor. Soc., doi: 10.1175/BAMS-D-12-00244.1, 2013.

Fiori, E., Parodi, A., and Siccardi, F.: Dealing with uncertainty: turbulent parameterizations and grid-spacing effects in numerical modelling of deep moist convective processes, Nat. Hazards Earth Sys. Sci., 9, 1871–1880, 2009.

Fiori, E., Parodi, A., and Siccardi, F.: Uncertainty in prediction of deep moist convective processes: Turbulence parameterizations, microphysics and grid-scale effects, Atmos. Res., 100, 447–456, 2011.

Fresnay, S., Hally, A., Garnaud, C., Richard, E., and Lambert, D.: Heavy precipitation events in the Mediterranean: sensitivity to cloud physics parameterisation uncertainties, Nat. Hazards Earth Sys. Sci., 12, 2671–2688, 2012.

Fritsch, J. M. and Carbone, R. E.: Improving quantitative precipitation forecasts in the warm season: A USWRP Research and Development Strategy, Bull. Amer. Meteor. Soc., 85, 955–965, 2004.

Gilmore, M. S., Straka, J. M., and Rasmussen, E. N.: Precipitation uncertainty due to variations in precipitation particle parameters within a simple microphysics scheme, Mon. Wea. Rev., 132, 2610–2627, 2004.

Hally, A., Richard, E., Fresnay, S., and Lambert, D.: Ensemble simulations with perturbed physical parameterisations: Pre-HyMeX case studies, Quart. J. Roy. Meteor. Soc., doi:10.1002/qj.2257, 2013.

Hohenegger, C. and Schär, C.: Predictability and error growth dynamics in cloud-resolving models, J. Atmos. Sci., 64, 4467–4478, 2007.

Honnert, R., Masson, V., and Couvreux, F.: A Diagnostic for Evaluating the Representation of Turbulence in Atmospheric Models at the Kilometric Scale, J. Atmos. Sci., 68, 3112–3131, 2011.

Houtekamer, P., Lefaivre, L., Derome, J., Ritchie, H., and Mitchell, H.: A System Simulation Approach to Ensemble Prediction, Mon. Wea. Rev., 124, 1225–1242, 1996.

Lafore, J.-P., Stein, J., Asencio, N., Bougeault, P., Ducrocq, V., Duron, J., Fischer, C., Héreil, P., Mascart, P., Masson, V., Pinty, J.-P., Redelsperger, J.-L., Richard, E., and Vilà-Guerau de Arellano, J.: The Meso-NH atmospheric simulation system. Part I: adiabatic formulation and control simulations, Ann. Geophys., 16, 90–109, 1998.

Lascaux, F., Richard, E., and Pinty, J.-P.: Numerical simulations of three different MAP IOPs and the associated microphysical processes, Quart. J. Roy. Meteor. Soc., 132, 1907–1926, 2006.

Lebeaupin, C., Ducrocq, V., and Giordani, H.: Sensitivity of torrential rain events to the sea surface temperature based on high-resolution numerical forecasts, J. Geophys. Res., 111, doi: 10.1029/2005JD006541, 2006.

Leoncini, G., Plant, R. S., Gray, S. L., and Clark, P. A.: Perturbation growth at the convective scale for CSIP IOP18, Quart. J. Roy. Meteor. Soc., 136, 653–670, 2010.

Leoncini, G., Plant, R. S., Gray, S. L., and Clark, P. A.: Ensemble forecasts of a flood-producing storm: comparison of the influence of model-state perturbations and parameter modifications, Quart. J. Roy. Meteor. Soc., 139, 198–211, 2013.

Llasat, M. C., Llasat-Botija, M., Petrucci, O., Pasqua, A. A., Rossello, J., Vinet, F., and Boissier, L.: Towards a database on societal impact of Mediterranean floods within the framework of the HYMEX project, Nat. Hazards Earth Sys. Sci., 13, 1337–1350, 2013.

Mlawer, E. J., Taubman, S. J., Brown, P. D., Iacono, M. J., and Clough, S. A.: Radiative transfer for inhomogeneous atmospheres: RRTM, a validated corrolated-k model for the longwave, J. Geophys. Res., 102D, 16 663–16 682, 1997.

Noilhan, J. and Mafhouf, J.: The ISBA land surface parameterisation, Global Planet Change, 13, 145–159, 1996.

Pergaud, J., Masson, V., Malardel, S., and Couvreux, F.: A Parameterization of Dry Thermals and Shallow Cumuli for Mesoscale Numerical Weather Prediction, Bound. Layer. Meteor., 132, 83–106, 2009.

Pinty, J.-P. and Jabouille, P.: A mixed-phase cloud parameterization for use in a mesoscale non-hydrostatic model: simulations of a squall line and of orographic precipitations, in: Tenth AMS

Cloud Physics Conference, pp. 217–220, American Meteorological Society, Everett, WA, USA, 17-21 August 1998.

Richard, E., Cosma, S., Tabary, P., Pinty, J. P., and Hagen, M.: High-resolution numerical simulations of the convective system observed in the Lago Maggiore area on 17 September 1999 (MAP IOP 2a), Quart. J. Roy. Meteor. Soc., 129, 543–564, 2003.

Seity, Y., Brousseau, P., Malardel, S., Hello, G., Benard, P., Bouttier, F., Lac, C., and Masson, V.: The AROME-France Convective-Scale Operational Model, Mon. Wea. Rev., 139, 976–991, 2011.

Stensrud, D., Bao, J., and Warner, T.: Using initial conditions and model physics perturbations in short-range ensemble simulations of mesoscale convective systems, Mon. Wea. Rev., 128, 2077–2107, 2000.

Vié, B., Nuissier, O., and Ducrocq, V.: Cloud-Resolving Ensemble Simulations of Mediterranean Heavy Precipitating Events: Uncertainty on Initial Conditions and Lateral Boundary Conditions, Mon. Wea. Rev., 139, 403–423, 2011.

Walser, A., Luthi, D., and Schar, C.: Predictability of precipitation in a cloud-resolving model, Mon. Wea. Rev., 132, 560–577, 2004.

Wisse, J. S. P. and de Arellano, J. V. G.: Analysis of the role of the planetary boundary layer schemes during a severe convective storm, Ann. Geophys., 22, 1861–1874, 2004.

Wyngaard, J. C.: Toward numerical modeling in the ”terra incognita”, J. Atmos. Sci., 61, 1816–1826, 2004.

| Simulation name | IC | BC |
|---|---|---|
| $AR$ | AROME | AROME |
| $WM$ | AROME-WMED | AROME-WMED |
| $WF$ | ECMWF | ECMWF |
| $AP$ | ARPEGE | ARPEGE |
| $AR-WM$ | AROME | AROME-WMED |
| $AR-WF$ | AROME | ECMWF |
| $AR-AP$ | AROME | ARPEGE |
| $WM-AR$ | AROME-WMED | AROME |
| $WF-AR$ | ECMWF | AROME |
| $AP-AR$ | ARPEGE | AROME |

**Table 4.1:** *The characteristics of the simulations presented in section 4.3.1. The characteristics of the simulations are identical for both IOP6 and IOP7a.*

## 4.3 Other factors in rainfall development

### 4.3.1 Initial and boundary conditions

As seen in sections 3.1.1 and 3.1.2 of the research article previously presented, changing the IC and BC leads to different rainfall fields developing. In order to investigate the respective contribution of the IC and BC to the rainfall evolution, six simulations were performed for the IOP6 and IOP7a cases. The first three simulations had AROME IC and either AROME-WMED (simulation $AR-WM$), ECMWF (simulation $AR-WF$) or ARPEGE (simulation $AR-AP$) analysis files as BC. The final three simulations used AROME BC and AROME-WMED (simulation $WM-AR$), ECMWF (simulation $WF-AR$) or ARPEGE (simulation $AP-AR$) files as IC. The simulation set-up is identical to that presented in section 2.3 of the research article. Table 4.1 presents the characteristics of the simulations referred to in this section. The location of the geographical features and departments of south-eastern France referred to in this section are given in Fig.3 of the research article presented in section 4.2.

#### IOP6

A plot of the simulated rainfall field for the $AR-WM$, $AR-WF$ and $AR-AP$ simulations is given in Fig. 4.2. Fig.2(a) of the research article presents the observed rainfall fields for this case while the simulated rainfall for the $AR$, $WM$, $WF$ and $AP$ simulations, i.e. the different members of the ICBC6 ensemble, is re-illustrated in Fig. 4.1. Comparisons between Fig. 4.1 and Fig. 4.2 show that the general form of the convective line is present in all simulations in Fig. 4.2. Further examination hints at the influence of the BC. The rainfall observed over the Vaucluse and Lozère departments in the $AR$ simulation (plot (a) Fig. 4.1) is not seen in the plots of the $AR-WM$, $AR-WF$ and $AR-AP$ simulations (Fig. 4.2). Secondly, the rainfall in the western Gard department seen for the $AR$ simulation is not repeated in the $AR-WM$, $AR-WF$ or $AR-AP$

simulations. Concurrently, its representation in $AR-WM$, $AR-WF$ and $AR-AP$ resembles that in $WM$, $WF$ and $AP$ respectively. However, the band of rain to the north-west of the domain, present in the $AR$ simulation is repeated in the $AR-WM$, $AR-WF$ and $AR-AP$ simulations, albeit with different levels of intensity. The presence of this rainfall would seem to be an influence of the IC. Plots of the hourly rainfall accumulations (not shown) illustrate that this rain-band occurred between 4 and 7 h after initialisation time and thus explains the influence of the IC upon its development.

The temporal evolution plot shown in Fig. 4.3 allows the differences between the simulations to be more easily distinguished. All simulations display a similar rainfall evolution until approximately 01UTC, when they begin to diverge. None of the evolutions of the $AR-WM$, $AR-WF$ or $AR-AP$ simulation follow the evolution of the $AR$ simulation. At approximately 05UTC, the $WM$ and $AP$ simulations display a peak, which is also simulated by the $AR-WM$ and $AR-AP$ simulations. The $AR-WM$ and $AR-AP$ simulations give higher rainfall peaks than the $WM$ and $AP$ simulations. The $WF$ simulation exhibits a peak at 04UTC which is delayed by an hour in the $AR-WF$ simulation. The value of the $AR-WF$ peak is weakened compared to the $WF$ peak.

The Taylor diagram displayed in Fig. 4.4 shows that in terms of spatial correlation, the $AR-WM$ and $AR-WF$ simulations give similar values to those of the $WM$ and $WF$ respectively. However, the $AR-AP$ simulation displays a worsening in spatial correlation compared to $AP$ but an improvement in the standard deviation value. Differences in the representation of the rainfall in the north-west of the domain will impact upon the spatial correlation and standard deviation values of the $AR-WM$, $AR-WF$ and $AR-AP$ simulations and may explain why the same coloured circles and triangles are not superposed on one another in Fig. 4.4.

The simulated rainfall of the $WM-AR$, $WF-AR$ and $AP-AR$ simulations is presented in Fig. 4.5. A comparison with the $AR$, $WM$, $WF$ and $AP$ (Fig. 4.1) simulations shows that the rainfall pattern of $WM-AR$, $WF-AR$ and $AP-AR$ strongly resemble that of $AR$. The shape and positioning of the convective line in $WM-AR$, $WF-AR$ and $AP-AR$ is almost identical to that in $AR$. There are slight differences in the accumulated rainfall amounts between $WM-AR$, $WF-AR$ and $AP-AR$.

The temporal evolution plot in Fig. 4.6 shows a striking contrast compared to the plot in Fig. 4.3. Simulations $WM-AR$, $WF-AR$ and $AP-AR$ display evolutions which follow very closely that of $AR$. The rainfall peak at 05UTC shown by $AR$ is also captured by the $WM-AR$, $WF-AR$ and $AP-AR$ simulations.

The Taylor diagram in Fig. 4.7 displays a similar situation with the $WM-AR$, $WF-AR$ and $AP-AR$ simulations clustered around the $AR$ simulation, giving comparable spatial correlation, RMSE and standard deviation values. Although the statistics of the $WM-AR$ simulation are similar to those of $WM$, Fig. 4.5 and Fig.4.6 show that its rainfall pattern most heavily resembles that of $AR$.

### Discussion - IOP6

It would appear that the BC play an important role in controlling the convective rainfall peak for this case. The IC seem to have a less important role, possibly influencing

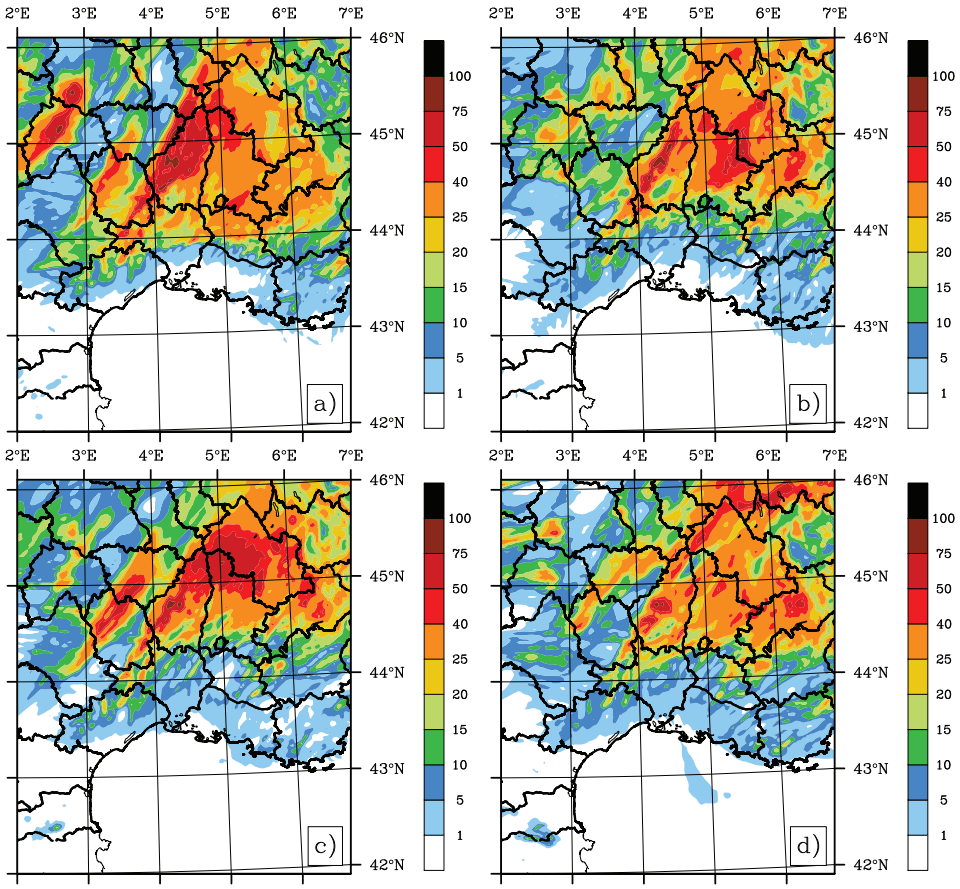


**Figure 4.1:** *The accumulated 24 h rainfall ($mm$) of the $AR$ (a), $WM$ (b) $WF$ (c) and $AP$ (d) simulations for IOP6.*

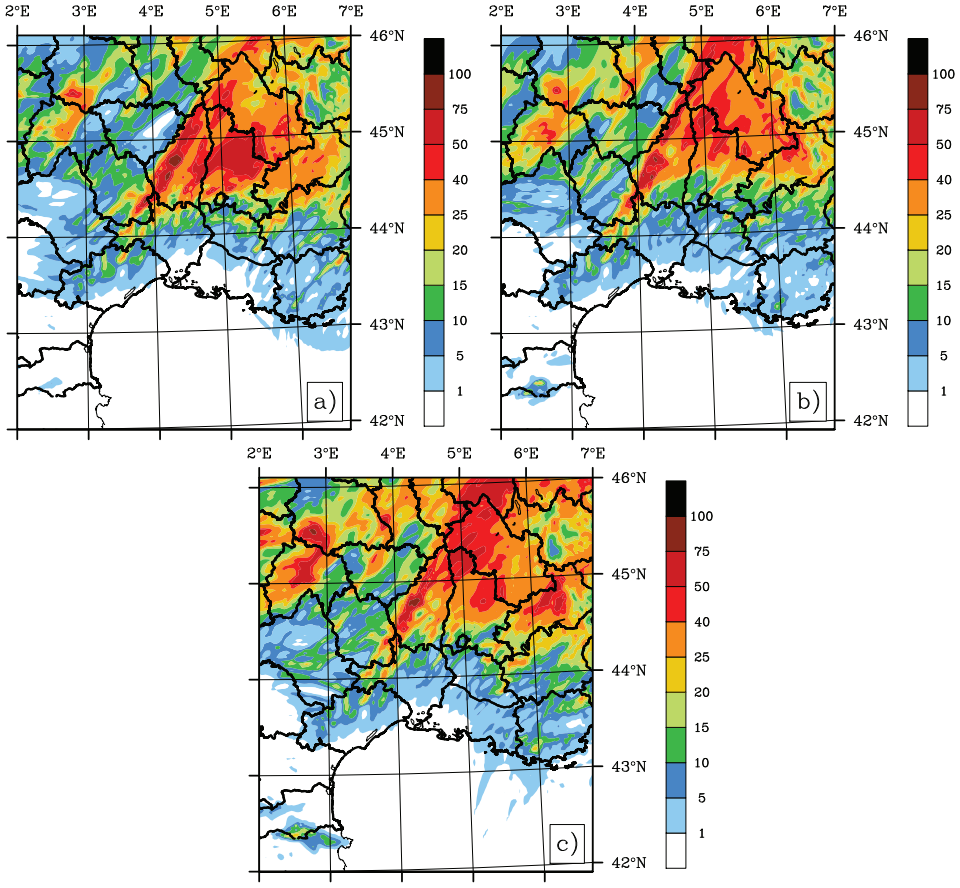


**Figure 4.2:** *The accumulated 24 h rainfall* $(mm)$ *of the* $AR - WM$ *(a),* $AR - WF$ *(b) and* $AR - AP$ *(c) simulations for IOP6 i.e. with changing boundary conditions*

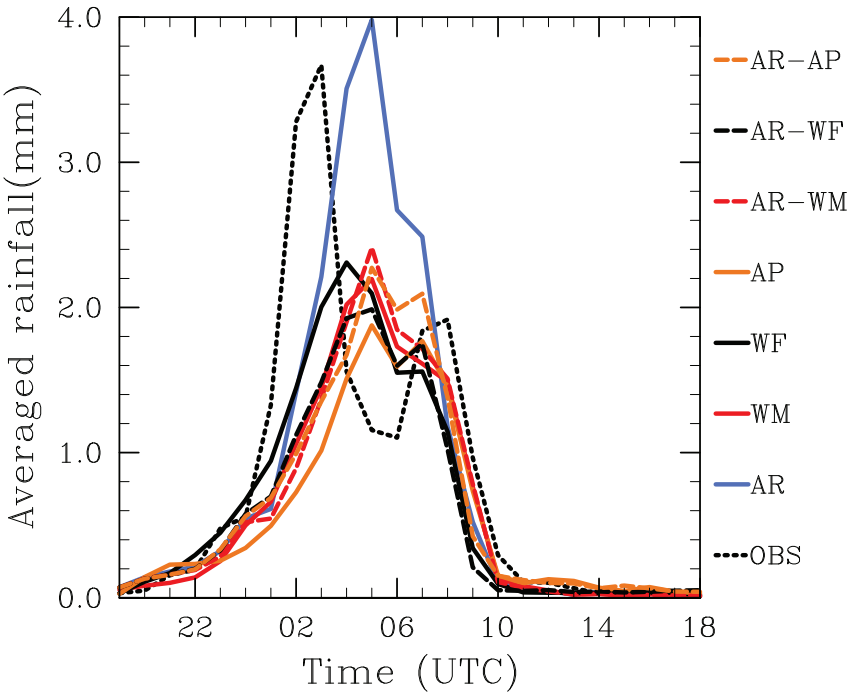


**Figure 4.3:** *The temporal evolution of the spatially-averaged hourly accumulated rainfall of the* $AR, WM, WF, AP, AR - WM, AR - WF$ *and* $AR - AP$ *simulations for IOP6.*

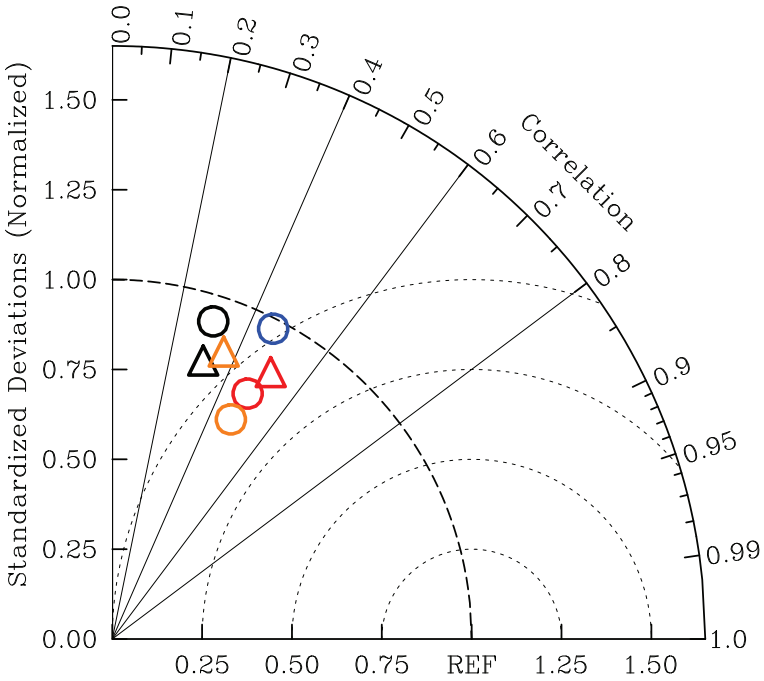


**Figure 4.4:** *24h Taylor diagram displaying the spatial correlation, standard deviation and RMSE of the simulated rainfall with the observed rainfall for the $AR$(blue circle), $WM$(red circle), $WF$(black circle), $AP$(orange circle), $AR-WM$(red triangle), $AR-WF$(black triangle) and $AR-AP$(orange triangle) simulations of the IOP6 case.*

a small band of rainfall which took place close to the initialisation time. The weaker role of the IC in controlling the peak can be somewhat explained by the fact that it was simulated at 05UTC, or 11 h after initialisation. This is a sufficiently long enough time difference to allow the signal of the IC to become much less important than that of the BC.

The different representations of the convective peak of the $AR$, $WM$, $WF$ and $AP$ simulations are thus related to differences in their BC. One factor which may explain the differences is the strength of the low-level flow entering the domain at the boundary. Fig. 4.8 illustrates the wind speed at 950hPa for the BC at 00UTC for each of the $AR$, $WM$, $WF$ and $AP$ simulations. For the southern boundary, the $AR$ simulation gives the strongest flow, reaching a maximum of over $18m/s$ compared to between 10 and $15m/s$ for the $WM$, $WF$ and $AP$ simulations. As shown in Bresson *et al.* (2012), the strength of this flow influences the rainfall pattern further upstream. Stronger flows trigger convection further north over orographic regions which in general lead to heavier precipitation accumulations. The $AR$, $WM$, $WF$ and $AP$ simulations seem to follow this hypothesis, with $AR$($AP$) having the strongest(weakest) low-level flow at the boundary and most(least) intense precipitation.

Fig. 4.9 illustrates the streamlines of the flow and the equivalent potential temperature ($\theta_e$) at 950hPa for the same BC files. The $WM$, $WF$ and $AP$ conditions in Fig. 4.9 (b), (c) and (d) show large areas of cold air entering the domain at the southern boundary between the longitudes 6.6E and 9.4E (highlighted on the Fig. 4.9 plots by an ellipse). As shown by the streamlines, this cold and thus drier air is advected towards the

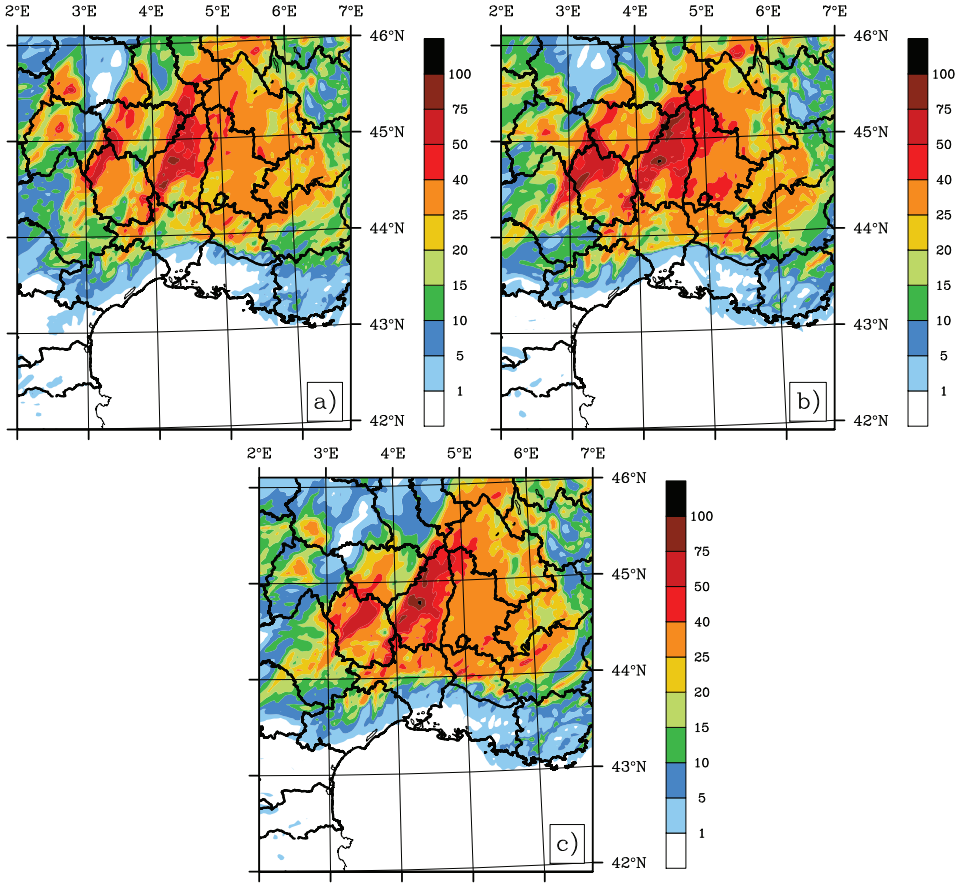


**Figure 4.5:** *The accumulated 24 h rainfall $(mm)$ of the $WM - AR$ (a), $WF - AR$ (b) and $AP - AR$ (c) simulations for IOP6 i.e. with changing initial conditions*

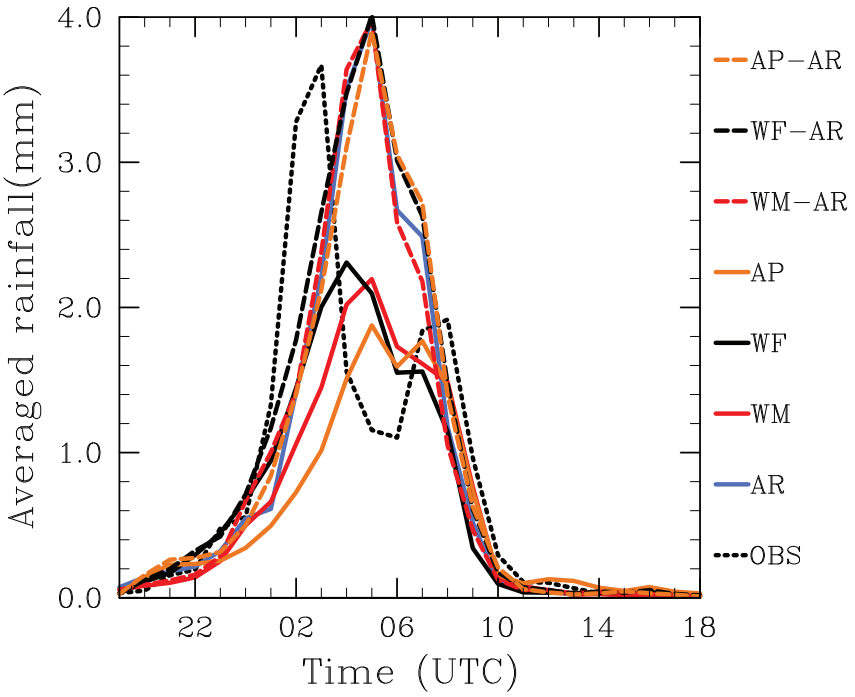


**Figure 4.6:** *The temporal evolution of the spatially-averaged hourly accumulated rainfall of the $AR$, $WM$, $WF$, $AP$, $WM - AR$, $WF - AR$ and $AP - AR$ simulations for IOP6.*

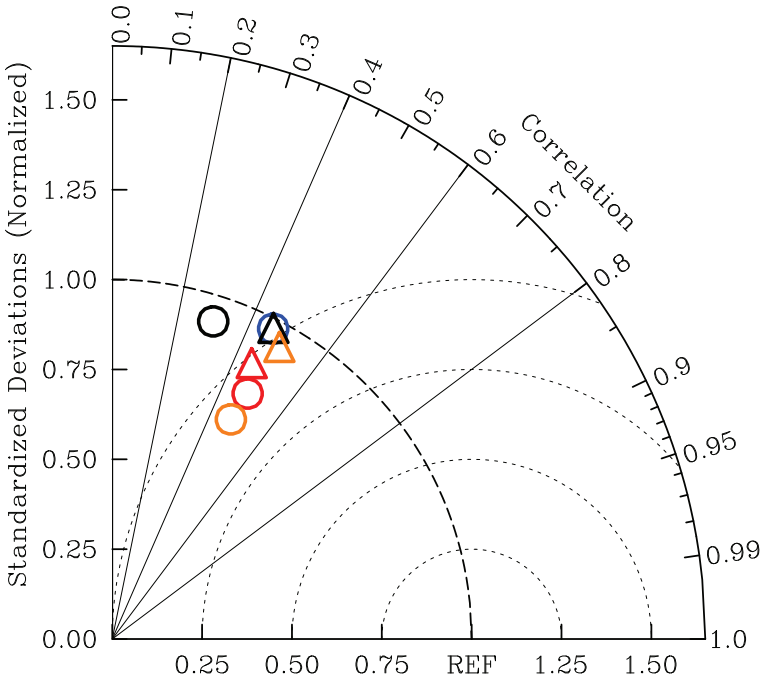


**Figure 4.7:** *24h Taylor diagram displaying the spatial correlation, standard deviation and RMSE of the simulated rainfall with the observed rainfall for the $AR$(blue circle), $WM$(red circle), $WF$(black circle), $AP$(orange circle), $WM - AR$(red triangle), $WF - AR$(black triangle) and $AP - AR$(orange triangle) simulations of the IOP6 case.*

precipitating zone, most notably for the $WF$ and $AP$ BC. The air entering the domain in $AR$ is warmer and thus more humid compared to the other BC. Coupled with the stronger boundary flow, this is most likely the reason the precipitation peak appeared heavier in the $AR$ simulation than in the others.

### IOP7a

As was done for the IOP6, six simulations were performed to determine the impact of the IC and BC on the rainfall development for this case. The configuration of the simulations is as was presented for the IOP6 case. The nomenclature and details of the simulations are given in Table 4.1. A plot of the observed rainfall for this case is given in Fig.2(b) of the research article in section 4.2. The simulated rainfall for the $AR$, $WM$, $WF$ and $AP$ simulations, i.e. the different members of the ICBC7 ensemble, is re-plotted in Fig. 4.10.

A plot of the simulated rainfall for the $AR - WM$, $AR - WF$ and $AR - AP$ simulations is given in Fig. 4.11. In contrast with the IOP6 case, there are similarities between the simulated rainfall in Fig. 4.10 and Fig. 4.11. The rainfall of the $WM$ member of the ICBC7 ensemble has several features in common with the $AR - WM$ simulation. The tail of precipitation which spreads south from the Bouches du Rhône department is seen in both plots. The layout of the rainfall pattern over the Isère and Drôme departments for the $AR - WM$ simulation resembles that of the $WM$ member of ICBC7. These similarities are also seen between the $AR - WF$ simulation and the $WF$ mem-

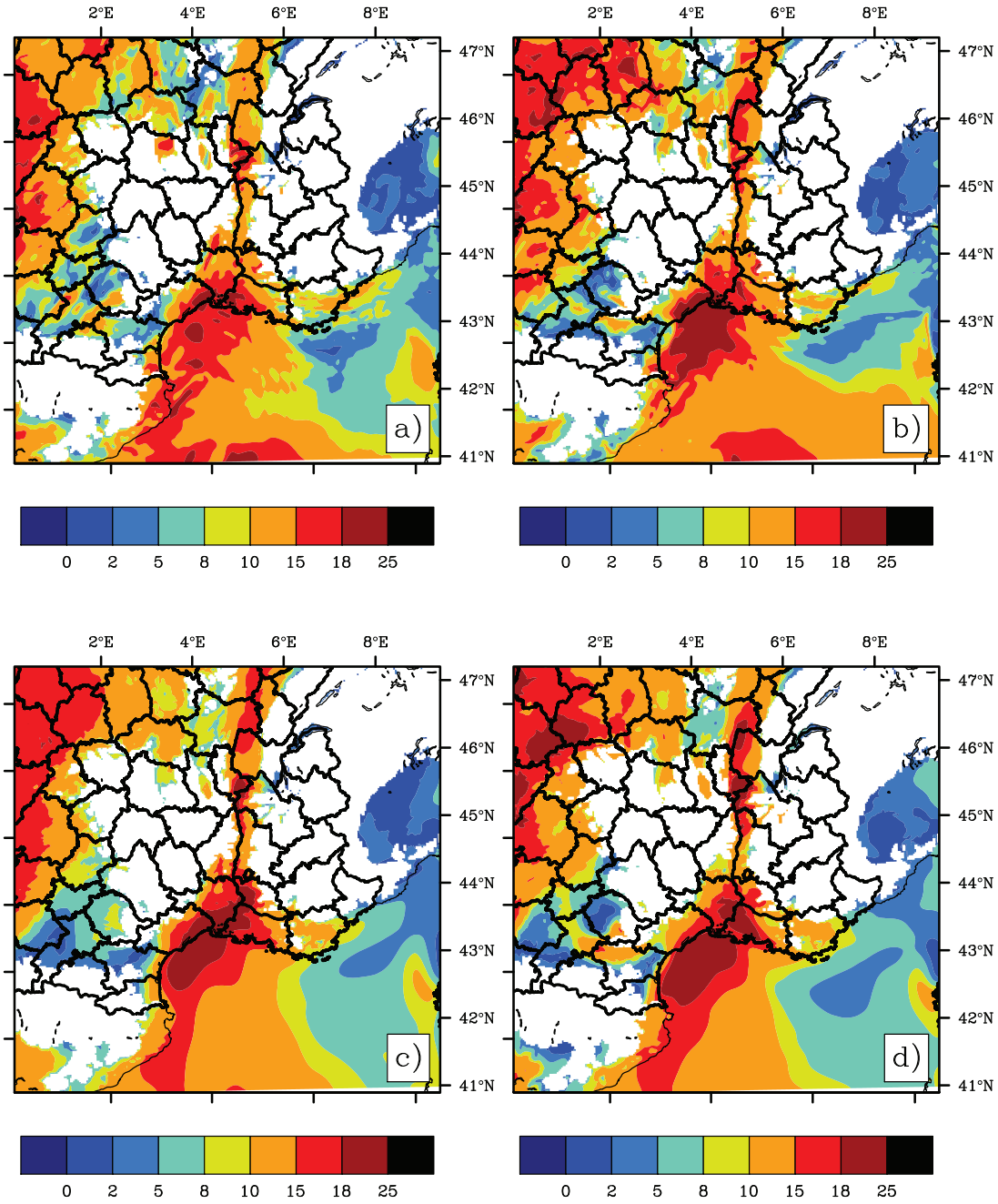


**Figure 4.8:** *The wind at 950hPa ($m/s$) for the BC of the $AR$ (a), $WM$ (b), $WF$ (c) and $AP$ (d) simulations at 00UTC on the 24th of September.*

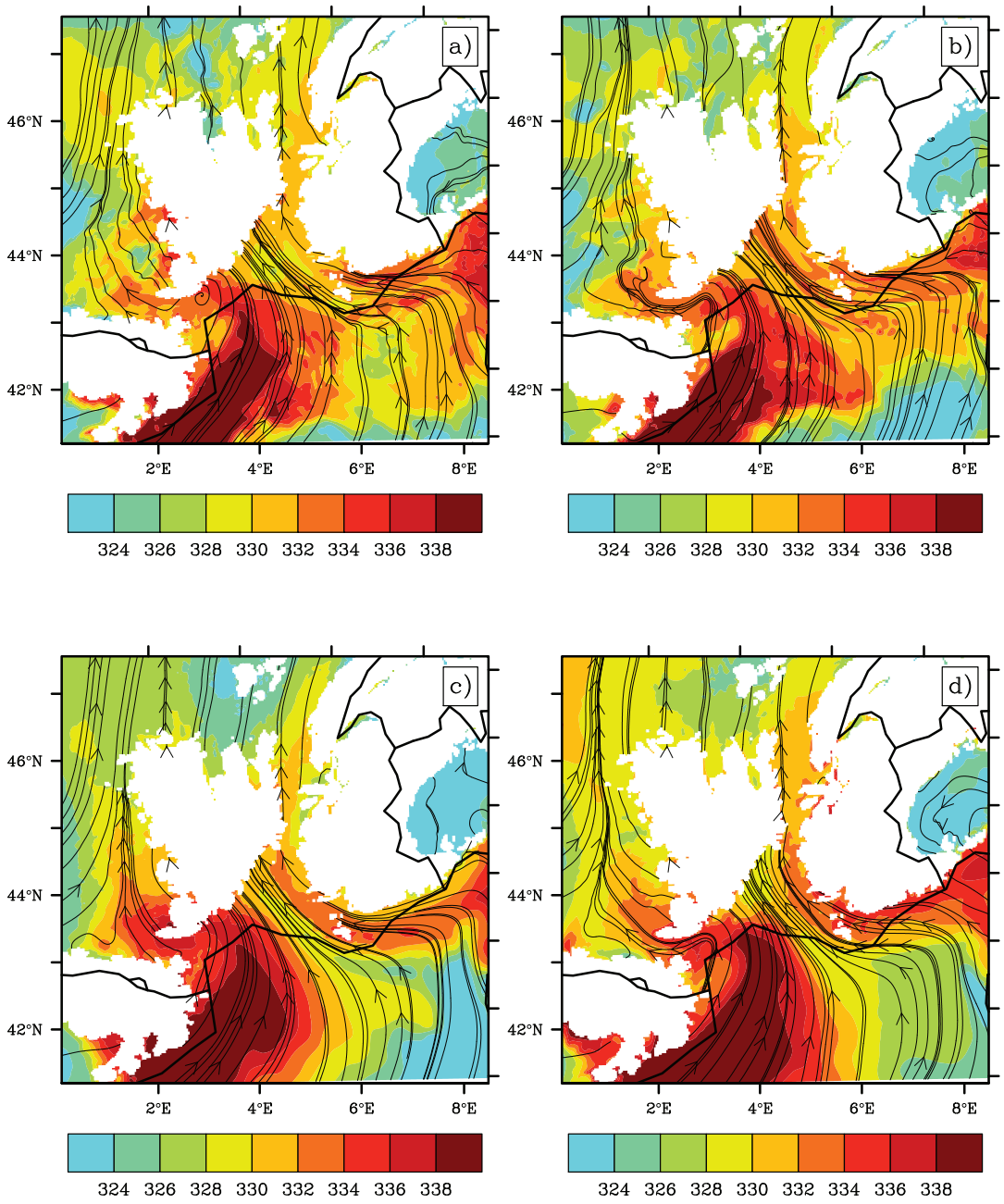


**Figure 4.9:** *The flow streamlines and $\theta_e$ (K) at 950hPa in the BC of the $AR$ (a), $WM$ (b), $WF$ (c) and $AP$ (d) simulations at 00UTC on the 24th of September for the domain shown in Fig.3 (a) of the research article in section 4.2.*

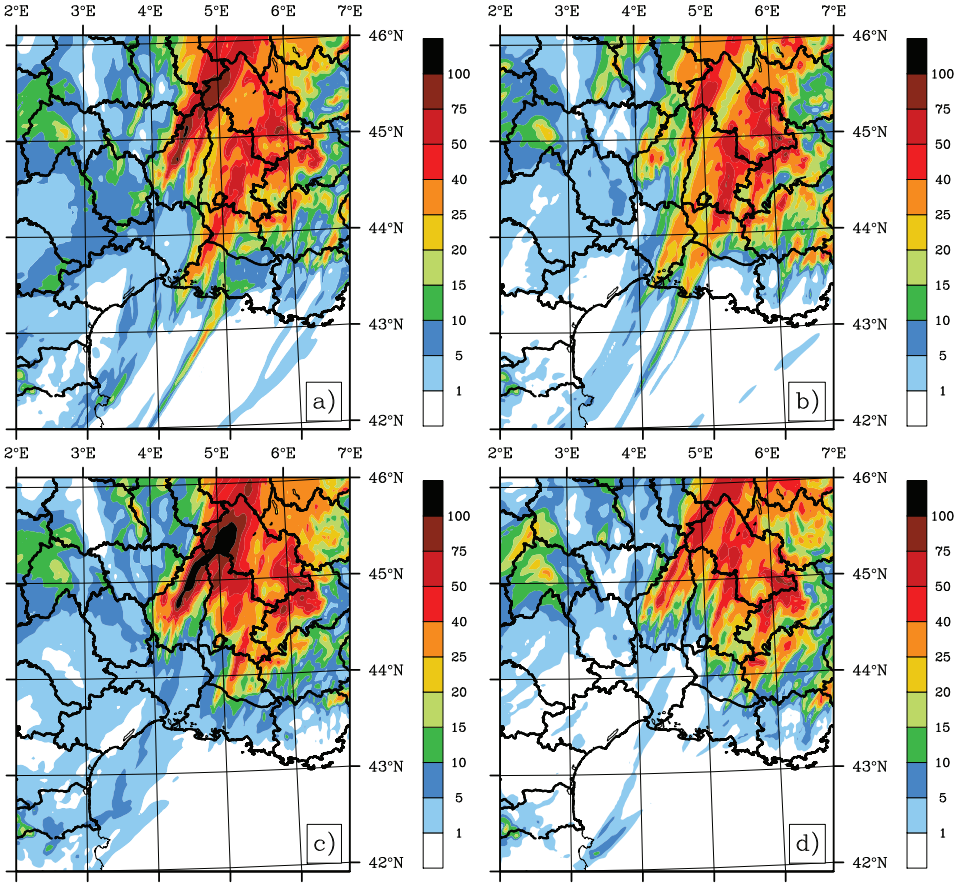


**Figure 4.10:** *The accumulated 24 h rainfall (mm) of the $AR$ (a), $WM$ (b), $WF$ (c) and $AP$ (d) simulations for IOP7a.*

ber of the ICBC7 ensemble. The general precipitation layout and rainfall over the sea are similar in both plots. The rainfall structure seen for the $AR-AP$ simulation and the $AP$ member of the ICBC7 ensemble also coincide well, shown noticeably by the lack of simulated rainfall over the Gard and Aude departments in both plots.

These 24 h accumulations can hide some details of the rainfall evolution which are more easily recognisable on a temporal evolution plot (Fig. 4.12). All simulations succeed in capturing the first rainfall peak at approximately 08UTC, albeit with differing levels of intensity. For the second rainfall peak at 17UTC a clear pattern is exhibited. Simulations with the same BC conditions give very similar rainfall evolutions. The $AR-WM$ ($AR-WF$)($AR-AP$) simulation evolves in a similar manner to that of the $WM$ ($WF$)($AP$) simulation. This signal was not seen for the first peak at 08UTC.

The Taylor diagram in Fig. 4.13 shows that the $AR$ and $AR-WM$ simulations display common standard deviation values, as do $WF$ and $AR-WF$. As was seen for the IOP6 case, the $AR-AP$ simulation gives a worsening spatial correlation compared to the $AP$ simulation, but an improvement in the standard deviation. The $AR-WM$ displays an improved spatial correlation value compared to the $WM$ simulation while also giving an ameliorated standard deviation value.

Comparing the simulated rainfall of the $WM-AR$, $WF-AR$ and $AP-AR$ simu-

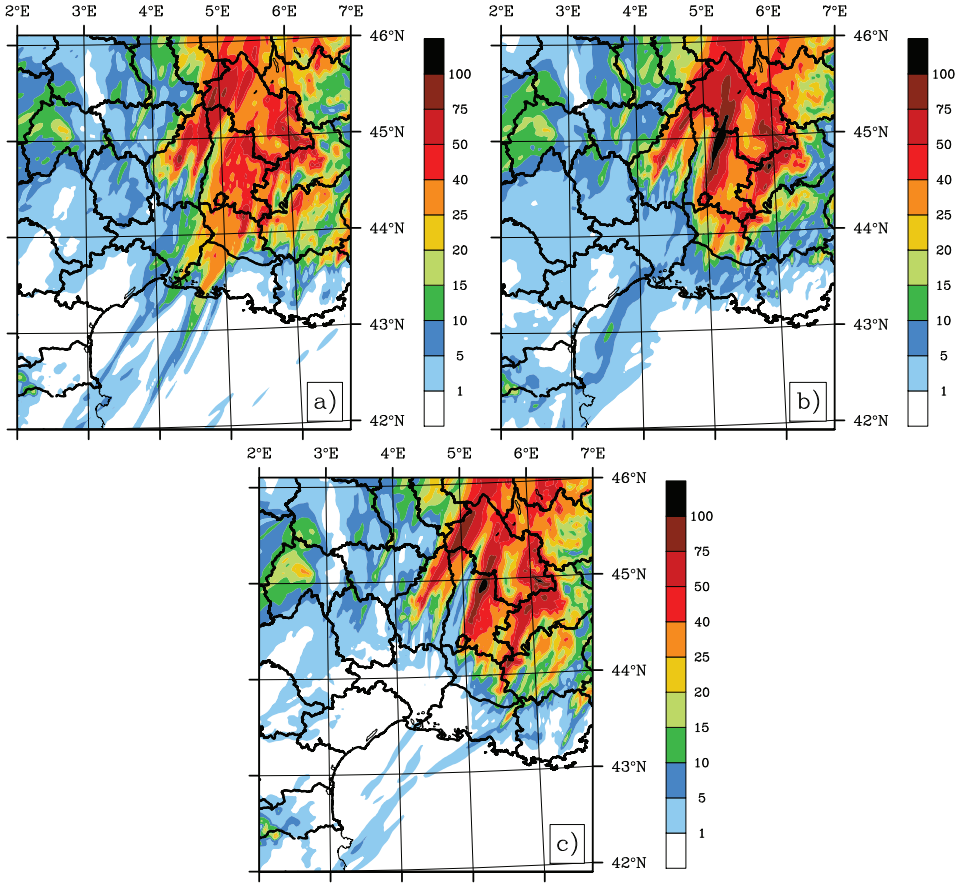


**Figure 4.11:** *The accumulated 24 h rainfall (mm) of the $AR - WM$ (a), $AR - WF$ (b) and $AR - AP$ (c) simulations for IOP7a i.e. with changing boundary conditions.*

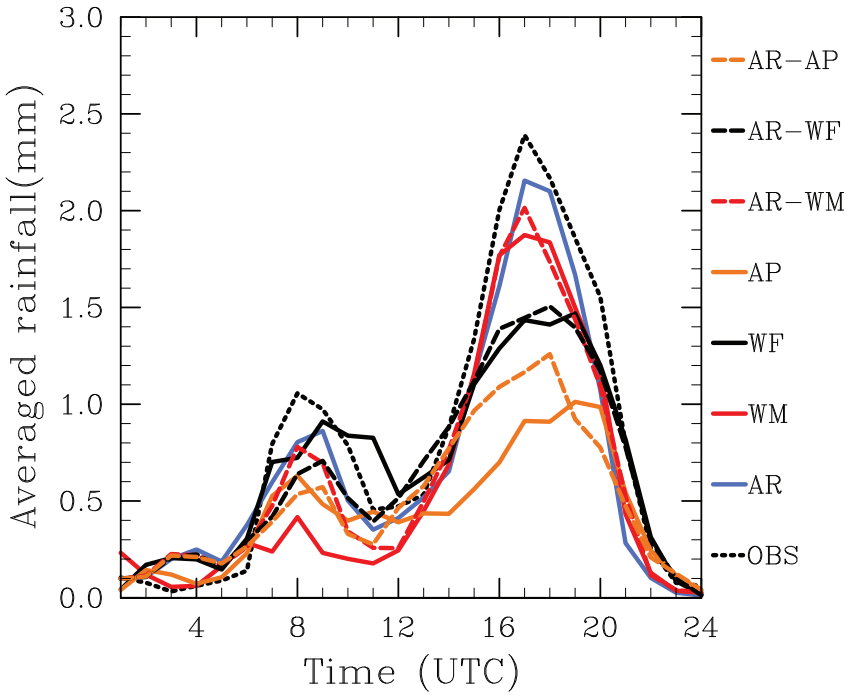


**Figure 4.12:** *The temporal evolution of the spatially-averaged hourly accumulated rainfall of the $AR$, $WM$, $WF$, $AP$, $AR - WM$, $AR - WF$ and $AR - AP$ simulations for IOP7a.*

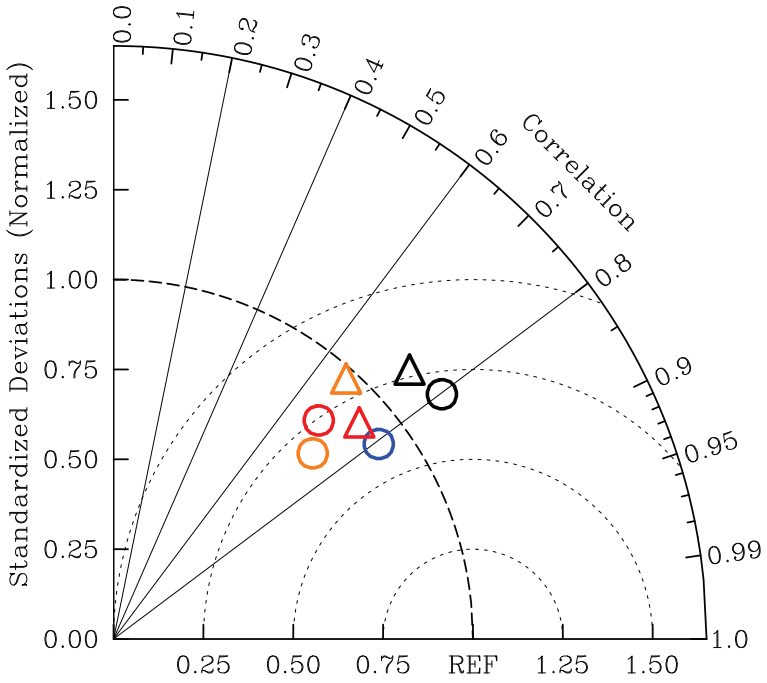


**Figure 4.13:** *24h Taylor diagram displaying the spatial correlation, standard deviation and RMSE of the simulated rainfall with the observed rainfall for the $AR$(blue circle), $WM$(red circle), $WF$(black circle), $AP$(orange circle), $AR-WM$(red triangle), $AR-WF$(black triangle) and $AR-AP$(orange triangle) simulations of the IOP7a case.*

lations in Fig. 4.14 to that of the $AR$, $WM$, $WF$ and $AP$ simulations (Fig. 4.10) demonstrates influences of both the IC and BC. The layout of the stratiform rainfall over the Drôme and Ardèche departments in the $WM-AR$, $WF-AR$ and $AP-AR$ simulations is comparable to that of the $AR$ simulation, especially in terms of localisation and intensity. However, the representation of the convective rainfall over the Cévennes differs between $WM-AR$, $WF-AR$ and $AP-AR$. The convective line is advected to the north-east of the Cévennes in the $WM-AR$, which is in agreement with the rainfall pattern of the $WM$ simulation. The over-forecasting of the convective rainfall intensity in $WF$ is repeated in $WF-AR$. The shape and positioning of the convective line in $AP-AR$ resembles that of $AP$.

An examination of the temporal evolution plot in Fig. 4.15 illustrates that for the convective rainfall peak at 08UTC, the evolutions of $WM-AR$ and $WF-AR$ follow those of $WM$ and $WF$ respectively but that the $AP$ simulation peak is increased in $AP-AR$ simulation. For the stratiform peak at 17UTC, the influence of the BC appears strong, as the evolutions of the $WM-AR$, $WF-AR$ and $AP-AR$ simulations follow that of the $AR$ simulation almost exactly. Concurrently, the representation of a second smaller peak at 18UTC is common to all four simulations.

Surprisingly, the Taylor diagram in Fig. 4.16 shows that the $WM-AR$ and $AP$ simulations share identical statistics, while the $AP-AR$ simulation statistics resemble those of $AR$ and $WF-AR$ of $WF$. This contradicts the results gleamed from Fig. 4.14 and Fig. 4.15. However, this can be explained by the nature of the two rain bands seen for this case. The calculation of the spatial correlation will be more sensitive to errors

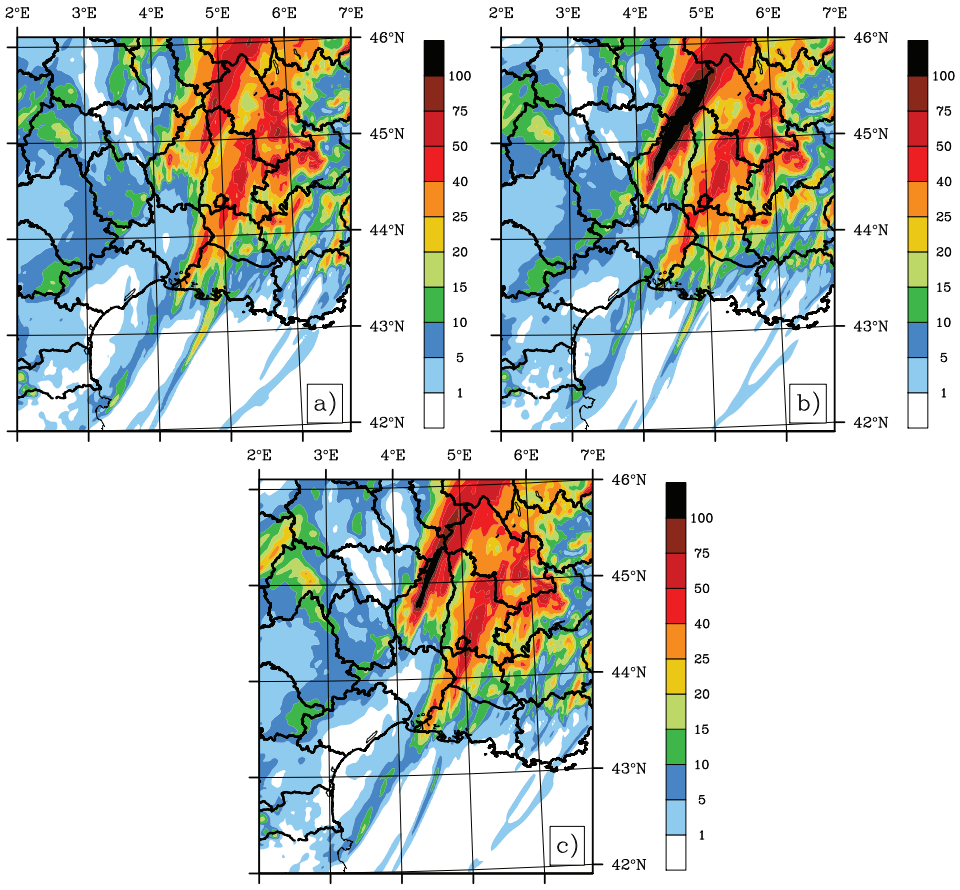


**Figure 4.14:** *The accumulated 24 h rainfall (mm) of the $WM - AR$ (a), $WF - AR$ (b) and $AP - AR$ (c) simulations for IOP7a i.e. with changing initial conditions.*

between the observed and simulated rainfall for the convective precipitation as it occurred in a more concentrated area compared to the second band of stratiform rainfall which occurred over a much wider region. Normalised standard deviation values will show the same pattern as there is a greater risk of the model missing the observed variability over a smaller rather than a larger area. For this reason, the $WF - AR$ and $WF$ simulations have comparable standard deviation and spatial correlation values. The $AP - AR$ simulation has an improved standard deviation compared to $AP$ most likely due to the heavier rainfall accumulations simulated for the convective line. The statistics of the $WM - AR$ simulation changes minimally compared to $WM$ except for a slight change in the spatial correlation, more than likely due to the improved simulation of the stratiform rainfall brought about by using AROME BC instead of AROME-WMED BC.

### Discussion - IOP7a

The influence of the IC appears important for the representation of the convective peak. However, the degree of that influence differs between the different analysis files. The convective precipitation peak illustrates a sensitivity to changing IC for the AROME, AROME-WMED and ECMWF conditions, but for the ARPEGE conditions, the influence

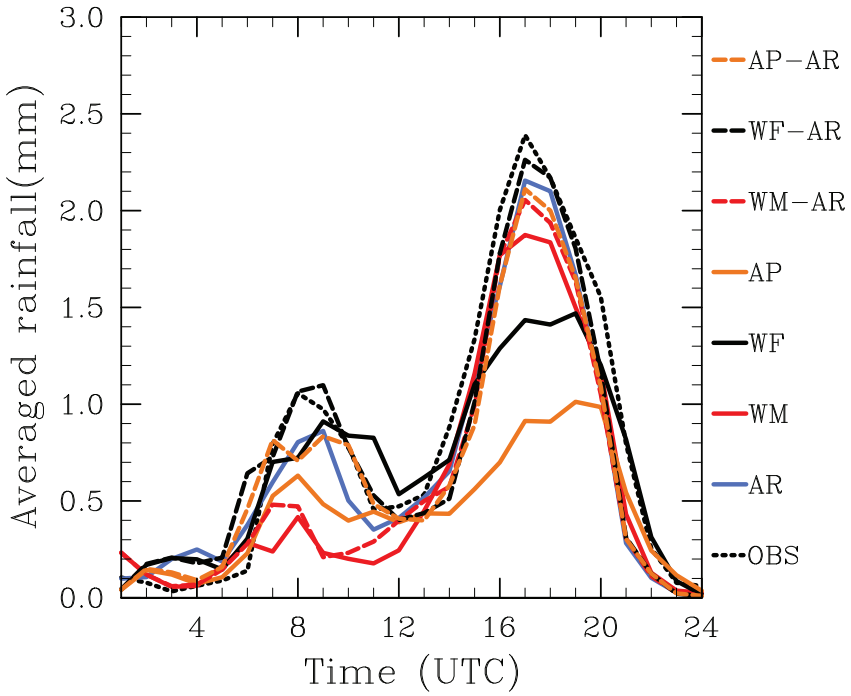


**Figure 4.15:** *The temporal evolution of the spatially-averaged hourly accumulated rainfall of the $AR$, $WM$, $WF$, $AP$, $WM-AR$, $WF-AR$ and $AP-AR$ simulations for IOP7a.*

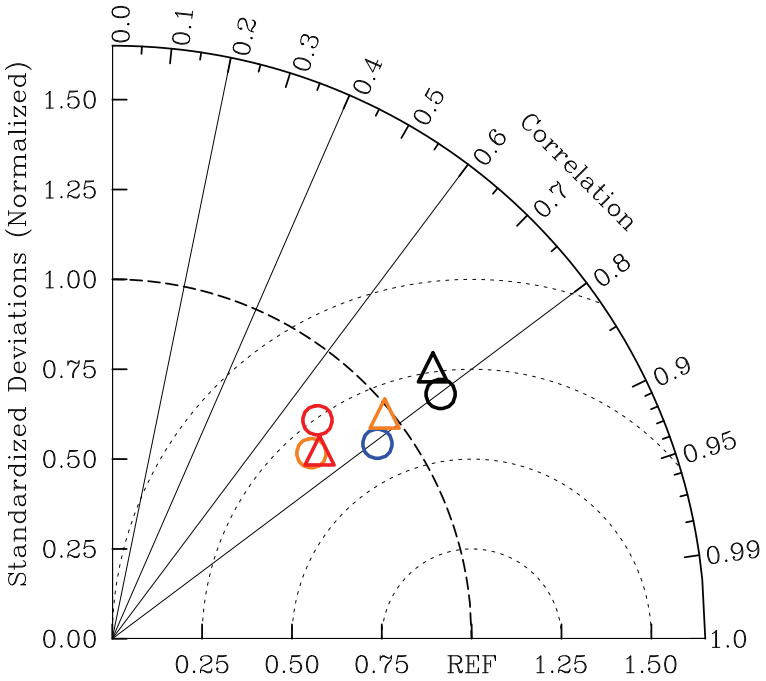


**Figure 4.16:** *24h Taylor diagram displaying the spatial correlation, standard deviation and RMSE of the simulated rainfall with the observed rainfall for the $AR$(blue circle), $WM$(red circle), $WF$(black circle), $AP$(orange circle), $WM-AR$(red triangle), $WF-AR$(black triangle) and $AP-AR$(orange triangle) simulations of the IOP7a case.*

of the BC seems greater. The convective peak is simulated 8 h after initialisation and thus may present a decreasing impact from the IC depending on the strength of the initial signal. To investigate the possible sources of these rainfall discrepancies, plots of the 950hPa wind and $\theta_e$ for the AROME, AROME-WMED, ECMWF and ARPEGE IC are given in Fig. 4.17 and Fig. 4.18.

The 950hPa wind of the ECMWF and ARPEGE conditions (Fig. 4.17 plots (c) and (d) respectively) both display a strong signal in the southern Gard and up along the Rhône Valley. The same winds in the AROME and AROME-WMED conditions (Fig. 4.17 plots (a) and (b) respectively) are weaker. However, further south at the boundary, the AROME and AROME-WMED conditions display stronger flows of above $18m/s$. Plots of the streamline flow and $\theta_e$ in Fig. 4.18 reveal more important differences. The ARPEGE conditions (Fig. 4.18 (d)) display a significant area of cool air to the south of the French coast over the sea which is not found in the other plots. The same area of air is more warmly represented in the ECMWF conditions. The AROME and AROME-WMED conditions give similar representations, both being cooler and thus drier than the ECMWF.

These different descriptions explain the increase in the convective peak of the $WF-AR$ simulation over the $AR$ simulation seen in Fig. 4.15 and the decrease and timing change of the peak of $AR-WF$ compared to $WF$ displayed in Fig. 4.12. However, Fig. 4.18 does not show a large difference between $\theta_e$ for the AROME and AROME-WMED conditions, thus this cannot explain the increased convective peak seen for the $AR$ simulation over the $WM$ simulation in Fig. 4.15 and Fig. 4.12. Simulation $AR-WM$ gives an increased peak compared to $WM$, demonstrating the importance of the IC. Re-examining Fig. 4.17, the AROME conditions give a more consistently stronger initial flow than the AROME-WMED conditions, which may serve as one explanation for the increased convective power of the AROME conditions. The ARPEGE conditions do not display a clear relationship to either the IC or BC, although the increased precipitation peak in Fig. **??** of the $AP-AR$ simulation compared to $AP$ would suggest that the role of the BC is greater.

The stratiform rainfall peak at 17UTC, related to the passage of a cold front, appears more strongly controlled by the BC. Similar to the IOP6 case, the timing of the rainfall peak in relation to the initialisation time of the simulation will modify the influence of the IC and BC. As in IOP6, the different rainfall patterns can be related to the strength of the low-level flow entering the domain at the boundary. Fig. 4.19 displays the wind at 950hPa in the BC at 12UTC for each of the $AR$, $WM$, $WF$ and $AP$ simulations. At the southern boundary, the $AR$ and $WM$ simulations give stronger flows than the $WF$ and $AP$ simulations. The $AR$ (in (a)) simulation in particular exhibits a large area close to the boundary where the wind speeds exceed $18m/s$. These speeds are also seen for $WM$ (b), but over a smaller zone. The $WF$ (c) and $AP$ simulations illustrate weaker flows, reaching maximums of $15m/s$. The temporal evolution plot in Fig. 4.15 clearly demonstrates that those simulations which employed $AR$ BC gave the strongest stratiform peaks. As previously explained for IOP6, the strength of the low-level flow impacts upon the localisation and intensity of the simulated precipitation. The contrasting strengths of the low-level flow in the BC for this case serve as one explanation for the

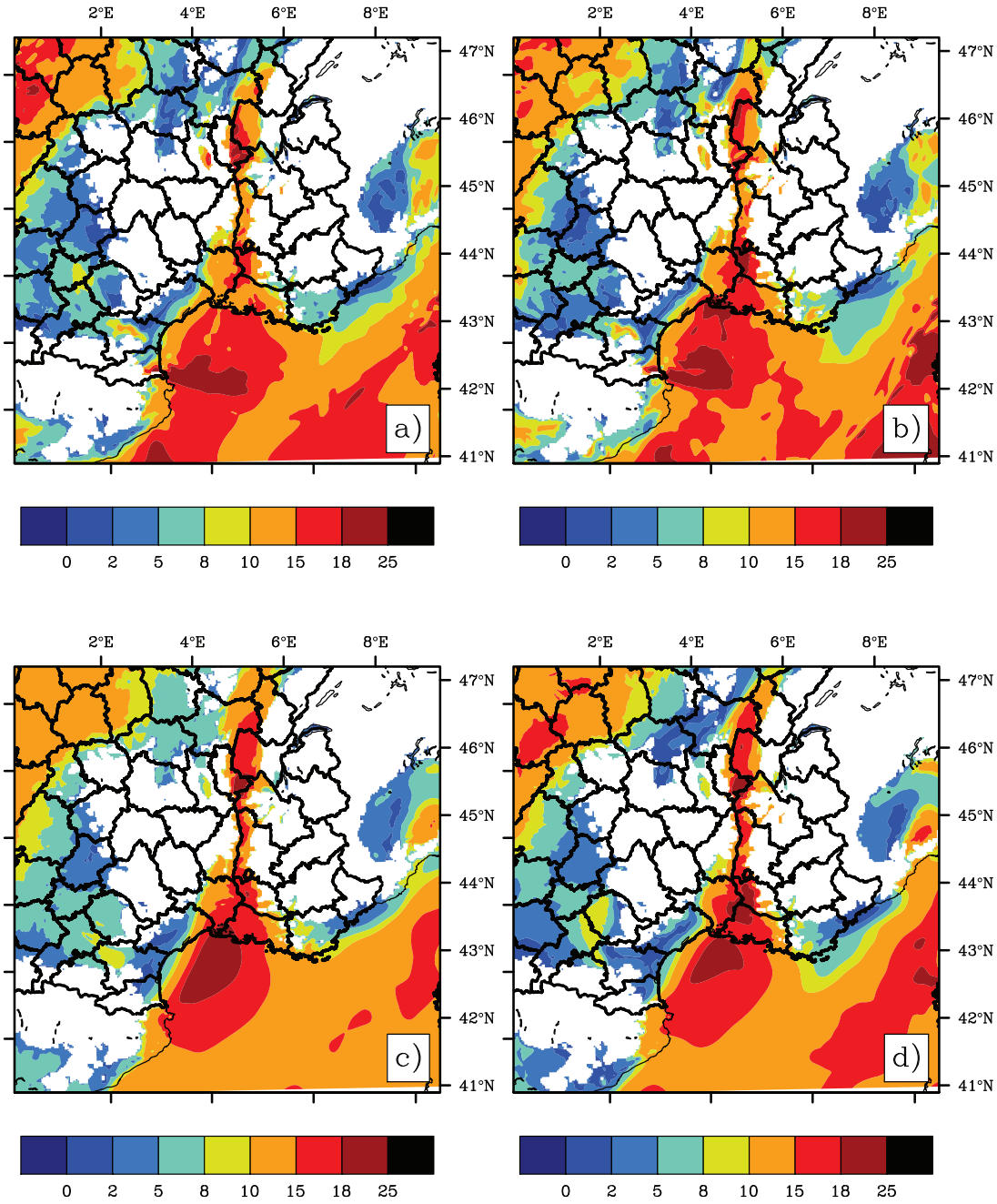


**Figure 4.17:** *The wind at 950hPa ($m/s$) for the IC of the $AR$ (a), $WM$ (b), $WF$ (c) and $AP$ (d) simulations at 00UTC on the 26th of September.*

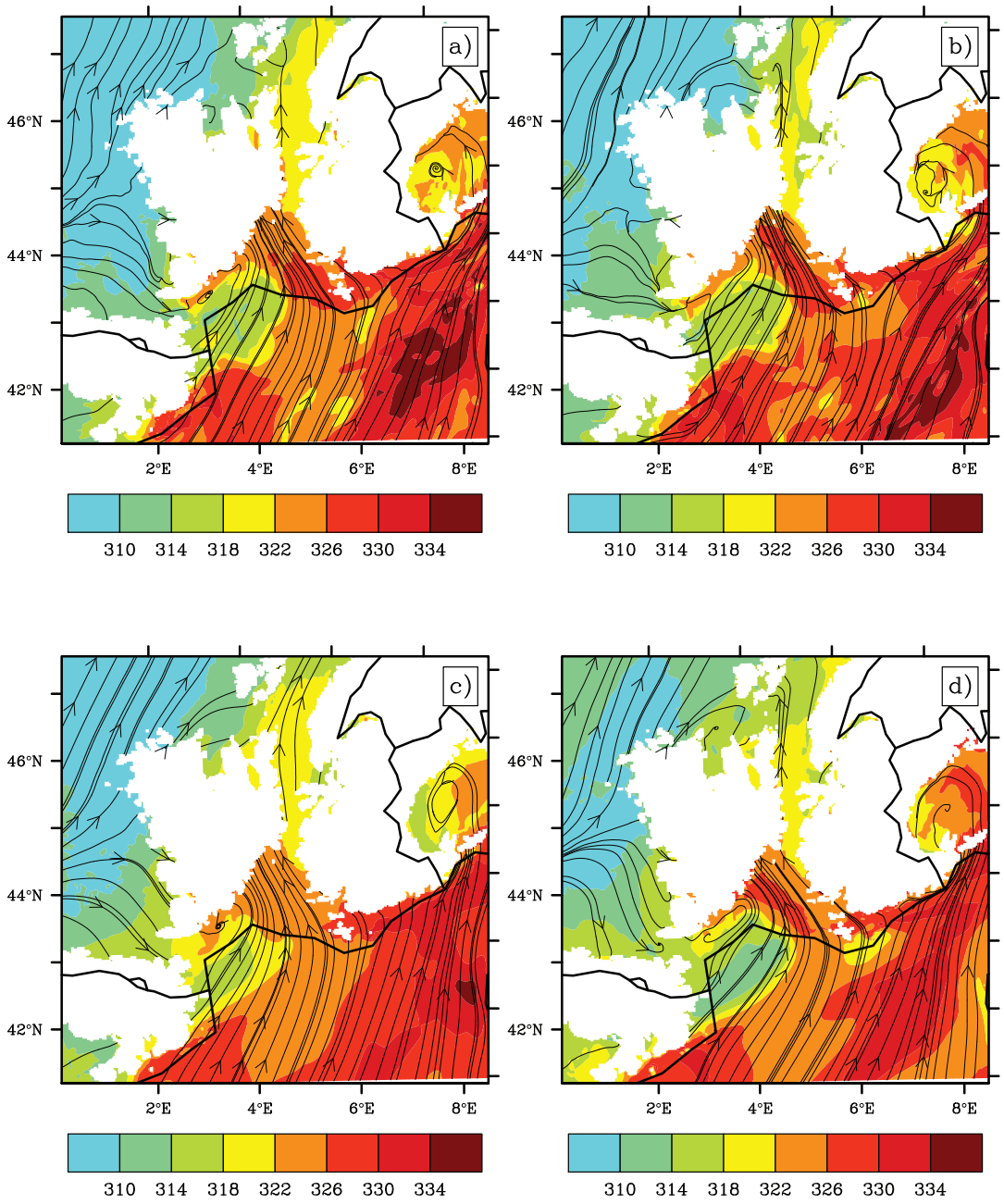


**Figure 4.18:** *The flow streamlines and $\theta_e$ (K) at 950hPa in the IC of the $AR$ (a), $WM$ (b), $WF$ (c) and $AP$ (d) simulations at 00UTC on the 26th of September for the domain shown in Fig.3 (a) of the research article in section 4.2.*

| Simulation name | Atmos conditions | Surf conditions |
|---|---|---|
| $WF$ | ECMWF | ECMWF |
| $AP$ | ARPEGE | ARPEGE |
| $WF - AP_s$ | ECMWF | ARPEGE |
| $AP - WF_s$ | ARPEGE | ECMWF |

**Table 4.2:** *The characteristics of the simulations presented in section 4.3.2.*

differences between the rainfall produced by the $AR$, $WM$, $WF$ and $AP$ simulations.

The $\theta_e$ and streamline flow plots in Fig. 4.20 confirm the points gleamed from Fig. 4.19. It is observed that the warmest air at the southern boundary will be advected away from the precipitating zone in all BC, as demonstrated by the direction of the streamline flow. However, the air entering between a longitude of 2.89E and 4.75E (i.e. along the Spanish coast) is directed toward the zone of precipitation. As in IOP6, the $AR$ simulation has the warmest air at the boundary. The $WF$ and $AP$ simulations give cooler and thus drier conditions.

Fig. 4.20 also illustrates the different descriptions of the approaching cold front between the four sets of BC. The temperature gradient and wind rotation patterns of the $AR$ BC at the eastern boundary in Fig. 4.20 plot (a) more clearly underline the presence of the front than in the $WM$ and $AP$ conditions in plots (b) and (d). Between the $AR$ and $WF$ conditions (plots (a) and (c)), a stronger wind rotation is present in the $WF$ conditions. However, the closeness of the streamlines in the $AR$ conditions indicates a more rapidly changing wind field and thus a more intense representation of the front. This, coupled with a stronger and warmer incident flow led to the $AR$ conditions producing the heaviest stratiform peak.

### 4.3.2 Atmospheric and surface conditions

The atmospheric and surface conditions will also impact the development of an HPE. Depending on the nature of the HPE, the atmospheric and surface conditions can take on different levels of importance. Using IOP6 and IOP7a, the impact of altering these conditions was investigated. The results of section 4.3.1 illustrate that uncertainties exist between the different conditions in their representation of the marine flow. Disrepancies between the ECMWF and ARPEGE/AROME-WMED/AROME surface conditions (not shown) served as motivation to examine the impact of the surface conditions. Table 4.2 presents the characteristics of the simulations referred to in this section.

#### IOP6

Two simulations were constructed in order to demonstrate the relative importance of the initial atmospheric and surface conditions for this case. Simulation $WF - AP_s$ uses IC containing the atmospheric conditions of an ECMWF analysis while the surface conditions were taken from the ARPEGE analysis. BC from the ECMWF analysis were used. Simulation $AP - WF_s$ had the inverse situation, with the initial atmospheric

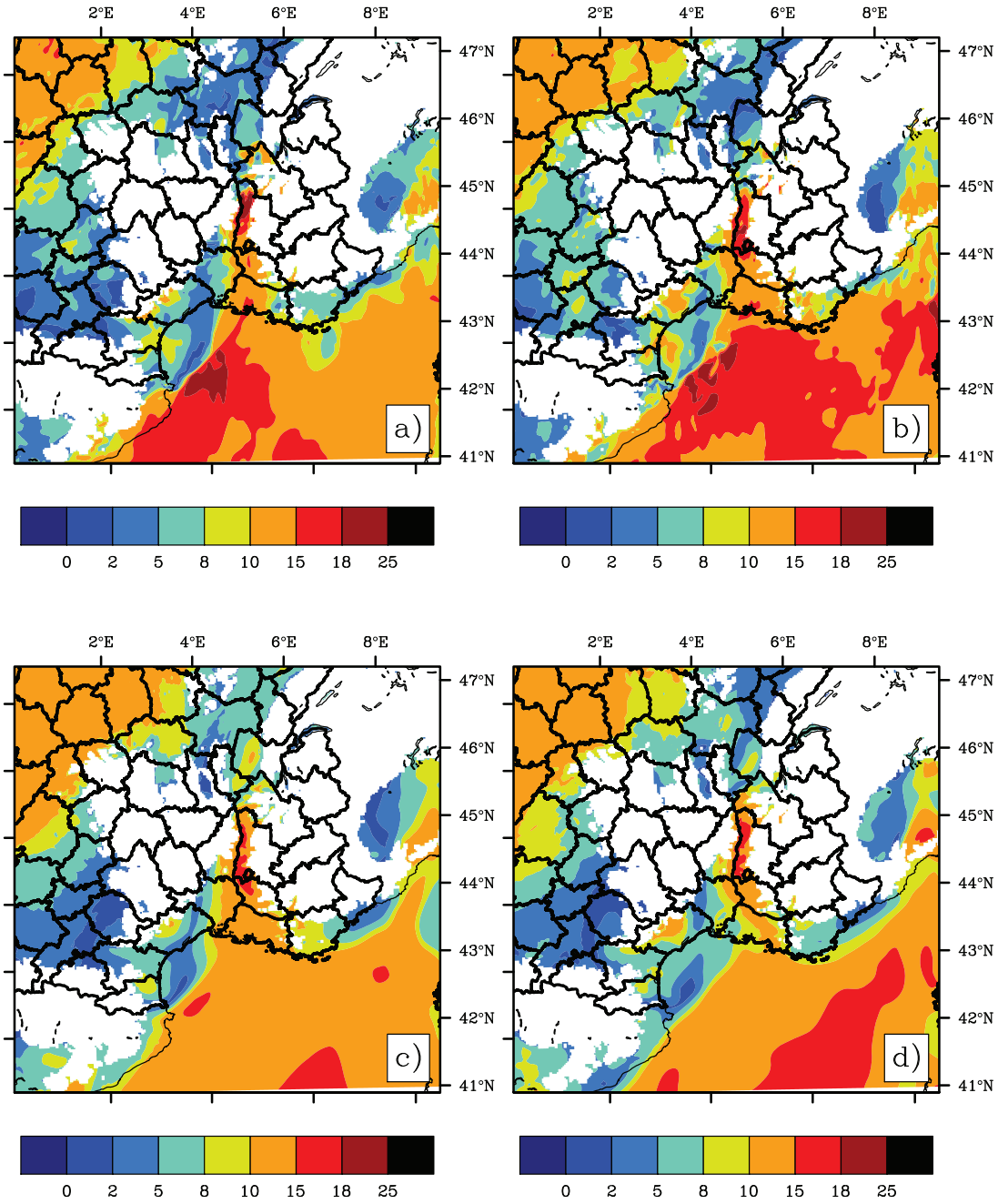


**Figure 4.19:** *The wind at 950hPa ($m/s$) for the BC of the $AR$ (a), $WM$ (b), $WF$ (c) and $AP$ (d) simulations at 12UTC on the 26th of September.*

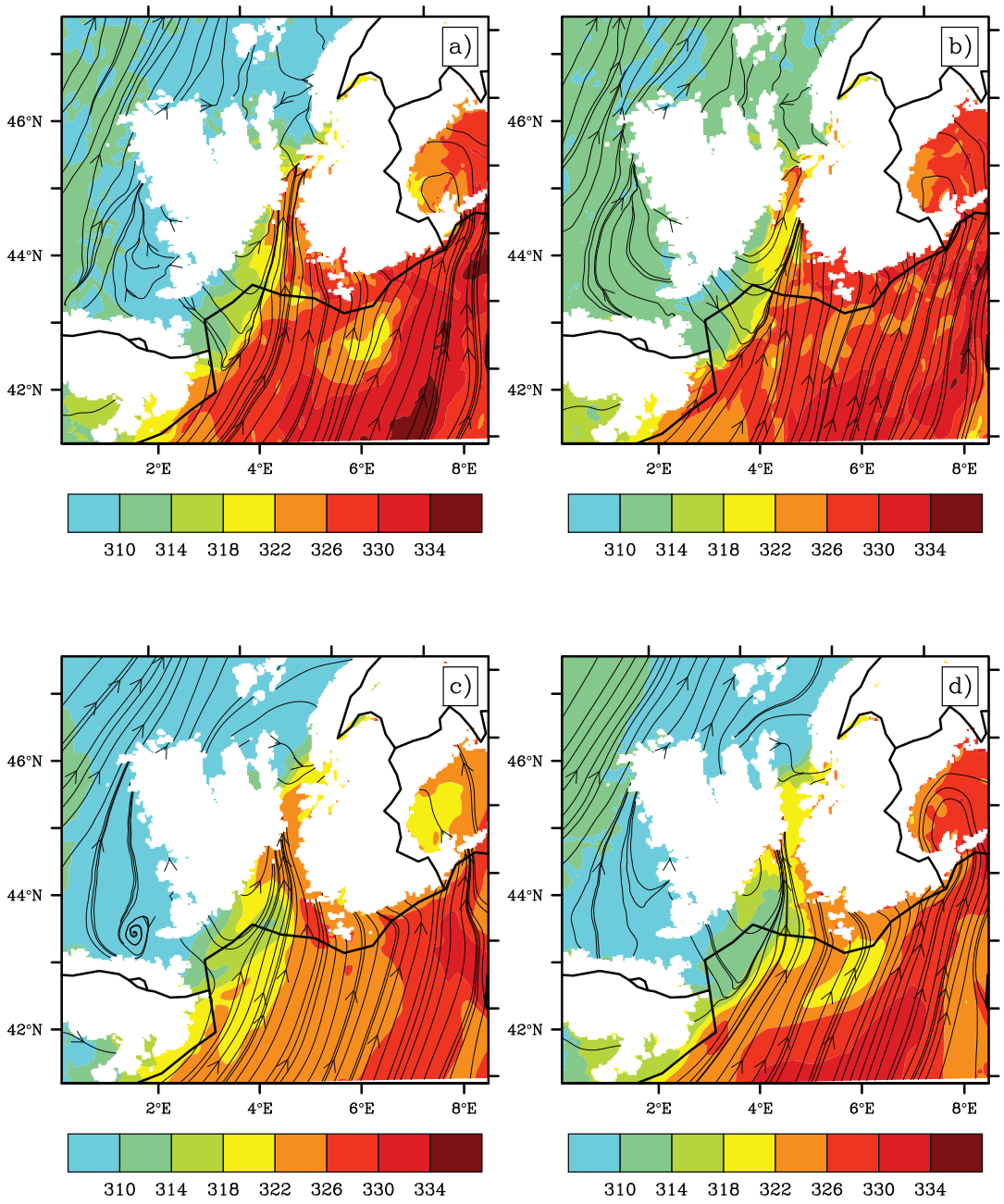


**Figure 4.20:** *The flow streamlines and $\theta_e$ (K) at 950hPa in the BC of the $AR$ (a), $WM$ (b), $WF$ (c) and $AP$ (d) simulations at 12UTC on the 26th of September for the domain shown in Fig.3 (a) of the research article in section 4.2.*

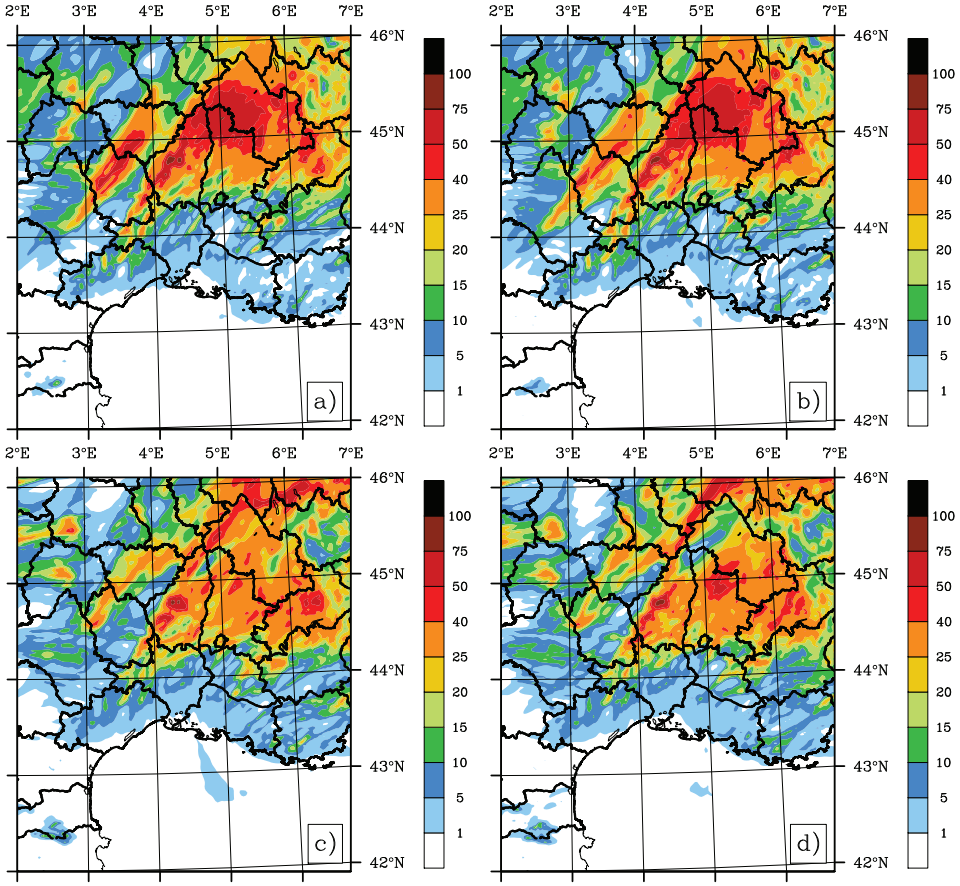


**Figure 4.21:** *The accumulated 24 h rainfall (mm) of the $WF$ (a), $WF - AP_s$ (b), $AP$ (c) and $AP - WF_s$ simulations (d) for IOP6.*

conditions of ARPEGE and initial surface conditions of ECMWF. BC from the ARPEGE analysis were employed for this simulation.

Fig. 4.21 displays the simulated rainfall for the $WF$ (a), $WF - AP_s$ (b), $AP$ (c) and $AP - WF_s$ simulations (d). The differences between the $WF(AP)$ and $WF - AP_s(AP - WF_s)$ simulations is almost negligible. The pattern of precipitation produced by $WF(AP)$ is almost identically reproduced by $WF - AP_s(AP - WF_s)$ with only minor changes to the simulated intensity. This suggests a much greater influence of the atmospheric conditions than the surface conditions. The temporal evolution plot in Fig. 4.22 and Taylor diagram in Fig. 4.23 confirm this point. The $WF - AP_s(AP - WF_s)$ simulation displays the same evolution profile and virtually identical statistics as the $WF(AP)$ simulation.

### IOP7a

This almost complete dependence on the atmospheric conditions is repeated for the IOP7a case. The 24 h accumulated rainfall fields in Fig. 4.24 show negligible if any difference between the $WF(AP)$ and $WF - AP_s(AP - WF_s)$ simulations, as seen for IOP6. The temporal evolution plot in Fig. 4.24 and Taylor diagram in Fig. 4.26 again confirm the lack of influence of the perturbed surface conditions, displaying identical

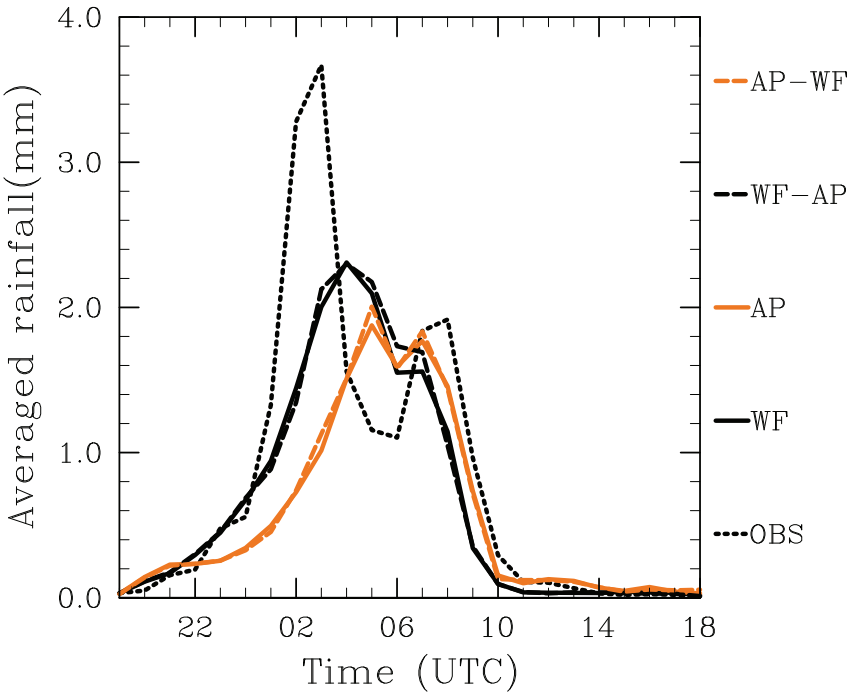


**Figure 4.22:** *The temporal evolution of the spatially-averaged hourly accumulated rainfall of the $WF$, $AP$, $WF - AP_s$ and $AP - WF_s$ simulations for IOP6.*

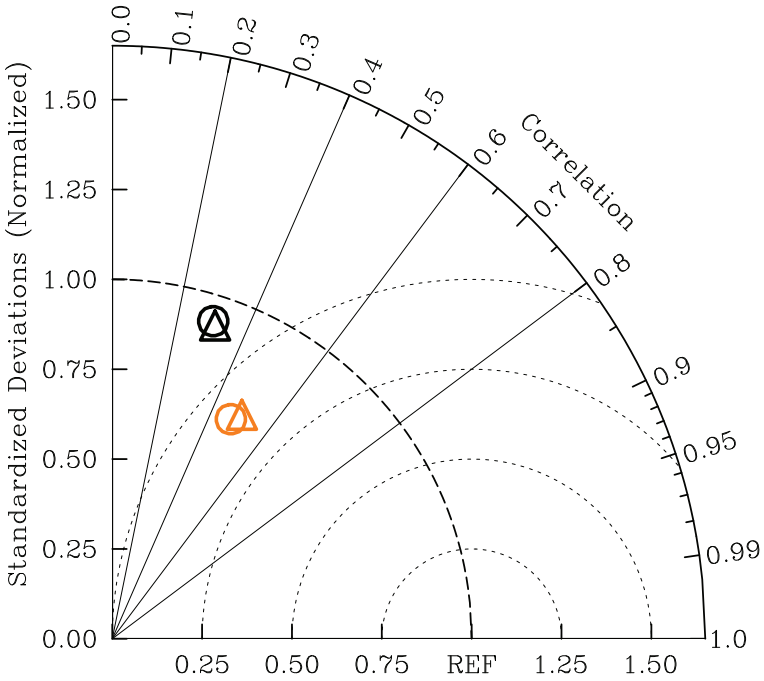


**Figure 4.23:** *24h Taylor diagram displaying the spatial correlation, standard deviation and RMSE of the simulated rainfall with the observed rainfall for the $WF$ (black circle), $AP$ (orange circle), $WF - AP_s$ (black triangle) and $AP - WF_s$ (orange triangle) simulations of the IOP6 case.*

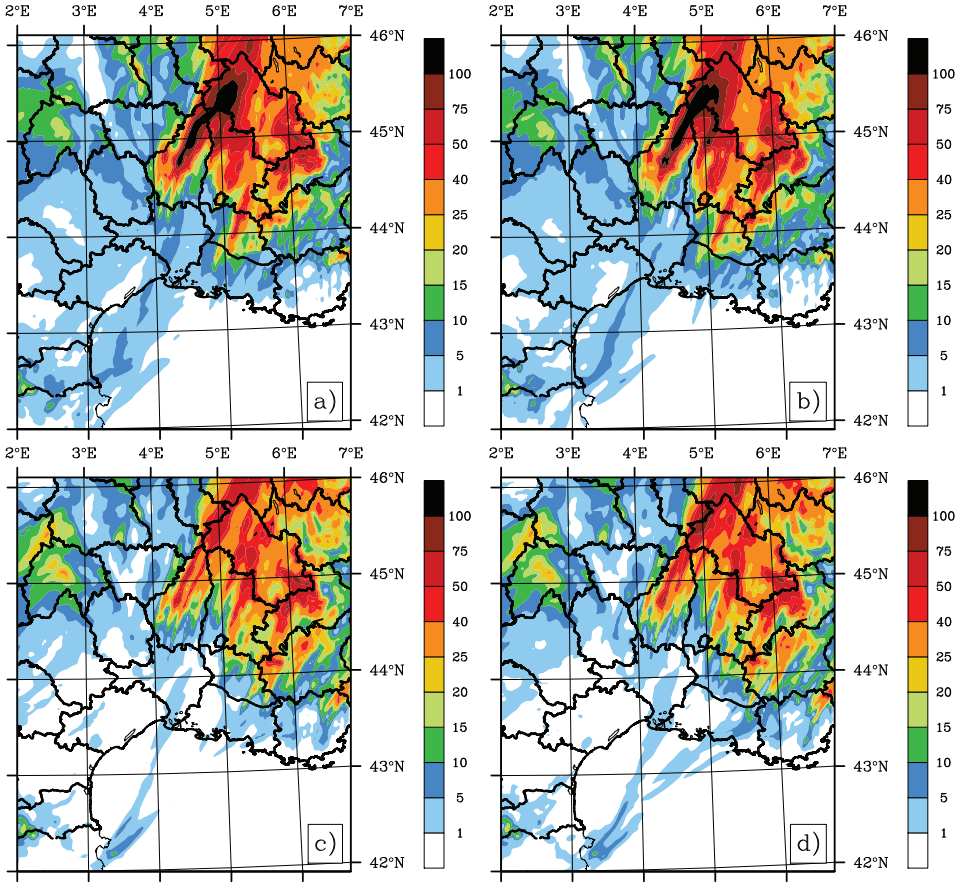


**Figure 4.24:** *The accumulated 24 h rainfall (mm) of the $WF$ (a), $WF - AP_s$ (b), $AP$ (c) and $AP - WF_s$ simulations (d) for IOP7a.*

rainfall evolutions and 24 h statistics.

The almost zero sensitivity to the surface conditions for both cases is perhaps related to two important details. For both cases, the convective rainfall was simulated at 05UTC and 08UTC. At night, the lack of a heat source reduces the amount of energy transfer between the surface and the atmosphere. This limits the relationship between the conditions at the surface and the triggering of convection. Secondly, and perhaps more importantly, both cases had strong synoptic forcing. IOP6 was related to a large-upper level trough over western Europe which in turn was associated to a low pressure system to the north-west of Ireland. IOP7a was influenced by the same upper-level trough, which deepened and pushed eastwards between the 24th and 26th of September. The rainfall peak seen at 17UTC was associated to a cold front which passed over the precipitating zone during the day of the 26th. Any signal introduced into the $WF - AP_s$ and $AP - WF_s$ simulations by modifying their initial surface conditions was quickly overcome by the much stronger synoptic signal.

If similar tests were performed for weakly synoptic cases, the impact upon the convective rainfall pattern could have been greater. Barthlott and Kalthoff (2011) undertook such sensitivity tests and demonstrated that when the synoptic signal is weak, the triggering of convection is most heavily related to soil-atmosphere interactions and the

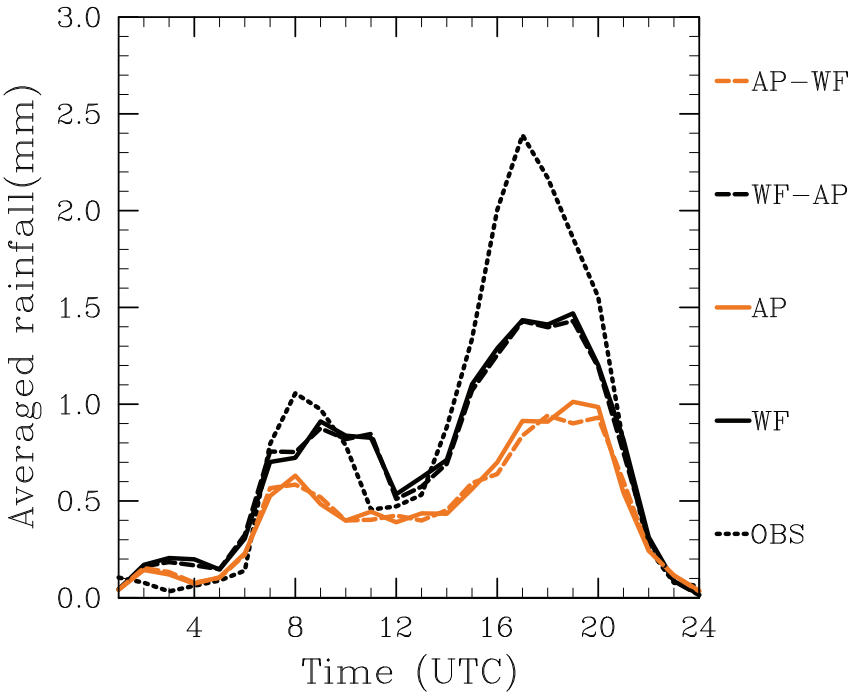


**Figure 4.25:** *The temporal evolution of the spatially-averaged hourly accumulated rainfall of the $WF$, $AP$, $WF - AP_s$ and $AP - WF_s$ simulations for IOP7a.*

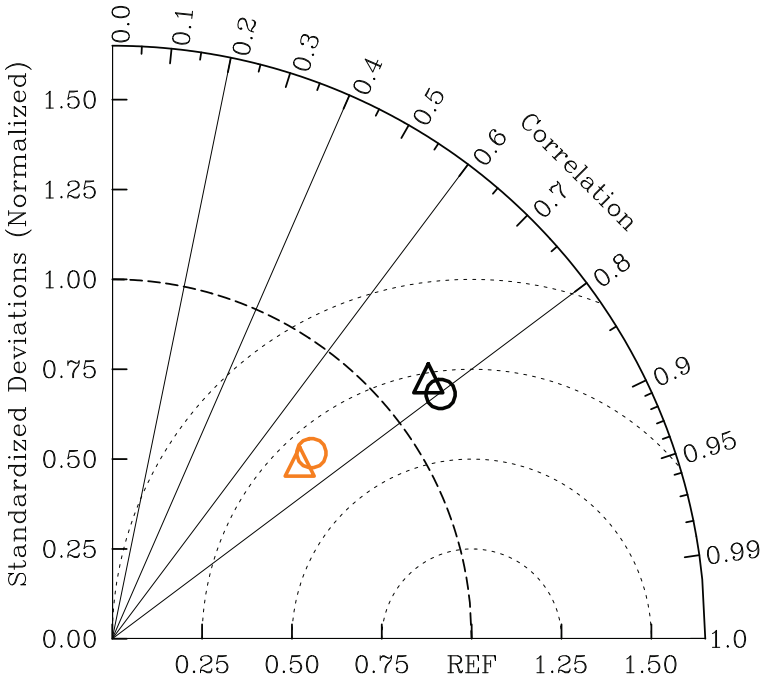


**Figure 4.26:** *24h Taylor diagram displaying the spatial correlation, standard deviation and RMSE of the simulated rainfall with the observed rainfall for the $WF$ (black circle), $AP$ (orange circle), $WF - AP_s$ (black triangle) and $AP - WF_s$ (orange triangle) simulations of the IOP7a case.*

boundary layer turbulent processes.

### 4.3.3 Conclusions - Other factors in rainfall development

A number of simulations were performed to examine the contribution of the initial condition (IC), boundary condition (BC) and atmospheric and surface conditions to the evolution of the surface rainfall for two convective events, IOP6 and IOP7a, from the HyMeX SOP1. The importance of the IC and BC for each IOP seems to depend upon the initialisation time of the simulation relative to the time at which the rainfall occurred. For IOP6, the convective rainfall was simulated at 05UTC on the 24th of September with an initialisation of the simulation at 18UTC on the 23rd. This led to the BC being more important for the rainfall development than the IC. It was suggested that the different rainfall representations of the $AR$, $WM$, $WF$ and $AP$ simulations were related to differences in the equivalent potential temperature ($\theta_e$) and strength of the low-level flow at the boundary. Simulations which demonstrated stronger flow and more humid air at the southern boundary of the domain ($AR$) gave heavier precipitation further downstream.

IOP7a presented two rainfall maximums. A convective rainfall peak was simulated at 08UTC on the 26th of September while a heavy stratiform peak occurred at 17UTC. For the peak at 08UTC, the IC appeared more important than the BC while the peak at 17UTC was strongly influenced by the BC. As for IOP6, it was suggested that the different intensities of both peaks were related to contrasting low-level flow strengths and differences in the representation of $\theta_e$. For both situations, these discrepancies in the IC and/or BC were especially apparent in the marine inflow where the density of observations is sparse. This justifies the large effort which was made during the HyMeX SOP1 to improve the quality and quantity of marine observations.

Sensitivity tests done to examine the contribution of the atmospheric and surface conditions showed that as both cases developed under strong synoptic forcing, the influence of the surface conditions was weak and the rainfall evolution was almost entirely controlled by the atmospheric conditions.

# Conclusions and perspectives

Heavy precipitation events (HPEs) affect the Mediterranean basin between September and November each year. These events have devastating effects on the local communities causing loss of life and social and economic upheaval. South-eastern France is one of the regions most affected with a number of catastrophic events occurring in recent years. Numerical forecasting of these HPEs has seen much progress in the last number of years but problems still remain with the representation of sub-scale processes which occur at resolutions below the current available horizontal resolution of most models. Because of this, these processes are modeled using sets of equations known as parameterisations. These parameterisations cannot give a full complete description of the interaction and evolution of the sub-scale processes and thus assumptions are made. Using these assumptions leads to the introduction of inaccuracies in the representation of the processes and thus can lead to an incorrect forecast of the development of a HPE. The microphysical cloud and boundary layer turbulence processes are two sets of sub-scale processes, important to the forecasting of a HPE, which are represented by sets of parameterisations.

In order to overcome this problem, the use of probabilistic forecasting systems in place of traditional deterministic systems was proposed. Ensemble prediction systems (EPSs) use a number of forecasts each containing individual perturbations which are supposed to represent the natural uncertainties present in the initial atmospheric state and in the model formulation. This allows the development of a probabilistic picture of future atmospheric situations rather than one single deterministic picture. A methodology was formulated whereby perturbations were introduced upon the microphysical and turbulence processes to take into account the inherent inaccuracies in their respective parameterisations. The perturbation factor employed allowed the value of the processes to be randomly increased or decreased by a maximum of 50%. Alternatively, a methodology which consisted of varying the adjustable parameters of the microphysical parameterisation scheme was also explored. All of the simulations were performed with the French research model, Méso-NH.

To assess and test the ensemble methodology, a number of idealised case studies were used. The evolution and sensitivity of the rainfall field of a supercell to perturbations upon the microphysical and turbulence parameterisations was tested. Ensemble simulations showed that the rainfall field was sensitive to the value of the rain and graupel distribution intercept parameters, $N_{0r}$ and $N_{0g}$. Individual cold microphysical processes were shown to have a limited impact upon the evolution of the rainfall field, while simultaneously perturbing all the cold processes induced moderate dis-

persion. An increased level of dispersion was found for perturbations upon the warm microphysical processes. The accretion of cloud droplets by raindrops and the rain evaporation processes were demonstrated to be particularly important in the rainfall evolution. A combination of perturbations upon the warm, cold and turbulence processes introduced the greatest degree of dispersion in the surface rainfall field. It was demonstrated however that perturbing the cold processes brings about little increase in the ensemble dispersion when compared to perturbations upon the warm and turbulence processes. The processes to which the rainfall field was most sensitive were perturbed in ensembles constructed for the meteorologically more complex situation of an idealised squall line. An ensemble where the warm, cold and turbulence processes were perturbed again led to the greatest dispersion in the surface rainfall field.

To test this methodology on real world HPEs, five events were chosen from September and November 2010 and 2011. The case of the 6th of September 2010 was used as a test case for the calibration of the perturbation factor for real world events. The range of the perturbation factor was extended to investigate the impact of using much stronger (weaker) perturbations upon the surface rainfall field. It was found that the range used for the idealised case studies (where the physical processes could be increased or decreased by a factor of 50%) gave the most dispersive rainfall fields. Following the results of the idealised case studies, perturbations were introduced solely upon the rain accretion, rain evaporation and turbulence processes for these five events. A maximum in ensemble dispersion was demonstrated when the warm and turbulent processes were simultaneously perturbed, as was the case for the idealised cases. HPEs where the control run (CTRL) had a high level of model skill demonstrated much less dispersion in ensembles with physical perturbations than those HPEs whose CTRL run had a moderate to low level of model skill. The level of dispersion was shown to be related to the convective trigger. When the HPE was triggered by the local orography, very little dispersion was induced in the rainfall field by physical perturbations. However, when the HPE convection was triggered by an evaporative cold pool, the level of dispersion was increased. The strength of the low-level flow towards the precipitating area was also a determining factor in the level of dispersion. Cases with strong inflow showed little dispersion, while more moderate flow led to an increase in sensitivity.

In order to compare to the idealised squall line tests, two real world convective lines were chosen from the SOP1 of the HyMeX project. These occurred on the 24th and 26th of September 2012 and produced contrasting rainfall patterns. The case of the 24th of September (IOP6 in the SOP1) had moderate to weak low-level inflow and rain which fell mainly on the plains towards the coast. The episode which occurred on the 26th (IOP7a in the SOP1) involved convective rainfall over the local mountainous regions accompanied by stratiform rainfall related to a cold front. Ensembles were constructed perturbing the warm, cold and turbulence processes as for the idealised cases. Results show that the hierarchy of dispersive processes uncovered for the idealised squall line is respected as the warm, cold and turbulence ensemble gave the greatest level of dispersion for both cases. The contribution of the cold processes to the dispersion, as also shown by the idealised simulations, was weak. The rainfall pattern

of IOP6 gave a greater level of sensitivity to the perturbations than the rainfall of IOP7a. This confirmed the results obtained for the events of 2010 and 2011. The sensitivity of the surface rainfall to physical perturbations is more important when precipitation is observed on the plains and under the influence of a weak incident low-level flow.

Ensembles were also constructed for IOP6 and IOP7a using four different sets of initial (IC) and boundary (BC) conditions from the AROME, AROME-WMED, ECMWF and ARPEGE model analysis. Comparing the level of dispersion in these ensembles to that of the physical process ensembles showed that depending on the model skill and strength of the low-level flow, the level of dispersion was comparable (IOP6), or greater in the ICBC ensembles (IOP7a). Additional simulations were performed to examine the respective roles of the IC and BC for both cases. For IOP6, it was found that the BC were important for the localisation, timing and intensity of the rainfall peak. The IC played a less important role and were possibly related to an area of rainfall occurring earlier than the peak. The IOP7a gave two rainfall peaks, one convective and one stratiform. The convective peak occurred shortly after the simulation initialisation while the stratiform peak appeared much later. The BC were demonstrated to be more important than the IC for the evolution of the stratiform peak, while the IC played a bigger role in localising and controlling the intensity of the convective precipitation. The contribution of the atmospheric and surface conditions to the rainfall pattern was also investigated. It was illustrated that, as both cases had strong synoptic forcing, the influence of the surface conditions was almost negligible and the evolution of the different rainfall peaks was virtually entirely controlled by the atmospheric conditions.

As a general conclusion, even though the impact of perturbations upon the parameterisations of the physical processes is relatively weak, it is sufficiently important in certain situations to justify an integration of such perturbations into an operational EPS. However, an EPS cannot be correctly evaluated solely on a series of case studies. Before implementing such an EPS in an operational framework, a prolonged investigation over a significant time period (e.g. for the entirety of the HyMeX SOP) would be needed. This would allow a verification of the system in terms of its accuracy, skill, reliability and resolution.

The methodology employed in constructing the EPS also leads to a number of questions. To simplify the approach, a random perturbation, constant in space and in time whose maximum amplitude was generally limited to plus/minus 50%, was chosen. These were arbitrary choices and thus demand further scrutiny. The perturbation amplitude could be better calibrated either by compiling different sets of observations or by using different parameterisation schemes. This would permit the range of uncertainty related to each process to be more accurately examined and thus allow a more suitable perturbation amplitude to be formulated. However, this task may prove difficult, particularly for the cold processes which control the interaction of hydrometeors whose nature and shape are quite variable. Using a coefficient of perturbation which is constant in space and time is also a questionable approach. One could envisage the use of time and space ranges which are based on precipitation or radar observation variogrammes and which could take into account spatio-temporal auto-correlation distances of the hydrometeors.

Finally, one other investigative route worthy of further study would be the impact of physical perturbations as a function of model resolution. The simulations undertaken during this thesis remained within the 1km - 2.5km range, but the impact of the perturbations demonstrated a sensitivity to an increase in the resolution. The simulations performed in Fresnay *et al.* (2012), on case studies similar to those presented in this study, seem to confirm this result. Other investigations of this sensitivity would be of great interest, with the HyMeX SOP again presenting itself as an appropriate dataset upon which this hypothesis could be tested.

# Conclusions et perspectives

Des événements fortement précipitants affectent la région de la Méditerranée nord-occidentale chaque année entre les mois de septembre et novembre. Ces événements ont des effets dévastateurs pour les communautés locales, conduisent souvent à des pertes de vie humaines et bouleversent la vie sociale et économique. Le sud-est de la France est une des régions les plus touchées et a connu un grand nombre d'événements catastrophiques dans les dernières années. La prévision numérique de ces événements a fortement progressé récemment mais demeure encore délicate, surtout dans la représentation des processus de fine-échelle qui pour la plupart se produisent à des échelles inférieures à la résolution horizontale actuelle des modèles. Ces processus sont représentés par une série d'équations ou de paramétrisations. Ces paramétrisations ne peuvent donner qu'une description incomplète de l'interaction et de l'évolution des processus sous-maille et reposent souvent sur des hypothèses grossières. En utilisant ces hypothèses, on introduit des erreurs dans la représentation des processus physiques, erreurs qui vont fortement limiter l'exactitude de la prévision. Les processus de la microphysique des nuages et de la turbulence dans la couche limite sont deux exemples de processus sous-maille qui sont essentiels pour la prévision d'un épisode de fortes pluies et qui sont néanmoins largement paramétrés.

Afin de surmonter ce problème, l'utilisation d'un système de prévision probabiliste offre des perspectives intéressantes. Les systèmes de prévision d'ensemble (*EPSs* en anglais) utilisent un grand nombre de prévisions. Chaque prévision contient une perturbation qui est censée décrire les incertitudes naturelles qui existent dans l'état initial de l'atmosphère ou encore les erreurs du modèle. Ceci permet le développement d'une vision probabiliste des événements météorologiques du futur plutôt que d'en figer une vision déterministe reposant sur une seule réalisation. Au cours de ce travail, nous avons proposé une méthodologie consistant à introduire des perturbations sur les processus de la microphysique des nuages et de la turbulence afin de prendre en compte les erreurs inhérentes à leurs paramétrisations respectives. Le facteur de perturbation utilisé a permis d'augmenter ou diminuer aléatoirement dans une gamme de +-50% chacun des processus mis en jeu. Alternativement, une méthodologie consistant à faire varier les paramètres ajustables du schéma microphysique a été explorée. Toutes les simulations ont été réalisées avec le modèle de recherche de la communauté française, Méso-NH.

Pour évaluer et tester ces méthodologies d'ensemble, un grand nombre de simulations académiques ont été réalisées. Dans un premier temps, l'évolution et la sensibilité du champ de précipitation d'une super-cellule aux perturbations sur les paramétri-

sations de la microphysique et de la turbulence ont été testées. Les résultats de ces simulations d'ensemble ont montré que le champ de précipitation a été sensible à la valeur des paramètres d'interception des distributions de la pluie et du graupel, $N_{0r}$ et $N_{0g}$. Individuellement, les processus de la micro-physique froide n'ont montré qu'un impact limité sur l'évolution du champ de précipitations, alors qu'une perturbation simultanée de tous les processus a donné de la dispersion modérée. Une augmentation du niveau de dispersion a été obtenue pour des perturbations sur les processus de la micro-physique chaude. L'accrétion des gouttelettes de nuages par les gouttes de pluie et l'évaporation de gouttes de pluie se sont révélées particulièrement importantes pour l'évolution de la pluie en surface. Une combinaison des perturbations sur les processus chauds, froids et turbulents ont introduit le plus grand degré de dispersion dans le champ de précipitation en surface. Il a été montré que des perturbations sur les processus froids n'amènent qu'une faible augmentation de la dispersion de l'ensemble en comparaison à la dispersion induite par des perturbations sur les processus chauds et turbulents. Par la suite, les expériences les plus pertinentes ont été reconduites dans le contexte d'une ligne de grains idéalisée. C'est à nouveau l'ensemble où les processus de la microphysique et de la turbulence étaient simultanément perturbés qui a conduit à la plus grande dispersion dans le champ de précipitations de surface.

Afin de tester la méthodologie des perturbations physiques sur des cas réels, cinq événements de fortes précipitations ayant eu lieu lors des automnes 2010 et 2011 ont été sélectionnés. Le cas du 6 septembre 2010 a été utilisé comme cas-test pour calibrer le facteur de perturbation pour des cas réels. La gamme du facteur de perturbation a été élargie dans le but d'étudier l'impact de l'intensité des perturbations sur le champ de précipitations. Il a été trouvé que la gamme de +-50% adoptée pour les cas idéalisés, était la plus satisfaisante. Pour les cinq situations, et suite aux résultats des cas idéalisés, les perturbations ont été introduites uniquement sur l'accrétion de la pluie, l'évaporation de la pluie et les processus turbulents. Un maximum de dispersion a été obtenu lorsque les processus chauds et turbulents ont été perturbés simultanément, conformément aux résultats obtenus pour les cas idéalisés. Les ensembles relatifs aux événements pour lesquels la simulation de contrôle avait une bonne performance se sont montrés moins dispersifs que ceux relatifs aux événements pour lesquels le modèle avait une performance moyenne ou faible. L'intensité de la dispersion a pu être analysée en fonction du mécanisme déclencheur de la convection. Pour les événements déclenchés par le relief local, les perturbations physiques ont induit très peu de dispersion. Par contre, pour les événements déclenchés par une plage froide évaporative, le niveau de dispersion a significativement augmenté. L'intensité du flux incident de basse couche s'est aussi révélé un facteur important pour la dispersion. Les événements associés à un flux fort ont montré moins de dispersion que ceux associés à un flux modéré.

Des simulations d'ensemble ont été réalisées pour deux lignes convectives observées lors la SOP1 d'HyMeX afin d'en comparer les résultats à ceux obtenus pour la ligne de grains idéalisée. Ces deux situations ont eu lieu les 24 et 26 septembre et ont conduit à des évolutions différentes du champ de précipitations. Le cas du 24 septembre (IOP6 de la SOP1) s'est produit sous l'influence d'un flux modéré et la plupart de la

précipitation a été observée sur les plaines. L'événement du 26 septembre (IOP7a de la SOP1) a produit deux maximums de précipitations, avec de la pluie convective sur les régions montagneuses puis de la pluie stratiforme liée à la progression d'un front froid. Des ensembles ont été construits où les processus de la microphysique et de la turbulence ont été perturbés, comme pour les cas idéalisés. Les résultats montrent que la hiérarchie de dispersion obtenue pour la ligne de grains idéalisée est respectée, avec l'ensemble perturbant les processus chauds, froids et turbulents donnant le plus de dispersion pour les deux cas. La contribution des processus froids à la dispersion est restée faible, comme pour les cas idéalisés. L'évolution de la pluie de la IOP6 a montré une plus grande sensibilité aux perturbations que l'évolution de la pluie de la IOP7a. Ceci a confirmé les résultats obtenus pour les événements des automnes 2010 et 2011. La sensibilité des précipitations aux perturbations physiques est plus importante sur les régions de plaine et par flux incident faible.

Des ensembles utilisant quatre jeux différents de conditions initiales et aux limites, provenant des analyses AROME, AROME-WMED, ECMWF and ARPEGE ont aussi été construits pour les cas de la IOP6 et de la IOP7a. Une comparaison entre la dispersion de ces ensembles et celle des ensembles à physique perturbée a montré que selon la performance du modèle et l'intensité du flux de basse couche, la dispersion induite était comparable (IOP6) ou plus forte (IOP7a) dans les ensembles aux conditions initiales et aux limites perturbées. Des simulations additionnelles ont été effectuées afin de discriminer les rôles respectifs des conditions initiales ou aux limites. Pour l'IOP6, ce sont les conditions aux limites qui ont conditionné la localisation, la chronologie et l'intensité de la pluie. Les conditions initiales ont joué un rôle moins important et ont peut-être influencé une zone de précipitations qui a été simulée plus tôt que le maximum. L'IOP7a a donné deux maximums de précipitations, l'un de nature convective, l'autre stratiforme. Le maximum convective a eu lieu peu de temps après l'initialisation de la simulation alors que le maximum stratiforme est arrivée plus tard. Les conditions aux limites ont été plus importantes que les conditions initiales pour l'évolution de la pluie stratiforme alors que les conditions initiales ont plus fortement contrôlé la localisation et l'intensité de la pluie convective. La contribution des conditions atmosphériques et en surface a aussi été étudiée. Il a été montré que comme les deux cas étaient fortement contrôlés par le forçage synoptique, l'influence des conditions en surface était quasiment négligeable et que l'évolution de la pluie était presque entièrement liée aux conditions atmosphériques.

L'ensemble des ces résultats suggère que bien que l'impact des perturbations physiques soit modéré et ne suffise pas à capturer l'erreur de prévision dans son ensemble, il est dans certaines situations suffisamment important pour justifier la prise en compte d'une physique perturbée dans un système de prévision d'ensemble opérationnel. Cependant, un système de prévision d'ensemble ne peut pas être correctement évalué sur une série de cas d'études seulement. Avant toute utilisation opérationnelle, il serait indispensable d'évaluer les résultats de ce travail sur une période de temps plus significative, comme par exemple l'ensemble de la SOP1 de HyMeX, et de vérifier que le système répond aux attentes en termes de précision, performance, fiabilité et résolution.

La méthodologie utilisée pendant cette étude pose différentes questions. Par souci de simplification, une perturbation aléatoire, constante dans l'espace et le temps et d'un amplitude maximale limitée à plus ou moins 50%, a été choisie. Ces choix sont arbitraires et mériteraient plus d'attention. L'amplitude pourrait être mieux calibrée, soit en compilant différents jeux d'observations, soit en utilisant différents jeux de paramétrisations. Ceci permettrait d'affecter à chacun des processus l'incertitude qui lui est propre. Toutefois, cette tâche peut s'avérer délicate, particulièrement pour les processus froids qui régissent l'évolution d'hydrométéores de forme et de nature très variables et pour lesquels moins d'observations sont disponibles. Le fait d'appliquer un coefficient constant dans l'espace et le temps est tout aussi discutable. Il est envisageable d'utiliser des plages d'espace et de temps dont l'estimation serait basée sur le variogramme des précipitations mesurées ou des observations radars et qui ainsi prendrait en compte les distances d'auto-corrélation spatiales et temporelle des hydrométéores.

Enfin, une dernière voie à suivre serait d'étudier l'impact des perturbations physiques en fonction de la résolution du modèle. Les simulations effectuées pour cette thèse sont restées dans la gamme 1km - 2.5km, mais indiquent une sensibilité à l'augmentation de la résolution. Les simulations de Fresnay *et al.* (2012), réalisées pour un cas d'étude à 2.5km et à 500m, semblent confirmer cette tendance. D'autres études sur cette sensibilité seraient d'un grand intérêt, notamment avec les cas observés pendant la SOP1 d'HyMeX qui disposent des données appropriées pour aborder cette étude.

# Appendix A

# List of important symbols

$A = 4\sigma_{w/a}/R_v T \rho_w$
$c$ and $d$ parameters of the fall speed-diameter relationship for the water drops
$C_{vv}$ heat capacity at constant volume of water vapor
$C_{pd}$, $C_{pv}$ and $C_w$ heat capacity at constant pressure of dry air, water vapor and liquid water
$D$, $D_1$ and $D_2$ drop diameters
$D_c$, $D_r$ mean volume drop diameter for cloud droplet and raindrop distributions
$D_v$ diffusivity of water vapor in the air
$e_v$ water vapor pressure
$e_{vs}$ saturation vapor pressure over water
$E_c$ collection efficiency
$\bar{f}$ ventilation factor
$F$ ventilation coefficient
$k_a$ heat conductivity of air
$L_v$ latent heat of vaporization
$n$, $n_c$ and $n_r$ total, cloud droplet and raindrop size distributions
$N_0$ intercept parameter of an exponential distribution law
$N_c$, $N_r$ cloud droplet and raindrop number concentration
$P$ and $P_{00}$ pressure and reference pressure (1000 hPa)
$r_v$, $r_c$ and $r_r$ water vapor, cloud water and rain water mixing ratios
$r_{vs}$ saturated vapor mixing ratio
$R_d$ and $R_v$ gas constant for dry air and water vapor
$Re$ Reynolds number
$t$ time
$T$ and $T_{00}$ temperature and reference temperature (273.16 K)
$V(D)$ drop fall speed of diameter $D$
$z$ height or vertical coordinate
$\alpha_c$, $\alpha_r$ dispersion parameter of the generalized gamma distribution law for the cloud droplets and the raindrops
$\delta t$ time step

$\Gamma(a)$ complete gamma function
$\epsilon = R_v/R_d$
$\theta$ potential temperature
$\lambda_c$, $\lambda_r$ slope parameter of the generalized gamma distribution law for the cloud droplets and the raindrops
$\nu_c$, $\nu_r$ dispersion parameter of the generalized gamma distribution law for the cloud droplets and the raindrops
$\rho_a$ and $\rho_w$ air and liquid water densities
$\rho_{00}$ air density at $P = P_{00}$ and $T = T_{00}$
$\tau$ timescale for autoconversion

# Appendix B

# Complimentary figures of Chapter 2

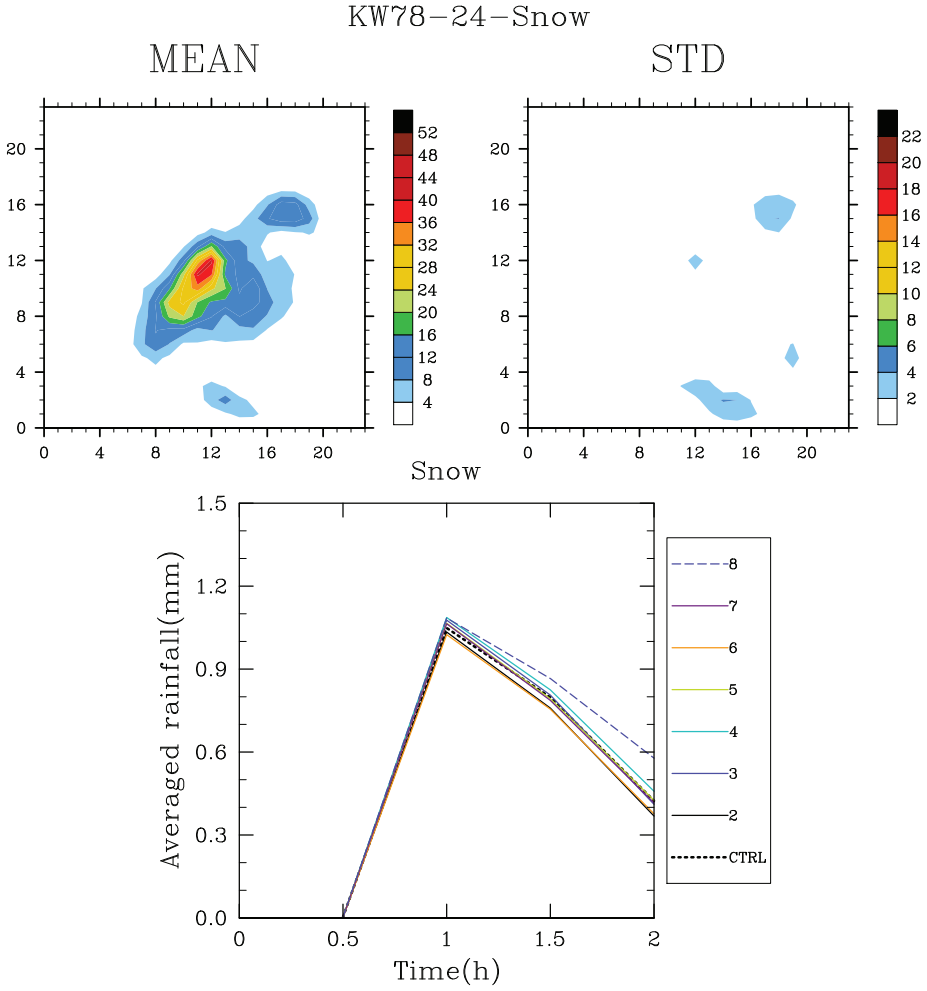


**Figure B.1:** *The mean and standard deviation from the mean of the rainfall field along with the temporal evolution of the rainfall for the Snow ensemble.*

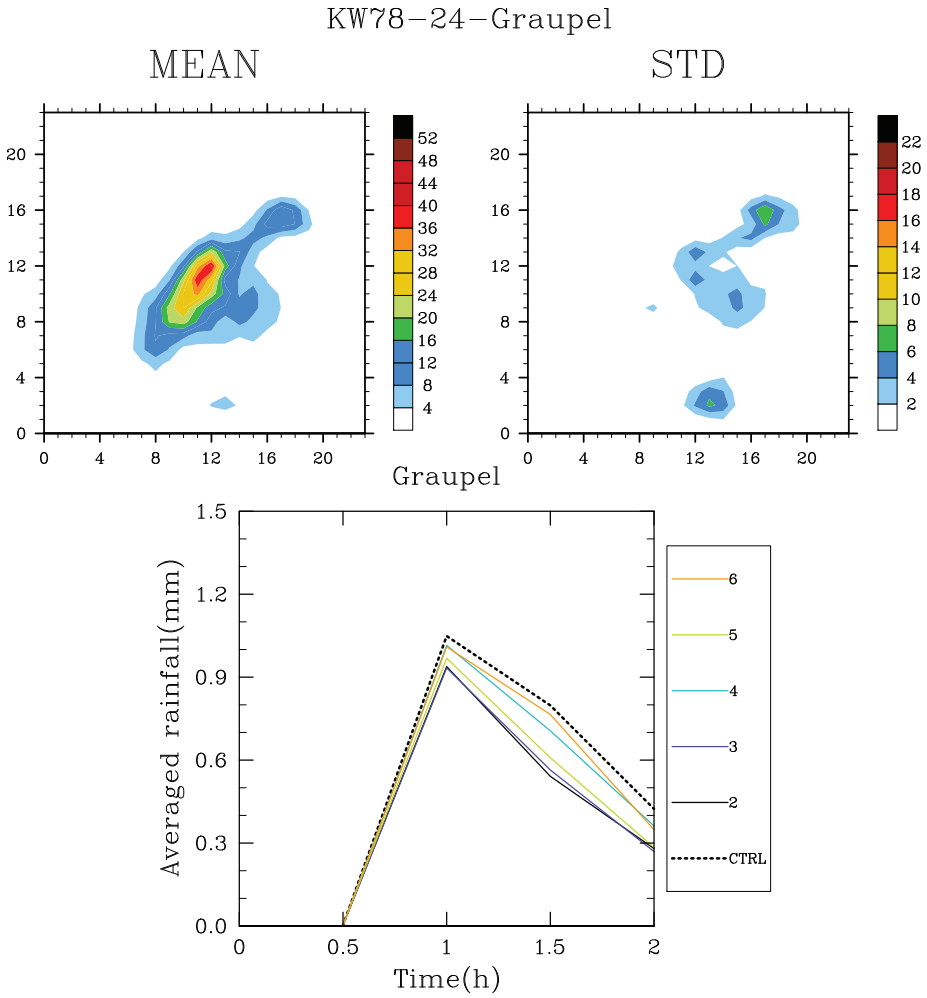


**Figure B.2:** *The mean and standard deviation from the mean of the rainfall field along with the temporal evolution of the rainfall for the Graupel ensemble.*

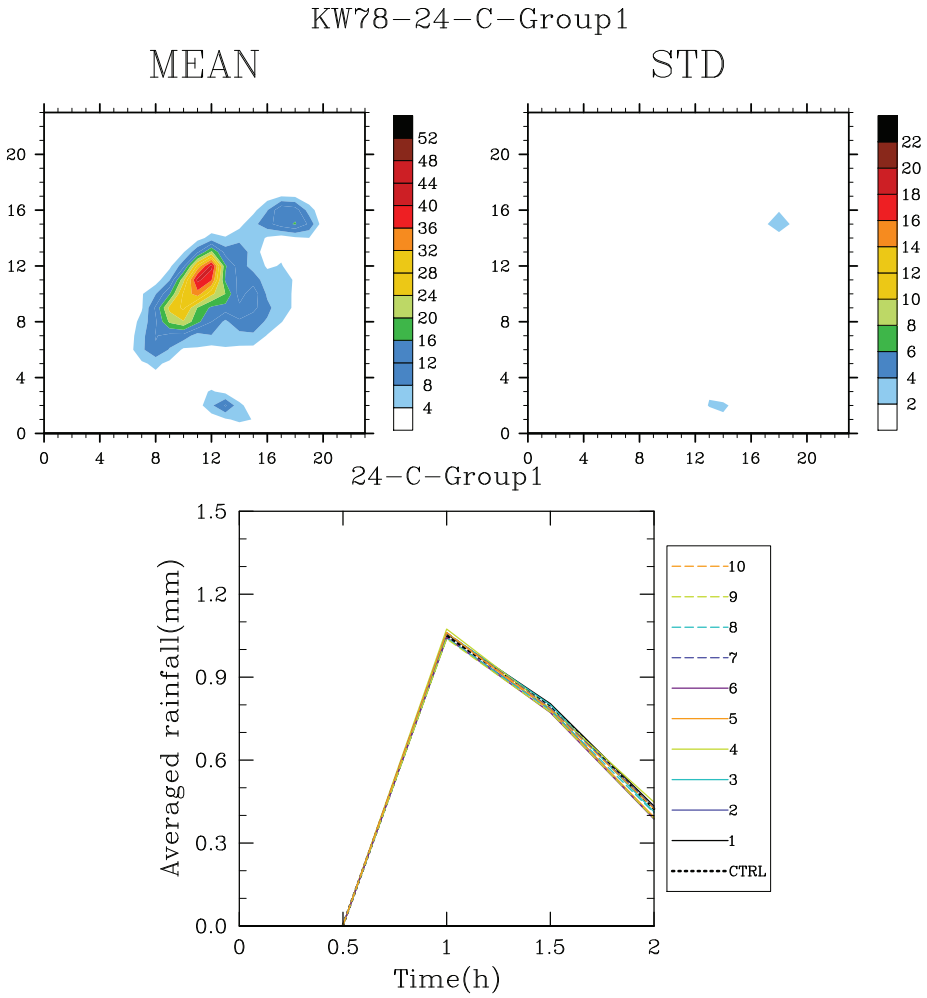


**Figure B.3:** *The mean and standard deviation from the mean of the rainfall field along with the temporal evolution of the rainfall for the 24-C-Group1 ensemble.*

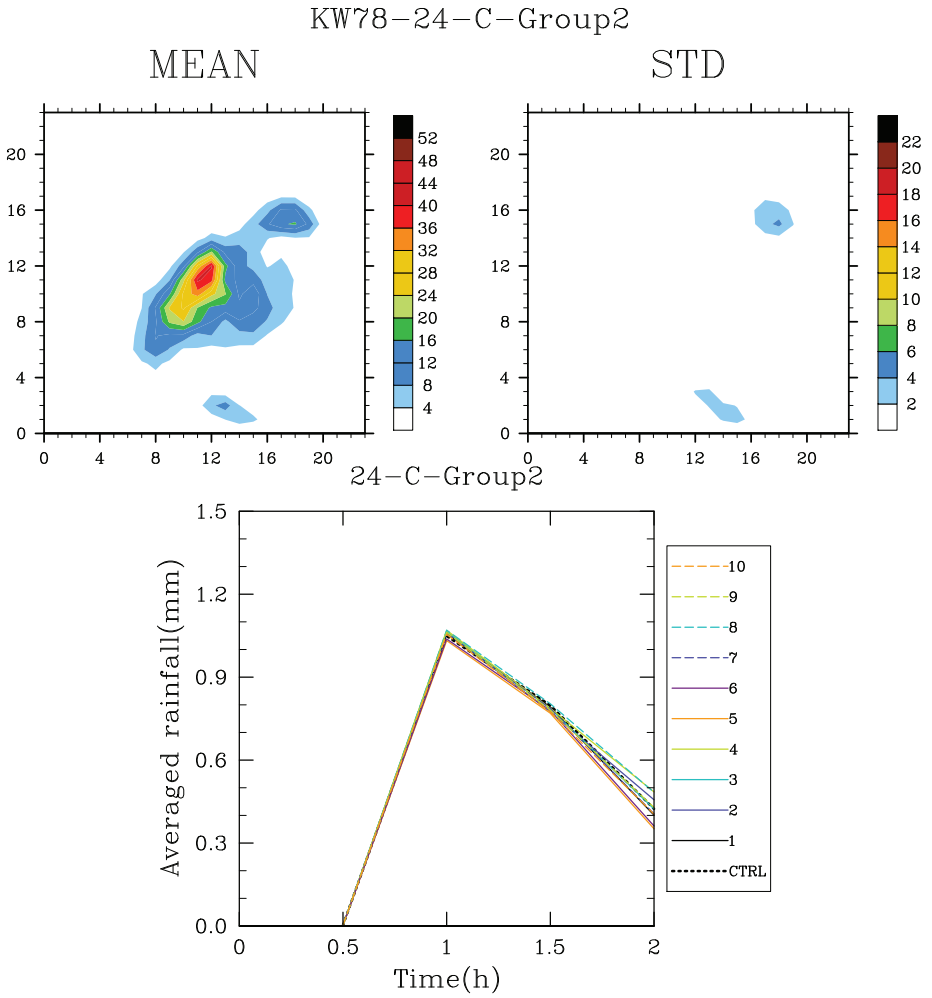


**Figure B.4:** *The mean and standard deviation from the mean of the rainfall field along with the temporal evolution of the rainfall for the 24-C-Group2 ensemble.*

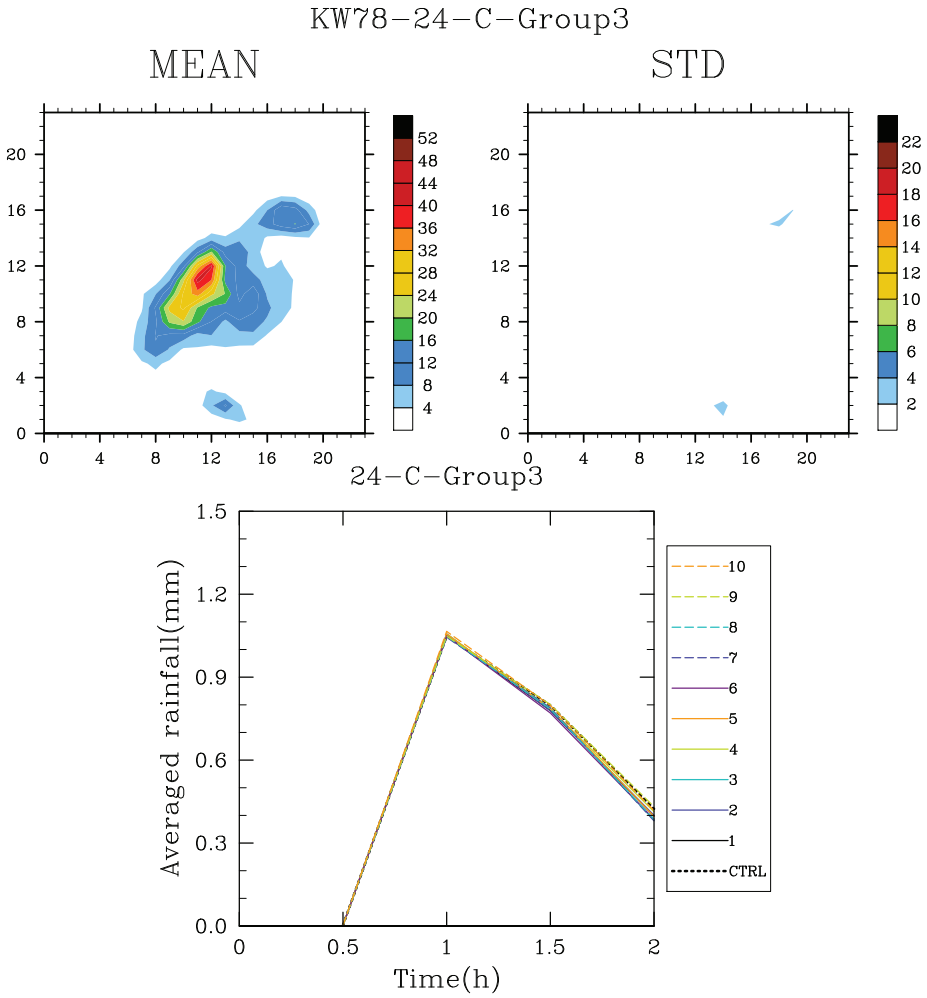


**Figure B.5:** *The mean and standard deviation from the mean of the rainfall field along with the temporal evolution of the rainfall for the 24-C-Group3 ensemble.*

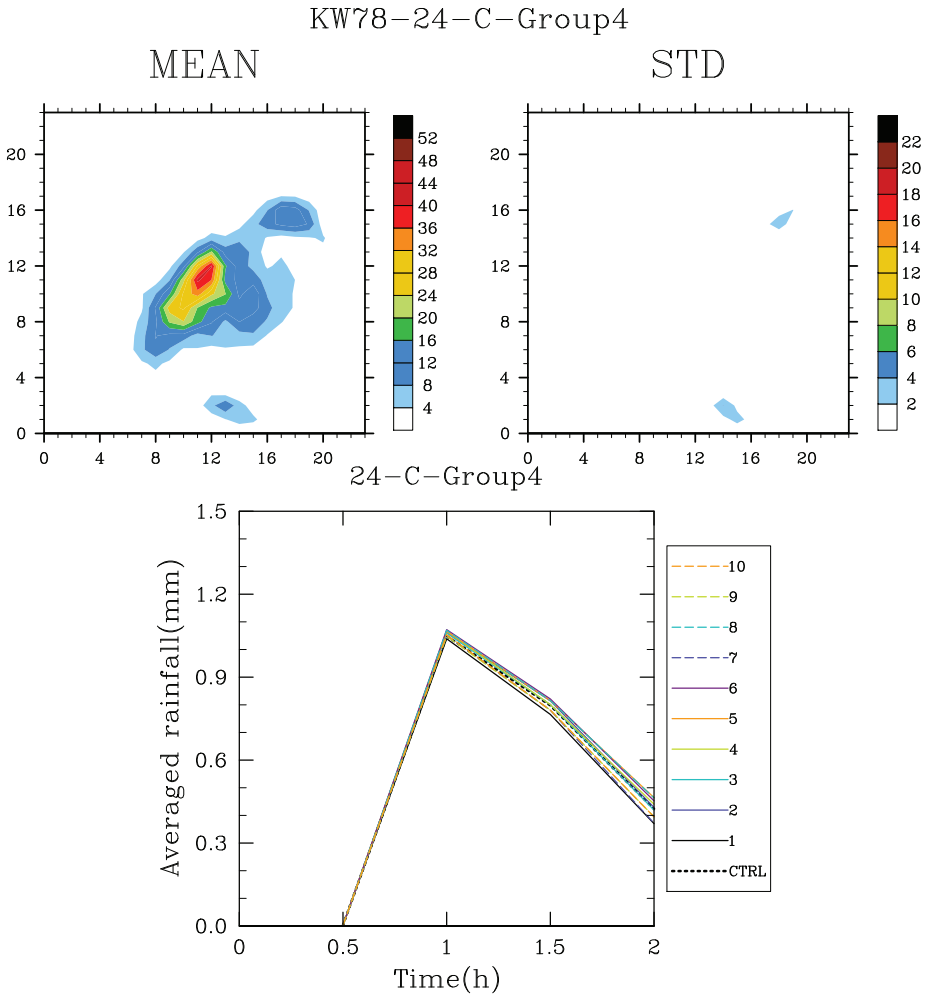


**Figure B.6:** *The mean and standard deviation from the mean of the rainfall field along with the temporal evolution of the rainfall for the 24-C-Group4 ensemble.*

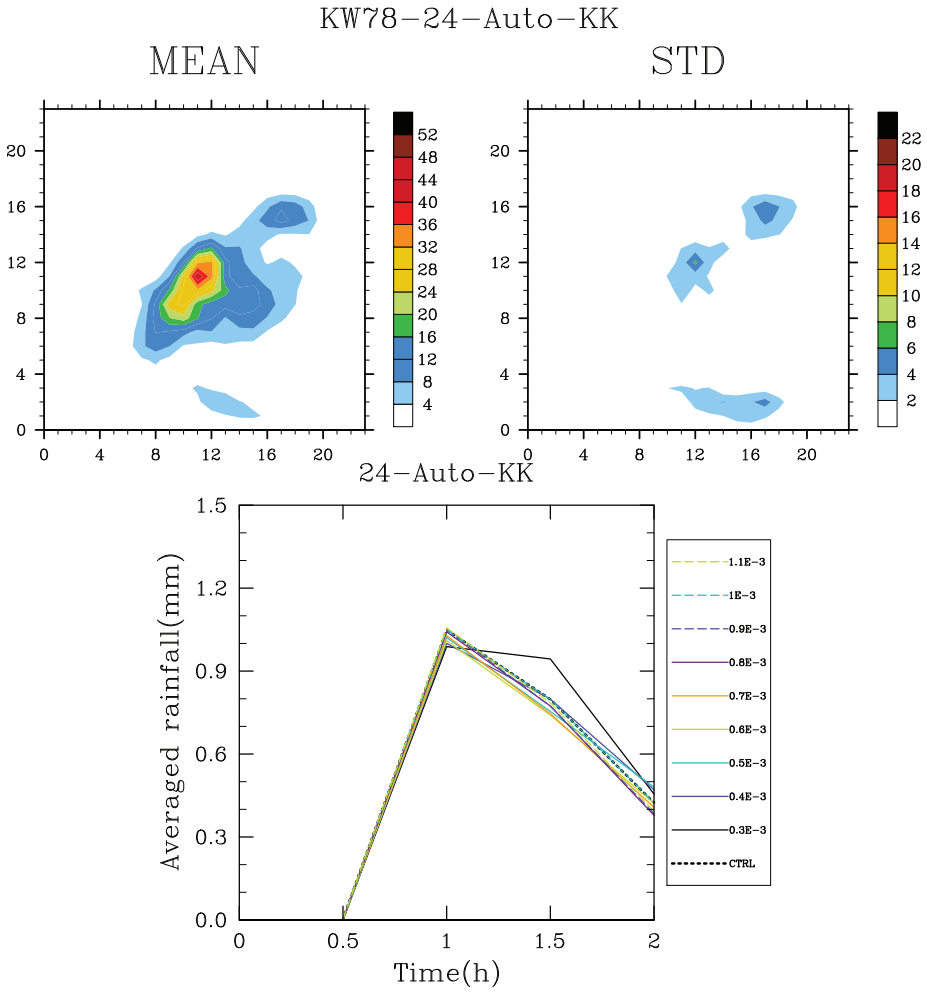


**Figure B.7:** *The mean and standard deviation from the mean of the rainfall field along with the temporal evolution of the rainfall for the 24-Auto-KK ensemble.*

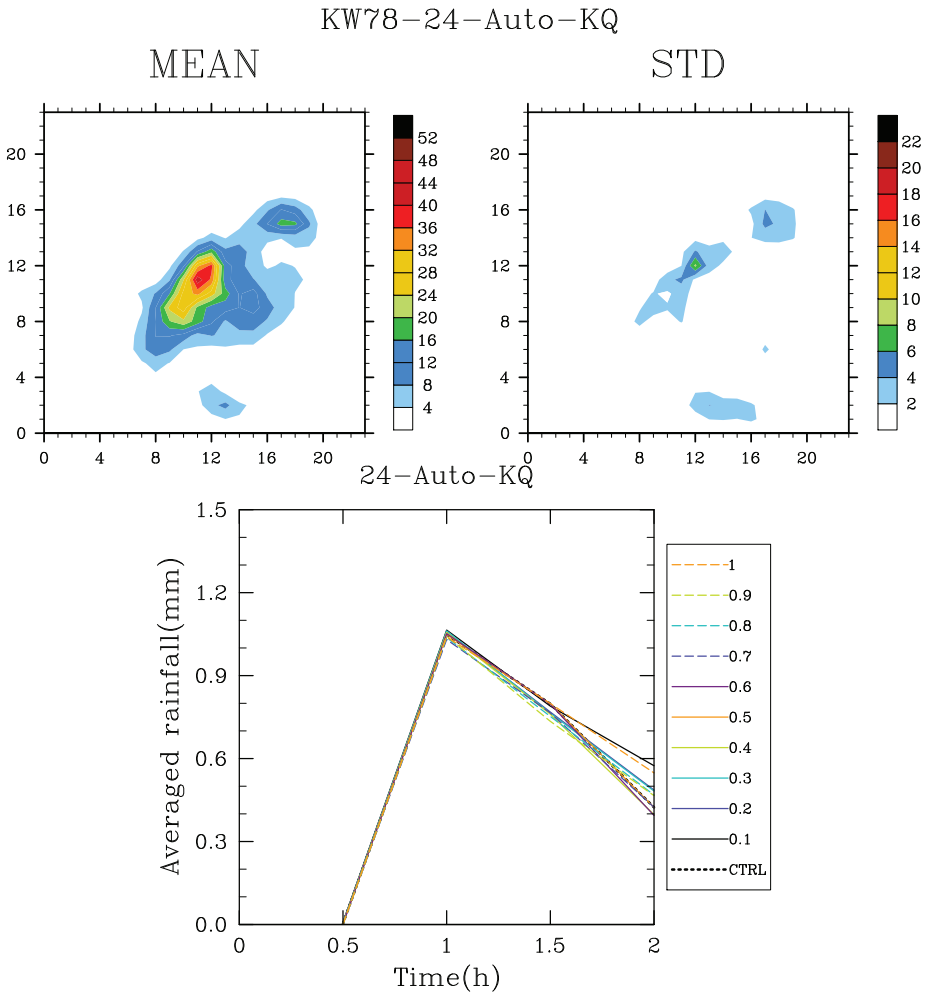


**Figure B.8:** *The mean and standard deviation from the mean of the rainfall field along with the temporal evolution of the rainfall for the 24-Auto-KQ ensemble.*

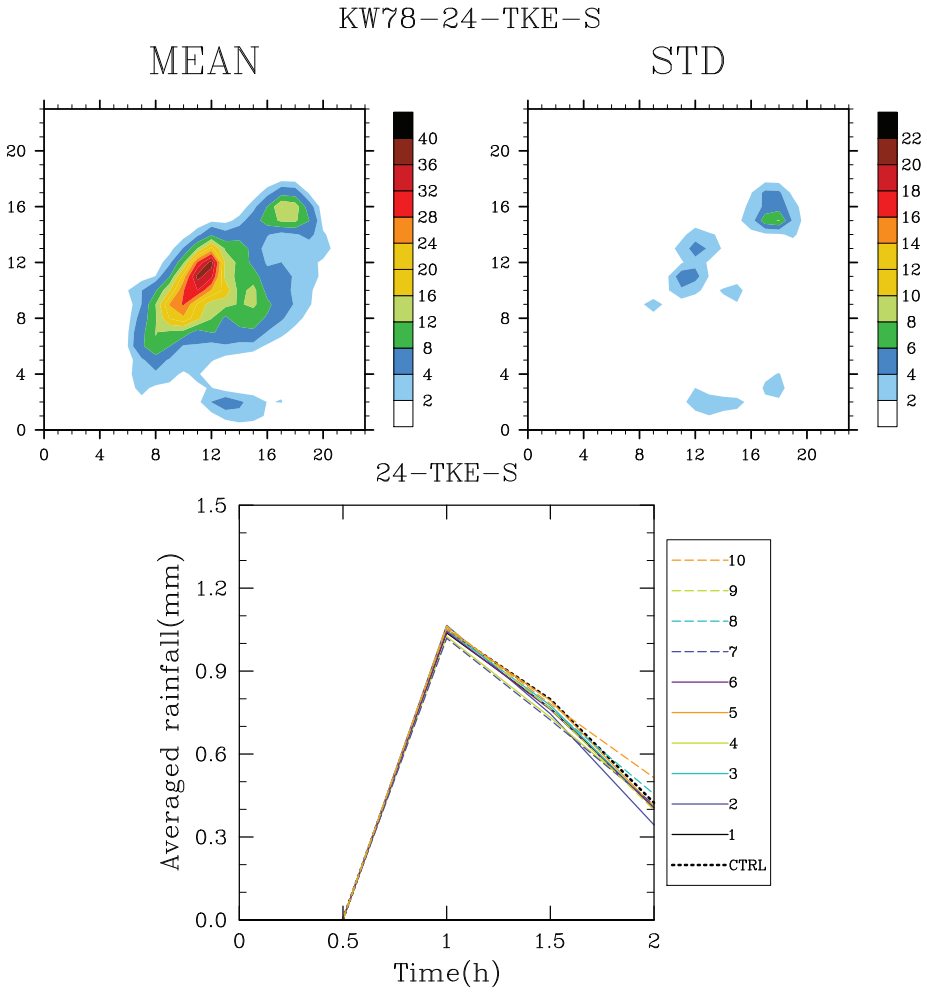


**Figure B.9:** *The mean and standard deviation from the mean of the rainfall field along with the temporal evolution of the rainfall for the 24-TKE-S ensemble.*

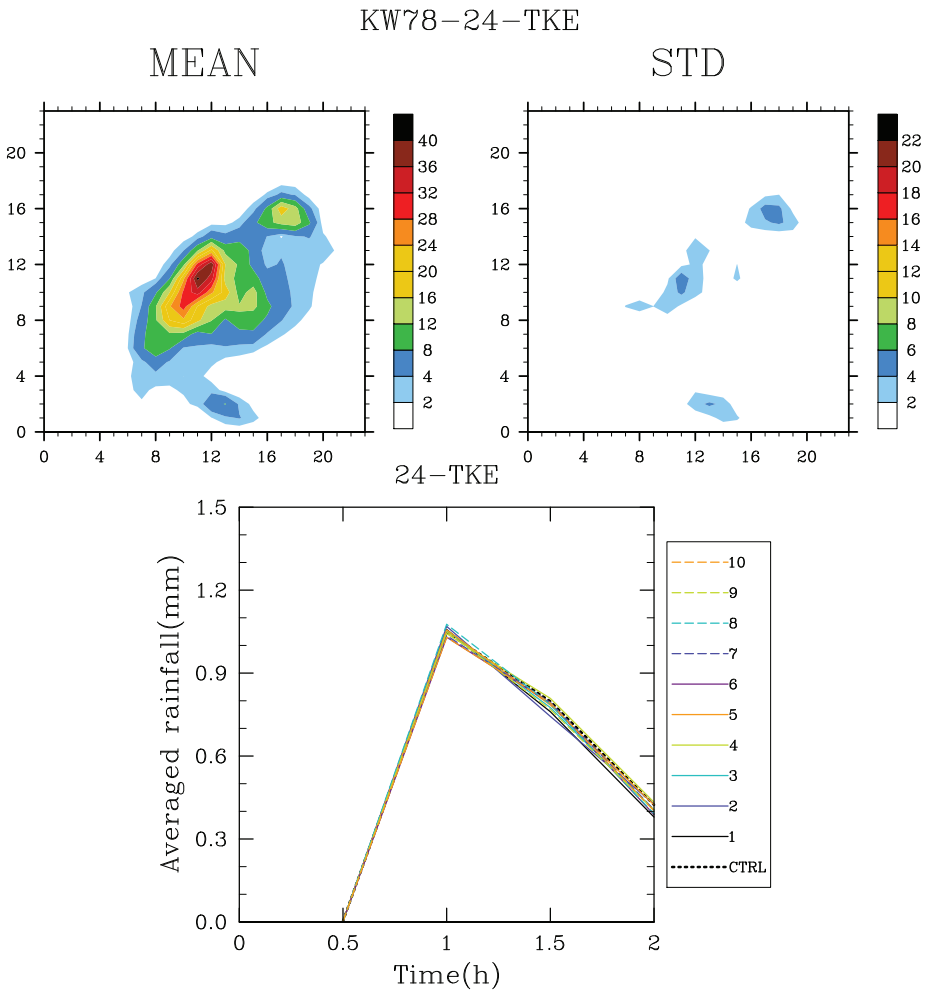


**Figure B.10:** *The mean and standard deviation from the mean of the rainfall field along with the temporal evolution of the rainfall for the 24-TKE ensemble.*

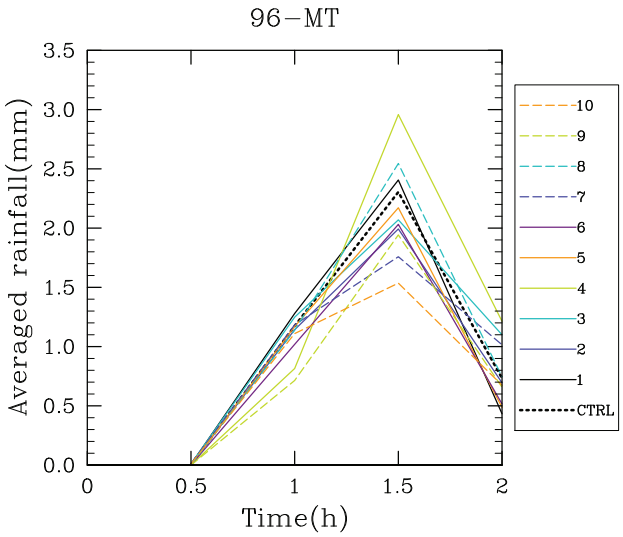


**Figure B.11:** *The temporal evolution of the rainfall for the 96-MT ensemble.*

# Bibliography


Argence S, Lambert D, Richard E, Chaboureau JP, Soehne N. 2008. Impact of initial condition uncertainties on the predictability of heavy rainfall in the mediterranean: a case study. *Quart. J. Roy. Meteor. Soc.* **134**(636): 1775–1788.

Barthlott C, Kalthoff N. 2011. A Numerical Sensitivity Study on the Impact of Soil Moisture on Convection-Related Parameters and Convective Precipitation over Complex Terrain. *J. Atmos. Sci.* **68**(12): 2971–2987.

Berry E, Reinhardt R. 1974a. An analysis of cloud drop growth by collection: Part ii. single initial distributions. *J. Atmos. Sci.* **31**: 1825–1831.

Berry E, Reinhardt R. 1974b. An analysis of cloud drop growth by collection: Part iii. accretion and self-collection. *J. Atmos. Sci.* **31**: 2118–2126.

Bougeault P, Lacarrère P. 1989. Parameterization of orographic induced turbulence in a mesobetascale model. *Mon. Wea. Rev.* **117**: 1872–1890.

Bouttier F, Vie B, Nuissier O, Raynaud L. 2012. Impact of stochastic physics in a convection-permitting ensemble. *Mon. Wea. Rev.* **140**(11): 3706–3721.

Bresson E, Ducrocq V, Nuissier O, Ricard D, de Saint-Aubin C. 2012. Idealized numerical simulations of quasi-stationary convective systems over the Northwestern Mediterranean complex terrain. *Quart. J. Roy. Meteor. Soc.* **138**(668): 1751–1763.

Bresson R, Ricard D, Ducrocq V. 2009. Idealized mesoscale numerical study of mediterranean heavy precipitating convective systems. *Meteorol. Atmos. Phys.* **103**(1-4): 45–55.

Bryan GH, Wyngaard JC, Fritsch JM. 2003. Resolution requirements for the simulation of deep moist convection. *Mon. Wea. Rev.* **131**(10): 2394–2416.

Buizza R, Miller M, Palmer TN. 1999. Stochastic representation of model uncertainties in the ECMWF ensemble prediction system. *Quart. J. Roy. Meteor. Soc.* **125**(560): 2887–2908.

Buzzi A, Tartaglione N, Malguzzi P. 1998. Numerical simulations of the 1994 Piedmont flood: Role of orography and moist processes. *Mon. Wea. Rev.* **126**(9): 2369–2383.

Caniaux G. 1993. Paraméterisation de la phase glace dans un modèle non hydrostatique de nuage: Application à une ligne de grains tropicale. PhD thesis, Université Paul Sabatier (Toulouse).

Caniaux G, Redelsperger JL, Lafore JP. 1994. A numerical study of the stratiform region of a fast-moving squall line .1. general description and water and heat budgets. *J. Atmos. Sci.* **51**(14): 2046–2074.

Clark AJ, Gallus William A J, Xue M, Kong F. 2009. A comparison of precipitation forecast skill between small convection-allowing and large convection-parameterizing ensembles. *Wea. Forecasting* **24**(4): 1121–1140.

Clark AJ, Kain JS, Stensrud DJ, Xue M, Kong F, Coniglio MC, Thomas KW, Wang Y, Brewster K, Gao J, Wang X, Weiss SJ, Du J. 2011. Probabilistic Precipitation Forecast Skill as a Function of Ensemble Size and Spatial Scale in a Convection-Allowing Ensemble. *Mon. Wea. Rev.* **139**(5): 1410–1418.

Cuxart J, Bougeault P, Redelsperger JL. 2000. A turbulence scheme allowing for mesoscale and large-eddy simulations. *Quart. J. Roy. Meteor. Soc.* **126**: 1–30.

Deardorff JW. 1980. Stratocumulus-capped mixed layers derived from a 3-dimensional model. *Boundary-Layer Meteorology* **18**(4): 495–527.

Drofa O. 1997. The parameterization of microphysical processes for atmospheric numerical models. *Il Nuovo Cimento* **26**(3): 233–262.

Du J, Mullen SL, Sanders F. 1997. Short-range ensemble forecasting of quantitative precipitation. *Mon. Wea. Rev.* **125**(10).

Ducrocq V, Nuissier O, Ricard D, Lebeaupin C, Thouvenin T. 2008. A numerical study of three catastrophic precipitating events over southern france. II: Mesoscale triggering and stationarity factors. *Quart. J. Roy. Meteor. Soc.* **134**(630): 131–145.

Ducrocq V, Ricard D, Lafore JP, Orain F. 2002. Storm-scale numerical rainfall prediction for five precipitating events over france: On the importance of the initial humidity field. *Wea. Forecasting* **17**(6): 1236–1256.

Dudhia J. 1989. Numerical study of convection observed during the winter monsoon experiment using a mesoscale two-dimensional model. *J. Atmos. Sci.* **46**(20): 3077–3107.

Dudhia J. 1993. A nonhydrostatic version of the penn state ncar mesoscale model - validation tests and simulation of an atlantic cyclone and cold-front. *Mon. Wea. Rev.* **121**(5): 1493–1513.

Fairall CW, Bradley EF, Hare JE, Grachev AA, Edson JB. 2003. Bulk parameterization of air-sea fluxes: Updates and verification for the COARE algorithm. *J. Climate* **16**(4): 571–591.

Feingold G, Grund CJ. 1994. Feasibility of using multiwavelength lidar measurements to measure cloud condensation nuclei. *Journal of Atmospheric and Oceanic Technology* **11**(6): 1543–1558.

Fernandez C, Gaertner MA, Gallardo C, Castro M. 1995. Simulation of a long-lived meso-beta scale convective system over the mediterranean coast of Spain .1. Numerical predictability. *Meteorol. Atmos. Phys.* **56**(3-4): 157–179.

Ferrier BS. 1994. A double-moment multiple-phase 4-class bulk ice scheme .1. description. *J. Atmos. Sci.* **51**(2): 249–280.

Fiori E, Parodi A, Siccardi F. 2009. Dealing with uncertainty: turbulent parameterizations and grid-spacing effects in numerical modelling of deep moist convective processes. *Nat. Hazards Earth Sys. Sci.* **9**: 1871–1880.

Fiori E, Parodi A, Siccardi F. 2010. Turbulence closure parameterization and grid spacing effects in simulated supercell storms. *J. Atmos. Sci.* **67**(12): 3870–3890.

Fiori E, Parodi A, Siccardi F. 2011. Uncertainty in prediction of deep moist convective processes: Turbulence parameterizations, microphysics and grid-scale effects. *Atmos. Res.* **100**(4): 447–456.

Foote G, Toit P. 1969. Terminal velocity of raindrops aloft. *J.Appl.Meteor.* **8**: 249–253.

Fresnay S, Hally A, Garnaud C, Richard E, Lambert D. 2012. Heavy precipitation events in the mediterranean: sensitivity to cloud physics parameterisation uncertainties. *Nat. Hazards Earth Sys. Sci.* **12**: 2671–2688.

Fritsch JM, Carbone RE. 2004. Improving quantitative precipitation forecasts in the warm season: A USWRP Research and Development Strategy. *Bull. Amer. Meteor. Soc.* **85**: 955–965.

Gebhardt C, Theis SE, Paulat M, Ben Bouallegue Z. 2011. Uncertainties in cosmode precipitation forecasts introduced by model perturbations and variation of lateral boundaries. *Atmos. Res.* **100**(2-3).

Gilmore MS, Straka JM, Rasmussen EN. 2004. Precipitation uncertainty due to variations in precipitation particle parameters within a simple microphysics scheme. *Mon. Wea. Rev.* **132**(11): 2610–2627.

Hally A, Richard E, Fresnay S, Lambert D. 2013. Ensemble simulations with perturbed physical parameterisations: Pre-hymex case studies. *Quart. J. Roy. Meteor. Soc.* doi:10.1002/qj.2257.

Harrington JY, Reisin T, Cotton WR, Kreidenweis SM. 1999. Cloud resolving simulations of arctic stratus - part ii: Transition-season clouds. *Atmos. Res.* **51**(1): 45–75.

Heymsfield AJ, Musil DJ. 1982. Case-study of a hailstorm in colorado .2. particle growth-processes at mid-levels deduced from insitu measurements. *J. Atmos. Sci.* **39**(12): 2847–2866.

Hong SY, Dudhia J, Chen SH. 2004. A revised approach to ice microphysical processes for the bulk parameterization of clouds and precipitation. *Mon. Wea. Rev.* **132**(1): 103–120.

Honnert R, Masson V, Couvreux F. 2011. A diagnostic for evaluating the representation of turbulence in atmospheric models at the kilometric scale. *J. Atmos. Sci.* **68**(12): 3112–3131.

Houtekamer PL, Mitchell HL, Deng XX. 2009. Model error representation in an operational ensemble Kalman filter. *Mon. Wea. Rev.* **137**(7): 2126–2143.

Houze RA, Hobbs PV, Herzegh PH, Parsons DB. 1979. Size distributions of precipitation particles in frontal clouds. *J. Atmos. Sci.* **36**(1): 156–162.

Jiang HL, Cotton WR, Pinto JO, Curry JA, Weissbluth MJ. 2000. Cloud resolving simulations of mixed-phase arctic stratus observed during base: Sensitivity to concentration of ice crystals and large-scale heat and moisture advection. *J. Atmos. Sci.* **57**(13): 2105–2117.

Kessler E. 1969. On the distribution and continuity of water substance in atmospheric circulations. *AMS Meteorological Monographs* **10**: 84.

Klemp JB, Wilhelmson RB. 1978. Simulation of 3-dimensional convective storm dynamics. *J. Atmos. Sci.* **35**(6): 1070–1096.

Knight C, Cooper W, Breed D, Paluch I, Smith P, Vali G. 1982. *Microphysics:hailstorms of the central high plains*, vol. 1. Colorado Associated University Press.

Lafore JP, Stein J, Asencio N, Bougeault P, Ducrocq V, Duron J, Fischer C, Héreil P, Mascart P, Masson V, Pinty JP, Redelsperger JL, Richard E, Vilà-Guerau de Arellano J. 1998. The Meso-NH atmospheric simulation system. part I: adiabatic formulation and control simulations. *Ann. Geophys.* **16**(1): 90–109.

Lascaux F, Richard E, Pinty JP. 2006. Numerical simulations of three different MAP IOPs and the associated microphysical processes. *Quart. J. Roy. Meteor. Soc.* **132**(619): 1907–1926.

Lin YL, Farley RD, Orville HD. 1983. Bulk parameterization of the snow field in a cloud model. *J. Climate. Appl. Meteorol.* **22**(6): 1065–1092.

Liu JY, Orville HD. 1969. Numerical modeling of precipitation and cloud shadow effects on mountain-induced cumuli. *J. Atmos. Sci.* **26**: 1283–1298.

Locatelli JD, Hobbs PV. 1974. Fall speeds and masses of solid precipitation particles. *J. Geophys. Res.* .

Lorenz EN. 1969. The predictability of a flow which possesses many scales of motion. *Tellus* **21**: 289–307.

Marecal V, Hauser D, Roux F. 1993. The 12/13 january 1988 narrow cold-frontal rainband observed during mfdp fronts-87 .2. microphysics. *J. Atmos. Sci.* **50**(7): 975–998.

Marshall J, Palmer W. 1948. The distribution of raindrops with size. *J.Appl.Meteor.* **5**: 165–166.

Mason S, Graham N. 2002. Areas beneath the relative operating characteristics (ROC) and relative operating levels (ROL) curves: Statistical significance and interpretation. *Quart. J. Roy. Meteor. Soc.* **128**(584): 2145–2166.

Masson V, Le Moigne P, Martin E, Faroux S, Alias A, Alkama R, Belamari S, Barbu A, Boone A, Bouyssel F, Brousseau P, Brun E, Calvet JC, Carrer D, Decharme B, Delire C, Donier S, Essaouini K, Gibelin AL, Giordani H, Habets F, Jidane M, Kerdraon G, Kourzeneva E, Lafaysse M, Lafont S, Lebeaupin C, Lemonsu A, Mahfouf JF, Marguinaud P, Mokhtari M, Morin S, Pigeon G, Salgado R, Seity Y, Taillefer F, Tanguy G, Tulet P, Vincendon B, Vionnet V, Voldoire A. 2013. The SURFEXv7.2 land and ocean surface platform for coupled or offline simulation of earth surface variables and fluxes. *Geosci. Model Dev.* **6**: 929–960.

Meyers MP, Walko RL, Harrington JY, Cotton WR. 1997. New rams cloud microphysics parameterization .2. the two-moment scheme. *Atmos. Res.* **45**(1): 3–39.

Miglietta MM, Rotunno R. 2009. Numerical simulations of conditionally unstable flows over a mountain ridge. *J. Atmos. Sci.* **66**(7): 1865–1885.

Miglietta MM, Rotunno R. 2010. Numerical simulations of low-cape flows over a mountain ridge. *J. Atmos. Sci.* **67**(7): 2391–2401.

Milbrandt JA, Yau MK. 2005. A multimoment bulk microphysics parameterization. part II: A proposed three-moment closure and scheme description. *J. Atmos. Sci.* **62**(9): 3065–3081.

Mlawer EJ, Taubman SJ, Brown PD, Iacono MJ, Clough SA. 1997. Radiative transfer for inhomogeneous atmospheres: RRTM, a validated corrolated-k model for the longwave. *J. Geophys. Res.* **102D**: 16 663–16 682.

Molteni F, Buizza R, Palmer TN, Petroliagis T. 1996. The ecmwf ensemble prediction system: Methodology and validation. *Quart. J. Roy. Meteor. Soc.* **122**(529): 73–119.

Morrison H, Curry JA, Khvorostyanov VI. 2005. A new double-moment microphysics parameterization for application in cloud and climate models. part I: Description. *J. Atmos. Sci.* **62**(6): 1665–1677.

Noilhan J, Mafhouf J. 1996. The ISBA land surface parameterisation. *Global Planet Change* **13**: 145–159.

Nuissier O, Ducrocq V, Ricard D, Lebeaupin C, Anquetin S. 2008. A numerical study of three catastrophic precipitating events over southern france. I: Numerical framework and synoptic ingredients. *Quart. J. Roy. Meteor. Soc.* **134**(630): 111–130.

Pantillon F, Chaboureau JP, Lac C, Mascart P. 2012. On the role of a Rossby wave train during the extratropical transition of hurricane Helene (2006). *Quart. J. Roy. Meteor. Soc.* **138**.

Passarelli RE. 1978. Approximate analytical model of vapor-deposition and aggregation growth of snowflakes. *J. Atmos. Sci.* **35**(1): 118–124.

Pergaud J, Masson V, Malardel S, Couvreux F. 2009. A parameterization of dry thermals and shallow cumuli for mesoscale numerical weather prediction. *Bound. Layer. Meteor.* **132**: 83–106.

Pinty JP, Jabouille P. 17-21 August 1998. A mixed-phase cloud parameterization for use in a mesoscale non-hydrostatic model: simulations of a squall line and of orographic precipitations. In: *Tenth AMS Cloud Physics Conference*. American Meteorological Society: Everett, WA, USA, pp. 217–220.

Prandtl L. 1925. Z.angew. *Math.Mech.* **5**: 136–139.

Pruppacher R, Klett J. 1978. *Microphysics of clouds and precipitation*. Reidel.

Redelsperger JL, Sommeria G. 1981. Method of representing subgrid scale turbulence for a 3-dimensional model of cloud convection. *Bound. Layer. Meteor.* **21**(4): 509–530.

Reisner J, Rasmussen RM, Bruintjes RT. 1998. Explicit forecasting of supercooled liquid water in winter storms using the mm5 mesoscale model. *Quart. J. Roy. Meteor. Soc.* **124**(548): 1071–1107.

Richard E, Chaumerliac N. 1989. Effects of different rain parameterizations on the simulation of mesoscale orographic precipitation. *J. Appl. Meteor.* **28**(11): 1197–1212.

Richard E, Cosma S, Tabary P, Pinty JP, Hagen M. 2003. High-resolution numerical simulations of the convective system observed in the Lago Maggiore area on 17 september 1999 (MAP IOP 2a). *Quart. J. Roy. Meteor. Soc.* **129**(588): 543–564.

Rutledge SA, Hobbs PV. 1983. The mesoscale and microscale structure and organization of clouds and precipitation in mid-latitude cyclones .part VIII: a model for the seeder-feeder process in warm-frontal rainbands. *J. Atmos. Sci.* **40**(5): 1185–1206.

Schwartz CS, Kain JS, Weiss SJ, Xue M, Bright DR, Kong F, Thomas KW, Levit JJ, Coniglio MC, Wandishin MS. 2010. Toward improved convection-allowing ensembles: Model physics sensitivities and optimizing probabilistic guidance with small ensemble membership. *Wea. Forecasting* **25**(1).

Seifert A, Beheng KD. 2001. A double-moment parameterization for simulating autoconversion, accretion and selfcollection. *Atmos. Res.* **59**: 265–281.

Seifert A, Beheng KD. 2006. A two-moment cloud microphysics parameterization for mixed-phase clouds. Part 1: Model description. *Meteorol. Atmos. Phys.* **92**(1-2): 45–66.

Seity Y, Brousseau P, Malardel S, Hello G, Benard P, Bouttier F, Lac C, Masson V. 2011. The AROME-France Convective-Scale Operational Model. *Mon. Wea. Rev.* **139**(3): 976–991.

Smagorinsky J. 1963. General circulation experiments with the primitive equations. *Mon. Wea. Rev.* **91**: 99–164.

Solomon A, Morrison H, Persson O, Shupe MD, Bao JW. 2009. Investigation of microphysical parameterizations of snow and ice in arctic clouds during m-pace through model-observation comparisons. *Mon. Wea. Rev.* **137**(9): 3110–3128.

Starr DO, Cox SK. 1985. Cirrus clouds .1. a cirrus cloud model. *J. Atmos. Sci.* **42**(23): 2663–2681.

Stensrud D, Bao J, Warner T. 2000. Using initial conditions and model physics perturbations in short-range ensemble simulations of mesoscale convective systems. *Mon. Wea. Rev.* **128**: 2077–2107.

Stensrud DJ. 2001. Using short-range ensemble forecasts for predicting severe weather events. *Atmos. Res.* **56**(1-4): 3–17.

Stensrud DJ, Brooks HE, Du J, Tracton MS, Rogers E. 1999. Using ensembles for short-range forecasting. *Mon. Wea. Rev.* **127**(4): 433–446.

Straka JM, Mansell ER. 2005. A bulk microphysics parameterization with multiple ice precipitation categories. *J. Appl. Meteor.* **44**(4): 445–466.

Taylor KE. 2001. Summarizing multiple aspects of model performance in a single diagram. *J. Geophys. Res.* **106**(D7): 7183–7192.

Thompson G, Field PR, Rasmussen RM, Hall WD. 2008. Explicit forecasts of winter precipitation using an improved bulk microphysics scheme. part II: Implementation of a new snow parameterization. *Mon. Wea. Rev.* **136**(12): 5095–5115.

Thompson G, Rasmussen RM, Manning K. 2004. Explicit forecasts of winter precipitation using an improved bulk microphysics scheme. part I: Description and sensitivity analysis. *Mon. Wea. Rev.* **132**(2): 519–542.

Vié B, Molinié G, Nuissier O, Vincendon B, Ducrocq V, Bouttier F, Richard E. 2012. Hydro-meteorological evaluation of a convection-permitting ensemble prediction system for mediterranean heavy precipitating events. *Nat. Hazards Earth Sys. Sci.* **12**(8): 2631–2645.

Vié B, Nuissier O, Ducrocq V. 2011. Cloud-resolving ensemble simulations of mediterranean heavy precipitating events: Uncertainty on initial conditions and lateral boundary conditions. *Mon. Wea. Rev.* **139**(2): 403–423.

Waldvogel A. 1974. The $n_0$ jump of raindrop spectra. *J. Atmos. Sci.* **31**: 1067–1078.

Walko RL, Cotton WR, Meyers MP, Harrington JY. 1995. New RAMS cloud microphysics parameterization:I the single-moment scheme. *Atmos. Res.* **38**(1-4): 29–62.

Walser A, Luthi D, Schar C. 2004. Predictability of precipitation in a cloud-resolving model. *Mon. Wea. Rev.* **132**(2): 560–577.

Weisman ML, Klemp JB. 1982. The dependence of numerically simulated convective storms on vertical wind shear and buoyancy. *Mon. Wea. Rev.* **110**(6): 504–520.

Weisman ML, Skamarock WC, Klemp JB. 1997. The resolution dependence of explicitly modeled convective systems. *Mon. Wea. Rev.* **125**(4): 527–548.

Wilks DS. 1995. *Statistical Methods in the Atmospheric Sciences*. Academic Press. 467 pp.

Williams R, Wojtowicz PJ. 1982. A simple-model for droplet size distribution in atmospheric clouds. *J. Appl. Meteor.* **21**(7).

Willis PT. 1984. Functional fits to some observed drop size distributions and parameterization of rain. *J. Atmos. Sci.* **41**(9): 1648–1661.

Wyngaard JC. 2004. Toward numerical modeling in the "terra incognita". *J. Atmos. Sci.* **61**(14): 1816–1826.

Ziegler CL. 1985. Retrieval of thermal and microphysical variables in observed convective storms .1. model development and preliminary testing. *J. Atmos. Sci.* **42**(14).